13.04 LECTURE NOTES
HYDROFOILS AND PROPELLERS *

Justin E. Kerwin

January 2001†

Contents

---

†Web document updated March 9

List of Figures

.

1 TWO DIMENSIONAL FOIL THEORY

1.1 Introduction

We will begin our examination of hydrofoil and propeller flows by looking at the flow around two-dimensional foil sections. It is important to recognize at the outset that a two-dimensional flow is an idealization. Flows around marine propellers, sailboat keels or control surfaces are inherently three-dimensional. Moreover, it is even impossible to create a truly two-dimensional flow in a wind or water tunnel. While the foil model may be perfectly placed between the walls of the tunnel test section, interaction between the tunnel wall boundary layers and the foil generate three-dimensional features that disturb the two-dimensionality of the flow field. Reliable experimental measurements of two-dimensional foil sections therefore require careful attention to the issue of avoiding unwanted three-dimensional effects.

Of course, two-dimensional flows can be modeled theoretically, and are much easier to deal with than three-dimensional flows. Moreover, the fundamental mechanism for creating lift as well as much of the methodology for designing optimum foil section shapes can be explained by two-dimensional concepts. Design methods for airplane wings, marine propellers, and everything in between rely heavily on the use of systematic foil section data. But, it is important to recognize that one cannot simply piece together a three-dimensional wing or propeller in a strip-wise manner from a sequence of two-dimensional foil sections and expect to get an accurate answer. We will see later why this is true, and how two and three-dimensional flows can be properly combined.

A surprisingly large number of methods exist for predicting the flow around foil sections, and it is important to understand their advantages and disadvantages. They can be characterized in the following three ways,

1. Analytical or Numerical
2. Potential Flow (inviscid) methods, Fully Viscous Methods or Coupled Potential Flow/Boundary Layer methods
3. Exact, Linearized, or Partially Linearized methods.

Not all combinations of these three characteristics are possible. For example, fully viscous flows (except in a few trivial cases) must be solved numerically. Perhaps one could construct a three-dimensional graph showing all the possible combinations, but this will not be attempted here! In this chapter, we will start with the method of conformal mapping, which can easily be identified as being *analytical, inviscid and exact.* We will then look at *inviscid,linear* theory, which is can either be *analytical* or *numerical.* The principal attribute of the *inviscid, linear, numerical* method is that can be readily extended to three-dimensional flows.

This will be followed by a brief look at some corrections to linear theory, after which we will look at panel methods, which can be categorized as *numerical, inviscid, and exact.* We will then look at *coupled potential flow/boundary layer methods*, which can be characterized as a *numerical, exact* method [1] Finally, we will take a brief look at results obtained by a *Reynolds Averaged Navier-Stokes (RANS)* code, which is *fully viscous, numerical, and exact* [2].

1.2 Foil Geometry

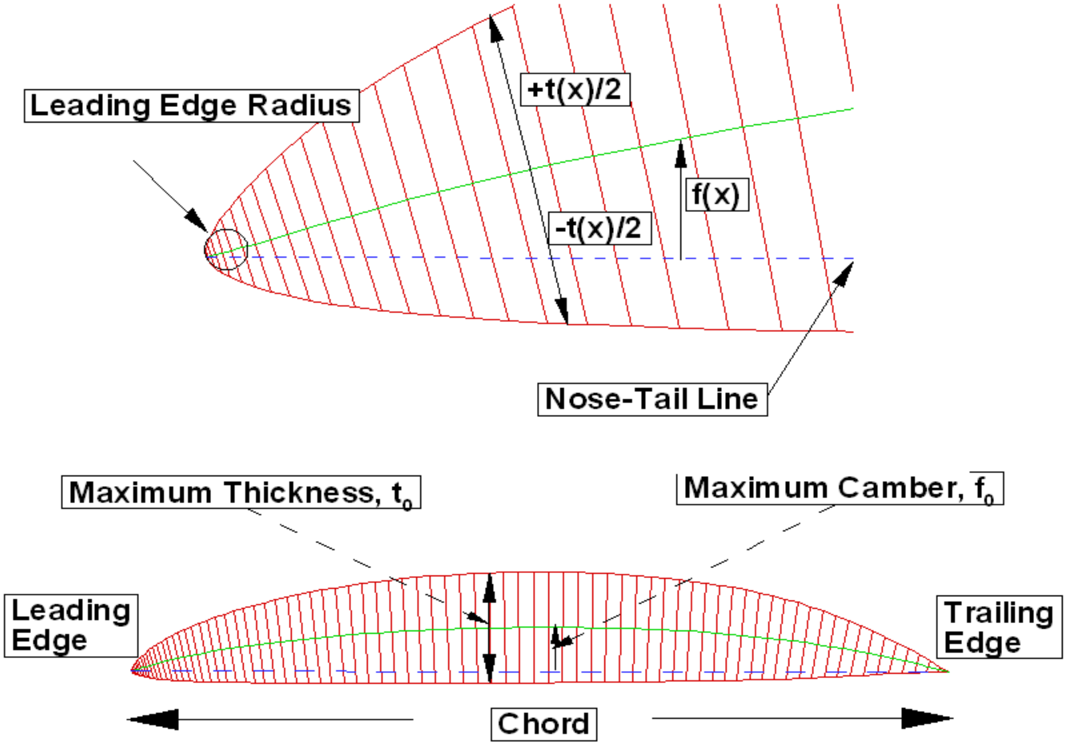

Figure 1: *Illustration of notation for foil section geometry.*

---

[1] Well, more or less. Boundary layer theory involves linearizing assumptions that the boundary layer is thin, but the coupled method makes no assumptions that the foil is thin.

[2] Here we go again! The foil geometry is exact, but the turbulence models employed in RANS codes are approximations.

Before we start with the development of methods to obtain the flow around a foil, we will first introduce the terminology used to define foil section geometry. As shown in figure 1, good foil sections are generally slender, with a sharp (or nearly sharp) trailing edge, and a rounded leading edge. The base line for foil geometry is a line connecting the trailing edge to the point of maximum curvature at the leading edge, and this is shown as the dashed line in the figure. This is known as the *nose-tail line*, and its length is the *chord,* c of the foil.

The particular coordinate system notation used to describe a foil varies widely depending on application, and one must therefore be careful when reading different texts or research reports. It is natural to use x, y as the coordinate axes for a two-dimensional flow, particularly if one is using the complex variable $z = x + iy$. The nose-tail line is generally placed on the x axis, but in some applications the x axis is taken to be in the direction of the onset flow, in which case the nose-tail line is inclined at an *angle of attack*, α with respect to the x axis. Positive x can be either oriented in the upstream or downstream direction, but we shall use the downstream convention here.

For three-dimensional planar foils, it is common to orient the y coordinate in the *span wise* direction. In this case, the foil section ordinates will be in the z direction. Finally, in the case of propeller blades, a special curvilinear coordinate system must be adopted, and we will introduce this later.

As shown in figure 1, a foil section can be thought of as the combination of a *mean line*, $f(x)$ with maximum value f_o and a symmetrical *thickness form*, $t(x)$, with maximum value t_o. The thickness form is added at right angles to the mean line, so that points on the upper and lower surfaces of the foil will have coordinates,

$$\begin{aligned}
x_u &= x - \frac{t(x)}{2}\sin\theta \\
y_u &= f(x) + \frac{t(x)}{2}\cos\theta \\
x_l &= x + \frac{t(x)}{2}\sin\theta \\
y_l &= f(x) - \frac{t(x)}{2}\cos\theta
\end{aligned} \tag{1}$$

where $\theta = \arctan(df/dx)$ is the slope of the mean line at point x.

The quantity f_o/c is called the *camber ratio*, and in a similar manner, t_o/c is called the *thickness ratio.* It has been common practice to develop foil shapes by scaling generic mean line and thickness forms to their desired values, and combining then by using equation 1 to obtain the geometry of the foil surface. A major source of mean line and thickness form data was created by the NACA (now NASA)in the 1930's and 1940's [3] For example, Figure 2 shows sample tabulations of the geometry of the NACA *Mean Line a=0.8* and the NACA 65A010 Basic Thickness Form. Note that the tabulated mean line has a camber ratio $t_o/c = 0.0679$, while the thickness form has a thickness ratio $t_o/c = 0.10$. Included in the tables is some computed velocity and pressure data that we will refer to later.

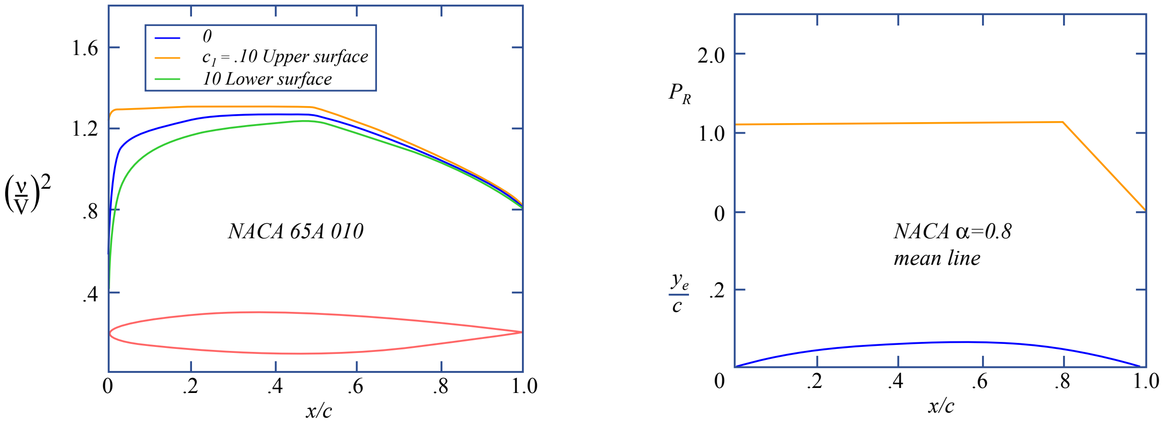

x (per cent c)	y (per cent c)	$(v/V)^2$	v/V	$\Delta v_a/V$
0	0	0	0	2.987
0.5	0.765	0.897	0.947	1.878
0.75	0.928	0.948	0.974	1.619
1.25	1.183	1.010	1.005	1.303
2.5	1.623	1.089	1.044	0.936
5.0	2.182	1.148	1.071	0.679
7.5	2.650	1.176	1.084	0.559
10	3.040	1.194	1.093	0.478
15	3.658	1.218	1.104	0.382
20	4.127	1.234	1.111	0.323
25	4.483	1.247	1.117	0.281
30	4.742	1.257	1.121	0.249
35	4.912	1.265	1.125	0.222
40	4.995	1.272	1.128	0.198
45	4.983	1.277	1.130	0.178
50	4.863	1.271	1.127	0.161
55	4.632	1.241	1.114	0.144
60	4.304	1.208	1.099	0.127
65	3.899	1.172	1.083	0.111
70	3.432	1.133	1.064	0.097
75	2.912	1.091	1.045	0.084
80	2.352	1.047	1.023	0.071
85	1.771	0.999	0.999	0.058
90	1.188	0.949	0.974	0.045
95	0.604	0.893	0.945	0.029
100	0.021	0	0	0
L.E. radius: 0.639 per cent c T.E. radius: 0.023 per cent c				

NACA 65A010 Basic Thickness Form

$c_{l_i} = 1.0$ α; = 1.54^0 $c_{m_{c/4}} = -0.202$				
x (per cent c)	Y_c (per cent c)	dy_c/dx	P_R	$\Delta v/V = P_R/4$
0	0			
0.5	0.287	0.48535		
0.75	0.404	0.44925		
1.25	0.616	0.40359		
2.5	1.077	0.34104		
5.0	1.841	0.27718		
7.5	2.483	0.23868		
10	3.043	0.21050		
15	3.985	0.16892		
20	4.748	0.13734		
25	5.367	0.11101		
30	5.863	0.08775	1.111	0.278
35	6.248	0.06634		
40	6.528	0.04601		
45	6.709	0.02613		
50	6.790	0.00620		
55	6.770	- 0.01433		
60	6.644	- 0.03611		
65	6.405	- 0.06010		
70	6.037	- 0.08790		
75	5.514	- 0.12311		
80	4.771	- 0.18412		
85	3.683	- 0.23921	0.833	0.208
90	2.435	- 0.25583	0.556	0.139
95	1.163	- 0.24904	0.278	0.069
100	0	- 0.20385	0	0

Data for NACA Mean Line α = 0.8

Sample of tabulated geometry and flow data for an NACA mean line and thickness form.

Figure by MIT OCW. Adapted from Abbott and von Doenhoff, 1959.

An important geometrical characteristic of a foil is its leading edge radius, r_L, as shown in figure 1. While this quantity is, in principle, contained in the thickness function $t(x)$, extracting an accurate value from sparsely tabulated data is risky. It is therefore provided explicitly in the NACA tables— for example, the NACA 65A010 has a leading edge radius of 0.639 percent of the chord. If you wish to scale this thickness form to another value, all of the ordinates are simply scaled linearly. However, the leading edge radius scales with the *square* of the thickness of the foil, so that a fifteen percent thick section of the same form would have a leading edge radius of 1.44 percent of the chord. We can show why this is true by considering an example where we wish to generate thickness form (2) by linearly scaling all the ordinates of thickness form (1),

$$t^{(2)}(x) = t^{(1)}(x)\frac{[t_o/c]^{(2)}}{[t_o/c]^{(1)}} \tag{2}$$

for all values of x. Then, the derivatives dt/dx and d^2t/dx^2 will also scale linearly with thickness/chord ratio. Now, at the leading edge, the radius of curvature, r_L is

$$r_L = \lim_{x\to 0} \frac{\left[1 + \left(\frac{dt}{dx}\right)^2\right]^{3/2}}{\frac{d^2t}{dx^2}} \tag{3}$$

evaluated at the leading edge, which we will locate at $x = 0$. Since the slope dt/dx goes to infinity at a rounded leading edge, equation 3 becomes

$$r_L = \lim_{x\to 0} \frac{\left(\frac{dt}{dx}\right)^3}{\frac{d^2t}{dx^2}} = (const)\left(\frac{t_o}{c}\right)^2 \tag{4}$$

which confirms the result stated earlier.

Some attention must also be given to the details of the trailing edge geometry. As we will see, the unique solution for the flow around a foil section operating in an inviscid fluid requires that the trailing edge be sharp. However, practical issues of manufacturing and strength make sharp trailing edges impractical. In some cases, foils are built with a square (but relatively thin) trailing edge, as indicated in figure 2, although these are sometimes rounded. An additional practical problem frequently arises in the case of foil sections for marine propellers. Organized vortex shedding from blunt or rounded trailing edges may occur at frequencies which coincide with vibratory modes of the blade trailing edge region. When this happens, strong discrete acoustical tones are generated, which are commonly referred to as *singing*. This problem can sometimes be cured by modifying the trailing edge geometry in such a way as to force flow separation on the upper surface of the foil slightly upstream of the trailing edge.

An example of an “anti-singing” trailing edge modification is shown in figure 3. It is important to note that the nose-tail line of the modified section no longer passes through the trailing edge, so that the convenient decomposition of the geometry into a mean line and thickness form is somewhat disrupted.

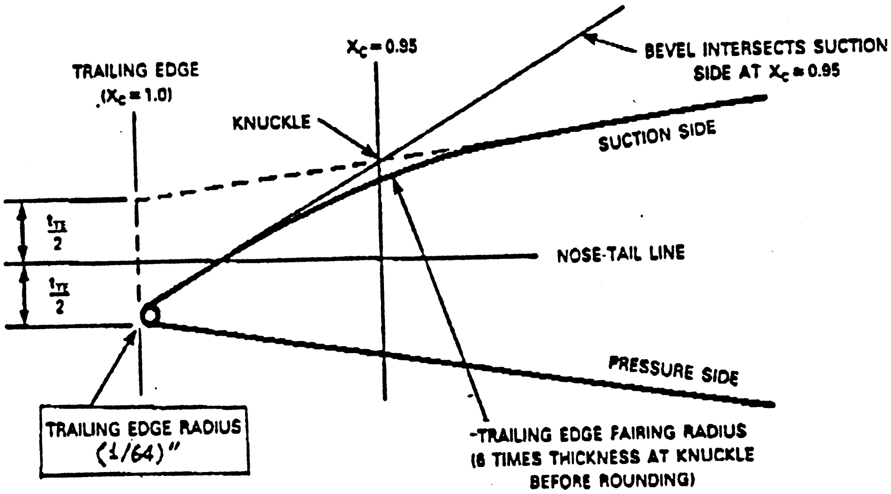

Figure 3: *An example of a trailing edge modification used to reduce singing. This particular procedure is frequently used for U.S. Navy and commercial applications.*

Courtesy of U.S. Navy. Used with permission.

The procedure for constructing foil geometry described so far is based on traditional manual drafting practices which date back at least to the early 1900’s. Defining curves by sparse point data, with the additional requirement of fairing into a specified radius of curvature leaves a lot of room for interpretation and error. In the present world of CAD software and numerically controlled machines, foil surfaces— and ultimately three-dimensional propeller blades, hubs and fillets— are best described in terms of standardized geometric “entities” such as *Non-Uniform Rational B-Splines* (NURBS) curves and surfaces. As an example, figure 4 shows a B-spline representation of a foil section with proportions typical of current marine propeller. In this case, the foil, together with it’s surface curvature and normal vector, is uniquely defined by a set of 16 (x, y) coordinates representing the vertices of the B-spline control polygon. This is all that is needed to introduce the shape into a computational fluid dynamics code, construct a model, or construct the full size object.

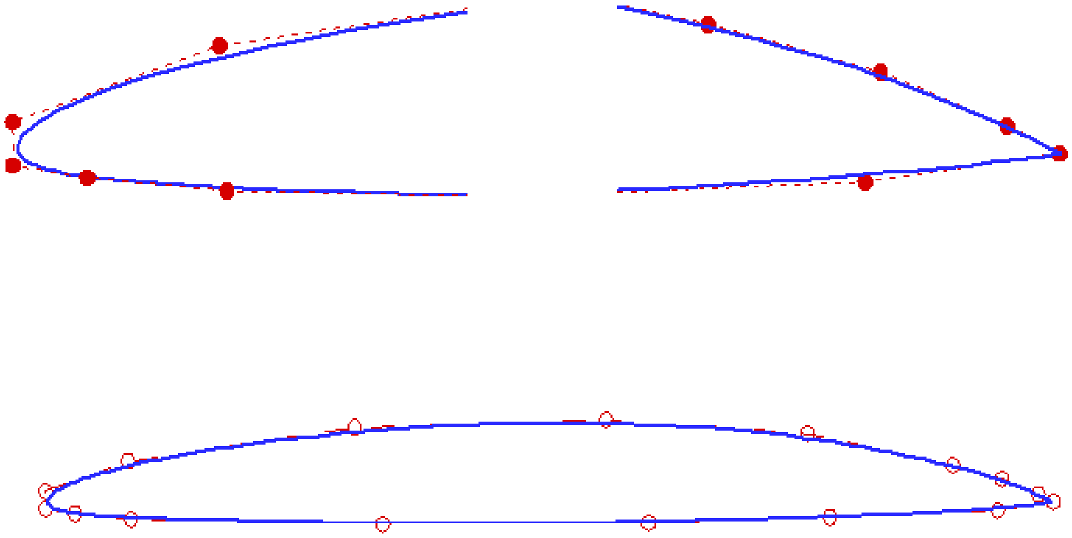

Figure 4: *An example of a complete geometrical description of a foil section (including anti-singing trailing edge modifications) using a fourth order uniform B-spline. The symbols connected with dashed lies represent the B-spline control polygon which completely defines the shape of the foil. The resulting foil surface evaluated from the B-spline is shown as the continuous curve. The upper curves show an enlargement of the leading and trailing edge regions. The complete foil is shown in the lower curve.*

1.3 Conformal Mapping

1.3.1 History

The initial development of the field of airfoil theory took place in the early 1900's, long before the invention of the computer. Obtaining an accurate solution for the flow around such a complex shape as a foil section, even in two-dimensions, was therefore a formidable task. Fortunately, one analytical technique, known as the method of conformal mapping, was known at that time, and provided a means of determining the *exact* inviscid flow around a limited class of foil section shapes. This technique was first applied by Joukowski [ ] in 1914, and the set of foil geometries created by the mapping function which he developed bears his name. A more general mapping function, which includes the Joukowski mapping as a special case, was then introduced by Karman and Trefftz [ ]. While other several investigators introduced different mapping functions, the next significant development was by Theodorsen [ ], who developed an approximate analytical/numerical technique for obtaining the mapping function for a foil section of arbitrary shape. Theodorsen's work was the basis for the development of an extensive systematic series of foil sections published by the National Advisory Commission on Aeronautics (NACA) in the late 1930's and 1940's [ ]. The old NACA section results were done, of necessity, by a combination of graphical and hand computation. An improved conformal mapping method of computing the flow around arbitrary sections, suitable for implementation on a digital computer, was developed by [4] who found, not surprisingly, that in accuracies existed in the earlier NACA data. Brockett's work led to the development of foil section design charts which are used for propeller design at the present time.

The theoretical basis for the method of conformal mapping is given in most advanced calculus texts [Hildebrand?], so only the essential highlights will be developed here. One starts with the known solution to a simple problem— in this case the flow of a uniform stream past a circle. The circle is then "mapped" into some geometry that resembles a foil section, and if you follow the rules carefully, the flow around the circle will be transformed in such a way as to represent the correct solution for the mapped foil section.

1.3.2 Potential Flow Around A Circle

Let us start with the flow around a circle. We know that in a two-dimensional ideal flow, the superposition of a uniform free stream and a dipole (whose axis is oriented in opposition to the direction of the free stream) will result in a dividing streamline whose form is circular. We also know that this is not the most general solution to the problem, because we can additionally superimpose the flow created by a point vortex of arbitrary

---

[4] DTMB Report 1780, 1966

strength located at the center of the circle. The solution is therefore not unique, but this problem will be addressed later when we look at the resulting flow around a foil.

To facilitate the subsequent mapping process, we will write down the solution for a circle of radius r_c whose center is located at an arbitrary point (x_c, y_c) in the $x - y$ plane, as shown in Figure 5. The circle will be required to intersect the positive x axis at the point $x = a$, so that the radius of the circle must be,

$$r_c = \sqrt{(x_c + a)^2 + y_c^2} \tag{5}$$

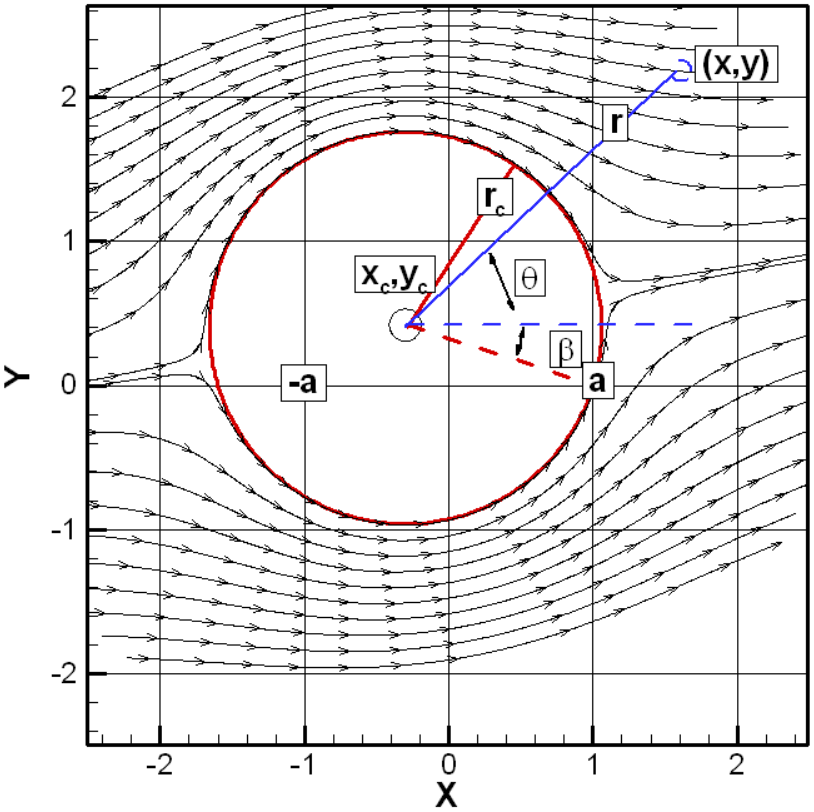

Figure 5: *Flow around a circle with zero circulation. The center of the circle is located at* $x = -.3, y = 0.4$. *The circle passes through* $x = a = 1.0$. *The flow angle of attack is 10 degrees.*

We will see later that in order to obtain physically plausible foil shapes, the point $x = -a$ must either be interior of the circle or lie on its boundary. This simply requires that $x_c \leq 0$. Finally, the uniform free stream velocity will be of speed U and will be inclined at an angle α with respect to the x axis.

With these definitions, the velocity components (u, v) in the x and y directions are

$$\begin{aligned} u(x,y) &= U\cos(\alpha) - U\left(\frac{r_c}{r}\right)^2 \cos(2\theta - \alpha) - \frac{\Gamma}{2\pi r} sin(\theta) \\ v(x,y) &= U\sin(\alpha) - U\left(\frac{r_c}{r}\right)^2 \sin(2\theta - \alpha) + \frac{\Gamma}{2\pi r} cos(\theta) \end{aligned} \tag{6}$$

where r and θ are polar coordinates with origin at *the center of the circle*, so that

$$\begin{aligned} x &= x_c + r\cos(\theta) \\ y &= y_c + r\sin(\theta) \end{aligned} \tag{7}$$

Note that we are following a strict right-handed coordinate system, so that positive angles and positive tangential velocities are in a counter clockwise direction. A vortex of positive strength, Γ, therefore induces a velocity which is in the *negative* x direction on the top of the circle and a *positive* x direction at the bottom.

Figure 5 shows the result in the special case where the circulation, Γ, has been set to zero, and the resulting flow pattern is clearly symmetrical about a line inclined at the angle of attack— which in this case was selected to be ten degrees. If, instead, we set the circulation equal to a value of $\Gamma = -7.778695$, the flow pattern shown in figure 6 results.

Clearly, the flow is no longer symmetrical, and the two stagnation points on the circle have both moved down. The angular coordinates of the stagnation points on the circle can be obtained directly from equation 6 by setting $r = r_c$ and solving for the tangential component of the velocity,

$$\begin{aligned} u_t &= v\cos(\theta) - u\sin(\theta) \\ &= -2U\sin(\theta - \alpha) + \frac{\Gamma}{2\pi r_c} \end{aligned} \tag{8}$$

If we set $u_t = 0$ in equation 8 and denote the angular coordinates of the stagnation points as θ_s, we obtain

$$\sin(\theta_s - \alpha) = \frac{\Gamma}{4\pi r_c U} \tag{9}$$

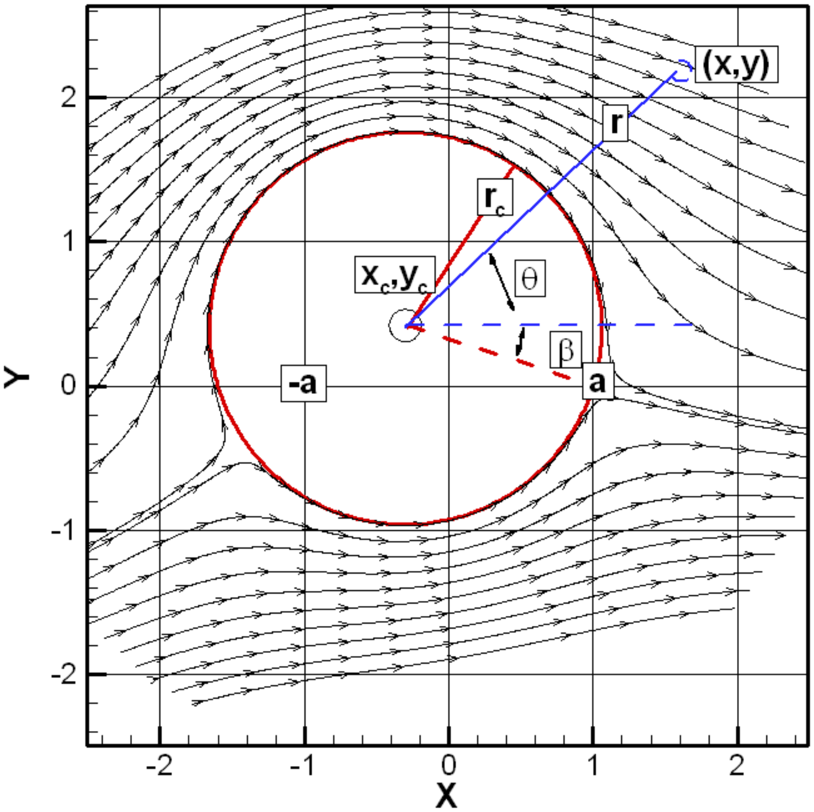

Figure 6: *Flow around a circle with circulation. The center of the circle is located at* $x = -.3, y = 0.4$*. The circle passes through* $x = a = 1.0$*. Note that the rear stagnation point has moved to* $x = a$*.*

For the example shown in figure 6, substituting $r_c = \sqrt{(1.3^2 + 0.4^2)} = 1.3602$, $\Gamma = -7.778695$, $U = 1.0$ and $\alpha = 10$ degrees into equation 9, we obtain

$$\sin(\theta_s - \alpha) = -0.45510 \quad : \quad \theta_s = -17.1deg, \ -142.9deg \tag{10}$$

In this special case, we see that we have carefully selected Γ in such a way as to move the rear stagnation point exactly to the point a on the x axis, since $\theta_s = -\beta$, where

$$\beta = \arcsin \frac{y_c}{r_c} \tag{11}$$

1.3.3 Conformal Mapping for Dummies

Conformal mapping is a useful technique for solving two-dimensional ideal fluid problems because of the analogy between the properties of an analytic function of a complex variable and the governing equations of a fluid. We know that the flow of an ideal fluid in two dimensions can be represented either by a scalar function $\phi(x, y)$ known as the *velocity potential*, or by a scalar function $\psi(x, y)$ known as the *stream function.* To be a legitimate ideal fluid flow, both must satisfy Laplace's equation. The fluid velocities can then be obtained from either, as follows,

$$\begin{aligned} u &= \frac{\partial \phi}{\partial x} = \frac{\partial \psi}{\partial y} \\ v &= \frac{\partial \phi}{\partial y} = -\frac{\partial \psi}{\partial x} \end{aligned} \tag{12}$$

Now let us suppose that the physical x, y coordinates of the fluid flow are the real and imaginary parts of a complex variable $z = x + iy$. We can construct a *complex potential* $\Phi(z)$ by assigning the real part to be the velocity potential and the imaginary part to be the stream function,

$$\Phi(z) = \phi(x, y) + i\psi(x, y) \tag{13}$$

Since the real and imaginary parts of Φ each satisfy Laplace's equation, Φ is an *analytic* function [5]. In addition, the derivative of Φ has the convenient property of being the conjugate of the "real" fluid velocity, $u + iv$. An easy way to show this is to compute $d\Phi/dz$ by taking the increment dz in the x direction,

$$\begin{aligned} \frac{d\Phi}{dz} &= \frac{\partial \Phi}{\partial x} = \frac{\partial \phi}{\partial x} + i\frac{\partial \psi}{\partial x} \\ &= u - iv \end{aligned} \tag{14}$$

where the second line of equation 14 follows directly from equation 12. If you are not happy with this approach, try taking the increment dz in the iy direction, and you will get the identical result. This has to be true, since Φ is analytic and it's derivative must therefore be unique.

---

[5] Remember, an analytic function is one that is single valued and whose derivative is uniquely defined, i.e. the value of it's derivative is independent of the path taken to obtain the limiting value of $\delta\Phi/\delta z$

We now introduce a *mapping function* $\zeta(z)$, with real part ξ and imaginary part η. We can interpret the z plane and the ζ graphically as two different *maps*. For example, if the z plane is the representation of the flow around a circle (shown in figures 5 or 6), then each pair of x, y coordinates on the surface of the circle, or on any one of the flow streamlines, will map to a corresponding point ξ, η in the ζ plane, depending on the particular mapping function $\zeta(z)$. This idea may make more sense if you take an advanced look at figure 7. The fancy looking foil shape was, indeed, mapped from a circle.

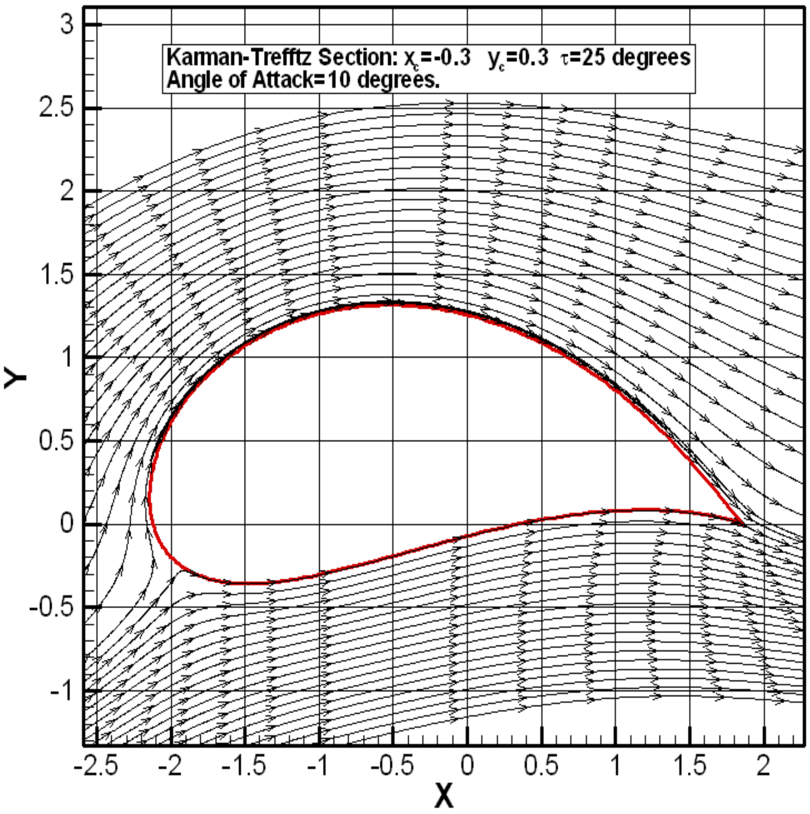

Figure 7: *Flow around a Karman-Trefftz foil derived from the flow around a circle shown in figure 6 with a specified tail angle of* $\tau = 25$ *degrees.*

While it is easy to confirm that the circle has been mapped into a more useful foil shape, how do we know that the fluid velocities and streamlines in the ζ plane are valid? The answer is that if $\Phi(z)$ and the mapping function $\zeta(z)$ are both analytic, then $\Phi(\zeta)$ is also analytic. It therefore represents a valid 2-D fluid flow, but it may not necessarily be one that we want. However, if the dividing streamline produces a shape that we accept, then the only remaining flow property that we need to verify is whether or not the flow at large distances from the foil approaches a uniform stream of speed U and angle of attack α. The latter is ensured if the mapping function is constructed in such a way that $\zeta = z$ in the limit as z goes to infinity.

Finally, the complex velocity in the ζ plane can simply be obtained from the complex velocity in the z plane,

$$[u - iv]_\zeta = \frac{d\Phi}{d\zeta} = \frac{\frac{d\Phi}{dz}}{\frac{d\zeta}{dz}} = \frac{[u - iv]_z}{\frac{d\zeta}{dz}} \tag{15}$$

Even though we introduced the concept of the complex potential, Φ, we don't actually need it. From equation 15, all we need to get the velocity field around the foil is the velocity around the circle and the derivative of the mapping function. And, of course, we need the mapping function itself to find the location of the actual point in the ζ plane where this velocity occurs.

Performing complex operations has been greatly facilitated by the availability of computer languages that understand how to do it. In particular, complex arithmetic is built into the *Fortran* language. A listing of a *Fortran90* computer code called *MAPSL* is provided in the last section of these notes. This code performs all of the operations described in this section, and may serve as a useful guide in understanding the process.

1.3.4 The Karman-Trefftz Mapping Function

The Karman-Trefftz transformation maps a point z to a point ζ using the following relationship

$$\zeta = \frac{\lambda a \left[(z+a)^\lambda + (z-a)^\lambda\right]}{(z+a)^\lambda - (z-a)^\lambda} \tag{16}$$

where λ and a are given real constants, whose purpose we will discover shortly. The derivative of the mapping function, which we will need to transform the velocities from the z plane to the ζ plane can be obtained directly from 16

$$\frac{d\zeta}{dz} = 4\lambda^2 a^2 \frac{\left[(z-a)^{\lambda-1}(z+a)^{\lambda-1}\right]}{\left[(z+a)^\lambda - (z-a)^\lambda\right]^2} \tag{17}$$

We can see immediately from equation 16 that $\lambda = 1$ the mapping function reduces to $\zeta = z$, so this produces an exact photocopy of the original flow! Note also, that when $z = \pm a$, $\zeta = \pm\lambda a$. Since we want to stretch out the circle, useful values of λ will therefore be greater that 1.0.

Finally, from equation 17, the derivative of the mapping function is zero when $z = \pm a$. These are called *critical points* in the mapping function, meaning that strange things are likely to happen there. Most difficult concepts of higher mathematics can best be understood by observing the behavior of small bugs. Suppose a bug is walking along the perimeter of the circle in the z plane, starting at some point z below the point a. The bug's friend starts walking along the perimeter of the foil in the ζ plane starting at the mapped point $\zeta(z)$. The magnitude and direction of the movement of the second bug is related to that of the first bug by the derivative of the mapping function. If $d\zeta/dz$ is non-zero, the relative progress of both bugs will be smooth and continuous. But when the first bug gets to the point a, the second bug stops dead in it's tracks, while the first bug continues smoothly. After point a, the derivative of the mapping function changes sign, so the second bug reverses it's direction. Thus, a sharp corner is produced, as is evident from figure 7.

The included angle of the corner (or tail angle in this case) depends on the way in which $d\zeta/dz$ approaches zero. While we will not prove it here, the tail angle τ (in degrees) and the exponent λ in the mapping function are simply related,

$$\lambda = 2 - \frac{\tau}{180} \quad \tau = 180(2 - \lambda) \tag{18}$$

so that the tail angle corresponding to $\lambda = 1.86111$ is 25 degrees, which is the value specified for the foil shown in figure 7. Note that if $\lambda = 2$ in equation 18 the resulting tail angle is zero, i.e. a cusped trailing edge results. In that case, the mapping function in equation 16 reduces to a much simpler form which can be recognized as the more familiar Joukowski transformation,

$$\zeta = z + \frac{a^2}{z} \tag{19}$$

Finally, if $\lambda = 1$, the tail angle is $\tau = 180$ degrees, or in other words, the sharp corner has disappeared. Since we saw earlier that $\lambda = 1$ results in no change to the original circle, this result is expected. Thus we see that the permissible range of λ is between $(1, 2)$. In fact, since practical foil sections have tail angles that are generally less than 30 degrees, the corresponding range of λ is roughly from $(1.8, 2.0)$.

If the circle passes outside of $z = -a$, there is no sharp leading edge. On the other hand, we can construct a foil with a sharp leading and trailing edge by placing the center of the circle on the imaginary axis, so that a circle passing through $z = a$ will also pass through $z = -a$. This is shown in figure 10. In this case, the upper and lower contours of the foil can be shown to consist of circular arcs. In the limit of small camber and thickness, these become the same as parabolic arcs.

1.3.5 The Kutta Condition

We can see from equation 6 that the solution for the potential flow around a circle is not unique, but contains an arbitrary value of the circulation, Γ. If we were only interested in this particular flow, it would be logical to conclude, from symmetry, that the only physically rational value for the circulation would be zero. On the other hand, if the cylinder were rotating about its axis, viscous forces acting in a real fluid might be expected to induce a circulation in the direction of rotation. This actually happens in the case of exposed propeller shafts which are inclined relative to the inflow. In this case, a transverse force called the *magnus effect* will be present. Similarly, if fluid is ejected through jets oriented tangent to the surface of the cylinder, a circulation can also be induced. However, these are not of interest in the present discussion, where the flow around a circle is simply an artificial means of developing the flow around a realistic foil shape.

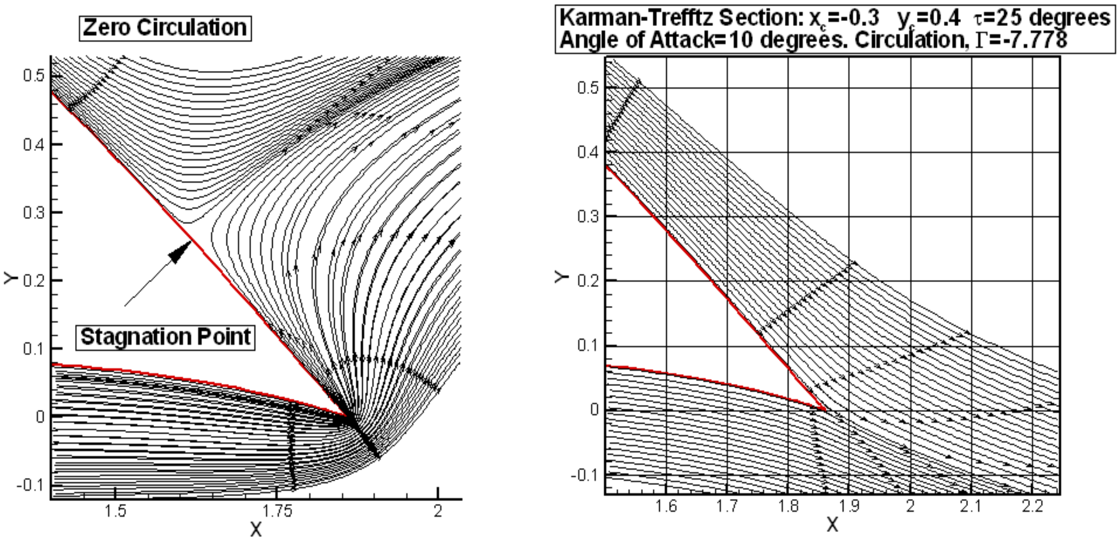

Figure 8: *Flow near the trailing edge. The figure on the left is for zero circulation. Note the flow around the sharp trailing edge and the presence of a stagnation point on the upper surface. The figure on the right shows the result of adjusting the circulation to provide smooth flow at the trailing edge.*

Figure 8 shows the local flow near the trailing edge for the Karman-Trefftz foil shown in figure 5. The flow in the left figure shows what happens when the circulation around the circle is set to zero. The flow on the right figure shows the case where the circulation is adjusted to produce a stagnation point at the point a on the x axis, as shown in figure 6. In the former case, there is flow around a sharp corner, which from equation 15 will result in infinite velocities at that point since $d\zeta/dz$ is zero. On the other hand, the flow in the right hand figure seems to leave the trailing edge smoothly. If we again examine equation 15, we see that the expression for the velocity is indeterminate, with both numerator and denominator vanishing at $z = a$. It can be shown from a local expansion of the numerator and denominator in the neighborhood of $z = a$ that there is actually a stagnation point there provided that the tail angle $\tau > 0$. If the trailing edge is cusped ($\tau = o$), the velocity is finite, with a value equal to the component of the inflow which is tangent to the direction of the trailing edge.

Kutta's hypothesis was that in a real fluid, the flow pattern shown in the left of figure 8 is physically impossible, and that the circulation will adjust itself until the flow leaves the trailing edge smoothly. His conclusion was based, in part, on a very simple but clever experiment carried out by L. Prandtl in the Kaiser Wilhelm Institute in Göttingen around 1910. A model foil section was set up vertically, protruding through the free surface of a small tank. Fine aluminum dust was sprinkled on the free surface, and the model was started up from rest. The resulting flow pattern was then photographed, as shown in figure 9 from an early text [6]. The photograph clearly shows the formation of a vortex at the trailing edge which is then shed into the flow. Since Kelvin's theorem states that the total circulation must remain unchanged, a vortex of equal but opposite sign develops around the foil. Thus, the adjustment of circulation is not arbitrary, but is directly related to the initial formation of vortex in the vicinity of the sharp trailing edge. While this process is initiated by fluid viscosity, once the vortex has been shed, the flow around the foil acts as though it is essentially inviscid.

This basis for setting the circulation is known as the *Kutta condition*, and is universally applied when inviscid flow theory is used to solve both two and three dimensional lifting problems. However, it is important to keep in mind that the Kutta condition is an idealization of an extremely complex real fluid problem. It works amazingly well much of the time, but it is not an exact solution to the problem. We will see later how good it really is!

In the case of the present conformal mapping method of solution, we simply set the position of the rear stagnation point to $\theta_s = -\beta$. The required circulation, from equation 9 is,

$$\Gamma = -4\pi r_c U \sin(\beta + \alpha) \tag{20}$$

---

[6] L. Prandtl and O.G. Tietjens, *Applied Hydro and Aerodynamics*, 1934. Dover edition published in 1957

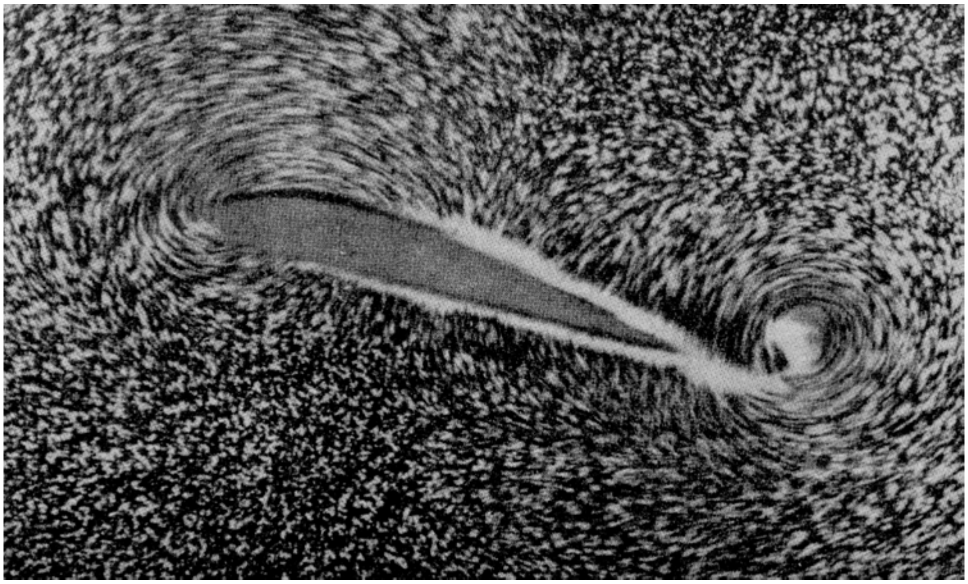

Figure 9: *Early flow visualization photograph showing the development of a starting vortex.*

1.3.6 Pressure Distributions

The distribution of pressure on the upper and lower surfaces of a hydrofoil is of interest in the determination of lift and drag forces, cavitation inception, and in the study of boundary layer behavior. The pressure field in the neighborhood of the foil is of interest in studying the interaction between multiple foils, and in the interaction between foils and adjacent boundaries. The pressure at an arbitrary point can be related to the pressure at a point far upstream from Bernoulli's equation,

$$p_\infty + \frac{1}{2}\rho U^2 = p + \frac{1}{2}\rho q^2$$

where q is the magnitude of the total fluid velocity at the point in question,

$$q \equiv \sqrt{u^2 + v^2}$$

and (u, v) are the components of fluid velocity obtained from equation 15. The quantity p_∞ is the pressure far upstream, taken at the same hydrostatic level. A non-dimensional pressure coefficient can be formed by dividing the difference between the local and upstream pressure by the upstream dynamic pressure,

$$C_P \equiv \frac{p - p_\infty}{\frac{1}{2}\rho U^2} = 1 - \left(\frac{q}{U}\right)^2$$

Note that at a stagnation point, $q = 0$, so that the pressure coefficient becomes $C_P = 1.0$. A pressure coefficient of zero indicates that the local velocity is equal in magnitude to the free stream velocity, U, while a negative pressure coefficient implies a local velocity which exceeds free stream. While this is the universally accepted convention for defining the non-dimensional pressure, many authors plot the *negative* of the pressure coefficient. In that case, a stagnation point will be plotted with a value of $-C_P = -1.0$.

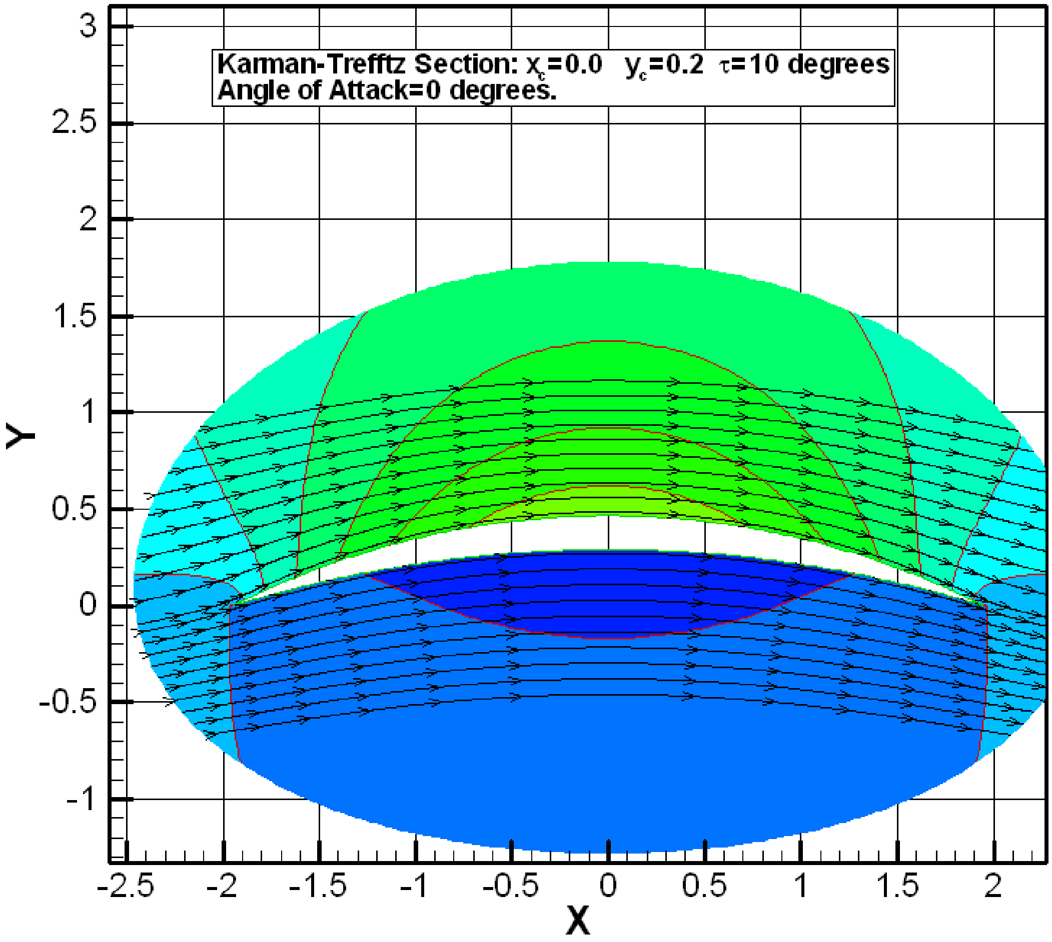

Figure 10: *Streamlines and pressure contours for a thin, highly cambered section at zero angle of attack. This section is symmetrical about mid-chord, and therefore has sharp leading and trailing edges. As expected, the pressure contours show low pressure on the upper surface (green) and high pressure on the lower surface (blue).*

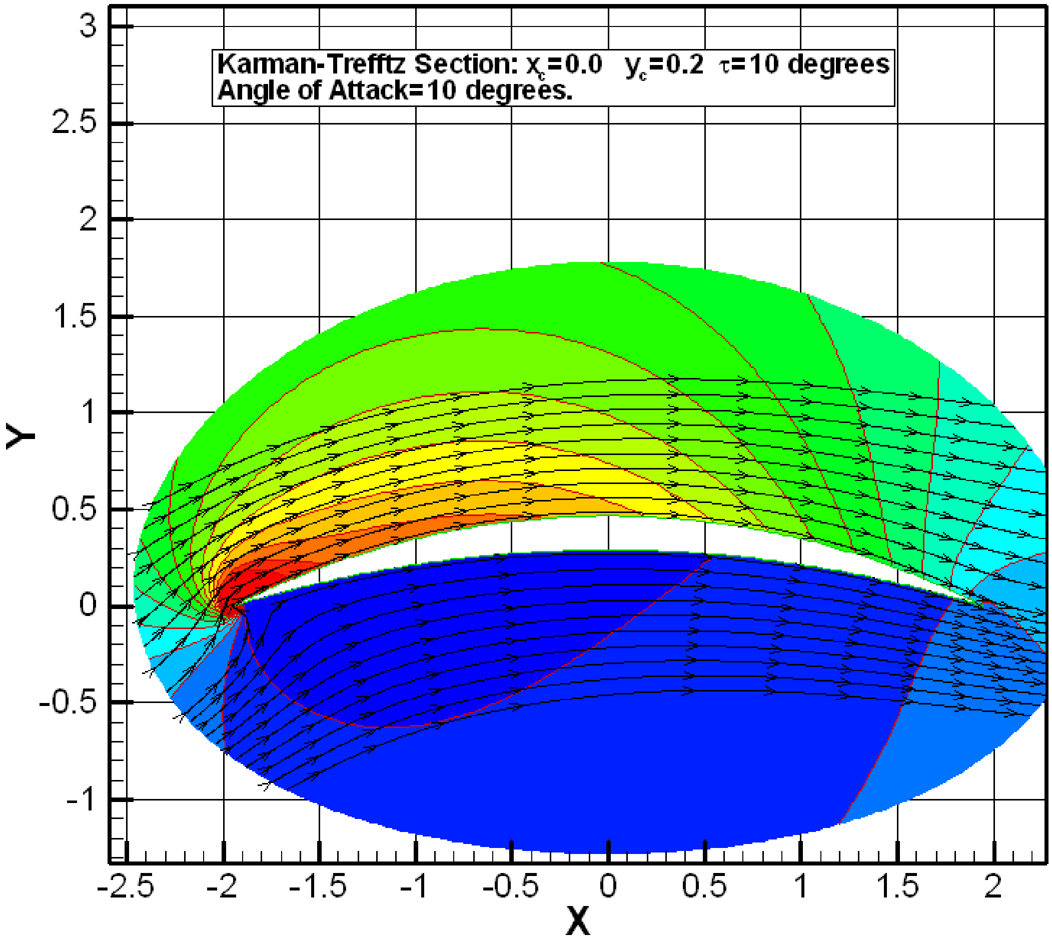

Figure 11: *This is the same section as before, but at an angle of attack of 10 degrees. The flow pattern is no longer symmetrical, with high velocities and hence low pressures (red) near the leading edge.*

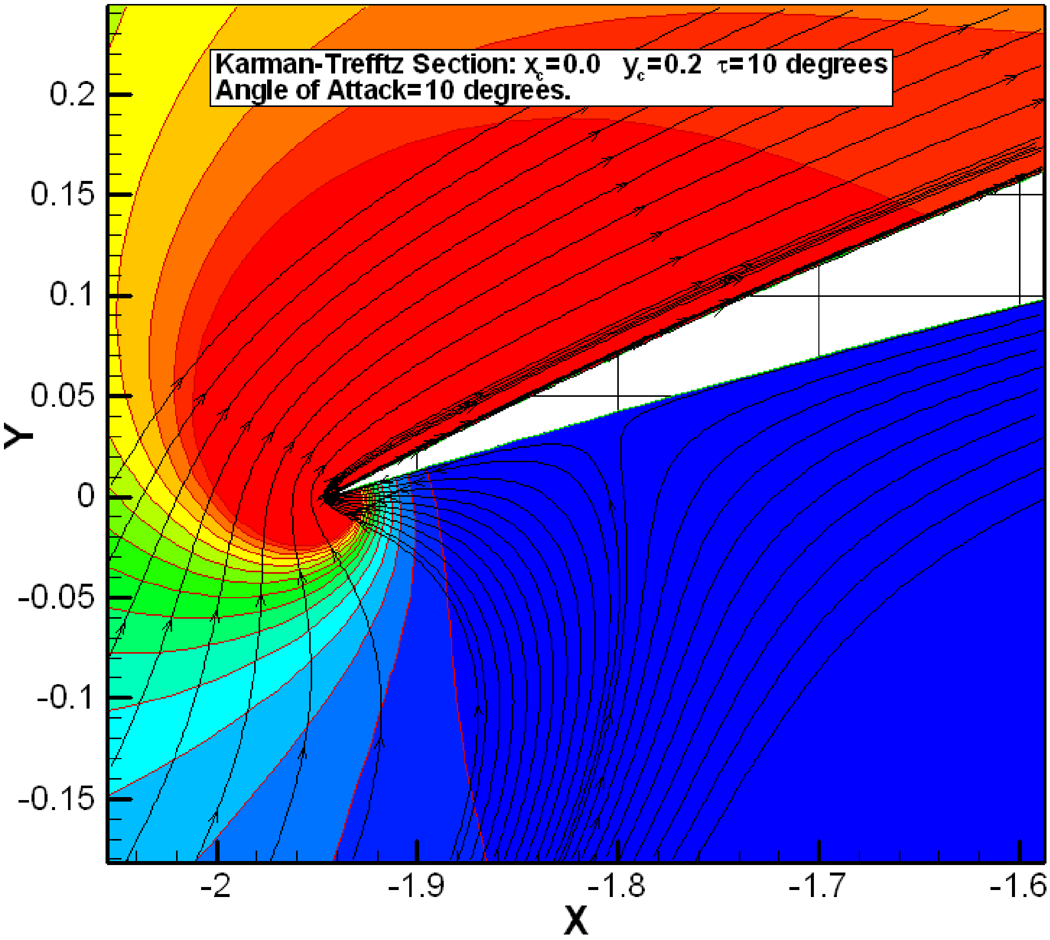

Figure 12: *Close up view of the flow near the leading edge at an angle of attack of 10 degrees.*

1.3.7 Lift and Drag

Determining the overall lift and drag on a two-dimensional foil section in inviscid flow is incredibly simple. The force (per unit of span) directed at right angles to the oncoming flow of speed U is termed *lift* and can be shown to be

$$L = -\rho U \Gamma \tag{21}$$

while the force acting in the direction of the oncoming flow is termed *drag* is zero. Equation 21 is known as *Kutta-Joukowsk's Law*[7].

We can easily verify that equation 21 is correct for the flow around a circle by integrating the y and x components of the pressure acting on its surface. Without loss of generality, let us assume that the circle is centered at the origin, and that the angle of attack is zero. In this case, the velocity on the surface of the circle, from equation 8 is,

$$u_t = -2U \sin\theta + \frac{\Gamma}{2\pi r_c} \tag{22}$$

As before, we can write down the pressure from Bernoulli's equation,

$$p - p_\infty = \frac{1}{2}\rho \left[U^2 - u_t^2\right] \tag{23}$$

and the lift is the integral of the y component of the pressure around the circle,

$$L = -\int_0^{2\pi} (p - p_\infty) \sin\theta r_c d\theta \tag{24}$$

By substituting equations 22 and 23 into equation 24, and recognizing that only the term containing $\sin^2\theta$ survives the integration, one can readily recover equation 21.

In a similar way, we can write down the integral for drag,

$$D = -\int_0^{2\pi} (p - p_\infty) \cos\theta r_c d\theta \tag{25}$$

and show that all terms are zero.

We could now resort to "fuzzy math" and argue that equation 21 must apply to any foil shape. The argument is that we could have calculated the lift force on the circle from an application of the momentum theorem around a control volume consisting of a circular path at some large radius $r >> r_c$. The result must be the same as the one obtained from pressure integration around the foil. But if this is true, the result must also apply to any foil shape, since the conformal mapping function used to create it requires that the flow field around the circle and around the foil become the same at large values of r.

---

[7] The negative sign in the equation is a consequence of choosing the positive direction for x to be downstream and using a right-handed convention for positive Γ

Mapping Solutions for Foils of Arbitrary Shape

Closed form mapping functions are obviously limited in the types of shapes which they can produce. While some further extensions to the Karman-Trefftz mapping function were developed, this approach was largely abandoned by the 1930's. Then, in 1931, T. Theodorsen published a method by which one could *start* with the foil geometry and develop the mapping function that would map it back to a circle [8]. This was done by assuming a series expansion for the mapping function and solving numerically for a finite number of terms in the series. The method was therefore approximate, and extremely time consuming in the pre-computer era. Nevertheless, extensive application of this method led to the development of the NACA series of wing sections, including the sample foil section shown in figure 2.

An improved version of Theodorsen's method, suitable for implementation on a digital computer, was developed by T. Brockett in 1966 [9]. He found, not surprisingly, that inaccuracies existed in the tabulated geometry and pressure distributions for some of the earlier NACA data. Brocket's modified NACA-66 thickness form was developed at that time, and has been used extensively for propeller sections.

By the mid 1970's, conformal mapping solutions had given way to panel methods, which we will be discussing later. This happened for three reasons,

1. Conformal mapping methods cannot be extended to three-dimensional flow, while panel methods can.
2. Both methods involve numerical approximation when applied to foils of a given geometry, and implementation and convergence checking is more straight forward with a panel method.
3. Panel methods can be extended to include viscous boundary layer effects.

---

[8] Theodore Theodorsen,*Theory of Wing Sections of Arbitrary Shape*, NACA Rept. No. 383, 1931

[9] Terry Brocket,*Minimum Pressure Envelopes for Modified NACA-66 Sections with NACA a=-.8 Camber and Buships Type I and Type II Sections*, DTMB Report 1780, 1966

1.4 Linearized Theory for a 2–Dimensional Foil Section

1.4.1 Problem Formulation

In this section we will review the classical linearized theory for 2-D foils in inviscid flow. The problem will be simplified by making the assumptions that the thickness and camber of the foil section is small and that the angle of attack is also small. The flow field will be considered as the superposition of a uniform oncoming flow of speed U and angle of attack α and a *perturbation velocity field* caused by the presence of the foil. We will use the symbols u, v to denote the perturbation velocity, so that the total fluid velocity in the x direction will be $U\cos\alpha + u$, while the component in the y direction will be $U\sin\alpha + v$.

The exact kinematic boundary condition is that the resultant fluid velocity must be tangent to the foil on both the upper and lower surface,

$$\begin{aligned} \frac{dy_u}{dx} &= \frac{U\sin\alpha + v}{U\cos\alpha + u} \quad on\ y = y_u \\ \frac{dy_l}{dx} &= \frac{U\sin\alpha + v}{U\cos\alpha + u} \quad on\ u = y_l \end{aligned} \tag{26}$$

However, since we are looking for the linearized solution, three simplifications can be made. First of all, since α is small, $\cos\alpha \approx 1$ and $\sin\alpha \approx \alpha$. But if the camber and thickness of the foil is also small, the perturbation velocities can be expected to be small compared to the inflow [10]. Finally, since the slope of the mean line, θ, is also small, the coordinates of the upper and lower surfaces of the foil shown in equation 1 will be approximately,

$$\begin{aligned} y_u(x) &\approx f(x) + \frac{t(x)}{2} \\ y_l(x) &\approx f(x) - \frac{t(x)}{2} \end{aligned} \tag{27}$$

Introducing these approximations into equation 26, we obtain the following,

$$\begin{aligned} \frac{dy_u}{dx} &= \frac{df(x)}{dx} + \frac{1}{2}\frac{dt(x)}{dx} = \frac{U\alpha + v^+(x)}{U} \quad on\ y = 0 \\ \frac{dy_l}{dx} &= \frac{df(x)}{dx} - \frac{1}{2}\frac{dt(x)}{dx} = \frac{U\alpha + v^-(x)}{U} \quad on\ y = 0 \end{aligned} \tag{28}$$

Note that the boundary condition is applied on the line $y = 0$ rather than on the actual foil surface, which is consistent with the linearizing assumptions made so far. This result

---

[10] Actually this assumption is not uniformly valid, since the perturbation velocity will not be small in the case of the flow around a sharp leading edge, nor is it small close to the stagnation point at a rounded leading edge. We will see later that linear theory will be locally invalid in those regions.

can be derived in a more formal way by carefully expanding the geometry and flow field in terms of a small parameter, but this is a lot of work, and is unnecessary to obtain the correct linear result. The notation $v+$ and v^- means that the perturbation velocity is to be evaluated just above and just below the x axis. Now, if we take half of the sum and half of the difference of the two equations above, we obtain,

$$\begin{aligned} \frac{df(x)}{dx} &= \alpha + \frac{[v^+(x) + v^-(x)]}{2U} \\ \frac{dt(x)}{dx} &= \frac{[v^+(x) - v^-(x)]}{U} \end{aligned} \tag{29}$$

We now see that the linearized foil problem has been conveniently decomposed into two parts. The mean value of the vertical perturbation velocity along the x axis is determined by the slope of the camber distribution $f(x)$ and the angle of attack, α. The jump in vertical velocity across the x axis is directly related to the slope of the thickness distribution, $t(x)$. This is the key to the solution of the problem, since we can generate the desired even and odd behavior of $v(x)$ by distributing vortices and sources along the x axis between the leading and trailing edge of the foil, as will be shown in the next section.

1.4.2 Vortex and Source Distributions

The velocity field of a point vortex of strength Γ located at a point ξ on the x axis is,

$$\begin{aligned} u(x,y) &= \frac{-\Gamma}{2\pi}\frac{y}{(x-\xi)^2+y^2} \\ v(x,y) &= \frac{\Gamma}{2\pi}\frac{x-\xi}{(x-\xi)^2+y^2} \end{aligned} \tag{30}$$

while the corresponding velocity field for a point source of strength $\mathcal{S}$ is,

$$\begin{aligned} u(x,y) &= \frac{\mathcal{S}}{2\pi}\frac{x-\xi}{(x-\xi)^2+y^2} \\ v(x,y) &= \frac{\mathcal{S}}{2\pi}\frac{y}{(x-\xi)^2+y^2} \end{aligned} \tag{31}$$

We next define a *vortex sheet* as a continuous distribution of vortices with strength γ per unit length. The velocity field of a vortex sheet distributed between $x = -c/2$ to $x = +c/2$ will be,

$$\begin{aligned} u(x,y) &= \frac{-1}{2\pi}\int_{-c/2}^{c/2}\frac{\gamma(\xi)y}{(x-\xi)^2+y^2}d\xi \\ v(x,y) &= \frac{1}{2\pi}\int_{-c/2}^{c/2}\frac{\gamma(\xi)(x-\xi)}{(x-\xi)^2+y^2}d\xi \end{aligned} \tag{32}$$

It is instructive to look at the velocity field in the special cases where the vortex strength is *constant* over the interval. This result will also be useful later when we look at panel methods. In this case γ comes outside the integral, and equation 32 can be integrated analytically, giving the result, [11]

$$\begin{aligned} u(x,y) &= -\frac{\gamma}{2\pi}\left[\tan^{-1}\frac{y}{x-c/2} - \tan^{-1}\frac{y}{x+c/2}\right] \\ v(x,y) &= -\frac{\gamma}{4\pi}\ln\left[\frac{(x-c/2)^2+y^2}{(x+c/2)^2+y^2}\right] \end{aligned} \tag{33}$$

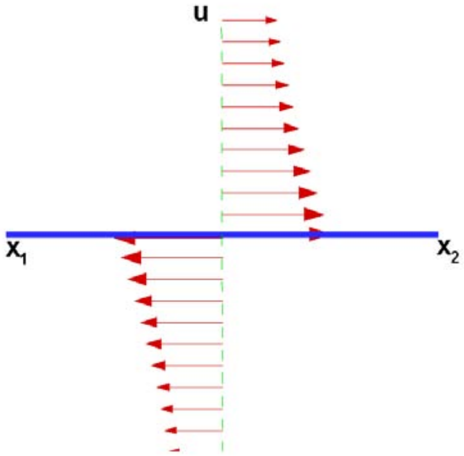

Figure 13: *Vertical distribution of the u velocity at the mid-chord of a constant strength vortex panel of strength* $\gamma = -1$.

Figure 13 shows the velocity field obtained from equation 33 for points along the y axis in the case where the vortex sheet strength has been set to $\gamma = -1$. Note that a jump in horizontal velocity exists across the sheet, and that the value of the velocity jump is equal to the strength of the sheet. This fundamental property of a vortex sheet follows directly from an application of Stokes theorem to a small circulation contour spanning the sheet, as shown in figure 14.

$$\begin{aligned} \gamma dx &= u^- dx + 0 + u^+(-dx) + 0 \\ \gamma &= u^- - u^+ \end{aligned} \tag{34}$$

---

[11] See, for example, J.Katz and A. Plotkin,*Low-Speed Aerodynamics, From Wing Theory to Panel Methods*,McGraw Hill, 1991

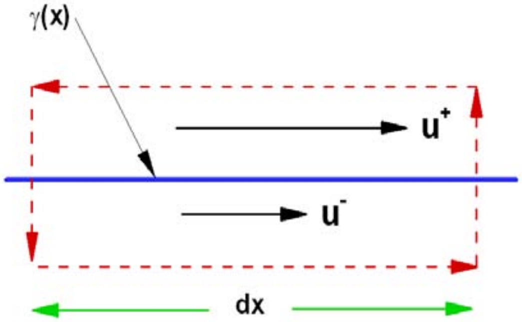

Figure 14: *Illustration of the circulation path used to show that the jump in u velocity is equal to the vortex sheet strength, γ.*

Even though figure 13 was computed for a uniform distribution of $\gamma(x)$ between x_1 and x_2, the local behavior of the u component of velocity close to the vortex sheet would be the same for any continously varying distribution. On the other hand, the v component of velocity depends on $\gamma(x)$, but is continuous across the sheet. Figure 15 shows the v component of velocity along the x axis, again for the case where $\gamma = -1$.

We can develop similar expressions for the velocity field of a uniform strength source sheet. If we let the strength of the source sheet be σ per unit length, the velocity field of a source sheet extending from $x = -c/2$ to $x = c/2$ will be,

$$\begin{aligned} u(x,y) &= \frac{1}{2\pi}\int_{-c/2}^{c/2} \frac{\sigma(\xi)(x-\xi)}{(x-\xi)^2+y^2}d\xi \\ v(x,y) &= \frac{1}{2\pi}\int_{-c/2}^{c/2} \frac{\sigma(\xi)y}{(x-\xi)^2+y^2}d\xi \end{aligned} \tag{35}$$

Again, if we specify that the source strength is constant, equation 35 can be integrated, so give the result,

$$\begin{aligned} u(x,y) &= \frac{\sigma}{4\pi}\ln\left[\frac{(x-c/2)^2+y^2}{(x+c/2)^2+y^2}\right] \\ v(x,y) &= \frac{\sigma}{2\pi}\left[\tan^{-1}\frac{y}{x-c/2} - \tan^{-1}\frac{y}{x+c/2}\right] \end{aligned} \tag{36}$$

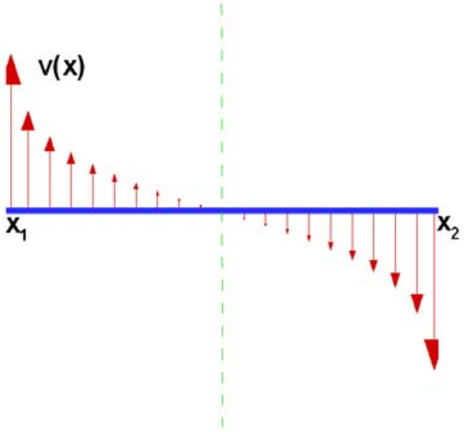

Figure 15: *Horizontal distribution of the v velocity along a constant strength vortex panel of strength $\gamma = -1$.*

Figure 16 shows the v component of the velocity obtained from equation 36 evaluated just above and just below the x axis for a value of $\sigma = 1$. The jump in the vertical velocity is equal to the value of the source sheet strength, which follows directly from a consideration of mass conservation.

Returning to equation 29, we now see that, within the assumptions of linear theory, a foil can be represented by a distribution of sources and vortices along the x axis. The strength of the source distribution, $\sigma(x)$ is known directly from the slope of the thickness distribution,

$$\sigma(x) = U\frac{dt}{dx} \tag{37}$$

while the vortex sheet distribution must satisfy the relationship,

$$\frac{df(x)}{dx} - \alpha = \frac{1}{2\pi U}\int\!\!\!\!\!\!\!c\;_{-c/2}^{c/2} \frac{\gamma(\xi)}{x-\xi}d\xi \tag{38}$$

The symbol “c” superimposed on the integral sign is there for a reason. This will be explained in the next section.

This decomposition of foil geometry, velocity fields and singularity distributions has revealed a very important result. According to linear theory, the vortex sheet distribution, and hence the total circulation, is unaffected by foil thickness, since it depends only on the mean line shape and the angle of attack. This means that the lift of a foil section is

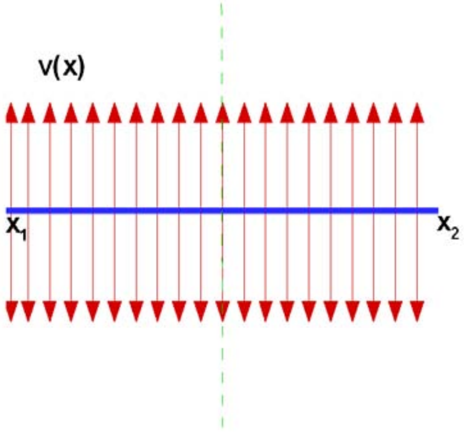

Figure 16: *Horizontal distribution of the v velocity along a constant strength source panel of strength $\sigma = 1$.*

unaffected by its thickness. Now, the exact conformal mapping procedure developed in the previous section shows that lift in creases with foil thickness, *but only slightly.* So, there is no contradiction, since linear theory is only supposed to be valid for small values of thickness. We will see later that viscous effects tend to reduce the amount of lift that a foil produces as thickness is in creased. So, in some sense, linear theory is more exact than exact theory! We will return to this fascinating tale later.

To complete the formulation of the linear problem, we must introduce the Kutta condition. Since the jump in velocity between the upper and lower surface of the foil is directly related to the vortex sheet strength, it is sufficient to specify that $gamma(c/2) = 0$. If this were not true, there would be flow around the sharp trailing edge.

1.4.3 Glauert's Theory

In this section, we will develop the relationship between the shape of a mean line and its bound vortex distribution following the approach of Glauert [12]. A distribution of bound circulation $\gamma(x)$ over the chord induces a velocity field $v(x)$ which must satisfy the linearized boundary condition developed earlier in equation 38

---

[12] H. Glauert, *The Elements of Aerofoil and Airscrew Theory*, Cambridge University Press, 1926

$$v(x) = U\left\{\frac{df}{dx} - \alpha\right\} \tag{39}$$

Glauert assumed that the unknown circulation $\gamma(x)$ could be approximated by a series in a transformed x coordinate,$\tilde{x}$,

$$x = -\frac{c}{2}\cos(\tilde{x}) \tag{40}$$

Note that at the leading edge, $x = -c/2,\ \tilde{x} = 0$, while at the trailing edge, $x = c/2,\ \tilde{x} = \pi$. The value of $\tilde{x}$ at the mid-chord is $\pi/2$. The series has the following form,

$$\gamma(\tilde{x}) = -2U\left\{a_0\frac{1+\cos(\tilde{x})}{\sin(\tilde{x})} + \sum_{n=1}^{\infty} a_n \sin(n\tilde{x})\right\} \tag{41}$$

All terms in equation 41 vanish at the trailing edge in order to satisfy the Kutta condition. Since the sine terms also vanish at the leading edge, they will not be able to generate an infinite velocity which may be present there. The first term in the series has therefore been included to provide for this singular behavior at the leading edge. This first term is actually the solution for a flat plate at unit angle of attack obtained from the Joukowski transformation, after introducing the approximation that $\sin\alpha = \alpha$. It goes without saying that it helps to know the answer before starting to solve the problem!

With the series for the circulation defined, we can now calculate the total lift force on the section from Kutta–Joukowski's law,

$$\begin{aligned} L &= -\rho U \Gamma \\ &= -\rho U \int_{-c/2}^{c/2} \gamma(x)dx \\ &= 2\rho U^2 \int_0^{\pi} \left\{a_0\frac{1+\cos(\tilde{x})}{\sin(\tilde{x})} + \sum_{n=1}^{\infty} a_n \sin(n\tilde{x})\right\}\frac{dx}{d\tilde{x}}d\tilde{x} \end{aligned} \tag{42}$$

Introducing the expression for the derivative,

$$\frac{dx}{d\tilde{x}} = \frac{c}{2}\sin(\tilde{x}) \tag{43}$$

and noting that the integral of $\sin(n\tilde{x})\sin(\tilde{x})$ over the interval $(0,\pi)$ is zero for $n > 1$, we obtain the final result,

$$\begin{aligned} L &= \rho c U^2 \left\{ a_0 \int_0^\pi (1+\cos(\tilde{x}))d\tilde{x} + \sum_{n=1}^{\infty} a_n \int_0^\pi \sin(n\tilde{x})\sin(\tilde{x})d\tilde{x} \right\} \\ &= \rho c U^2 \left\{ \pi a_0 + \frac{\pi}{2} a_1 \right\} \end{aligned} \tag{44}$$

Equation 44 can be expressed in non–dimensional form in terms of the usual lift coefficient,

$$C_L = \frac{L}{\frac{1}{2}\rho U^2 c} = 2\pi a_0 + \pi a_1 \tag{45}$$

We will next develop an expression for the distribution of vertical velocity, v, over the chord induced by the bound vortices,

$$v(x) = \frac{1}{2\pi} \int_{-c/2}^{c/2} \!\!\!\!\!\!\!\! c \quad \frac{\gamma(\xi)}{x-\xi} d\xi \tag{46}$$

Note that the integral in equation 46 is singular, since the integrand goes to infinity when $x = \xi$. This is termed a *Cauchy Principal Value* integral, which means it is not one that you can simply look up in the tables, and the c symbol centered on the integral sign is put there to serve as a warning sign. The next step is to re-write equation 46 in terms of the transformed x coordinate, and to introduce the series for the circulation,

$$\frac{v(\tilde{x})}{U} = \frac{1}{\pi} \int_0^\pi \!\!\!\!\!\!\! c \quad \frac{\left\{ a_0(1+\cos\tilde{\xi}) + \sum_{n=1}^{\infty} a_n \sin(n\tilde{\xi})\sin(\tilde{\xi}) \right\}}{\cos\tilde{x} - \cos\tilde{\xi}} d\tilde{\xi} \tag{47}$$

We will next introduce the following trigonometric identities in order to put equation 47 into a form suitable for integration,

$$\begin{aligned} \sin(n\theta)\sin(\theta) &= \frac{1}{2}\left[\cos((n-1)\theta) - \cos((n+1)\theta)\right] \\ \cos(n\theta)\sin(\theta) &= \frac{1}{2}\left[\sin((n+1)\theta) - \sin((n-1)\theta)\right] \end{aligned} \tag{48}$$

which then gives the result,

$$\frac{v(\tilde{x})}{U} = \frac{1}{\pi}\oint_{0}^{\pi} \frac{\left\{a_0(1+\cos\tilde{\xi}) + \frac{1}{2}\sum_{n=1}^{\infty} a_n\left[\cos((n-1)\tilde{\xi}) - \cos((n+1)\tilde{\xi})\right]\right\}}{\cos\tilde{x} - \cos\tilde{\xi}} \tag{49}$$

With the substitution of the first identity above, the integral of each term of the series has the form,

$$I_n(\tilde{x}) = \oint_{0}^{\pi} \frac{\cos n\tilde{\xi})}{\cos\tilde{x} - \cos\tilde{\xi}} d\tilde{\xi} \tag{50}$$

A Cauchy principal value integral is obtained by taking the limit as ϵ approaches zero of,

$$\oint_{0}^{\pi} f(\tilde{\xi})d\tilde{\xi} = \lim_{\epsilon\to 0}\left[\int_{0}^{\tilde{\xi}-\epsilon} f(\tilde{\xi})d\tilde{\xi} + \int_{\tilde{\xi}+\epsilon}^{\pi} f(\tilde{\xi})d\tilde{\xi}\right] \tag{51}$$

As shown in the appendix, Glauert showed that $I_0 = 0$ and $I_1 = \pi$. Using trigonometric identities, he then developed a recursion formula expressing I_n in terms of I_{n-1} and $In - 2$. The solution of this recursion formula produced the general result,

$$I_n(\tilde{x}) = -\pi\frac{\sin(n\tilde{x})}{\sin\tilde{x}} \tag{52}$$

Substituting equation 52 into equation 50, and making use of the second trigonometric identity in equation 48, the final expression for the velocity comes out in an amazingly simple form,

$$\frac{v(\tilde{x})}{U} = -a_0 + \sum_{n=1}^{\infty} a_n\cos(n\tilde{x}) \tag{53}$$

Solving equation 39 for df/dx and substituting equation 53 for v, we obtain the desired relationship between the shape of the mean line and the series coefficients for the chordwise distribution of the bound circulation,

$$\frac{df}{dx} = \alpha - a_0 + \sum_{n=1}^{\infty} a_n \cos(n\tilde{x}) \tag{54}$$

The resulting expression looks line the Fourier cosine series representation for the function df/dx. Hence equation 54 can be inverted by the usual method of harmonic analysis to give the result

$$\begin{aligned} \alpha - a_0 &= \frac{1}{\pi}\int_0^{\pi} \frac{df}{dx} d\tilde{x} \\ a_n &= \frac{2}{\pi}\int_0^{\pi} \frac{df}{dx} \cos(n\tilde{x}) d\tilde{x} \end{aligned} \tag{55}$$

A particularly important result is obtained by solving equation 55 for the angle of attack for which the a_0 coefficient vanishes,

$$\alpha_{ideal} \equiv \frac{1}{\pi}\int_0^{\pi} \frac{df}{dx} d\tilde{x} \tag{56}$$

This is known as the ideal angle of attack, and is particularly important in hydrofoil and propeller design since it relates to cavitation inception at the leading edge. For any shape of mean line, one angle of attack exists for which the velocity is finite at the leading edge. From the symmetry of equation 56, we see that the ideal angle of attack is zero for any mean line which is symmetrical about the mid–chord.

1.4.4 Example–The Flat Plate

For a flat plate at angle of attack α we can see immediately from the Glauert results that $a_0 = \alpha$ and $a_n = 0$ for $n > 0$. The lift coefficient is then found to be $C_L = 2\pi\alpha$ and the bound circulation distribution over the chord is

$$\gamma(\tilde{x}) = -2U\alpha\left(\frac{1 + \cos\tilde{x}}{\sin\tilde{x}}\right)$$

This result, together with some other cases that we will deal with next, are plotted in figure 17. In this figure, all of the mean lines have been scaled to produce a lift coefficient of $C_L = 1.0$. In the case of a flat plate, the angle of attack has therefore been set to $\alpha = 1/(2\pi)$ radians.

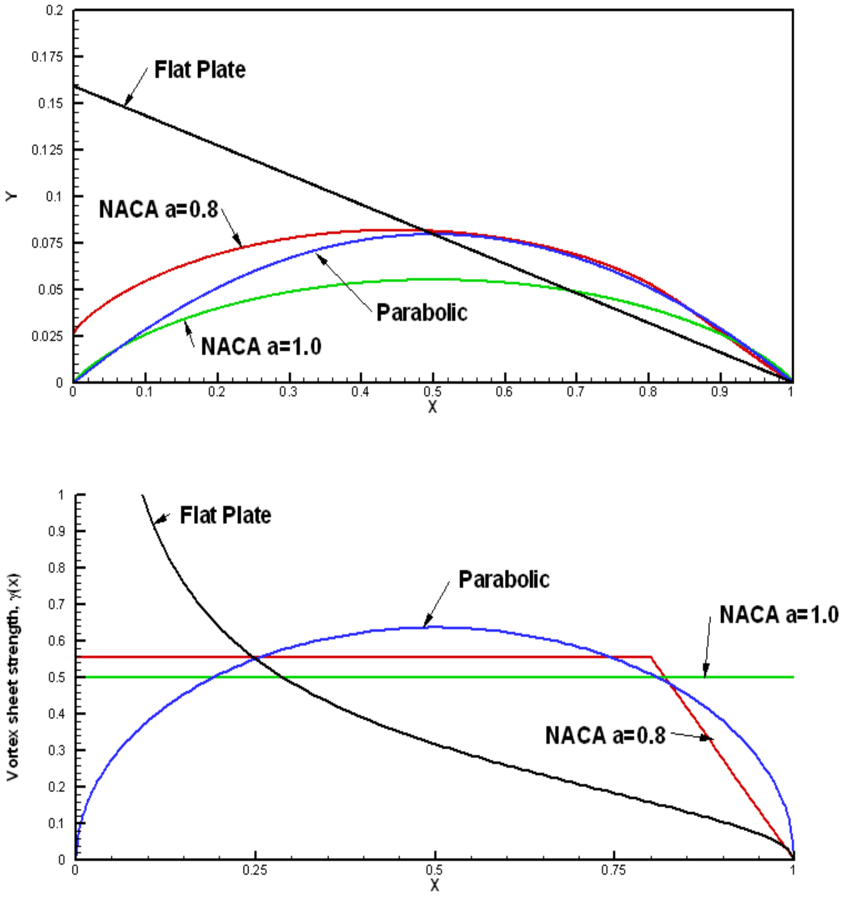

Figure 17: *Horizontal distribution of the v velocity along a constant strength vortex panel of strength $\gamma = -1$.*

1.4.5 Example–The Parabolic Mean Line

The equation of a parabolic mean line with maximum camber f_0 is

$$f(x) = f_o \left[1 - (\frac{2x}{c})^2 \right]$$

so that the slope is

$$\frac{df}{dx} = -\frac{8 f_o x}{c^2}$$

but since $x = -c/2 \cos \tilde{x}$, the slope can be written as

$$\frac{df}{dx} = 4 \frac{f_o}{c} \cos \tilde{x}$$

We can therefore again solve for the Glauert coefficients of the circulation very easily,

$$\alpha - a_0 = \frac{1}{\pi}\int_0^\pi \frac{df}{dx} d\tilde{x} = 0$$

$$a_1 = \frac{2}{\pi}\frac{4f_0}{c}\int_0^\pi \cos^2\tilde{x} d\tilde{x} = 4\frac{f_0}{c}$$

$$a_n = 0 \quad for \quad n > 1$$

The lift coefficient is then given by the expression

$$C_L = 2\pi a_0 + \pi a_1 = 2\pi\alpha + 4\pi\frac{f_0}{c}$$

and the circulation distribution becomes,

$$\gamma(\tilde{x}) = -2U\alpha\Big(\frac{1+\cos\tilde{x}}{\sin\tilde{x}}\Big) - 8U\frac{f_0}{c}\sin\tilde{x}$$

The solution for the parabolic camber line therefore consists of the sum of two parts— a lift and circulation distribution proportional to the angle of attack and a lift and circulation distribution proportional to the camber ratio. This is true for any mean line, except that in the general case the lift due to angle of attack is proportional to the difference between the angle of attack and the ideal angle of attack. The latter is zero for the parabolic mean line due to its symmetry about the mid chord. The result plotted in figure 17 is for a parabolic mean line operating with a lift coefficient of $C_L = 1.0$ at it's deal angle of attack— which is zero.

1.4.6 The Design of Mean Lines-The NACA a-Series

From a cavitation point of view, the ideal camber line is one which produces a constant pressure difference over the chord. In this way, a fixed amount of lift is generated with the minimum reduction in local pressure. Since the local pressure jump is directly proportional to the bound vortex strength, such a camber line has a constant circulation over the chord. Unfortunately, this type of camber line does not perform up to expectations, since the abrupt change in circulation at the trailing edge produces an adverse pressure gradient which separates the boundary layer. One must therefore be less greedy, and accept a load distribution which is constant up to some percentage of the chord, and then allow the circulation to decrease linearly to zero at the trailing edge. A series of such mean lines was developed by the NACA[13], and is known as the a-series, where the parameter “a” denotes the fraction of the chord over which the circulation is constant.

---

[13] Abbott and Von Doenhoff,**Theory of Wing Sections**, Dover 1959

The original NACA development of these mean lines, which dates back to 1939, was to achieve laminar flow wing sections. The use of these mean lines in hydrofoil and propeller applications to delay cavitation inception was a later development.

These shapes could, in principle, be developed from the formulas developed in the preceding section by expanding the desired circulation distribution in a sine series. However, the sine series approximation to a square wave converges very slowly, so that a large number of terms would be required. It is therefore better to derive the shape directly for this special family of shapes.

We will do the $a = 1.0$ camber line here, since we already have the expression for the velocity induced by a constant strength vortex distribution from equation 33. The general case involves the combination of a constant and a linearly varying vortex distribution, and we will simply provide the final result.

If we set $y = 0$ in equation 33, shift the origin so that the foil goes from $(0, c)$ rather than from $-c/2, c/2$ in order to match the original NACA convention, we obtain, [14]

$$v(x) = -\frac{\gamma}{2}\left[\log(1 - x/c) - \log(x/c)\right] \tag{57}$$

We know that the total circulation Γ is related to the lift coefficient

$$C_L = -\frac{2\Gamma}{Uc}$$

and in the special case of uniform bound vortex strength over the chord,

$$\Gamma = \gamma c$$

so that

$$\frac{\gamma}{U} = -\frac{C_L}{2}$$

The non dimensional vertical induced velocity over the chord is therefore

$$\frac{v(x)}{U} = \frac{C_L}{4\pi}\left[\log(1 - x/c) - \log(x/c)\right] \tag{58}$$

The linearized boundary condition is

$$\frac{df}{dx} = \frac{x(x)}{U}$$

---

[14] To avoid the embarrassment of a negative logarithm, I replaced $(x - c/2)^2$ with $(c/2 - x)^2$ in deriving the equation

so that

$$\frac{f(x)}{c} = \int_0^x \frac{v(\xi)}{U}\frac{d\xi}{c}$$

$$\frac{f(x)}{c} = -\frac{C_L}{4\pi}\left[(1-x/c)\log(1-x/c) + x/c\log(x/c)\right]$$

For example, the maximum camber, which occurs at the mid chord, $x = c/2$, is

$$\frac{f_0}{c} = -\frac{C_L}{4\pi}(1/2\log(1/2) + 1/2\log(1/2)) = 0.05516C_L$$

Note that the slope of the mean line is logarithmically infinite at the leading and trailing edges, which is expected since the induced vertical velocities, from equation 57are infinite there. This is obviously a non-physical situation which needs to be treated with some suspicion! As indicated at the beginning of this section, maintaining uniform vortex sheet strength right up to the trailing edge certainly violates the "spirit" of the Kutta condition, and can be expected to result in flow separation.

The corresponding equations for the shape of the general series of mean lines are much more complicated, and will not be derived here. However, they are still logarithmic in form, as indicated below,

$$\begin{aligned}\frac{f(x)}{c} &= \frac{C_L}{2\pi(a+1)}\left\{\frac{1}{1-a}\left[\frac{1}{2}(a-\frac{x}{c})^2\log|a-\frac{x}{c}| - \frac{1}{2}(1-\frac{x}{c})^2\log(1-\frac{x}{c})\right.\right.\\ &\quad \left.\left. + \frac{1}{4}(1-\frac{x}{c})^2 - \frac{1}{4}(a-\frac{x}{c})^2\right] - \frac{x}{c}\log(\frac{x}{c}) + g - h\frac{x}{c}\right\}\end{aligned}$$

where

$$g = \frac{-1}{1-a}\left[a^2(\frac{1}{2}\log a - \frac{1}{4}) + \frac{1}{4}\right]$$

$$h = \frac{1}{1-a}\left[\frac{1}{2}(1-a)^2\log(1-a) - \frac{1}{4}(1-a)^2\right] + g$$

Except for the NACA $a = 1.0$ mean line, this series of mean lines is not symmetrical about the mid chord. The ideal angles of attack are therefore non-zero, and may be found from the following equation,

$$\alpha_{ideal} = \frac{1}{\pi}\int_0^\pi \frac{df}{dx}d\tilde{x} = \frac{-C_L h}{2\pi(a+1)}$$

Experience has shown that the best compromise between maximum extent of constant circulation, and avoidance of boundary layer separation corresponds to a choice of $a = 0.8$. The tabulated characteristics of the mean line, taken from *Theory of Wing Sections* are given in figure 2.

1.4.7 Linearized Pressure Coefficient

The distribution of pressure on the upper and lower surfaces of a hydrofoil is of interest both in the determination of cavitation inception and in the study of boundary layer behavior. We saw in the preceding section on conformal mapping methods that the pressure at an arbitrary point can be related to the pressure at a point far upstream from Bernoulli's equation,

$$p_\infty + \frac{1}{2}\rho U^2 = p + \frac{1}{2}\rho q^2$$

where q is the magnitude of the total fluid velocity at the point in question,

$$q \equiv \sqrt{(U+u)^2 + v^2}$$

and p_∞ is the pressure far upstream, taken at the same hydrostatic level. A non-dimensional pressure coefficient can be formed by dividing the difference between the local and upstream pressure by the upstream dynamic pressure,

$$C_P \equiv \frac{p - p_\infty}{\frac{1}{2}\rho U^2} = 1 - \left(\frac{q}{U}\right)^2$$

Since the disturbance velocities (u, v) are assumed to be small compared with the free stream velocity in linear theory,

$$\left(\frac{q}{U}\right)^2 = 1 + 2\frac{u}{U} + (\frac{u}{U})^2 + (\frac{v}{U})^2 \approx 1 + 2\frac{u}{U}$$

so that the pressure coefficient can be approximated by

$$C_P \approx -2\frac{u}{U}$$

This is known as the *linearized pressure coefficient*, which is valid only where the disturbance velocities are small compared to free stream. In particular, at a stagnation point where $q = 0$ the exact pressure coefficient becomes one, while the linearized pressure coefficient gives an erroneous value of two!

For a linearized two-dimensional hydrofoil without thickness, the u component of the disturbance velocity at points just above and below the foil is $u = \pm\gamma/2$. Thus, the linearized pressure coefficient and the local vortex sheet strength are directly related, with

$$C_P = \frac{\gamma}{U}$$

on the upper surface, and

$$C_P = +\frac{\gamma}{U}$$

on the lower surface.

Cavitation inception can be investigated by comparing the minimum value of the pressure coefficient on the foil surface to the value of the cavitation index,

$$\sigma = \frac{p_\infty - p_v}{\frac{1}{2}\rho U^2}$$

where p_v is the vapor pressure of the fluid at the operating temperature of the foil. Comparing the definitions of σ and C_P, it is evident that if $-C_P > \sigma$, then $p < p_v$. Suppose that a foil is operating at a fixed angle of attack at a value of the cavitation index sufficiently high to insure that the pressure is well above the vapor pressure everywhere. It is therefore safe to assume that no cavitation will be present at this stage. Now reduce the cavitation number, either by reducing p_∞ or increasing U. The point on the foil surface with the minimum pressure coefficient, $(C_P)_{min}$ will reach vapor pressure first, and this will occur when $-(C_P)_{min} = \sigma$. At this point equilibrium can exist between liquid and vapor, so that in principle fluid can evaporate to form a cavity.

The physics of this process is actually very complicated, and it turns out that the actual pressure at which a cavity forms may be below the vapor pressure, and will depend on the presence of cavitation nuclei in the fluid. These may be microscopic free air bubbles or impurities in the fluid or on the surface of the foil. If there is an abundance of free air bubbles, as is generally the case near the sea surface, cavitation will occur at a pressure very close to vapor pressure. On the other hand, under laboratory conditions in which the water may be too pure, cavitation may not start until the pressure is substantially below vapor pressure. This was responsible for erroneous cavitation inception predictions in the past, before the importance of air content was understood.

1.4.8 Comparison of Pressure Distributions

Since the vortex sheet strength $\gamma(x)/U$ and the linearized pressure coefficient is equivalent, we now have all the necessary equations to compare the shape and pressure distributions for a flat plate, a parabolic camber line, an NACA $a = 1.0$ mean line and an NACA $a = 0.8$ mean line. We will compare them at a lift coefficient of one, with all three mean lines operating at their ideal angles of attack. Figure 17 shows the shape (including angle of attack) of the four sections in question. Note that the slope of the flat plate and parabolic mean line is the same at the three quarter chord, which is an interesting result that we will come back to later. It is also evident that the slope of the NACA $a = 0.8$ mean line is also about the same at the three quarter chord, and that the combination of ideal angle of attack and mean line slope makes the back half of the parabolic and NACA $a = 0.8$ mean lines look about the same.

The NACA $a = 1.0$ mean line looks strange, since it looks more or less the same as the parabolic mean line, but with much less camber, yet it is supposed to have the same lift coefficient. The logarithmic form of the latter makes a difference, and we can see that in the blow up of the first ten percent of the chord shown in Figure 18. Even at this large scale, however, there is no evidence of the logarithmically infinite slope at the end. As indicated earlier, lift predicted for the NACA $a = 1.0$ is not achieved in a real fluid, so that our first impression gained from Figure 18 is to some extent correct.

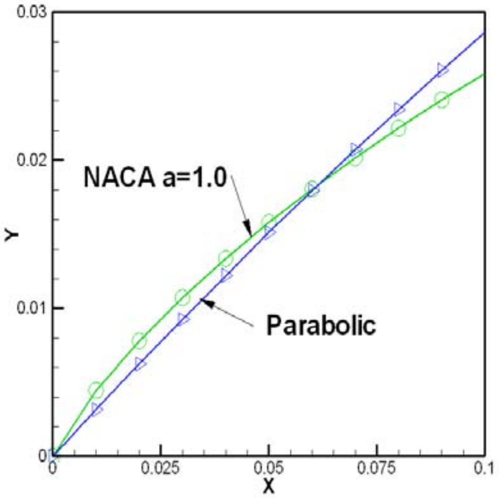

Figure 18: *Enlargement of figure showing the difference between an NACA* $a = 1.0$ *and parabolic mean line near the leading edge.*

1.4.9 Solution of the Linearized Thickness Problem

We will now turn to the solution of the thickness problem. Equation 37 gives us the source strength, $\sigma(x)$ directly in terms of the slope of the thickness form, while equation 35 gives us the velocity at any point (x, y). Combining these equations, and setting $y = 0$ gives us the equation for the distribution of horizontal perturbation velocity due to thickness,

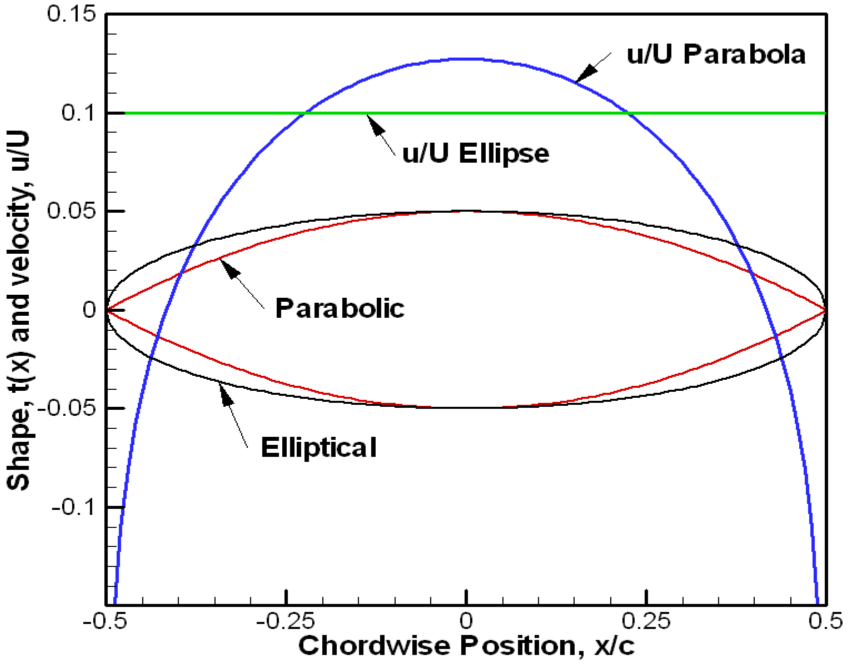

Figure 19: *Shape and velocity distribution for elliptical and parabolic thickness forms from linear theory. The thickness/chord ratio,* $t_o/c = 0.1$*. The vertical scale of the thickness form plots has been enlarged for clarity.*

$$\frac{u}{U} = \frac{1}{2\pi}\oint_{-c/2}^{c/2} \frac{dt/d\xi}{x-\xi} d\xi \tag{59}$$

1.4.10 The Elliptical Thickness Form

The thickness distribution for an elliptical section is

$$t(x) = t_0\sqrt{1-\left(\frac{2x}{c}\right)^2}$$

where the origin is taken at the mid chord, so that the leading edge is at $x = -c/2$ and the trailing edge is at $x = c/2$. Transforming the chordwise variable as before,

$$x = -\frac{c}{2}\cos(\tilde{x})$$

the thickness function becomes

$$t(x) = t_0\sqrt{1-\cos^2(\tilde{x})} = t_0 \sin(\tilde{x})$$

and it's slope is

$$\frac{dt}{dx} = t_0 \cos(\tilde{x})\frac{d\tilde{x}}{dx} = t_0 \frac{cos\tilde{x}}{\frac{c}{2}sin\tilde{x}}$$

The integral for the velocity then becomes,

$$\frac{u}{U} = \frac{-1}{2\pi}\oint_0^\pi \left[\frac{t_0\frac{\cos(\tilde{\xi})}{c/2\sin(\tilde{\xi})}}{\frac{c}{2}(\cos(\tilde{x}) - \cos(\tilde{\xi}))}\right]\frac{c}{2}\sin(\tilde{\xi})d\xi$$

$$\frac{u}{U} = \frac{-t_0}{\pi c}\oint_0^\pi \frac{\cos(\tilde{\xi})}{\cos(\tilde{x}) - \cos(\tilde{\xi}))}d\xi = \frac{t_0}{c}$$

Linear theory therefore yields the very simple result in this case that the non-dimensional horizontal disturbance velocity,u/U, is constant over the chord, with a value equal to the thickness/chord ratio of the elliptical section. It turns out that this result is exact at the mid-chord, and very nearly correct over most of the chord. However, linear theory has a serious flaw in that no stagnation point results at the leading and trailing edge. Of course, the assumption of small slopes is not valid at the ends, so that the breakdown of linear theory in these regions is inevitable.

1.4.11 The Parabolic Thickness Form

The parabolic thickness form has the same shape as a parabolic mean line, except that it is symmetrical about $y = 0$. This is sometimes referred to as a bi-convex foil. The shape of this thickness form, and its slope are,

$$t(x) = t_0\left[1 - \left(\frac{2x}{c}\right)^2\right]$$

$$\frac{dt}{dx} = \frac{-8t_0x}{c^2}$$

and the horizontal disturbance velocity is

$$\begin{aligned}\frac{u}{U} &= \frac{1}{2\pi}\oint_{-c/2}^{c/2} \frac{\frac{-8t_0\xi}{c^2}}{x - \xi}d\xi \\ &= \frac{-4t_0}{\pi c^2}\oint_{-c/2}^{c/2} \frac{\xi}{x - \xi}d\xi\end{aligned}$$

The above Cauchy principal value integral is one of a series of such integrals whose evaluation is given by Van Dyke[15],

$$\fint_{-1}^{1} \frac{\xi}{x-\xi} d\xi = x \log \left[\frac{1+x}{1-x}\right] - 2$$

which, if transformed to the interval $(-c/2, c/2)$ yields the result,

$$\frac{u}{U} = \frac{-4t_0}{\pi c^2} \left\{ x \log \left[\frac{c/2+x}{c/2-x}\right] - c \right\}$$

In this case the velocity is logarithmically infinite at the leading and trailing edge, so that linear theory fails once again to produce a stagnation point! However, the logarithmic singularity is very local, so that the result is quite accurate over most of the chord. The following table gives the horizontal disturbance velocity for a thickness/chord ratio of one tenth. This result is also plotted in figure 19, together with the result for an elliptical thickness form.

|x/c|	u/U	|x/c|	u/U
0.498	-0.267	0.460	-0.059
0.497	-0.240	0.450	-0.041
0.496	-0.221	0.400	0.015
0.495	-0.206	0.350	0.050
0.494	-0.194	0.300	0.074
0.493	-0.184	0.250	0.092
0.492	-0.175	0.200	0.106
0.491	-0.167	0.150	0.116
0.490	-0.159	0.100	0.122
0.480	-0.111	0.050	0.126
0.470	-0.081	0.000	0.127

Note that the maximum velocity occurs at the mid-chord and has a value $u/U = 0.127$. An elliptical thickness form with a thickness/chord ratio of one tenth would have a value $u/U = 0.100$ and would therefore have a lower value of $(-C_P)_{min}$, and would therefore be better from the point of view of cavitation inception.

1.4.12 Superposition

We can combine mean lines and thickness forms to produce a wide range of section shapes. The linearized pressure coefficient can be determined simply by adding the

---

[15] Van Dyke,M.D.,"Second-Order Subsonic Airfoil Theory and its Practical application", NACA TN 3390,March 1955

pressure coefficients due to camber at ideal angle of attack, flat plate loading due to departure from ideal angle of attack, and thickness. For example, by adding a parabolic mean line with a camber ratio of $f_0/c = 0.05$ to parabolic thickness form with thickness ratio $t_0/c = 0.10$, we obtain a section with a flat bottom and parabolic top. This is known as an *ogival*[16] section, which was commonly used for ship propellers in the past, and is still used for many quantity produced propellers for small vessels.

At the ideal angle of attack of the mean line, which is zero in this case, the disturbance velocity due to camber at the mid chord will be

$$\frac{u}{U} = \frac{1}{2}\frac{\gamma}{U} = 4\frac{f_0}{c}\sin(\tilde{x}) = 4 \times 0.05 \times 1.0 = 0.200$$

on the upper surface, and -0.200 on the lower surface. The velocity due to thickness, we see from the above table, will be $u/U = 0.127$ on both the upper and the lower surface. Hence, on the upper surface,

$$\frac{u}{U} = 0.327 \quad C_P = -.654$$

while on the lower surface,

$$\frac{u}{U} = -.073 \quad C_P = 0.146$$

---

[16] Actually the upper contour of an ogival section is a circular arc, but this approaches a parabolic arc as the thickness becomes small.

1.4.13 Lighthill's Rule

We saw in the preceding sections that linear theory cannot predict the local behavior of the flow near a round leading edge because the assumption of small slopes is clearly violated. While this does not affect the overall lift, any attempt to predict pressure distributions (and cavitation inception) near the leading edge will clearly fail. However, since the problem is local, a relatively simple correction to linear theory can be used to overcome this difficulty. This problem was first solved by Lighthill[17] in 1951. A more recent mathematical treatment of this problem may be found in VanDyke[18]. An improved formulation of Lighthill's method has been recently introduced by Scherer [19], who also cited earlier work by Brockett in 1965, who discovered a 1942 publication (in German) by F.W. Riegels. The derivation presented here is based, in part, on class notes prepared by Robert J. VanHouten in 1982.

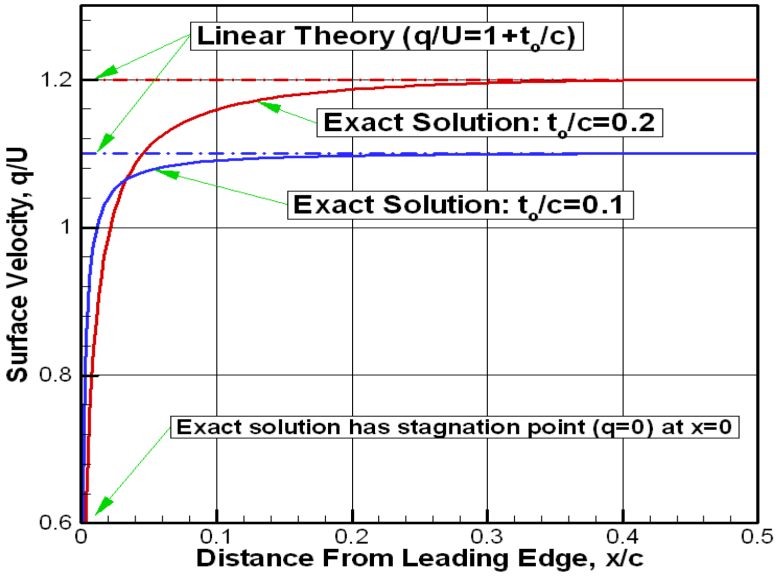

Figure 20: *Comparison of surface velocity distributions for an elliptical thickness form with* $t_o/c = 0.1$ *and* $t_o/c = 0.2$ *obtained from an exact solution and from linear theory.*

Figure 20 shows the velocity distribution near the leading edge of an elliptical thickness form obtained both by linear and exact theory. Linear theory gives the correct answer at the mid-chord, regardless of thickness ratio, but fails to predict the stagnation

---

[17] Lighthill,M.J.,"A New Approach to Thin Aerofoil Theory" *Aero. Quart* 3,193-210

[18] VanDyke,M.,*Perturbation Methods in Fluid Mechanics*,Academic Press,1964

[19] Otto Scherer,*Second Order Wing Theory—The analytical Method used in Computer Code BBF*, publication pending

point at the leading edge. On the other hand, as the thickness ratio is reduced, the region of discrepancy between exact and linear theory becomes more local. If the foil is thin, linear theory can be expected to provide the correct global result, but that it must be supplemented by a local solution in order to be correct at the leading edge. The technique of combining a global and local flow solution is known formally as the *method of matched asymptotic expansions*. However, we will follow a more informal path here.

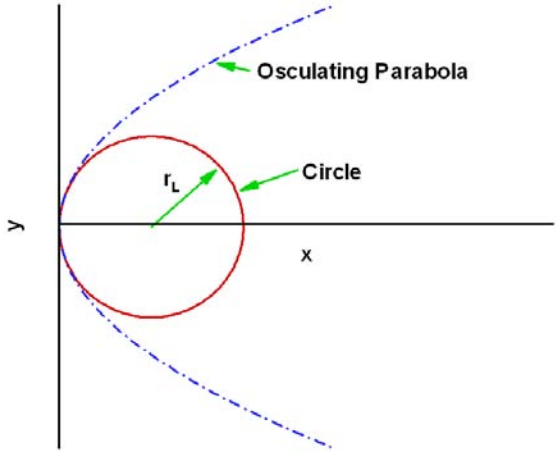

Figure 21: *Local representation of the leading edge region of a foil by a parabola with matching curvature at $x = 0$. This is sometimes referred to as an 'osculating parabola".*

We saw earlier that the leading edge radius of a foil, r_L, scales with the square of the thickness/chord ratio. If we are concerned with the local flow in the leading edge region, the maximum thickness of the foil occurs at a point which is far away from the region of interest. In fact, if we consult our resident small bug— as far as she is concerned, the foil extends to infinity in the x direction. The relevant length scale for the local problem is therefore the leading edge radius. As shown in figure 21, a shape which does this is a parabola (turned sideways). We can find the equation for the desired parabola easily by starting with the equation of a circle of radius r_L with center on the x axis at a distance r_L back from the leading edge, and examining the limit for $x \ll r$

$$y_p^2 + (x - r_L)^2 = r_L^2 \quad y_p(x) = \pm\sqrt{2r_L x - x^2} \sim \pm\sqrt{2r_L x} \quad x = \frac{y_p^2}{2r_L} \tag{60}$$

The velocity distribution on the surface of a parabola in a uniform stream U_i can be found by conformal mapping to be [20]

---

[20] The procedure is to start with the potential solution for the flow approaching an infinite flat wall

$$q_p = U_i \sqrt{\frac{x}{x + r_L/2}} \tag{61}$$

and this is plotted in figure 22. We used U_i in equation 61 rather than the foil free stream velocity, U, because the local leading edge flow is really buried in the global flow field. The only remaining task, therefore, is to assign the proper value to U_i.

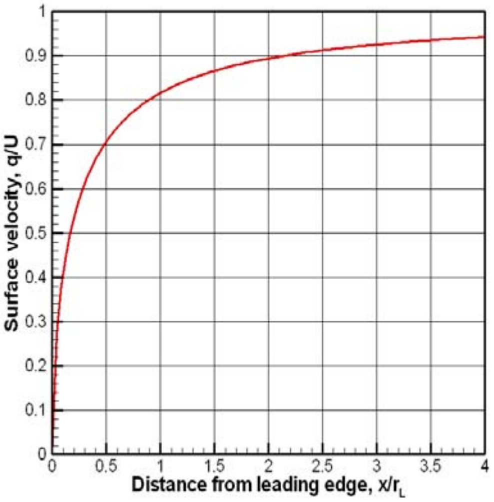

Figure 22: *Surface velocity distribution near the leading edge of a semi-infinite parabola.*

Let us define $u_t(x)$ as the perturbation velocity due to thickness obtained from linear theory. The total surface velocity according to linear theory is then $q(x) \approx U + u_t(x)$. In the limit of $x \ll c$, the linear theory result becomes $q(x) \sim U + u_t(0)$. On the other hand, in the limit of $x \gg r_L$ the local leading edge solution becomes $q(x) \sim U_i$. Thus, the "free stream" in the local leading edge solution must approach $U_i = U + u_t(0)$, and the complete expression for the surface velocity then becomes,

$$q(x) = [U + u_t(x)] \sqrt{\frac{x}{x + r_L/2}} \tag{62}$$

The Lighthill correction can be extended to include the effects of camber and angle of attack. If we define $u_c(x)$ as the perturbation velocity due to camber at ideal angle of attack,the linear theory result in this case can be written as

---

(sometimes called "corner flow") and mapping the flat wall into a parabola. The derivation will not be presented here

$$q(x) = U + u_t(x) + u_c(x) + U(\alpha - \alpha_{ideal})\sqrt{\frac{c-x}{x}} \tag{63}$$

Multiplying equation 63 by the same factor representing the local leading edge flow gives the result,

$$\frac{q(x)}{U} = \left[1 + \frac{u_t(x)}{U} + \frac{u_c(x)}{U}\right]\sqrt{\frac{x}{x + r_L/2}} + (\alpha - \alpha_{ideal})\sqrt{\frac{c-x}{x + r_L/2}} \tag{64}$$

Note that square root infinity in equation 63 has now been canceled, and that the velocity at the leading edge has the finite value

$$\frac{q(0)}{U} = (\alpha - \alpha_{ideal})\sqrt{\frac{2}{r_L/c}} = \frac{C_L - C_L^{ideal}}{2\pi}\sqrt{\frac{2}{r_L/c}} \tag{65}$$

The velocity predicted from equation 65 can be compared with NACA tabulated results obtained from Theodorsen's conformal mapping method for a variety of foil types. This is done in the table below, and it is clear that the Lighthill correction works very well.

Velocity q/U at the leading edge for various thickness forms at unit lift coefficient

Section Type	r_L/c	Lighthill	Theodorsen
NACA 16-0006	0.00176	5.37	5.47
NACA 16-0012	0.00703	2.68	2.62
NACA 16-0021	0.02156	1.53	1.57
NACA 63A006	0.00265	4.37	4.56
NACA 0006	0.00400	3.56	3.99

In addition to correcting the velocity right at the leading edge, we can use Lighthill's rule to modify the velocity and pressure distribution from linear theory over the whole forward part of the foil. However, if we were to apply equation 64 to an elliptical thickness form, we would find that the result would be *worse* at the mid chord. For example, we know that the exact value of the surface velocity at $x/c = 0.5$ for an elliptical thickness form with a thickness/chord ratio of 20 percent is $q/U = 1.2$, and that results in a pressure coefficient of $C_P = -0.44$. We would also get the same result with linear theory. However, if we apply equation 64, we would get,

$$
\begin{aligned}
r_L &= 0.5\left[\frac{t_o}{c}\right]^2 = 0.02 \\
q/U &= \left(1+\frac{t_o}{c}\right)\sqrt{\frac{0.5}{0.5+r_l/2}} = 1.177 \\
C_P &= -0.385
\end{aligned}
\tag{66}
$$

As suggested by Scherer, a variant of the original Lighthill formula solves this problem, and can be derived as follows. If we take the derivative equation 60,

$$
\frac{dy}{dx} = \sqrt{\frac{r_L}{2x}} \tag{67}
$$

and form the quantity

$$
\frac{1}{\sqrt{1+(\frac{dy}{dx})^2}} = \sqrt{\frac{x}{x+\frac{r_L}{2}}} \tag{68}
$$

we see that we recover the same multiplicative factor as shown before in equation 61. However, for actual foil leading edge shapes, the slope will differ from that of a parabola as x increases, and naturally goes to zero at the point of maximum thickness. The result is exact for an ellipse, and appears to give better results for typical foil shapes. We will show this later when we look at numerical methods for solving the problem of an arbitrary two-dimensional foil.

1.5 2-D Vortex Lattice Theory

In the preceding sections, we saw how the solution for the linearized problem of a two dimensional foil section could be solved. In particular, analytic solutions could be derived for a variety of mean lines and thickness forms. However, this is generally not possible for three dimensional foils. As a result, one must resort to numerical methods for solving such problems. It therefore makes sense to first develop numerical solutions to the two-dimensional problem, where we can check the results against known "exact" answers. One very effective way of solving three dimensional lifting problems is to represent the continuous vortex sheet by a lattice of concentrated, straight line, vortex elements. Figure 23 is an example of a vortex lattice representation of a marine propeller.

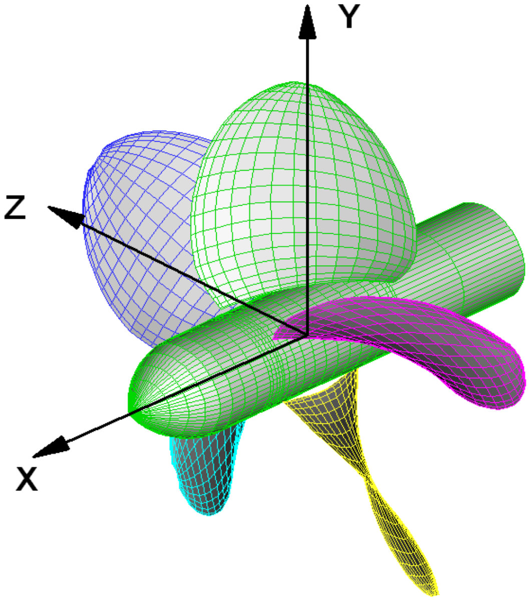

Figure 23: *Vortex lattice approximation of the vortex sheets representing a marine propeller.*

To develop a vortex lattice solution to the two-dimensional foil problem, we simply divide the chord into N panels, concentrate the continuous vortex sheet $\gamma(x)$ into discrete point vortices Γ_n somewhere within each panel, and compute the vertical velocity $v(x)$ by summing the influence of the point vortices. If we are given the shape of the mean line, then the integral equation for the bound vortex sheet strength becomes a set of linear equations for the discrete vortex strengths.

1.5.1 Constant Spacing

The earliest vortex lattice method (VLM) was due to Faulkner [21], who divided the chord into equally spaced panels, and located the vortex at the quarter chord of each panel, and computed the velocity at control points located at the three quarter chord. We saw in figure 17 that the slope (and hence the vertical velocity) at the three quarter chord of a flat plate and a parabolic mean line was the same. This fact probably led to Faulkner's discovery that the optimum location of the control point in each panel was at this same location. One can easily verify numerically that the quarter chord/three quarter chord arrangement of vortices and control points gives the exact total circulation for any number of panels for a flat plate and a parabolic mean line. However, the detailed chordwise distribution of circulation is not exact for these cases, but gets more accurate with increasing numbers of panels. Curiously, the strength of the first panel is always eleven percent too low!

It is interesting to note that no explicit Kutta condition is employed with this method. As long as the control points are placed downstream of the vortices, the vortex lattice method will converge to the desired solution in which the circulation vanishes at the trailing edge.

A formal proof of these properties of the constant spacing VLM is given by James [22].

1.5.2 Cosine Spacing

While the constant spacing scheme works well, better arrangement employs *cosine spacing.* This algorithm was proved to be rigorous independently by Lan [23] and Stark[24]. Another proof can be obtained by first solving for the flow around a circle at an angle of attack using point vortices and control points distributed at uniform angular intervals around the circumference. It can be shown that the local vortex sheet strength, obtained by dividing the point vortex strengths by the interval arc length, is *exact.* Mapping the circle to the x axis using the Joukowski transformation again leads to the same cosine distribution for control points and vortices.

We first define an auxiliary angular variable $\tilde{x}$ such that

---

[21] Falkner,V.M., "The Solution of Lifting-Plane Problems by Vortex Lattice Theory",Aeronautical Research Council R&M No.2591, 1947

[22] James,R.M., "On the Remarkable Accuracy of the Vortex Lattice Method", Comput. Methods Appl. Mech. Eng. Vol.1, 1972

[23] Lan,C.E., "A Quasi-Vortex Lattice Method in Thin Wing Theory", J.Aircraft,Vol 11,No. 9,September, 1974

[24] Stark,V.J.E., "A Generalized Quadrature Formula for Cauchy Integrals", AIAA Journal Vol 9, No.9, 1970

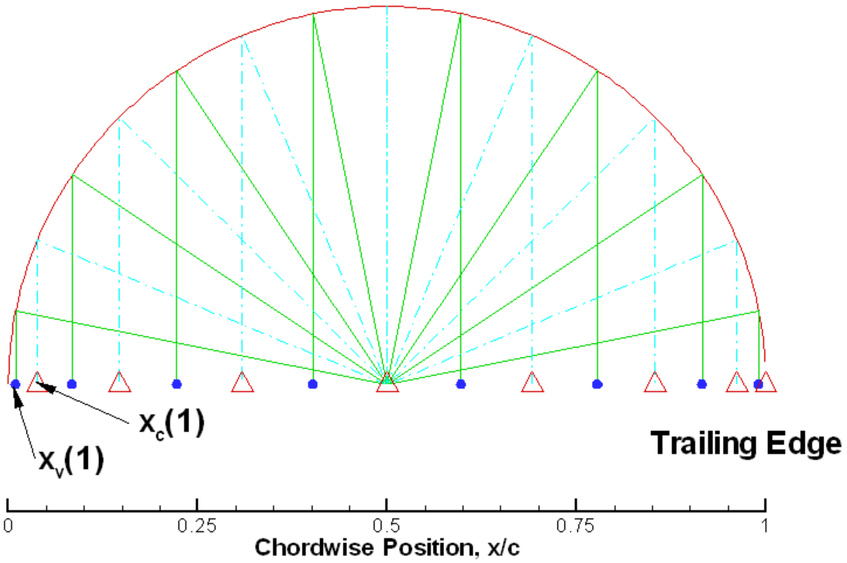

Figure 24: *Arrangement of vortex positions, x_v, and control point positions, x_c. The vortices are plotted as filed circles, and the control points are shown as open triangles. The number of panels, $N = 8$.*

$$x = \frac{c}{2}(1 - \cos \tilde{x}) \tag{69}$$

so that $\tilde{x} = 0$ corresponds to the leading edge and $\tilde{x} = \pi$ corresponds to the trailing edge $x = c$. This is the same as the change of variables introduced by Glauert, except that the x coordinate has been shifted by $c/2$ to place the leading edge at $x = 0$. We next divide the chord into N equal intervals of $\tilde{x}$ with common interval $\delta\tilde{x} = \pi/N$. Point vortices Γ_n are located at the mid-points of each $\tilde{x}$ interval, and control points are located at the downstream boundary of each $\tilde{x}$ interval,

$$\begin{aligned} x_v(n) &= \tfrac{c}{2}\left[1 - \cos\left(\tfrac{(n-1/2)\pi}{N}\right)\right] \\ x_c(n) &= \tfrac{c}{2}\left[1 - \cos\left(\tfrac{n\pi}{N}\right)\right] \end{aligned} \tag{70}$$

Note that with this spacing algorithm the last control point is at the trailing edge, $x = c$.

The velocity induced at the $n'th$ control point is simply,

$$v_n = -\frac{1}{2\pi}\sum_{m=1}^{N}\frac{\Gamma_m}{x_v(m) - x_c(n)} = U\left[\frac{df}{dx} - \alpha\right] \tag{71}$$

where the last equality in 71 is a statement of the boundary condition developed earlier Equation 71, written for each of the N control points, represents a set of simultaneous equations for the unknown point vortex strengths Γ_n.

1.5.3 Converting from Γ_n to $\gamma(x)$

Converting each point vortex strength to vortex sheet strength requires division by an appropriate interval δx_n. Since the common interval in the $\tilde{x}$ variable is $\delta\tilde{x}_n = \pi/N$, the corresponding interval in the physical coordinate is

$$\begin{aligned} \delta x_n &= \frac{dx}{d\tilde{x}}\delta\tilde{x} \\ &= \frac{c}{2}\sin\tilde{x}\frac{\pi}{N} \\ &= \frac{\pi\sqrt{x(c-x)}}{N} \end{aligned} \tag{72}$$

where we have converted from $\tilde{x}$ to x in the last equation by using equation 69. Thus, the vortex sheet strengths are

$$\gamma(x_n) = \frac{N\Gamma_n}{\pi\sqrt{x_n(c-x_n)}} \tag{73}$$

This procedure is illustrated in the computer code *VLM2D* which is listed in the Codes section of the notes. This program solves for the chordwise distribution of circulation for a flat plate, a parabolic mean line and an NACA $a = .8$ mean line, all with a prescribed camber and angle of attack.

As with constant spacing, the total circulation is exact for the flat plate and the parabola for any number of panels (including 1). The distribution of circulation is exact for the flat plate for one panel or greater. It is exact for a parabola with two elements or greater.

The total lift and the distribution of circulation is not exact for the NACA $a = .8$ mean line for any number of panels, but the results with ten panels are accurate enough for most purposes. With ten panels the total circulation is 0.6 percent low, while for twenty panels it is 0.2 percent low. One could not possibly manufacture a model and test it with sufficient accuracy to detect this small discrepancy!

The following figures show the results obtained with *VLM2D* for the cases just described.

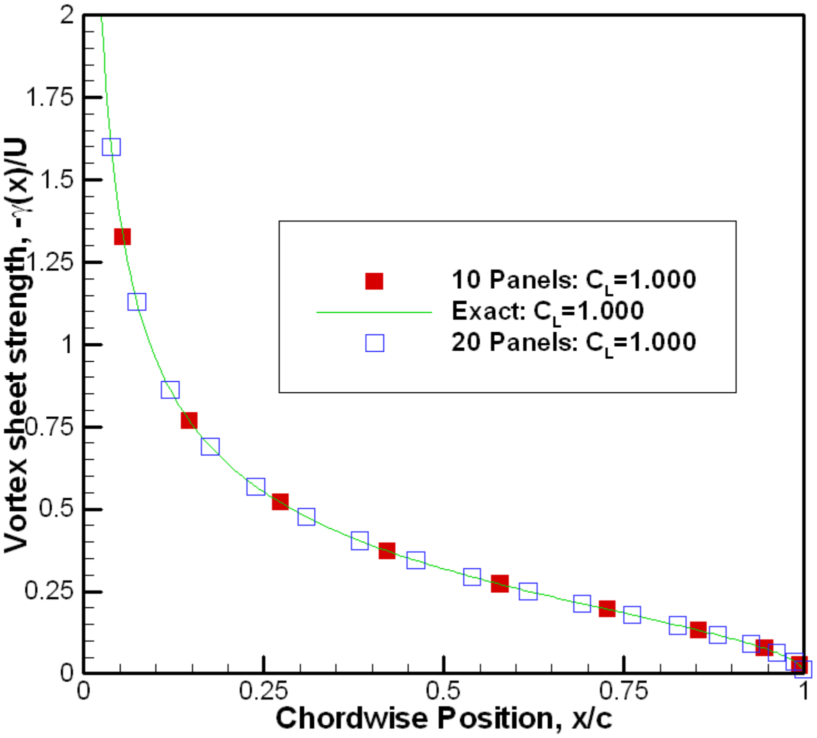

Figure 25: *Comparison of exact solution and vortex lattice method for a flat plate using 10 and 20 panels. The vortex sheet strength and total lift coefficient is exact. Increasing the number of panels improves the resolution in the representation of* $\gamma(x)$*.*

1.5.4 Drag and Leading Edge Suction

We know that the drag of a two-dimensional foil is zero in the absence of viscous forces. However, anticipating that vortex lattice methods will be used for three-dimensional flows where induced drag is not zero, it is useful to look at the problem of computing drag for two-dimensional foils.

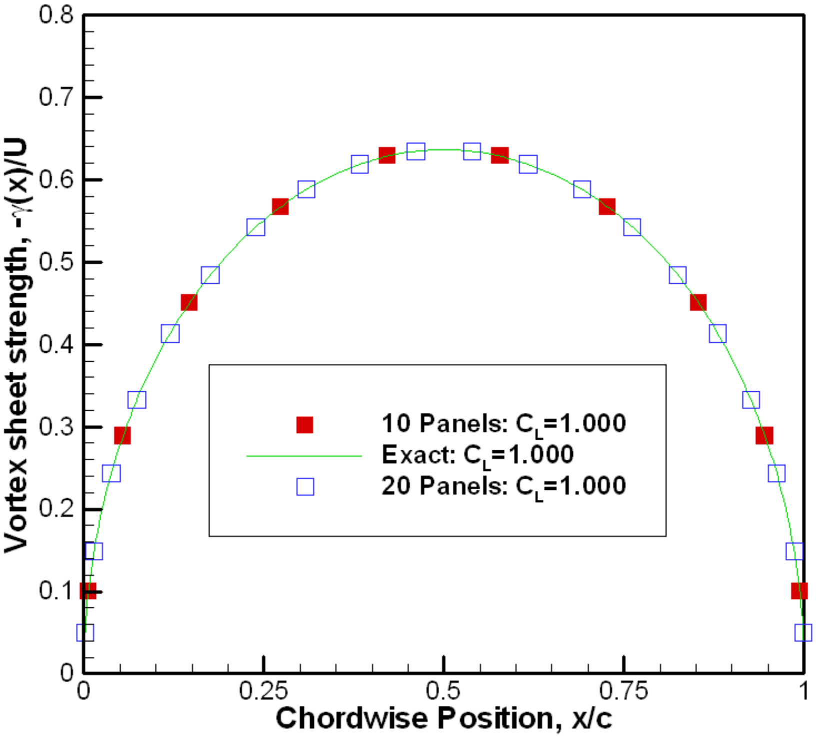

Figure 26: *Comparison of exact solution and vortex lattice method for a parabolic mean line using 10 and 20 panels. The vortex sheet strength and total lift coefficient is exact. Increasing the number of panels improves the resolution in the representation of* $\gamma(x)$*.*

Consider the simple case of a flat plate at angle of attack α. The exact solution for the vortex sheet strength is

$$\gamma(x) = -2U \sin\alpha \sqrt{\frac{c-x}{x}} \tag{74}$$

The total velocity on the upper surface of the plate is $U\cos\alpha - \gamma(x)/2$, while the corresponding velocity on the lower surface is $U\cos\alpha + \gamma(x)/2$. Integrating the resulting pressure jump over the chord of the plate results in a force *normal* to the plate,

$$F_N = \frac{1}{2}\rho U^2 c 2\pi sin\alpha \cos\alpha \tag{75}$$

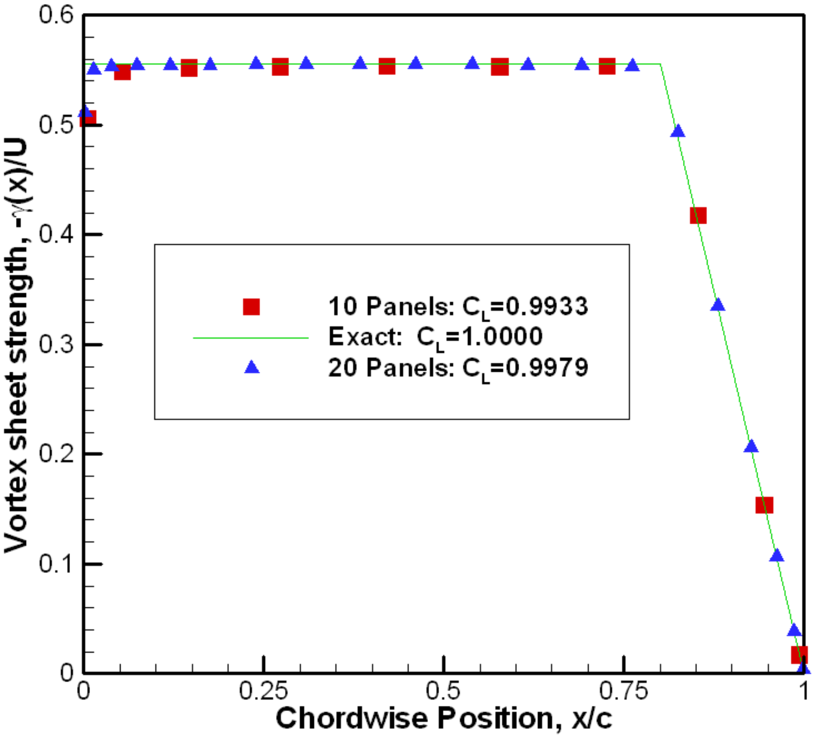

Figure 27: *Comparison of exact solution and vortex lattice method for an NACA* $a = .8$ *mean line using 10 and 20 panels. The vortex sheet strength and total lift coefficient is not exact, but very close to the analytic result. The error in* γ *is visible near the leading edge, where VLM cannot deal with the logarithmic singularity in slope of the mean line.*

Converting F_N to a force coefficient by dividing by $\frac{1}{2}\rho U^2 c$, and resolving the force into components normal to and in the direction of the undisturbed flow gives,

$$\begin{aligned} C_N &= 2\pi \sin\alpha \cos\alpha \\ C_L^* &= 2\pi \sin\alpha \cos^2\alpha \\ C_D^* &= 2\pi \sin^2\alpha \cos\alpha \end{aligned} \tag{76}$$

Obviously there is something wrong since the drag should be zero, and we have labeled C_L and C_D in equation 76 with asterisks as a warning that these are *apparent* values. The missing ingredient is the *leading edge suction* which can be thought of as the limiting case of an infinite velocity (and hence infinitely low pressure) acting on the infinitely small frontal area of the plate.

We know that the circulation, and hence local velocity, goes to infinity at the leading edge as,

$$\gamma(0) \sim -2U \sin\alpha \sqrt{\frac{c}{x}} \tag{77}$$

so that the strength of the leading edge singularity, which we will call C, is,

$$C = -\lim_{x\to 0}\left[\gamma(x)\sqrt{x/c}\right] = 2U\sin\alpha \tag{78}$$

A formal analysis involving the integration of pressure around the leading edge of a foil in the limiting case of vanishing leading edge radius yields the result that the there is a finite suction force which is proportional to the square of the leading edge singularity, C. However, we can avoid this mathematical extravaganza by imposing the requirement that, from Kutta Joukouwski's law, the drag must be zero. As illustrated in figure 28, the necessary leading edge suction force, F_S must be,

$$\begin{aligned} F_s &= \frac{1}{2}\rho U^2 c 2\pi \sin^2\alpha = \pi\rho c C^2/4 \\ C_S &= 2\pi\sin^2\alpha = \frac{\pi}{2}\left(\frac{C}{U}\right)^2 \end{aligned} \tag{79}$$

which acts in the negative x direction. If we resolve the suction force into components at right angles to, and in the direction of the inflow and add these to the corresponding components of the normal force from equation 76, we obtain,

$$\begin{aligned} C_L &= C_N\cos\alpha + C_S\sin\alpha = 2\pi\sin\alpha \\ C_D &= C_N\sin\alpha - C_S\cos\alpha = 0 \end{aligned} \tag{80}$$

Equation 80 confirms that the net drag is now zero, but also, that the lift force now agrees with the value given by Kutta Joukowski's law.

In a numerical solution we only know discrete values of the concentrated bound vortices and therefore do not know the value of C. However, we can approximate it in two different ways—either by extrapolating the bound vortex sheet strength in such a way as to obtain the singularity parameter C, or by using a method developed by Lan, in which C is related to the *upwash* computed at the leading edge.

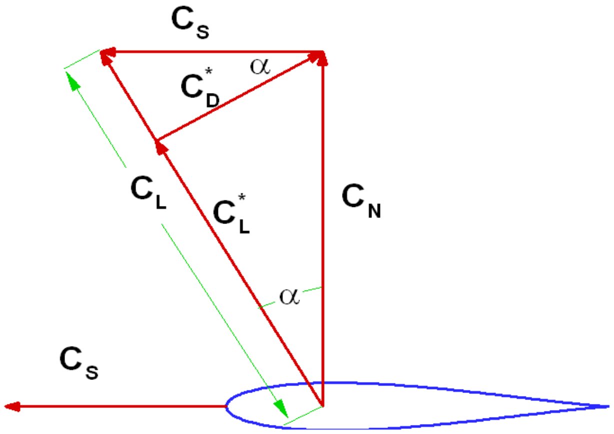

Figure 28: *Vector diagram of force components on a flat plate. For clarity, the angle of attack, α, has been drawn at an unrealistically high value of 30 degrees*

For the first method, we define a *suction parameter* $C(x)$ as

$$C(x) \equiv -\frac{N\Gamma(x_v)}{\pi c} = -\gamma(x_v)\sqrt{\frac{x(c-x)}{c^2}} \tag{81}$$

Comparing equations 81 and 78, we see that in the limit as $x \longrightarrow 0$, $C(x)$ approaches the leading-edge singularity parameter C. For the special case of a flat plate, combining equations 74 and 81 gives the result for unit angle of attack and inflow speed,

$$C(x) = 2(c-x) \quad C(0) \equiv C = 2 \tag{82}$$

Figure 29 provides a check on the numerical results produced by *VLM2D*. The discrete values of Γ_n are converted to $C(x)$ using equation 81 and plotted for $N = 8$ and $N = 64$. The results for both discretizations are exactly on the line (at least to 5 significant digits). This demonstrates that one could obtain a numerical value for the leading edge singularity parameter, C, by linear extrapolation of $C(x)$.

Figure 30 provides a comparison of $C(x)$ for a flat plate, parabolic mean line and NACA $a = 0.8$ mean line, all with unit lift coefficient. The results were computed using

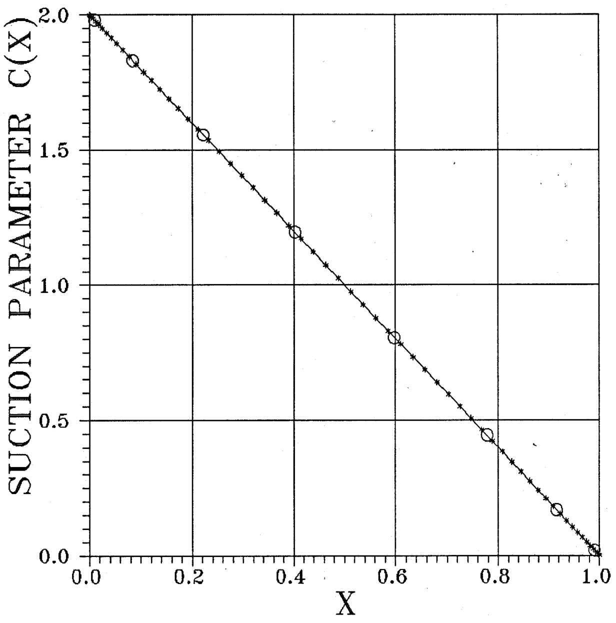

Figure 29: *Suction parameter $C(x)$ for a flat plate computed with 8 and 64 vortex elements for unit angle of attack, α*

64 vortex elements. Note that there is no leading edge suction, i.e. $C = 0$, for the parabolic and $a = 0.8$ mean lines since they are at their ideal angle of attack. The numerical results are exact for the parabola, but slightly off for the $a = 0.8$ mean line. However, the slight error is not visible on the graph.

The second method makes use of a curious result derived by Lan which states that the leading edge singularity parameter C is equal to the total vertical velocity (*upwash*) computed at the leading edge divided by the number of elements, N. The proof will not be given here, but numerical validation is very simple. Moving the control point in equation 71 to the leading edge and adding the vertical component of the inflow gives

$$v_{le}(n) = -U \sin \alpha + \frac{1}{2\pi} \sum_{m=1}^{N} \frac{\Gamma_m}{x_v(m)} \tag{83}$$

Numerical evaluation of equation 83, using discrete values of Γ_n, recovers the exact value of C for the flat plate and parabolic mean line.

Before leaving the topic of leading edge suction, it is worthwhile to consider what happens in the case of a real fluid, or in the case of an ideal fluid with cavitation present. Clearly, if there is a sharp leading edge, the leading edge suction force cannot materialize,

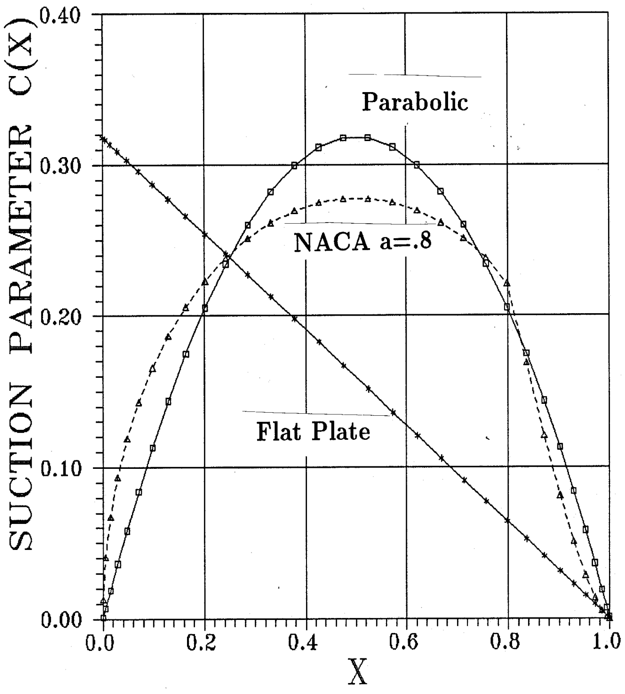

Figure 30: Suction parameter $C(x)$ for a flat plate, parabolic and NACA $a = .8$ mean line at unit lift coefficient, computed with 32 vortex elements

so the apparent drag given in equation 76 is real, and adversely affects the efficiency of the foil section. If the foil has a rounded leading edge, but one that is poorly designed or manufactured, some or all of the theoretical leading edge suction may be lost. Finally, if the section is cavitating at the leading edge, the local low pressure at the leading edge will be limited by vapor pressure, thus reducing (or even eliminating) the leading edge suction.

1.5.5 Adding Foil Thickness to VLM

The continuous distribution of source strength, $\sigma(x)$, which represents foil thickness can also be approximated by a set of concentrated point sources of strength $\mathcal{S}_n$. It makes sense to locate the point sources in the same positions, x_v as the discrete vortices. To maintain the same mass flux, the strength of the $n'th$ point source must be,

$$\begin{aligned}\mathcal{S}_n &= \int_{x_c(n-1)}^{x_c(n)} \sigma(\xi)d\xi \\ &= U\int_{x_c(n-1)}^{x_c(n)} \frac{dt}{d\xi}d\xi\end{aligned}$$

$$= \quad U\left[t_(n) - t_{(n-1)}\right] \tag{84}$$

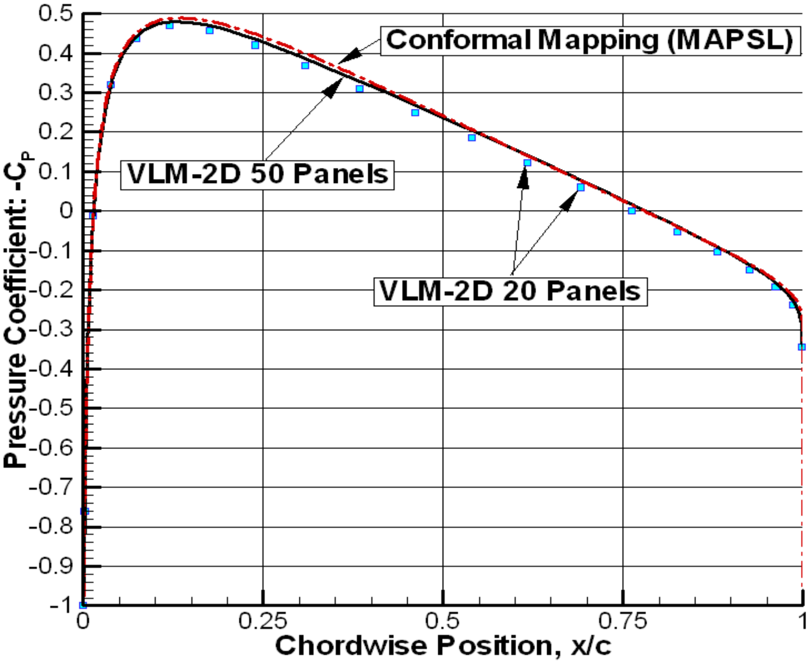

Figure 31: *Comparison of source lattice and exact conformal mapping calculations of the pressure distribution around a symmetrical Karman-Trefftz foil. The foil was generated with* $x_c = -0.1$, $y_c = 0.0$ *and* $\tau = 5$ *degrees. Source lattice results are given for 20 panels (symbols) and 50 panels (continuous curve). The Scherer/Riegels version of Lighthill's leading edge correction has been applied.*

where $t_n \equiv t(x_c(n))$. The discrete source strengths are therefore simply proportional to the difference in foil thickness between the two control point positions surrounding the source. The one exception is the first source, whose strength is proportional to the difference between the thickness at the first control point (which is downstream of the source) and the thickness at leading edge, which is zero. The singular integral given in equation 59 for the horizontal velocity induced by the sources then reduces to the simple summation,

$$\frac{u_n}{U} = \frac{1}{2\pi} \sum_{m=1}^{N} \frac{\mathcal{S}_m}{x_c(n) - x_v(m)} \tag{85}$$

The velocity induces by thickness can therefore be easily added to the velocity due to the vortex sheet in order to obtain an approximate foil pressure distribution. In addition, the Lighthill leading edge correction can be applied to the total computed velocity prior to computing the pressure. This procedure is contained in the program *VLM-2D*, which is listed in the appendix. The program can accommodate either parabolic or NACA $a = .8$ mean lines with DTMB modified NACA 66 thickness forms. In order to enable comparison with exact conformal mapping solutions, the program can also import a symmetrical Karman Trefftz thickness form generated by *MAPSL*.

The latter feature was used to generate figures 31 and 32. In the first figure, a symmetrical section with a thickness/chord ratio of about 12 percent was set at zero angle of attack in order to test only the source lattice feature of the program. The results obtained with 20 and 50 panels are quite close to each other, although it is evident that the 50 panel result is slightly closer to the exact conformal mapping solution. The Scherer/Riegels version of the Lighthill leading edge correction, as given in equation 68 has been applied, and does a remarkably good job of predicting the pressure distribution near the leading edge.

Figure 32 shows the same foil at an angle of attack of 5 degrees, so that now both sources and vortices are present. The results obtained with 20 panels look very similar to the exact results, but clearly indicate less lift. This is not surprising, since linear theory does not account for the coupling between lift and thickness. In this case, the conformal mapping solution indicates that this particular foil section generates about ten percent more lift than a flat plate at the same angle of attack. If the conformal mapping solution is run at a reduced angle of attack (actually 4.53 degrees rather than 5.00 degrees), the resulting pressure distribution is shown as the dashed line in the figure. The latter agrees almost perfectly with the linear theory result, and the Lighthill correction captures the finite pressure peak near the leading edge very well.

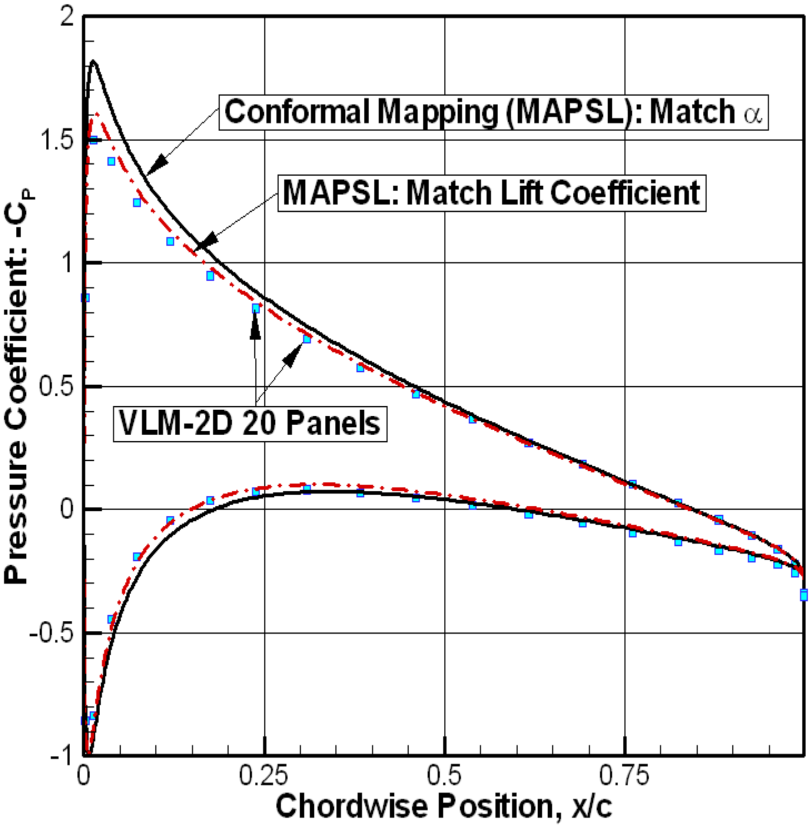

Figure 32: *Vortex lattice approximation of the vortex sheets representing a marine propeller.*

1.5.6 The Cavitation Bucket Diagram

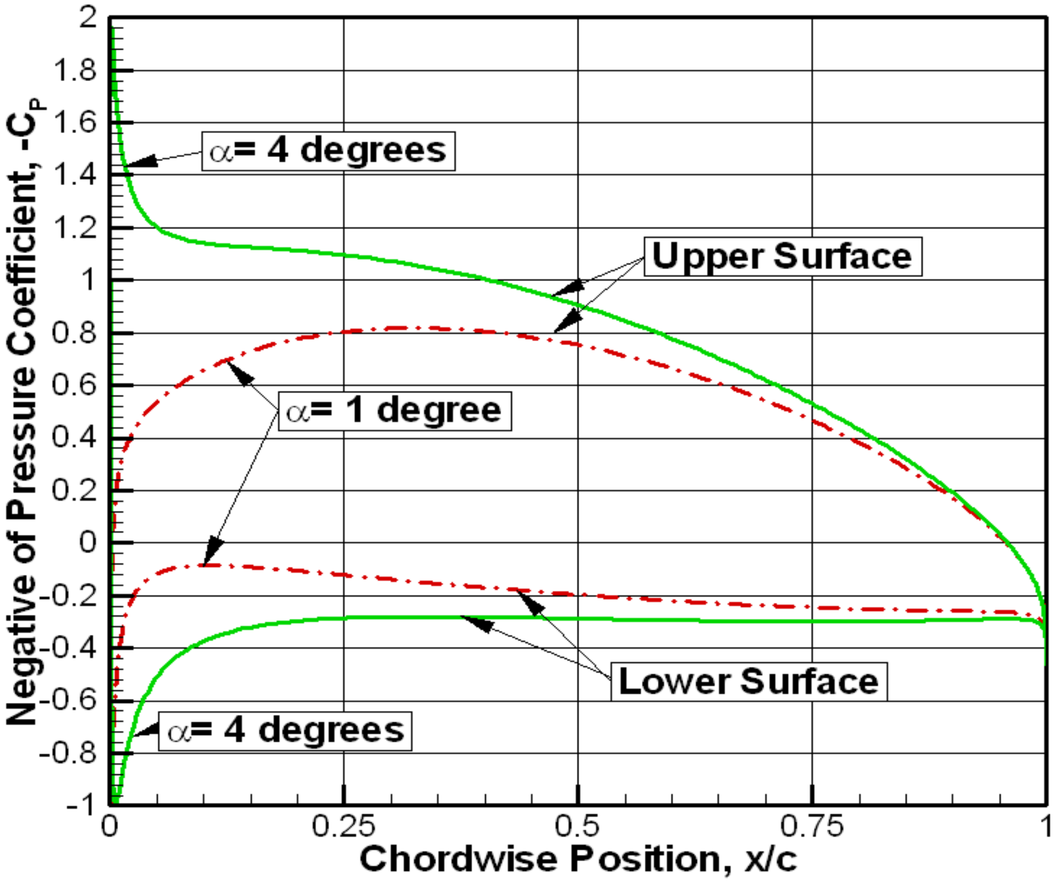

Figure 33: *Pressure distributions for a cambered Karman Trefftz section at two different angles of attack.*

The preceding sections have described a variety of methods for determining the pressure distributions around foils. They can therefore be used to determine cavitation inception by finding the minimum pressure on the foil, and comparing it with vapor pressure. In non-dimensional terms, this is the same as equating the *negative* of the minimum pressure coefficient, $-[C_P]_{min}$ with the cavitation number, σ. This can be illustrated by figure 33, which shows the pressure distribution around a foil section at two different angles of attack. At an angle of attack of one degree, the minimum pressure occurs at a point approximately 35% of the chord from the leading edge where the pressure coefficient is $-C_P \approx 0.8$. At an angle of attack of 4 degrees, the minimum pressure occurs practically at the leading edge, with a pressure coefficient of $-C_P \approx 2.0$.

But, to obtain this kind of information, we do not need the entire pressure distribution on the foil— just the minimum value at the particular angle of attack in question. We will now describe a convenient way of presenting this information, called the *cavitation bucket diagram.*

The surface velocity, q, at a *fixed* point on the foil varies with angle of attack as

$$q(x) = a(x)\cos\alpha + b(x)\sin\alpha \tag{86}$$

where a, b depend on the shape of the foil and the position along the chord on either the upper or lower surface. The reason that this is true can be seen both from linear theory and from an exact conformal mapping solution. The linear theory result [25] is directly evident from equation 63, where

$$\begin{aligned} a(x) &= U + u_t(x) + u_c(x) - U\alpha_{ideal}\sqrt{\frac{c-x}{x}} \\ b(x) &= U\sqrt{\frac{c-x}{x}} \end{aligned} \tag{87}$$

The exact conformal mapping result can be obtained by combining equations 8 and 20. The surface velocity on the mapping circle is

$$\begin{aligned} [q]_z &= 2U\left[\sin(\theta+\alpha) + \sin(\beta+\alpha)\right] \\ &= 2U\left[\sin\theta\cos\alpha + \cos\theta\sin\alpha + \sin\beta\cos\alpha + \cos\beta\cos\alpha\right] \\ &= 2U\left[(\sin\theta + \sin\beta)\cos\alpha + (cos\theta + \cos\beta)\ \sin\alpha\right] \end{aligned} \tag{88}$$

Since the velocity on the foil, $[q]_\zeta$, is obtained from the velocity on the circle by dividing by the derivative of the mapping function (which is obviously independent of α), the form of equation 88 is unchanged, and the combination of all the factors that are multiplied by $\cos\alpha$ and $\sin\alpha$ yields the coefficients a, b in equation 86. Thus, regardless of the complexity of the shape of the foil, the dependence of the surface velocity on α at any point on the foil is very smooth, and is practically a linear function for small values of the angle of attack.

This is illustrated in figure 34 for a symmetrical Karman-Trefftz foil. Note, in particular, that the variation in pressure coefficient right at the leading edge, ($x/c = 0$), is approximately parabolic in form. This follows directly from equation 65, which shows that the total velocity at $x = 0$ is zero at the ideal angle of attack, and increases linearly with $\alpha - \alpha_{ideal}$ at a rate which is inversely proportional to the square root of the leading edge radius. The pressure coefficient is therefore quadratic in α.

---

[25] Keeping in mind that as far as linear theory is concerned, $\cos\alpha = 1.0$ and $\sin\alpha = \alpha$.

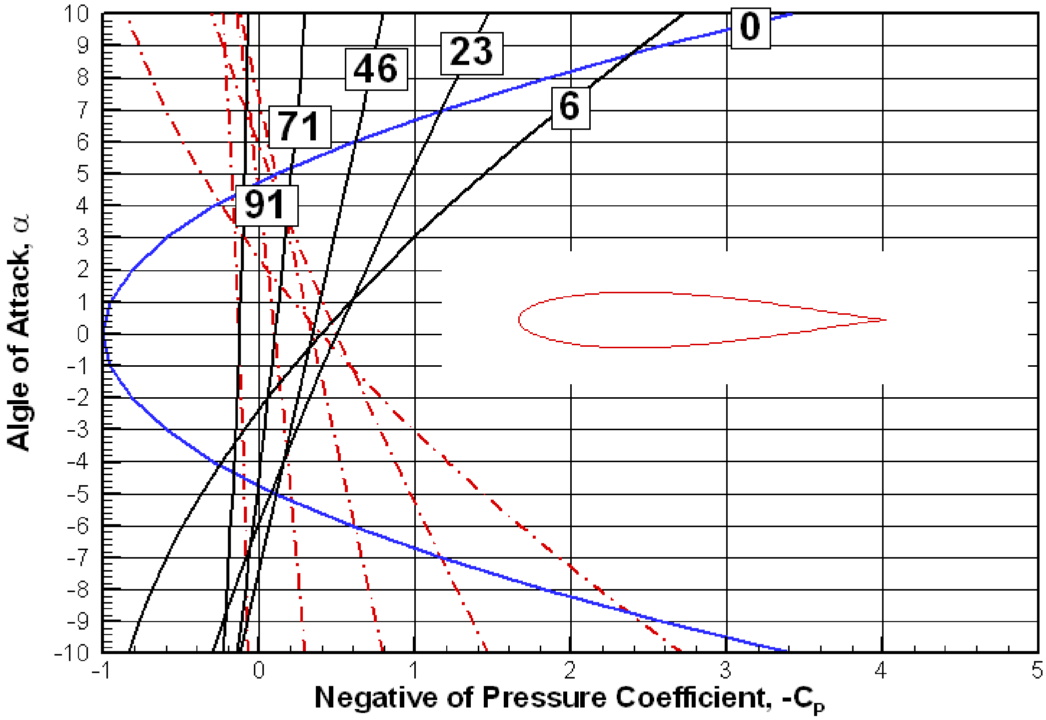

Figure 34: *Variation of pressure coefficient with angle of attack at several fixed chordwise locations for a symmetrical Karman Trefftz section. The numbers indicate the approximate chorwdise locations, in percent of chord from the leading edge. The dashed curves are for the corresponding points on the lower surface. Since the foil is symmetrical, the curves for points on the lower surface are the mirror image of the corresponding points on the upper surface. The foil was generated with* $x_c = -0.1, y_c = 0.0, \tau = 10$ *degrees.*

It is also evident from figure 34 that the pressure coefficient increases rapidly with angle of attack for points near the leading edge, and is relatively insensitive to angle of attack for points near the trailing edge. This follows directly from equation 87.

If we reconstruct figure 34 with a large number of points along the foil surface, the individual $-C_P(\alpha)$ lines form an intricate spider-web pattern which reveals a distinct *envelope curve*, as illustrated in figure 35. This envelope curve [26] actually contains all the information that we need to determine cavitation inception. For example, suppose that this foil were to be operated at an angle of attack of, say, five degrees. We can then see immediately from the graph that $[-C_P]_{min} \approx 1.7$. Thus, cavitation can be

---

[26] Evidently someone thought this looked like a bucket turned sideways. This particular one looks more like a spade to me, but we will stick to tradition here!

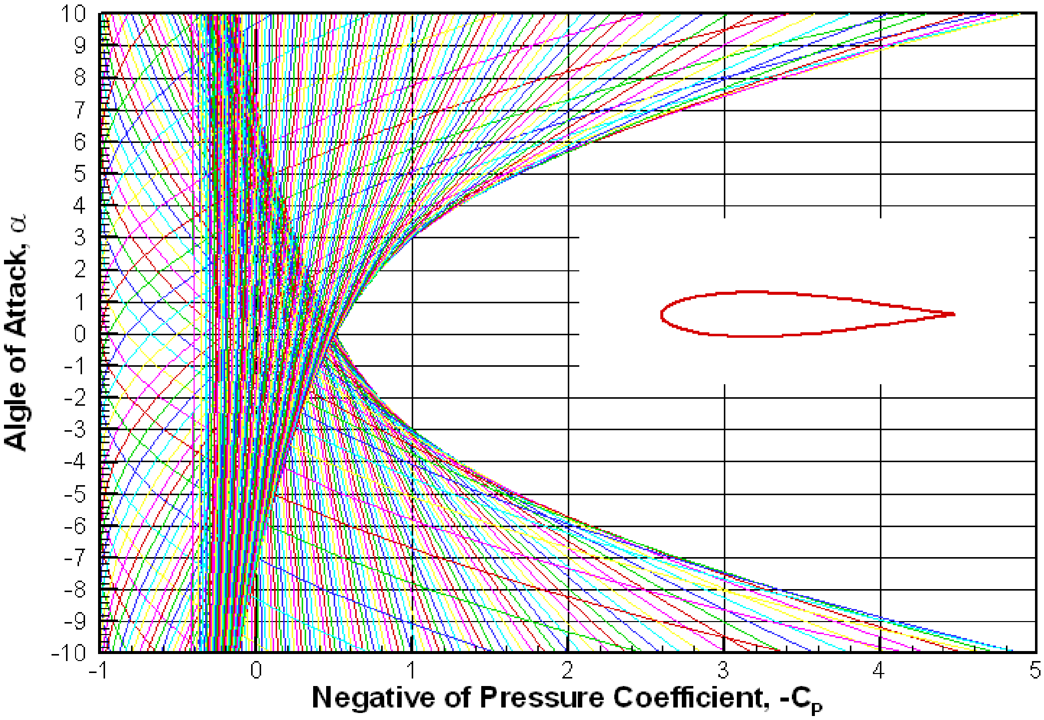

Figure 35: *This is the same data as is shown in Figure 34, except that it is plotted for 180 chordwise positions on the foil. Note that a well defined envelope curve is now apparent.*

expected to occur [27] when the cavitation number $\sigma = 1.7$. On the other hand, suppose the cavitation number is fixed at a value of $\sigma = 2.0$. Then, it is evident from the bucket diagram that the foil will be expected to operate free of cavitation over a range of angles of attack between ±5.8 degrees.

Figure 36 shows the results of a similar calculation for a cambered foil. The bucket now shows three distinct regions. The top of the bucket indicates the inception of cavitation near the leading edge on the upper surface, and the bottom of the bucket indicates inception near the leading edge of the lower surface. The left side of the bucket indicates cavitation inception on the upper surface somewhere in the mid-chord region.

The next example shows the results for a (nearly) ogival section, which has a small but finite leading edge radius. Due to the rapid increase in velocity with angle of attack at the leading edge, the bucket is extremely narrow, indicating a vary small cavitation-free range of angle of attack.

---

[27] Assuming that the fluid contains sufficient cavitation nuclei for inception to occur when $p = p_v$.

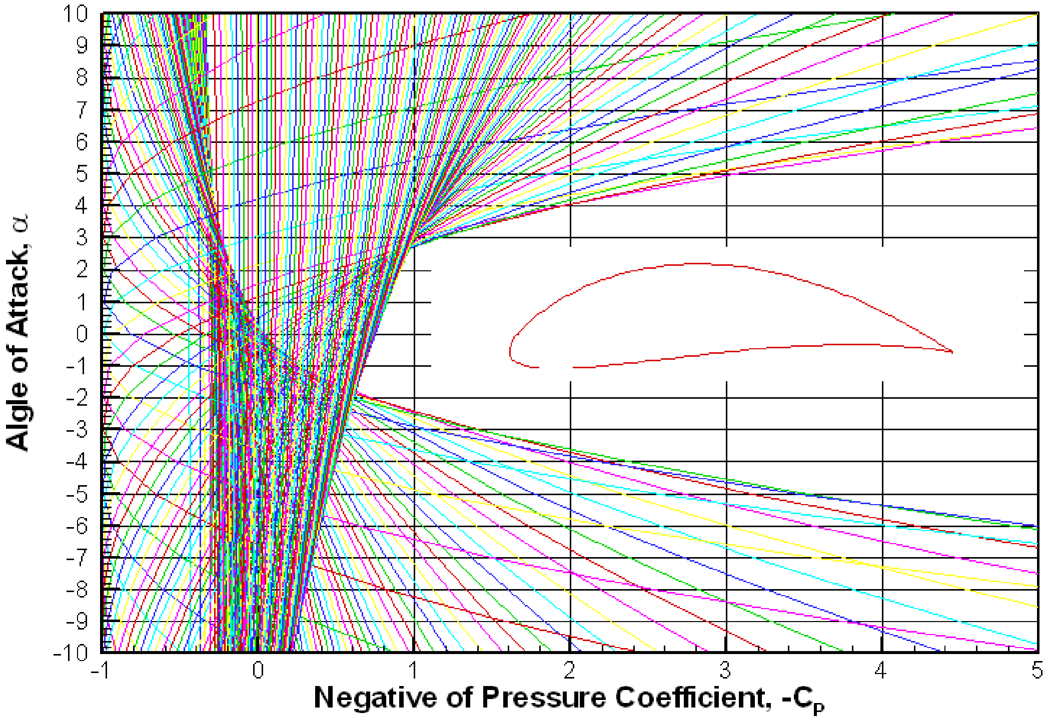

Figure 36: *This is the same presentation of data as shown in Figure 35, but for the cambered Karman Trefftz foil computed in Figure 33. The envelope curve is no longer symmetrical, and shows two distinct "knuckles" at angles of attack of approximately* $+3$ *and* -2 *degrees.The mapping parameters are* $x_c = -.05, y_c = 0.1, \tau = 10$ *degrees.*

Practical design charts can be constructed by omitting the "spider-webs" shown in the preceding figures, and plotting the buckets for systematically varying foil geometries. An example of this type of chart developed by Brockett is shown in figure 38. This clearly shows that a thin foil (with a small leading edge radius) has a very narrow bucket, but can operate at a very low cavitation number (and hence high vehicle speed) at it's ideal angle of attack. Conversely, thick foils have wide buckets, but cannot operate at as low a cavitation number.

For any specified operating cavitation number, an optimum foil thickness ratio exists which results in cavitation free operation at it's ideal angle of attack, yet also provides for the maximum possible "tolerance" for angle of attack variations. This type of diagram was devised by Brockett and is shown in figure 39.

The use of this diagram can be shown by a specific example. Suppose that we need to find the optimum foil section to operate at a lift coefficient of $C_L = 0.295$ at a cavitation

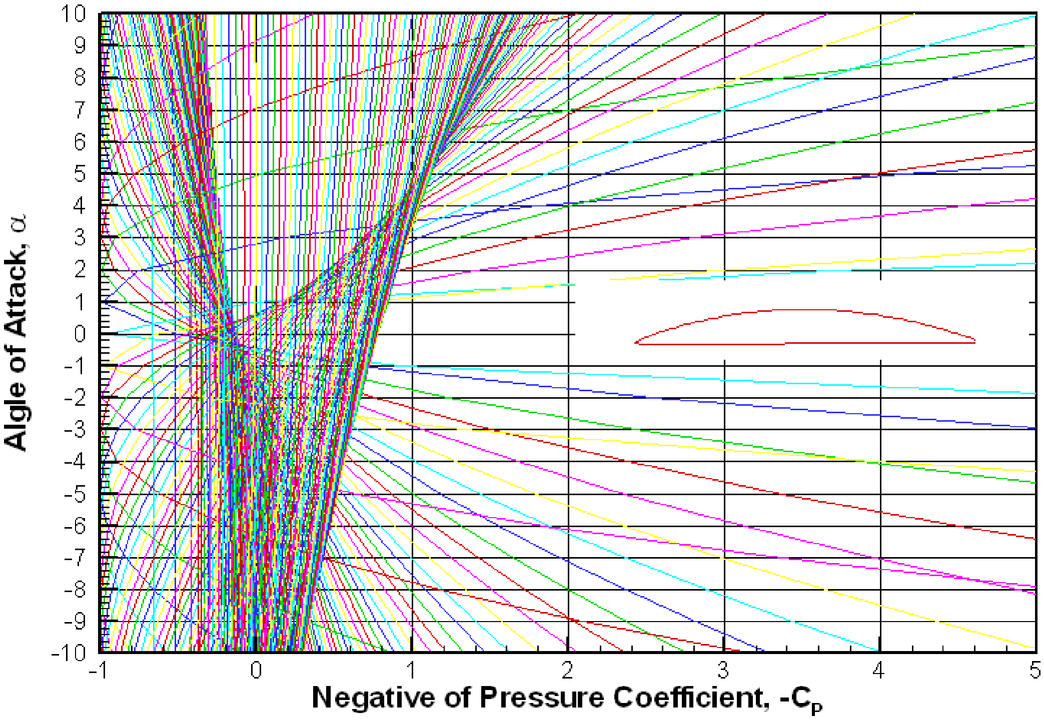

Figure 37: *Here is the same type of data presentation, but for a nearly ogival foil section. The mapping parameters in this case are* $x_c = -0.01, y_c = 0.1, \tau = 20$ *degrees. The region within the envelope curve has now narrowed considerably in comparison to Figure 36.*

number of $\sigma = 0.5$, using an NACA-66 thickness form and an NACA $a = .8$ mean line. The first step is to find the camber ratio such that the foil will generate it's designed lift at its ideal angle of attack. We know from the table in figure 2 that the camber ratio of an NACA $a = .8$ mean line with unit lift coefficient is $f_o/c = 0679$ and the ideal angle of attack is 1.54 degrees. Scaling this to a lift coefficient of $C_L = 0.295$ gives a camber ratio of $f_o/c = 0.02$ [28] and an angle of attack of 0.45 degrees. Entering the left portion of the chart in figure 39 at this value of camber ratio, and at a value of $-[C_P]_{min} = 0.5$ gives a value of thickness/chord ratio of $t_o/c = 0.10$. The right hand chart then shows that the width of the bucket is about three degrees. We can then confirm this result by entering figure 38 at a value of $\alpha = 0.45$ degrees and $-[C_P]_{min} = 0.5$, and we see that the operating point falls perfectly within the bucket curve for t_o/c

---

[28] Yes, this is a remarkable coincidence that the camber ratio happened to comes out to match the chart in figure 38.

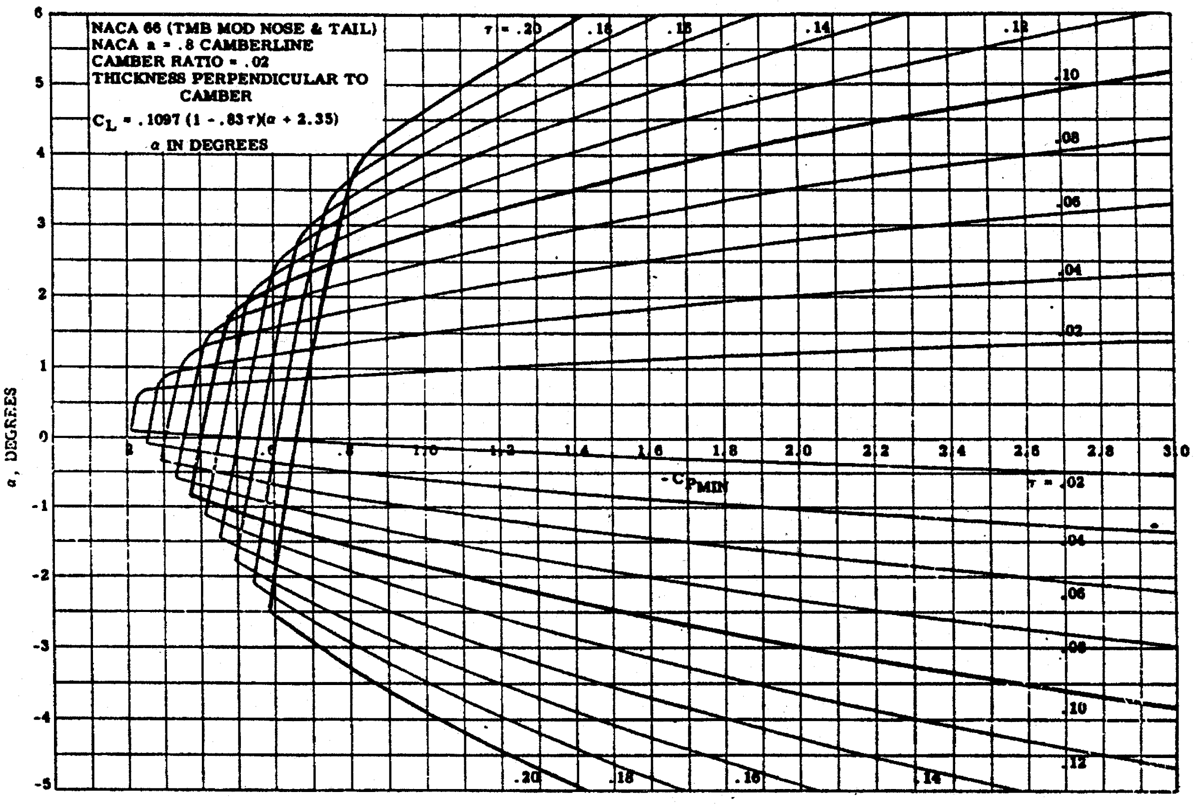

Figure 38: *Sample family of bucket diagrams for NACA-66 thickness forms with NACA* $a = .8$ *mean lines, all with a camber ratio of* $f_o/c = 0.02$. *The section thickness/chord ratios (labeled as* τ *on the chart) range from* $t_o/c = 0.02$ *to* $t_o/c = 0.20$. *The data is from T. Brockett, " Minimum Pressure Envelopes for Modified NACA-66 Sections with NACA* $a = .8$ *Camber and BuShips Type I and Type II Sections", DTMB Report 1780, February 1966.*

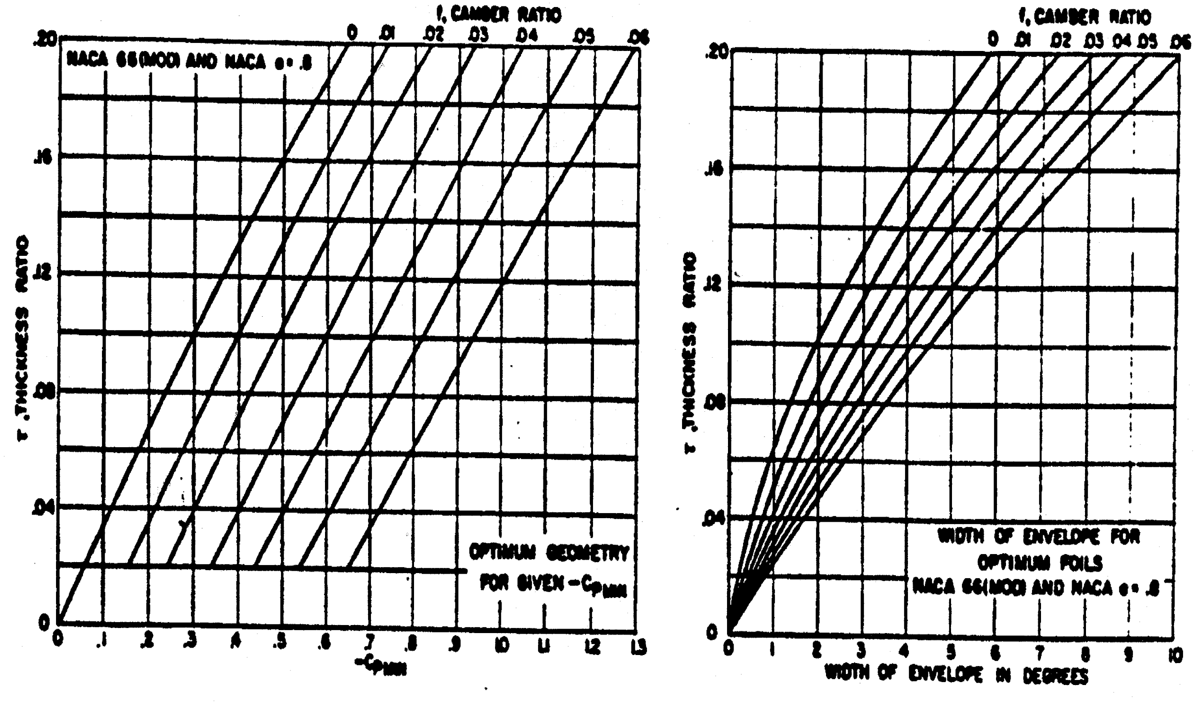

Figure 39: *Design chart for optimum NACA-66 sections from Brockett. The left hand plot shows* $-C_P(min)$ *along the* x *axis versus* t_o/c *along the* y *axis. The lines on the graph are for constant camber ratio,* f_o/c *ranging from zero to* 0.06*. The right hand graph shows the resulting width, in degrees, of the cavitation free range within the bucket.*

2 LIFTING SURFACES

2.1 Introductory Concepts

We saw in the preceding section that a two-dimensional foil could be represented in linear theory by a vortex and source distribution, and that the lift on the section was due entirely to the former. We also saw that linear theory yielded surprisingly accurate results in comparison to exact theory, particularly for foil sections that were relatively thin. In this section, we will therefore extend the concept of a thin, lifting 2-D foil section to three dimensions. Such an idealization is termed a *lifting surface.*

We will start by considering a surface of vanishing thickness, but otherwise arbitrary shape, as illustrated in Figure 40. We will further assume that this lifting surface is placed in a steady, irrotational flow field, and that the fluid, as in the case of 2-D flow, may be regarded as incompressible and inviscid.

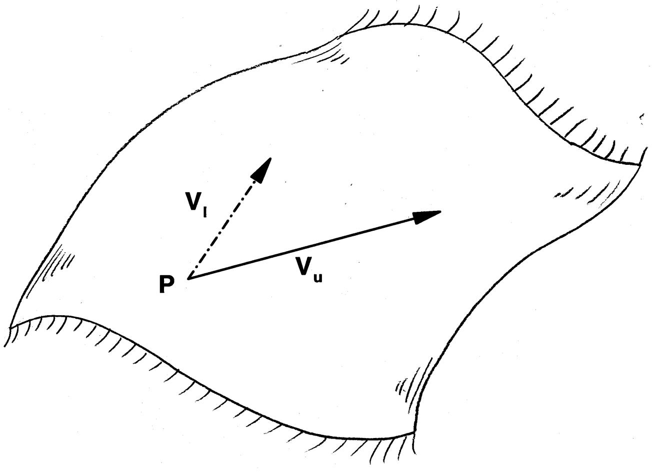

Figure 40: *A lifting surface.*

The fluid velocities at an arbitrary point P on the lifting surface must, of course, be tangent to the surface. However, the velocities at corresponding points on the upper and lower sides of the surface need not be equal in either magnitude or direction. The boundary condition simply requires that they be coplanar.

Let us denote the velocity on the upper surface as $\vec{V_u}$ and the velocity on the lower surface as $\vec{V_l}$. These can be viewed in a plane tangent to the surface at point P, as shown in figure 41, and represented as the vector sum of a mean velocity, $\vec{V_m}$, and a difference velocity, $\vec{V_d}$. Therefore,

$$\vec{V_u} = \vec{V_m} + \vec{V_d}$$

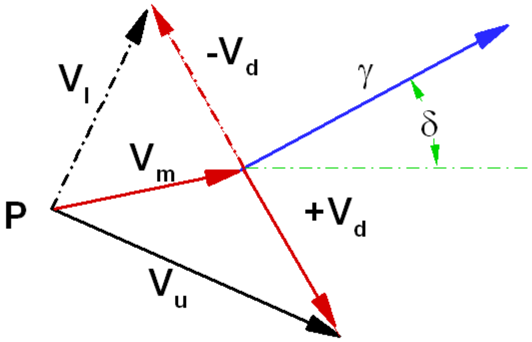

Figure 41: *Velocity diagram in the tangent plane.*

$$\vec{V}_l = \vec{V}_m - \vec{V}_d \tag{89}$$

where

$$\vec{V}_m = \frac{1}{2}(\vec{V}_u + \vec{V}_l)$$
$$\vec{V}_d = \frac{1}{2}(\vec{V}_u - \vec{V}_l) \tag{90}$$

A non-zero difference velocity implies the presence of a vortex sheet whose strength at the point P is [29]

$$\vec{\gamma} = 2\left[\vec{n} \times \vec{V}_d\right] \tag{91}$$

and whose direction is normal to the plane formed by the surface normal vector, $\vec{n}$, and the difference velocity vector, $\vec{V}_d$. Equation 91 may be verified simply by calculating the circulation around a small contour, as illustrated in figure 42.

---

[29] The quantity γ is frequently referred to as the "vorticity", even though it is really the vortex sheet strength. Vorticity, strictly speaking, is the curl of the velocity vector, and a vortex sheet is the limit of a thin layer of fluid containing vorticity as the thickness of the layer goes to zero and the vorticity goes to infinity.

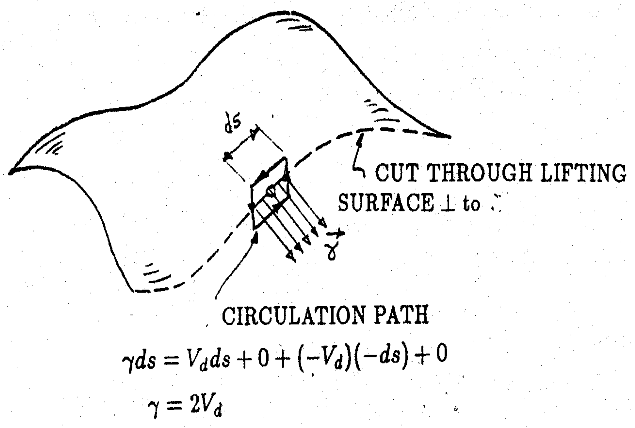

Figure 42: *Relating γ to Velocity Difference.*

We now define δ as the angle between the mean flow and the vorticity vector at point P, and proceed to calculate the pressure jump across the lifting surface using Bernoulli's equation,

$$\Delta p = p_l - p_u = \frac{1}{2}\rho(V_u^2 - V_l^2) \tag{92}$$

A simple application of the law of cosines relates the upper and lower velocities to the mean and difference velocities as follows,

$$\begin{aligned} V_l^2 &= V_m^2 + V_d^2 - 2V_m V_d \cos(\pi/2 - \delta) \\ V_u^2 &= V_m^2 + V_d^2 - 2V_m V_d \cos(\pi/2 + \delta) \end{aligned} \tag{93}$$

which may then be combined with equations 91 and 92 to give the result

$$\Delta p = \rho V_m \gamma \sin\delta \tag{94}$$

Thus we see that the pressure jump across a lifting surface vanishes if the vorticity is aligned with the mean flow. On the other hand, if $\delta = \pi/2$ equation 94 reduced to Kutta-Joukowski's law for the force on a vortex in two dimensional flow. These two special cases are illustrated using the current notation in figure 43.

In the more general case, it is convenient to resolve the vector $\vec{\gamma}$ into components along and normal to the mean flow. The former is customarily defined as the free vorticity (or free vortex sheet strength), γ_f, while the latter is known as the bound vorticity, γ_b. Hence equation 94 may be restated as

$$\Delta p = \rho V_m \gamma_b$$

The distribution of $\vec{\gamma}$ over a lifting surface of prescribed shape is uniquely determined by the following four requirements:

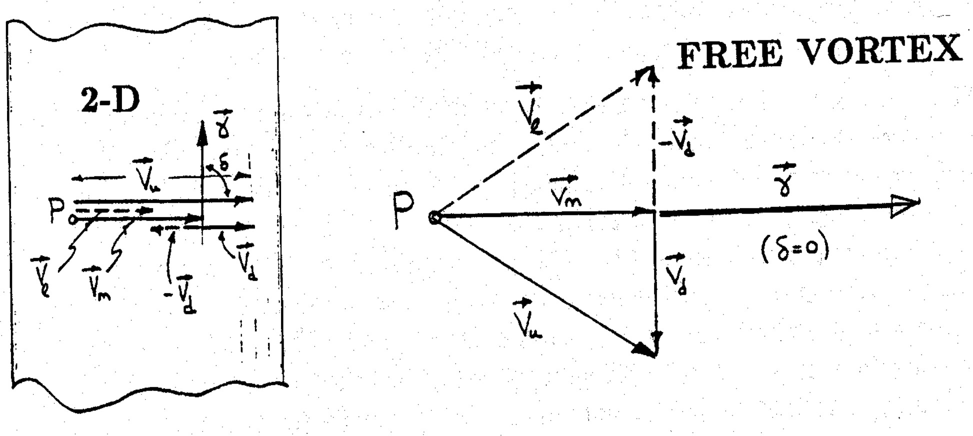

Figure 43: *Velocity and vortex sheet strength for the special cases of two-dimensional flow and free vortex flow.*

- The boundary condition $\vec{V} \cdot \vec{n} = 0$ must be satisfied at all points on the surface.
- The Kutta condition, which requires that there be no flow around the trailing edge, must be imposed.
- Kelvin's theorem must be imposed in determining the relationship between the bound and free vorticity.
- The trailing vortex wake must be force free. Therefore it must consist only of free vorticity, which by definition is aligned with the local mean flow.

The first two requirements are equally applicable to two and three dimensional flows, and are therefore familiar. The last two requirements result in a fundamental difference between two and three dimensional flow. In the latter case, the bound vorticity can vary over the span and this requires that free vorticity develop to provide for continuity of vorticity as required by Kelvin's theorem. The latter will exist not only on the lifting surface, but must proceed into the wake, as shown in the next section. This free vortex wake must deform in order to remain force free, so that its final position must be determined as part of the solution to the problem.

2.2 The Strength of the Free Vortex Sheet in the Wake

The relationship between the bound vorticity on the lifting surface and the free vorticity in the wake can be derived from Kelvin's theorem which states that the circulation around a closed contour contained in a simply connected region of potential flow is zero. This

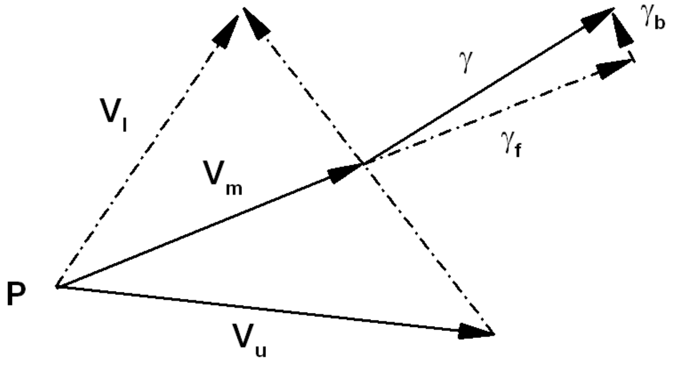

Figure 44: *General case— Bound and free vorticity is present.*

is shown in figure 45. The selected closed contour is first shown out in the middle of the fluid, where it obviously must have zero circulation. We now carefully move the contour over the lifting surface and wake in such a way as to avoid cutting through it. The circulation around the displaced contour must therefore remain zero. We must now look in more detail at how the contour is placed. First define a curvilinear s_1 coordinate which begins at a point s_L at the leading edge, and is everywhere tangent to the mean velocity vector $\vec{V}_m$. This passes the trailing edge at some point s_T and proceeds into the wake. Next define an s_2 coordinate with an origin at an arbitrary point in the wake, which lies in the wake and is orthogonal to the s_1 coordinate. Let s_W be the intersection of the s_1 and s_2 coordinates. Thus, s_L and s_T are functions of the parameter s_W. Finally, define s_E as the s_2 coordinate of a point just outside the wake.

We now see that the selected circulation contour starts just upstream of s_L, passes over the hydrofoil to a point just above s_T, follows down into the wake keeping just above the s_1 coordinate, makes a left turn at the point s_W, and proceeds over the wake to the point s_E. The return trip is similar, except that the contour remains below the wake and the hydrofoil until it reaches the starting point at s_L. The contour therefore consists of two almost closed loops, connected by a pair of parallel curves. The circulation around the forward loop, from Stokes theorem, is

$$\Gamma_1(s_W) = \int_{s_L}^{s_T} \gamma_b(s_1; s_W) ds_1$$

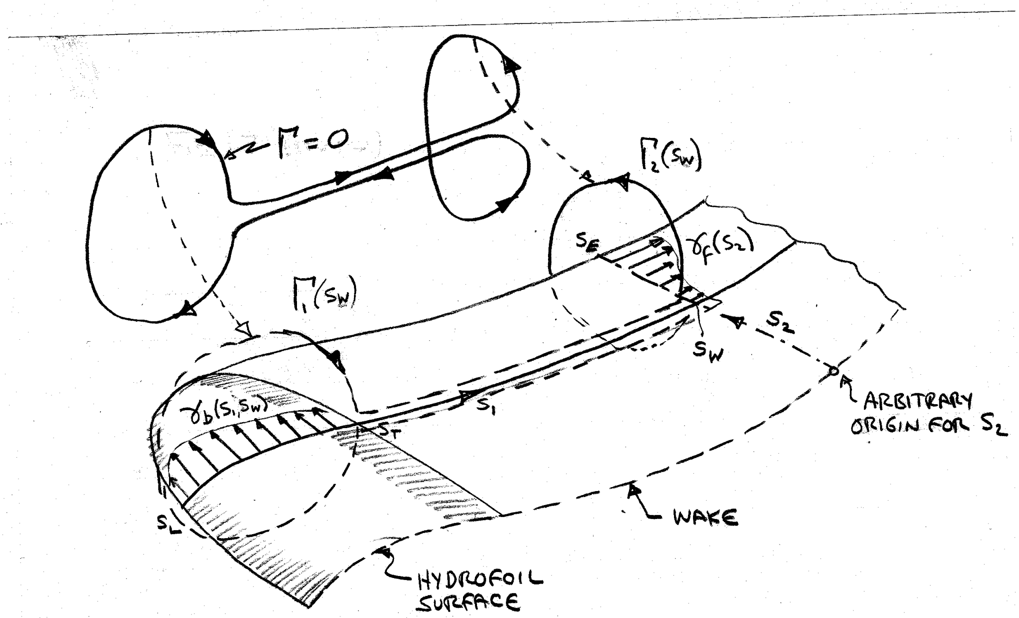

Figure 45: *Circulation path used to determine the strength of the free vorticity in the wake.*

The circulation around the portion of the contour consisting of the two parallel connecting paths is zero, since it is everywhere tangent to the vorticity vector. Therefore, to keep the total circulation zero,

$$\Gamma_2(s_W) = -\int_{s_W}^{s_E} \gamma_f(s_2)ds_2 = -\Gamma_1 \tag{95}$$

where Γ_2 is the circulation around the second loop in the wake. The final result is obtained by differentiating equation 95 with respect to s_W,

$$\frac{d\Gamma_1}{ds_W} = \frac{d}{ds_W}\int_{s_W}^{s_E} \gamma_f(s_2)ds_2 = -\gamma_f(s_w) \tag{96}$$

Thus we see that the strength of the free vorticity is related to the spanwise derivative of the bound circulation around the hydrofoil. However, the differential ds_2 must be taken in the wake, not on the hydrofoil. If the free vortex lines were to move straight back (which will be assumed subsequently in linearized hydrofoil theory), then the spanwise increment in the wake and on the hydrofoil would be the same, and this distinction would be unimportant. However, in the more general case in which deformation of the free vortex wake is allowed, equation 96 is an exact result.

2.3 The velocity induced by a three-dimensional vortex line

As a first step in the solution of the lifting surface problem just formulated, we need to be able to compute the velocity field induced by three dimensional vortex sheets. Since these sheets can be thought of as being composed of elementary vortex lines, we can first determine their individual velocity field, and then obtain the velocity induced by entire vortex sheet by integration. The expression for the velocity induced by an arbitrary three dimensional vortex line is known as Biot-Savart's law.

We will start the derivation by considering a flow in which the vorticity is confined to a volume $\mathcal{V}$ within the fluid. We wish to find the velocity $\vec{V}$ at a general point $P(x, y, z)$ as illustrated in figure 46

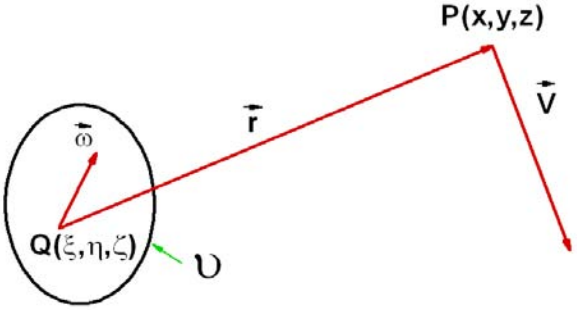

Figure 46: *Notation for velocity,* $\vec{V}$ *at point* $P(x, y, z)$ *induced by a volume distribution of vorticity* $\omega(\xi, \eta, \zeta)$ *contained in volume* $\mathcal{V}$.

An element of vorticity within $\mathcal{V}$ is shown at the point $Q(\xi, \eta, \zeta)$, and the distance vector $\vec{r}$ to the field point P is

$$\vec{r} = \vec{i}(x - \xi) + \vec{j}(y - \eta) + \vec{k}(z - \zeta)$$

$$r = \sqrt{(x - \xi)^2 + (y - \eta)^2 + (z - \zeta)^2}$$

Any vector field whose divergence is zero everywhere, and whose curl is non-zero in a portion of the field can be expressed as the curl of a vector field whose divergence is zero.[30] Interpreting the former as the velocity,$\vec{V}$, and the latter as the vector potential $\vec{A}$,

$$\vec{V} = \nabla \times \vec{A} \qquad \nabla \cdot \vec{A} = 0 \tag{97}$$

The vorticity is $\vec{\omega} = \nabla \times \vec{V}$. Introducing 97 and using a particular vector identity, we can express the vorticity in terms of the vector potential $\vec{A}$,

$$\vec{\omega} = \nabla \times \vec{V} = \nabla \times (\nabla \times \vec{A}) = \nabla(\nabla \cdot \vec{A}) - (\nabla \cdot \nabla)\vec{A}$$

---

[30] See, for example, Newman,“Marine Hydrodynamics”p115.

Since the divergence of $\vec{A}$ is zero, this reduces to

$$\vec{\omega} = -\nabla^2 \vec{A} \tag{98}$$

The solution of equation 98, which is a vector form of Poisson's equation, is,

$$\vec{A} = \frac{1}{4\pi} \int_{\mathcal{V}} \frac{\vec{\omega} d\mathcal{V}}{r} \tag{99}$$

At this point we can verify directly that the divergence of $\vec{A}$ is zero,

$$\nabla \cdot \vec{A} = \frac{1}{4\pi} \int_{\mathcal{V}} \nabla \cdot \left[\frac{\vec{\omega} d\mathcal{V}}{r} \right] = \frac{1}{4\pi} \int_S \frac{\vec{\omega} \cdot \vec{n} dS}{r}$$

The last integral can be seen to be zero as a consequence of Kelvin's theorem which requires that vortex lines not end in the fluid.

We can now roll out the volume into a long, thin vortex tube, which in the limit becomes a vortex line. As shown in figure 47, *dl* is a differential element of length along the vortex line and $\vec{s}$ is a unit vector tangent to the vortex. The volume integral in equation 99 then becomes a line integral,

$$\vec{A} = \frac{\Gamma}{4\pi} \oint \frac{\vec{s} dl}{r}$$

and the velocities may then be obtained by taking the curl of $\vec{A}$.

$$\vec{V} = \nabla \times \vec{A} = \frac{\Gamma}{4\pi} \oint \nabla \times \left[\frac{\vec{s}}{r} \right] dl = \frac{\Gamma}{4\pi} \oint \frac{\vec{s} \times \vec{r}}{r^3} dl \tag{100}$$

The latter form of equation 100 is known as Biot-Savart's law. The last step can be verified by working out each component. For example, the x component is,

$$\nabla \times \frac{\vec{s}}{r} = \begin{vmatrix} \vec{i} & \vec{j} & \vec{k} \\ \frac{\delta}{\delta x} & \frac{\delta}{\delta y} & \frac{\delta}{\delta z} \\ \frac{s_x}{r} & \frac{s_y}{r} & \frac{s_z}{r} \end{vmatrix} = \vec{i} \left[\frac{\delta}{\delta y} (\frac{s_z}{r}) - \frac{\delta}{\delta z} (\frac{s_y}{r}) \right] + \ldots \tag{101}$$

Remembering that r is a function of (x, y, z) but $\vec{s}$ is not, the x component then becomes,

$$s_z \frac{\delta}{\delta y} (\frac{1}{r}) - s_y \frac{\delta}{\delta z} (\frac{1}{r}) = -s_z \frac{(y - \eta)}{r^3} + s_y \frac{(z - \zeta)}{r^3} \tag{102}$$

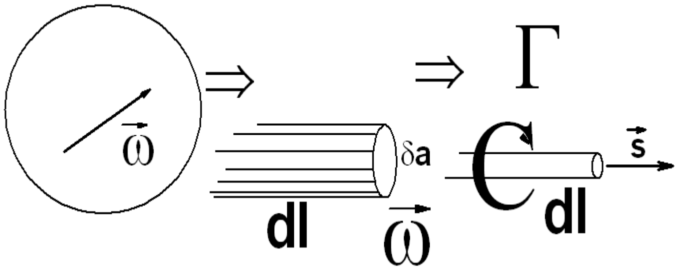

Figure 47: *Development of a vortex line. On the left is a volume distribution of vorticity* $\vec{\omega}$. *In the middle, the volume hs been put through a pasta machine to form a noodle with cross section area da. On the right, the noodle has been turned into angel's hair, with zero cross sectional area and infinite vorticity, but with the total circulation kept fixed.*

Going through the same operation with the x component of the last form of equation 100,

$$\frac{\vec{s}\times\vec{r}}{r^3} = \frac{1}{r^3}\begin{vmatrix} \vec{i} & \vec{j} & \vec{k} \\ s_x & s_y & s_z \\ x-\xi & y-\eta & z-\zeta \end{vmatrix} = \vec{i}\left[\frac{s_y(z-\zeta)-s_z(y-\eta)}{r^3}\right] \tag{103}$$

we see that this is the same as equation 102 thus verifying equation 100.

In summary, the velocity field of a concentrated vortex line of strength Γ is,

$$\vec{V} = \frac{\Gamma}{4\pi}\oint \frac{\vec{s}\times\vec{r}}{r^3}dl \tag{104}$$

which can be written out in component form as follows,

$$u = \frac{\Gamma}{4\pi}\oint \frac{s_y(z-\zeta)-s_z(y-\eta)}{r^3}dl$$

$$v = \frac{\Gamma}{4\pi}\oint \frac{s_z(x-\xi)-s_x(z-\zeta)}{r^3}dl$$

$$w = \frac{\Gamma}{4\pi}\oint \frac{s_x(y-\eta)-s_y(x-\xi)}{r^3}dl \tag{105}$$

Equation 105 is particularly useful in deriving expressions for the velocity induced by particular shapes of vortex lines, as we will see later.

Some comments should be made about the limits of the integral in Biot-Savart's law. From Kelvin's theorem, a vortex line must have constant strength and cannot end in the interior of the fluid. If we are really solving for the velocity field of a concentrated vortex, then the integral must be taken over a closed path. However, we started out this section with the observation that a vortex sheet could be considered to be made up of individual vortex filaments representing bound and free vorticity. In this case, the strengths of the vortex filaments can vary along their length, provided that the variation of bound and free vorticity is always set in such a way that Kelvin's theorem is satisfied. The velocity induced by one component of the vortex distribution can still be obtained from Biot-Savart's law, but the strength of the vortex in equation 104 will have to be moved inside the integral, and the contour of integration will not necessarily be closed.

2.4 Velocity Induced by a Straight Vortex Segment

The velocity field of a straight vortex segment serves as a simple illustration of the application of Biot-Savart's law. However, it is also a very useful result since the numerical solution of more complicated geometries can be obtained by discretizing the vortex sheet into a lattice of straight concentrated vortex elements. The result to be derived here therefore serves as the *influence function* for such a computational scheme.

We can simplify the analysis by choosing a coordinate system such that the vortex segment coincides with the x axis and the field point, P, lies on the y axis, as shown in figure 48. This is not really a restriction, since one can always make a coordinate transformation to do this, and the resulting velocity vector can then be transformed back to the original global coordinate system.

The vortex extends along the x axis from x_1 to x_2. In this case

$$\vec{s} = (1,0,0) \quad and \quad \vec{r} = (-\xi, y, 0)$$

and from equation 104 we can see immediately that $u = v = 0$, so that we only need to develop the expression for w,

$$w(y) = \frac{\Gamma}{4\pi}\int_{x_1}^{x_2} \frac{y d\xi}{(\xi^2+y^2)^{3/2}} = \frac{\Gamma}{4\pi y}\left[\frac{\xi}{\sqrt{\xi^2+y^2}}\right]_{x_1}^{x_2} = \frac{\Gamma}{4\pi y}\left[\frac{x_2}{b} - \frac{x_1}{c}\right] \qquad (106)$$

Where $b = \sqrt{x_2^2 + y^2}$ and $c = \sqrt{x_1^2 + y^2}$. This result can also be expressed in terms of the two angles θ_1 and θ_2 which are illustrated in figure 48,

$$w(y) = \frac{\Gamma}{4\pi y}[\cos\theta_2 + \cos\theta_1]$$

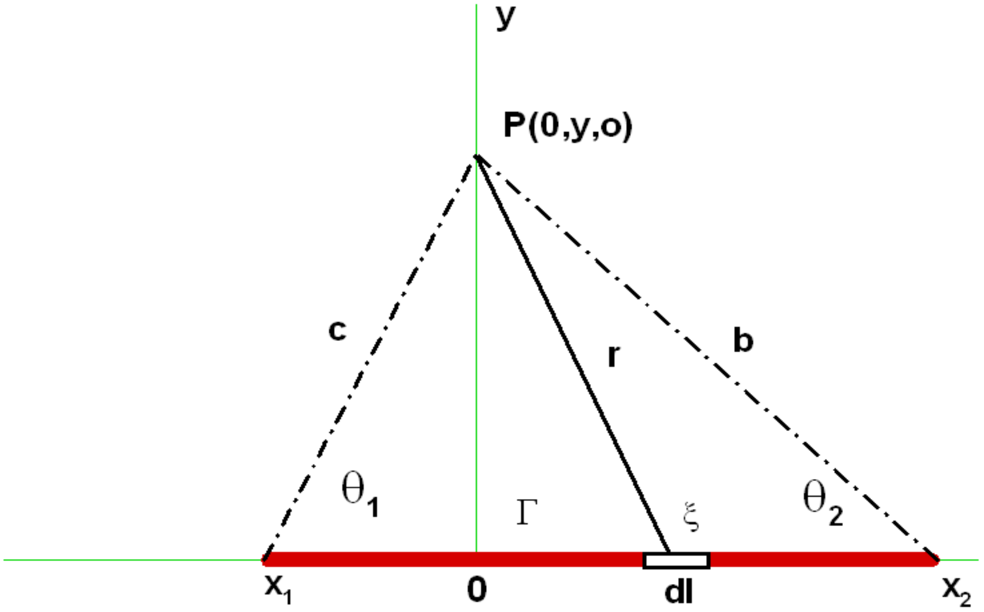

Figure 48: *Notation for a straight line vortex segment using a local coordinate system with the x axis coincident with the vortex, and the field point, P located on the y axis.*

Two limiting cases are of particular interest. For an infinitely long vortex, $\theta_1 = \theta_2 = 0$ so that

$$w(y) = \frac{\Gamma}{2\pi y}$$

which is the correct result for a two dimensional vortex. For a semi infinite vortex extending from $x = 0$ to infinity, $\theta_1 = \pi/2$ and $\theta_2 = 0$ so that the velocity is half that of an infinite vortex. This result is useful in lifting line theory which we will be looking at later.

The complete velocity field is shown in figure 49 for a vortex extending along the x axis from -1 to $+1$. The variation in velocity with y is shown for several fixed values of x. In this plot, the velocity has been non-dimensionalized by the factor $\Gamma/2\pi y$ so that the results can be interpreted as the ratio of the velocity induced by the vortex segment to that induced by an infinite vortex of the same strength located the same distance away. Therefore, for $|x| < 1$ the result approaches a value of unity as y becomes small. For $|x| > 1$ the result approaches zero for small y. For large y distances away from the vortex segment, the non-dimensional velocity becomes independent of x and decays as $1/y$. The dimensional velocity therefore decays as $1/y^2$.

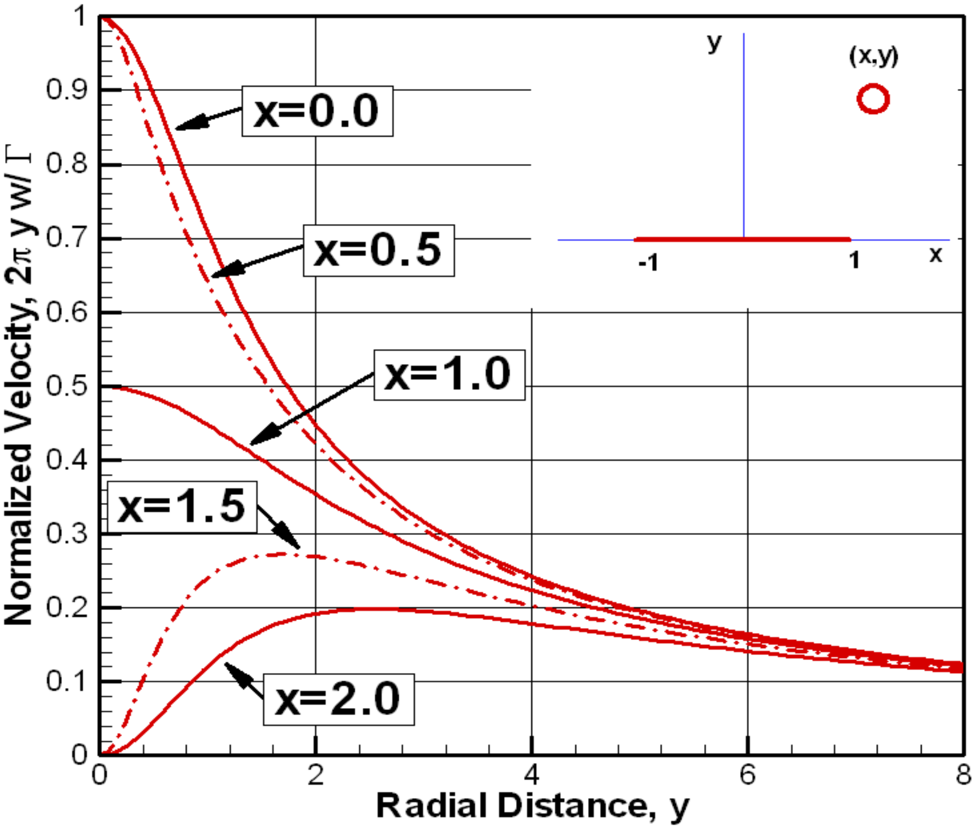

Figure 49: *Normalized velocity,* $2\pi y w(x, y)/\Gamma$ *induced by a straight vortex segment.*

2.5 Linearized Lifting-Surface Theory for a Planar Foil

2.5.1 Formulation of the Linearized Problem

We will now consider the case of a hydrofoil of zero thickness, whose surface lies very nearly in a plane which is aligned with the oncoming flow. Such a surface, for example, might be exactly flat but inclined at a small angle of attack with respect to the flow. More generally, however, the surface may have some arbitrary distribution of camber and angle of attack. The only restrictions are that the resulting deviation of the surface from the reference plane be small and that the slopes of the surface be everywhere small.

Figure 50 illustrates the particular notation for this problem. A Cartesian coordinate system is oriented with the positive x axis in the direction of a uniform onset flow of magnitude U. The y axis normal to U, and the (x, y) plane serves as the reference surface. The tips of the hydrofoil are located at $y = \pm s/2$, so that its total span is s.

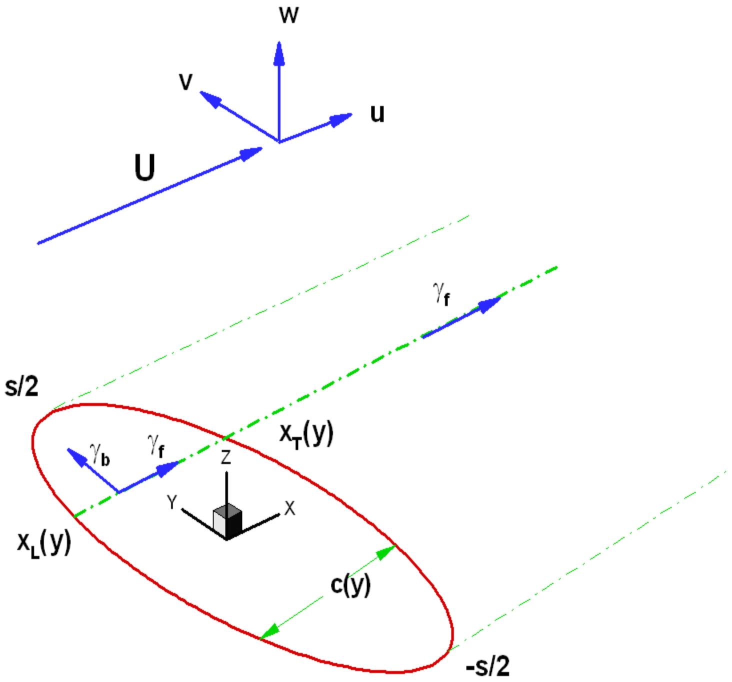

Figure 50: *Notation for a planar hydrofoil.*

The outline, or planform, of the hydrofoil is described by the curves $x = x_L(y)$ and $x = x_T(y)$, denoting respectively the projection of the leading and trailing edges on the (xy) plane.

A section of the surface at spanwise position y is shown in figure 51. The notation is the same as for a two-dimensional foil, as illustrated in figure 1, except that the angle of attack, $\alpha(y)$, and the vertical displacement of the nose-tail line, $z_0(y)$ must be considered as part of the three-dimensional geometry. In addition, the vertical coordinate is now z, rather than y. The angle of attack of the nose–tail line relative to the oncoming flow is $\alpha_{(}y)$ and the distribution of camber is denoted by the function $f(x, y)$. The camber is measured in a direction normal to the nose–tail line, and its maximum value at any spanwise station is $f_0(y)$. When we add thickness later, it will similarly be denoted by the function $t(x, y)$ with a maximum value $t_0(y)$ at each spanwise location. The thickness function will then be added at right angles to the camber line, with $t/2$ projecting on each side. Finally, the chord length $c(y)$ is the length from the leading to the trailing edge measured along the nose–tail line.

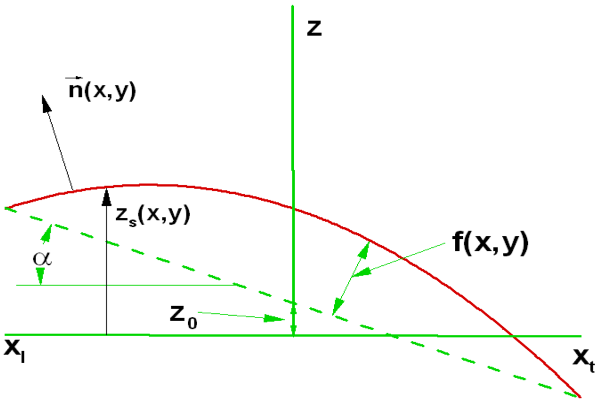

Figure 51: *Cut through foil section at fixed spanwise location, y.*

If the angle of attack is small, we can assume that $cos\ \alpha \approx 1$ so that the chord length is essentially the same as its projection on the (xy) plane,

$$c(y) \approx x_T(y) - x_L(y)$$

Similarly, since the angle of attack has been assumed to be small, we can write the z coordinate of a point on the surface as follows,

$$z_s(x, y) \approx z_0(y) - \alpha(y)x + f(x, y)$$

where $z_0(y)$ is the elevation of the nose–tail line at $x = 0$.

2.5.2 The Linearized Boundary Condition

The exact boundary condition is that the normal component of the total fluid velocity vanish at all points on the hydrofoil surface,

$$\vec{V} \cdot \vec{n} = 0 \qquad on \;\; z = z_s(x, y)$$

If the slopes of the surface are small, the unit normal vector can be approximated as

$$\vec{n} \approx \vec{\imath}\left(-\frac{\partial z_s}{\partial x}\right) + \vec{\jmath}\left(-\frac{\partial z_s}{\partial y}\right) + \vec{k}\,(1)$$

The fluid velocity can be expressed as the sum of the oncoming flow U and a disturbance velocity field with components (u, v, w). The total velocity is therefore

$$\vec{V} = \vec{\imath}(U + u) + \vec{\jmath}v + \vec{k}w$$

and its dot product with the normal vector is

$$\vec{V} \cdot \vec{n} \approx -(U + u)\frac{\partial z_s}{\partial x} - v\frac{\partial z_s}{\partial y} + w \tag{107}$$

If the camber and angle of attack is small, we can expect that the disturbance velocities will be small compared with the oncoming flow. We can therefore eliminate the products of small quantities in equation 107 to obtain the final form of the linearized boundary condition,

$$w \approx U\frac{\partial z_s}{\partial x} \qquad on \;\; z = 0 \tag{108}$$

Note that the boundary condition is satisfied on the reference plane $z = 0$ rather than on the actual surface, which is the same approximation as was made for linearized 2D theory.

It is important to note that equation 108 does not involve the slope of the surface in the spanwise direction, and actually looks just like the boundary condition for two–dimensional flow. This is not the result of any assumption that the spanwise slopes are smaller than the chordwise ones, but follows from the assumption that the predominant velocity is in the chordwise direction.

2.5.3 Determining the Velocity

The next step is to determine the vertical component of the disturbance velocity induced by the bound and free vortices representing the hydrofoil and its wake. If the disturbance velocities are small, we can assume that the mean inflow is equal in magnitude and direction to the oncoming flow. This means, in particular, that the bound vorticity will be oriented in the y direction, and that the free vorticity will be oriented in the x direction. The vortex sheets are projected onto the (xy) plane, and the trailing vortex wake will consist only of semi–infinite straight vortices extending downstream in the x direction from the trailing edge.

It is important to remark at this point that this assumption regarding the wake does not conform to reality even for hydrofoils which have small angles of attack and camber. The planar free vortex sheet which we are assuming is actually unstable, and its outboard edges tend to roll up and form concentrated tip vortices. While this is a matter of concern in many applications (as we shall see subsequently in looking at marine propellers) it is fortunately not of great importance to the problem at hand. The reason is that the velocity induced at points on the lifting surface by an element of free vorticity in the distant wake is both small and insensitive to its precise position.

An expression for the velocity induced at a point $(x, y, 0)$ on the projection of the hydrofoil surface by the bound vorticity γ_b can be obtained directly from equation 105,

$$w^{(b)}(x, y, 0) = -\frac{1}{4\pi} \int_{-s/2}^{s/2} \fint_{x_L(\eta)}^{x_T(\eta)} \frac{\gamma_b(\xi, \eta)(x - \xi)}{r^3} d\xi d\eta \tag{109}$$

Here ξ and η are dummy variables corresponding to x and y. The integral over the span is in the direction of the elementary bound vortex lines, as in equation 104, while the integration in the chordwise direction of the continuous vortex sheet is equivalent to the total circulation of a concentrated vortex line. Since the denominator in equation 109 vanishes when $x = \xi$ and $y = \eta$, the integral is singular. The singularity is of the Cauchy principal value type, which we saw earlier in the solution of the 2D problem.

The exact distance vector, $\vec{r}$, from an element of vorticity on the hydrofoil surface located at (ξ, η, ζ_s) to another point on the surface (x, y, z_s) where we want to calculate the velocity has a magnitude,

$$r = \sqrt{(x-\xi)^2 + (y-\eta)^2 + (z_s - \zeta_s)^2}$$

but since linear theory projects everything onto the (xy) plane, this reduces to,

$$r \approx \sqrt{(x-\xi)^2 + (y-\eta)^2}$$

The velocity induced by the free vorticity can be developed from equation 104 in the same way, giving the result,

$$w^{(f)}(x,y,0) = \frac{1}{4\pi}\int_{-s/2}^{s/2}\int_{x_L(\eta)}^{\infty}\frac{\gamma_f(\xi,\eta)(y-\eta)}{r^3}d\xi d\eta \tag{110}$$

Note that in this case that the upper limit of the ξ integration is not the trailing edge, but extends to infinity downstream.

2.5.4 Relating the Bound and Free Vorticity

The relationship between the bound and free vorticity can be obtained using the same approach as was used in section 2.2. However, things are now simpler, since the s_1 and s_2 coordinates in figure 45 are now just the x and y coordinates. If we chose a circulation path as shown in figure 52, where the two connected loops almost touch the hydrofoil at the point (x,y), it is evident from Stokes theorem that,

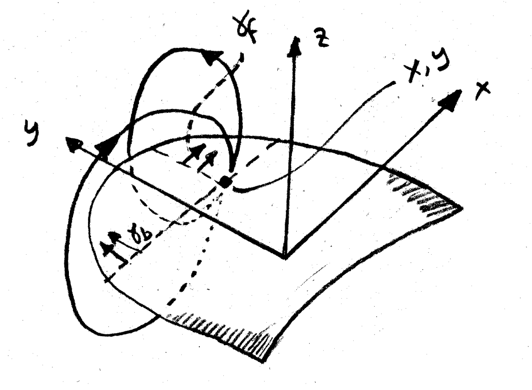

Figure 52: *Circulation contours to get free vorticity on the foil.*

$$\int_{x_L(y)}^{x}\gamma_b(\xi,y)d\xi - \int_{y}^{s/2}\gamma_f(x,\eta)d\eta = 0 \tag{111}$$

Differentiating equation 111 with respect to y, keeping in mind that the lower limit of the first integral is a function of y, we obtain an expression for the free vorticity at any point within the hydrofoil,

$$\gamma_f(x,y) = \gamma_b(x_L,y)\frac{dx_L}{dy} - \int_{x_L}^{x} \frac{\partial\gamma_b(\xi,y)}{\partial y} d\xi \tag{112}$$

The first term in equation 112 can be interpreted as the bound vorticity which runs into the leading edge being turned ninety degrees to become free vorticity. For example, if a hydrofoil had constant bound vortex strength over its surface, the second term in equation 112 would be zero, and the only source of free vorticity on the hydrofoil would be due to the first term.

If the point x moves downstream of the trailing edge, equation 111 becomes,

$$\int_{x_L(y)}^{x_T(y)} \gamma_b(\xi,y)d\xi - \int_{y}^{s/2} \gamma_f(x,\eta)d\eta = 0 \tag{113}$$

which looks almost the same, except that the upper limit of the first integral is now also a function of y. Differentiation with respect to y therefore results in one additional term,

$$\gamma_f(y) = \gamma_b(x_L,y)\frac{dx_L}{dy} - \int_{x_L(y)}^{x_T(y)} \frac{\partial\gamma_b(\xi,y)}{\partial y} d\xi - \gamma_b(x_T,y)\frac{dx_T}{dy} = -\frac{d\Gamma}{dy} \tag{114}$$

Thus, the free vorticity in the wake is independent of x and depends only on the spanwise derivative of the total bound circulation around the hydrofoil. This result agrees with the more general result given in equation 96.

The formulation of the linearized planar hydrofoil problem is now complete. The boundary condition given in equation 108 relates the geometry and angle of attack of the hydrofoil to the vertical induced velocity. The latter is related to the bound and free vorticity by equations 109 and 110. Finally, the free vorticity is related to the bound vorticity by equations 112 and 114. Thus, the relationship between the hydrofoil geometry and its bound vortex distribution is established. Finally, the distribution of pressure jump (which is commonly referred to as the *load distribution* across the lifting surface is directly related to the bound vorticity from equation 94.

If we are given the geometry and angle of attack, we can solve for the load distribution using the above equations. Since the unknown bound vortex distribution appears inside an integral in this case, we must solve an integral equation. This is known as the *analysis problem.*

On the other hand, if we are given the load distribution, the quantities inside the integrals are known, and we can obtain the slope of the hydrofoil section directly by integration. One more integration is then required to get the actual shape of the hydrofoil from the slope of its surface. This is known as the *design problem.*

While this is simple enough in principle, the problem is complicated by the fact that the integrals in either case are singular, and no closed form solution exists even for this linearized problem. One must therefore resort to numerical procedures, or to a combination of analytical and numerical techniques to solve the problem. Before we get into this, we will develop expressions for the overall lift and drag forces on a hydrofoil, which can be done analytically.

2.6 Lift and Drag

The resultant force per unit span on a section at spanwise location y can be resolved into components $F_z(y)$ in the z direction and $F_x(y)$ in the x direction. The force in the z direction, being at right angles to the direction of the oncoming flow, as we saw earlier in looking at two-dimensional flow, is termed *lift*, while the force in the x direction is termed *drag.* In a real fluid, the drag force consists of a contribution due to viscous stresses on the surface of the hydrofoil, and a contribution due to the presence of the trailing vortex system. The latter is termed *induced drag* and is the only component of drag considered in our present inviscid analysis. In the case of two- dimensional flow, there is no free vorticity, and hence, no induced drag.

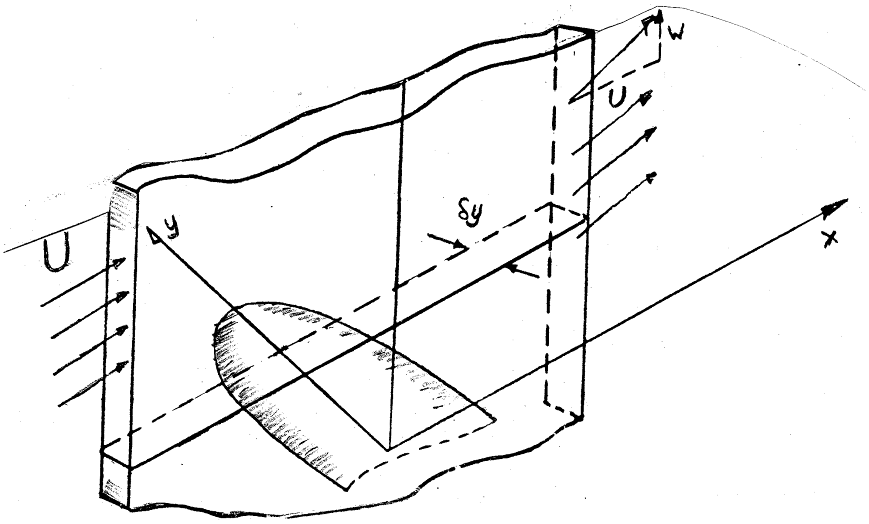

Figure 53: *Control volume for momentum analysis for lift.*

We can derive the force acting on a section by applying the momentum theorem to a control volume of infinitesimal spanwise extent δy extending to infinity in the x and z directions, as shown in figure 53. The force in the z direction is

$$F_z(y)\delta y = -\rho \int_S w(\vec{V} \cdot \vec{n}) dS \tag{115}$$

where the integral is taken over all surfaces of the control volume.

The contributions of the top, bottom and front surfaces to equation 115 can be seen to be zero, since the velocity at large distances decays at a faster rate than the area increases. The contribution of the sides is also zero due to the fact that w is an even function of z while $\vec{V} \cdot \vec{n}$ is odd. This leaves the flux of momentum through the aft surface. Since this is far from the hydrofoil, the velocity induced by the bound vorticity goes to zero. The only induced velocity is that due to the free vortices, which has no component in the x direction. Thus, the momentum flux is

$$F_z(y)\delta y = -\rho U \int_{-\infty}^{\infty} w(\infty, y, z) dz \delta y \tag{116}$$

Since we are infinitely far downstream, the velocity induced by the free vortices appears as that due to a sheet of vortices of infinite extent in the x direction,

$$w(\infty, y, z) = \frac{1}{2\pi} \int_{-s/2}^{s/2} -\frac{\partial \Gamma}{\partial \eta} \frac{y-\eta}{[(y-\eta)^2 + z^2]} d\eta \tag{117}$$

Combining equations 116 and 117, and reversing the order of integration gives the result

$$F_z(y) = \frac{\rho U}{2\pi} \int_{-s/2}^{s/2} \frac{\partial \Gamma}{\partial \eta} \int_{-\infty}^{\infty} \frac{y-\eta}{[(y-\eta)^2 + z^2]} dz d\eta \tag{118}$$

The integral in equation 118 is

$$\int \frac{y-\eta}{[(y-\eta)^2 + z^2]} dz = \tan^{-1}\left(\frac{z}{y-\eta}\right) \tag{119}$$

which is simple enough, except that we have to be careful in evaluating the limits. As $z \to \infty$ the inverse tangent becomes $\pm\pi/2$ depending on the sign of z and $y - \eta$. The safe way is to break up the spanwise integral into two intervals, depending on the sign of $y-\eta$,

$$F_z(y) = \frac{\rho U}{2\pi}\int_{-s/2}^{y} \frac{\partial\Gamma}{\partial\eta}\tan^{-1}\left|\frac{z}{y-\eta}\right|_{-\infty}^{\infty} d\eta + \frac{\rho U}{2\pi}\int_{y}^{s/2} \frac{\partial\Gamma}{\partial\eta}\tan^{-1}\left|\frac{z}{y-\eta}\right|_{-\infty}^{\infty} d\eta \tag{120}$$

which leads us to the final result

$$F_z(y) = \frac{\rho U}{2}\left[\Gamma(y) - \Gamma(-s/2)\right] - \frac{\rho U}{2}\left[\Gamma(s/2) - \Gamma(y)\right] = \rho U \Gamma(y) \tag{121}$$

Thus, the total lift force on a section is the same as that which would result if the distribution of bound circulation over the chord were concentrated in a single vortex of strength $\Gamma(y)$.

We cannot use the same control volume to determine the drag, since x directed momentum is convected across the sides of the control volume, and we would need to know more about the details of the flow to calculate it. However, we can determine the total induced drag by equating the work done by the drag force when advancing the hydrofoil a unit distance to the increase in kinetic energy in the fluid. For this purpose we can make use of Green's formula

$$E = \frac{\rho}{2}\int_S \phi\frac{\partial\phi}{\partial n} dS \tag{122}$$

to determine the kinetic energy, E in the fluid region bounded by the surface S. In equation 122, ϕ is the velocity potential and $\vec{n}$ is a unit normal vector directed outwards from the control volume, as illustrated in figure 54.

The contribution to the integral in 122 from all the surfaces except for those cut by the free vortex wake is zero as the outer boundaries move to infinity. On the inner surface, the normal derivative of the velocity potential is $-w(\infty, y, 0)$ on the upper portion, and $w(\infty, y, 0)$ on the lower portion. The jump in potential $(\phi_u - \phi_l)$ is equal to the circulation $\Gamma(y)$ around the hydrofoil at spanwise position y.

The kinetic energy imparted to the fluid as the foil advances a unit distance in the x direction is the total induced drag, $F_x(total)$. This, in turn, can be equated to the total kinetic energy between two planes far downstream separated by unit x distance,

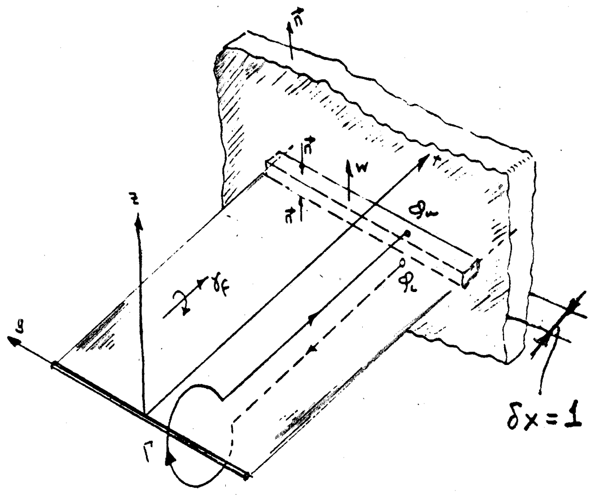

Figure 54: *Control volume for kinetic energy far downstream.*

$$
\begin{aligned}
F_x(total) &= \frac{\rho}{2}\int_{-s/2}^{s/2}\phi_l w(\infty,y,0)dy + \frac{\rho}{2}\int_{s/2}^{-s/2}\phi_u(-w(\infty,y,0))(-dy) \\
&= \frac{\rho}{2}\int_{-s/2}^{s/2}(\phi_l - \phi_u)w(\infty,y,0)dy \\
&= -\frac{\rho}{2}\int_{-s/2}^{s/2}\Gamma(y)w(\infty,y,0)dy \qquad (123)
\end{aligned}
$$

We can relate this to the velocity field near the hydrofoil as follows. Suppose that the total bound circulation were concentrated on a single vortex line coincident with the y axis, as shown in figure 55. The velocity $w(0,y,0)$ induced by the free vortices would be half the value induced at infinity, as shown earlier. Defining a *downwash velocity*

$$w^*(y) \equiv w(0,y,0)$$

equation 123 becomes

$$F_x(total) = -\rho\int_{-s/2}^{s/2}\Gamma(y)w^*(y)dy \qquad (124)$$

The total induced drag force is therefore the same as that which would result if the resultant force on each spanwise section were normal to the induced inflow velocity,

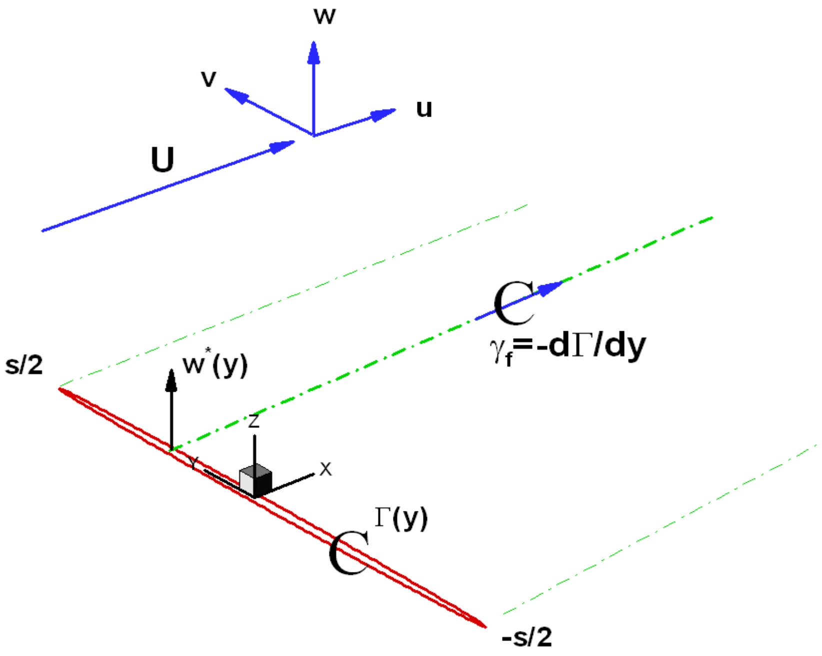

Figure 55: *Concentration of bound vorticity along a lifting line.*

$V^*(y)$, as shown in figure 56. Here $V^*(y)$ is the resultant of U and $w*(y)$, and $F(y)$ is the resultant of the lift $F_z(y)$ and the induced drag $F_x(y)$.

A simple interpretation of this result follows from a consideration of the flow field seen by a small bug traveling on the concentrated vortex at spanwise position y. The flow appears to be two-dimensional to the bug, but with an inflow represented by V^* rather than U. Hence the force, from Kutta Joukowski's law is at right angles to the local flow, and therefore has components in both the lift and drag directions.

There is one danger in this interpretation. It would appear from equation 124 that we have determined the spanwise distribution of induced drag, yet Greens formula for kinetic energy is a global result. The answer to this paradox is that the integrand of 124 only represents the local force if the foil is really a straight lifting line, which allowed us to relate the downwash to the value of w at infinity. This spanwise distribution of induced drag is also reasonably correct for straight, high aspect ratio foils. But if the foil is swept, the actual spanwise distribution of induced drag can be completely different, yet the total drag will be correctly predicted by equation 124.

Thus, the spanwise distribution of lift, and the total induced drag of a hydrofoil is a function only of its spanwise distribution of circulation. The planform of the foil, and its chordwise distribution of circulation has no affect on these quantities. This is a

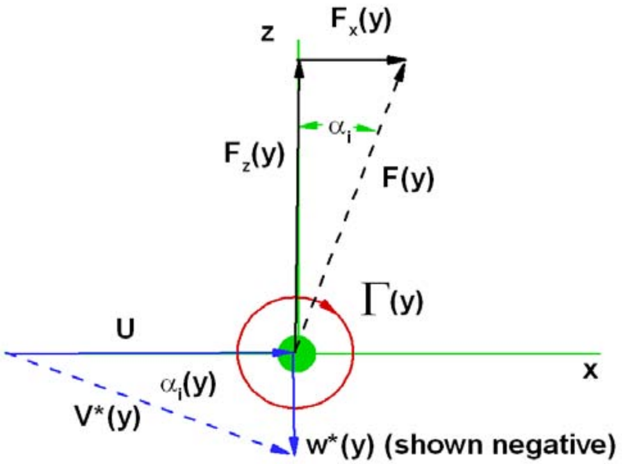

Figure 56: *Interpretation of lift and drag in terms of local flow at a lifting line.*

direct consequence of the linearizing assumptions made, particularly with regard to the position of the free vortex wake. Nevertheless, predictions of lift and drag made on this basis are generally in close agreement with measurements except in cases where extreme local deformation of the free vortex sheet occurs.

Lifting line theory is therefore extremely useful *preliminary design tool* for foils of arbitrary planform, since it will tell us how much we have to pay in drag for a prescribed amount of lift. In order to do this, we need to know how to calculate $w^*(y)$ as a function of the circulation distribution $\Gamma(y)$. Read the next section to find out!

2.7 Lifting Line Theory

2.7.1 Glauert's Method

We will now develop an expression for the velocity $w^*(y)$ induced on a lifting line by the free vortex sheet shed from an arbitrary distribution of circulation $\Gamma(y)$ over the span. We will follow the classical method of Glauert [31]. It will be evident that the approach is very similar to the method used by Glauert to find the velocity induced by a two-dimensional vortex distribution. Once this is done, expressions for the lift and induced drag can be obtained from the results of the preceding section.

We first define a new spanwise variable $\tilde{y}$ which is related to the physical coordinate y as follows,

$$y = -\frac{s}{2}\cos(\tilde{y}) \tag{125}$$

so that $\tilde{y} = 0$ when $y = -s/2$ and $\tilde{y} = \pi$ when $y = s/2$. The spanwise distribution of circulation is assumed to be represented by the following sine series in $\tilde{y}$,

$$\Gamma(y) = 2Us\sum_{n=1}^{\infty} a_n \sin(n\tilde{y}) \tag{126}$$

which has the property that $\Gamma = 0$ at the tips for any values of the coefficients a_n. The free vortex strength is then obtained by differentiating 126 with respect to y,

$$\begin{aligned}
\gamma_f(y) &= -\frac{d\Gamma}{dy} = -\frac{d\Gamma}{d\tilde{y}}\frac{d\tilde{y}}{dy} \\
&= \left\{-2Us\sum_{n=1}^{\infty} na_n\cos(n\tilde{y})\right\}\left\{\frac{1}{\frac{s}{2}\sin(\tilde{y})}\right\} \\
&= -\frac{4U}{\sin(\tilde{y})}\sum_{n=1}^{\infty} na_n\cos(n\tilde{y}) \qquad (127)
\end{aligned}$$

The velocity $w^*(y)$ can now be expressed as an integral over the span, keeping in mind that the velocity induced by the semi–infinite free vortices is simply half of the two–dimensional value,

---

[31] *Elements of Aerofoil and Airscrew Theory*, Cambridge University Press, 1926

$$w^*(y) = \frac{1}{4\pi} \oint_{-s/2}^{s/2} \frac{\gamma_f(\eta)}{y-\eta} d\eta \tag{128}$$

Introducing equation 127 into equation 128 and defining a dummy spanwise variable $\tilde{\eta}$ as in equation 125,

$$\eta = -\frac{s}{2}\cos(\tilde{\eta}) \tag{129}$$

we can obtain the final result for $w^*(y)$,

$$\begin{aligned} w^*(y) &= \frac{1}{4\pi} \oint_0^{\pi} \frac{\left\{ \frac{-4U}{\sin\tilde{\eta}} \sum_{n=1}^{\infty} n a_n \cos(n\tilde{\eta}) \right\} \left\{ \frac{s}{2}\sin(\tilde{\eta}) d\tilde{\eta} \right\}}{-\frac{s}{2}\left\{\cos\tilde{y} - \cos\tilde{\eta}\right\}} \\ &= \frac{U}{\pi} \oint_0^{\pi} \frac{\sum_{n=1}^{\infty} n a_n \cos(n\tilde{\eta})}{\cos\tilde{y} - \cos\tilde{\eta}} d\tilde{\eta} \\ &= -U \sum_{n=1}^{\infty} \frac{n a_n \sin(n\tilde{y})}{\sin\tilde{y}} \end{aligned} \tag{130}$$

The last step in equation 130 makes use of Glauert's integral, which we saw before in the solution of the two-dimensional foil problem,

$$I_n(\tilde{y}) = \oint_0^{\pi} \frac{\cos(n\tilde{\eta})}{\cos\tilde{y} - \cos\tilde{\eta}} d\tilde{\eta} = -\pi \frac{\sin(n\tilde{y})}{\sin\tilde{y}} \tag{131}$$

Figure 57 shows the first four terms of the Glauert series for the spanwise distribution of circulation, while figure 58 shows the resulting induced velocity. Note that the leading term produces a constant velocity of -1 over the span, while the higher terms produce progressively larger and more oscillatory velocity distributions. Note that the velocity given in equation 130 is indeterminate at the tips, where $\sin\tilde{y} = 0$, but that it can easily be evaluated, giving the result that $w^*/U = \pm n^2 a_n$. The fact that the velocity at the tips induced by each term in the series grows quadratically with n has important practical consequences which we will discuss later.

At this point the total force in the z direction can be found,

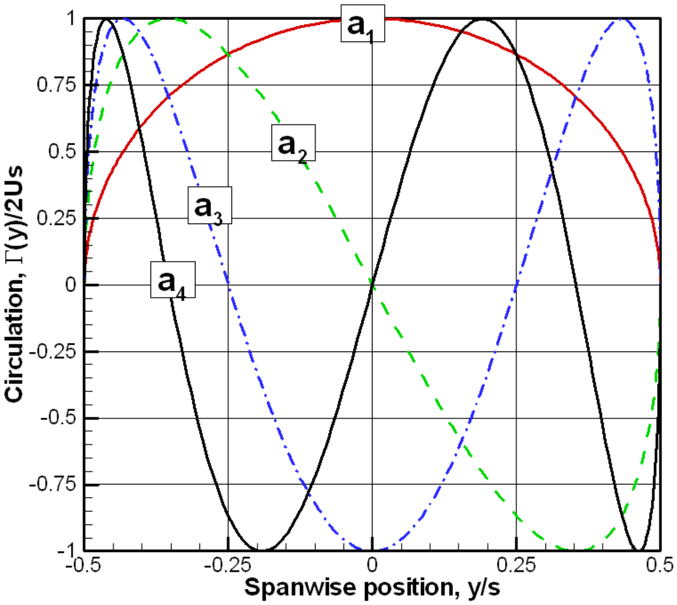

Figure 57: *Plot of first four terms of Glauert's circulation series.*

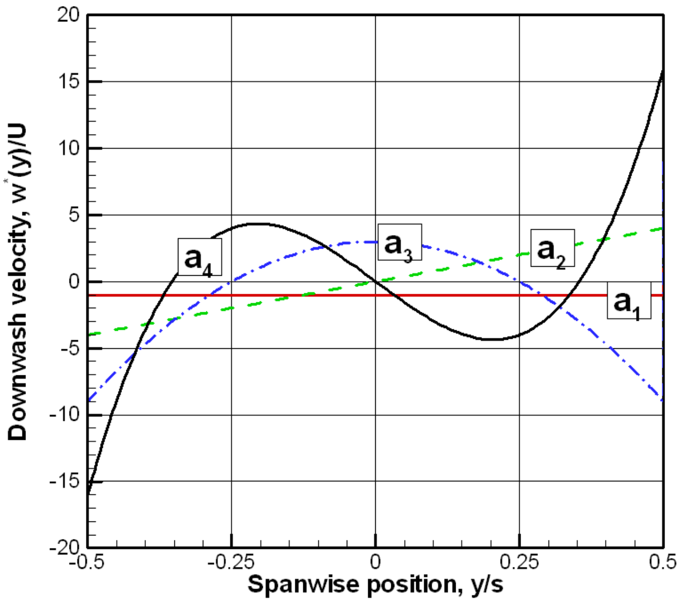

Figure 58: *Plot of velocity induced by first four terms of Glauert's circulation series.*

$$\begin{aligned}\bar{F}_z &= \int_{-s/2}^{s/2} F_z(y)dy = \rho U \int_{-s/2}^{s/2} \Gamma(y)dy \\ &= \rho U^2 s^2 \int_0^{\pi} \sum_{n=1}^{\infty} a_n \sin(n\tilde{y}) \sin\tilde{y} d\tilde{y} \\ &= \frac{\pi}{2}\rho U^2 s^2 a_1 \end{aligned} \tag{132}$$

which is seen to depend only on the leading term in the assumed series for the spanwise distribution of circulation. The remaining terms serve to redistribute the lift over the span, but do not affect the total.

The total induced drag force can now be computed from the formula obtained in the previous section,

$$\bar{F}_x = -\rho \int_{-s/2}^{s/2} w^*(y)\Gamma(y)dy \tag{133}$$

which can be accomplished by substituting equations 126 and 130 into 133. Since this involves the product of two series, two summation indices are required. Noting that all but the diagonal terms in the product of the two series vanish upon integration $(0, \pi)$, the steps necessary to obtain the final result are as follows,

$$\begin{aligned}\bar{F}_x &= -\rho \int_0^{\pi} \left\{ \frac{-U \sum_{n=1}^{\infty} n a_n \sin(n\tilde{y})}{\sin\tilde{y}} \right\} \left\{ 2Us \sum_{m=1}^{\infty} a_m \sin(m\tilde{y}) \right\} \frac{s}{2} \sin\tilde{y} d\tilde{y} \\ &= \rho U^2 s^2 \int_0^{\pi} \sum_{n=1}^{\infty} n a_n \sin(n\tilde{y}) \sum_{m=1}^{\infty} a_m \sin(m\tilde{y}) d\tilde{y} \\ &= \frac{\pi}{2}\rho U^2 s^2 \sum_{n=1}^{\infty} n a_n^2 \end{aligned} \tag{134}$$

It is instructive to extract the leading coefficient in the circulation series, and to express it in terms of the total lift force $\bar{F}_z$ from 132,

$$
\begin{aligned}
\bar{F}_x &= \frac{\pi}{2}\rho U^2 s^2 a_1^2 \left\{1+\sum_{n=2}^{\infty} n\left(\frac{a_n}{a_1}\right)^2\right\} \\
&= \frac{2\bar{F}_z^2}{\pi\rho U^2 s^2}\left\{1+\sum_{n=2}^{\infty} n\left(\frac{a_n}{a_1}\right)^2\right\} \qquad (135)
\end{aligned}
$$

Thus, we see that the reciprocal of the term in brackets is a form of efficiency which is maximized when $a_n = 0$ for $n > 1$. The presence of higher terms in the circulation series does not change the lift, but increases the drag. The optimum spanwise distribution of circulation is therefore one in which the lift is distributed as $\sin\tilde{y}$, or in physical coordinates, as an ellipse.

For a fixed spanwise distribution of lift, equation 135 shows that induced drag is directly proportional to the square of the total lift, inversely proportional to the square of the speed, and inversely proportional to the square of the span.

This result is frequently presented in terms of lift and drag coefficients based on planform area. This requires the introduction of a non-dimensional parameter $\mathcal{A}$ called *aspect ratio*, which is the ratio of the span squared to the area, $\mathcal{S}$ of the hydrofoil,

$$\mathcal{A} = \frac{s^2}{\mathcal{S}} \qquad (136)$$

Defining the total lift and induced drag coefficients as,

$$
\begin{aligned}
\bar{C}_L &= \frac{\bar{F}_z}{\frac{1}{2}\rho U^2 \mathcal{S}} \\
\bar{C}_D &= \frac{\bar{F}_x}{\frac{1}{2}\rho U^2 \mathcal{S}} \qquad (137)
\end{aligned}
$$

the non-dimensional form of equation 135 becomes,

$$\bar{C}_D = \frac{\bar{C}_L^2}{\pi\mathcal{A}}\left\{1+\sum_{n=2}^{\infty} n\left(\frac{a_n}{a_1}\right)^2\right\} \qquad (138)$$

While equation 138 is more concise, it can lead to the erroneous conclusion that increasing aspect ratio always reduces induced drag. It does reduce induced drag if the increase in aspect ratio is achieved by increasing the span. However, if it is achieved by keeping the span fixed and reducing the chord, equation 135 shows that the drag is the same. The confusion is caused by the fact that if the area is reduced, the lift coefficient must be increased in order to obtain the same lift. Therefore, in this case both the lift and drag coefficients increase, but the dimensional value of the drag remains the same.

2.7.2 Vortex Lattice Solution for the Planar Lifting Line

We saw in the previous section that Glauert's analytical solution for the two dimensional foil could be replicated with high precision by a discrete vortex lattice method. It is therefore reasonable to expect that the same success can be achieved with a vortex lattice lifting line method. In both cases, the motivation is obviously not to solve these particular problems, but to "tune up" the vortex lattice technique so that it can be applied to more complicated problems for which there is no analytical solution.

As illustrated in figure 59, the span of the lifting line is divided into M panels, which may or may not be equally spaced, and which may be inset a given distance from each tip[32]. The continuous distribution of circulation over the span is considered to be replaced by a stepped distribution which is constant within each panel. The value of the circulation in each panel is equal to the value of the continuous distribution at some selected value of the y coordinate within each panel. The induced velocity will be computed at a set of *control points* . Using the notation of the *FORTRAN90* program which contained in appendix, the coordinate of the control point in the n'th panel is $y_c(n)$, and the corresponding circulation is $\Gamma(n)$.

Since the circulation is piecewise constant, the free vortex sheet is replaced by a set of concentrated vortex lines shed from each panel boundary, with strength equal to the difference in bound vortex strength across the boundary. This is equivalent to replacing the continuous vortex distribution with a set of discrete horseshoe vortices, each consisting of a bound vortex segment, and two concentrated tip vortices. The y coordinate of the panel boundaries, which are then the coordinates of the free vortices, will be denoted $y_v(n)$. If there are M panels, there will be $M + 1$ free vortices.

The velocity field of this discrete set of concentrated vortices can be computed very easily at points on the lifting line, since the singular integral encountered in the continuous case is replaced by the summation

$$w^*(y_c(n)) \equiv w_n^* = \sum_{m=1}^{M} \Gamma_m w_{n,m} \qquad (139)$$

---

[32] The optimum tip inset is not at all obvious at this point, but will be addressed later

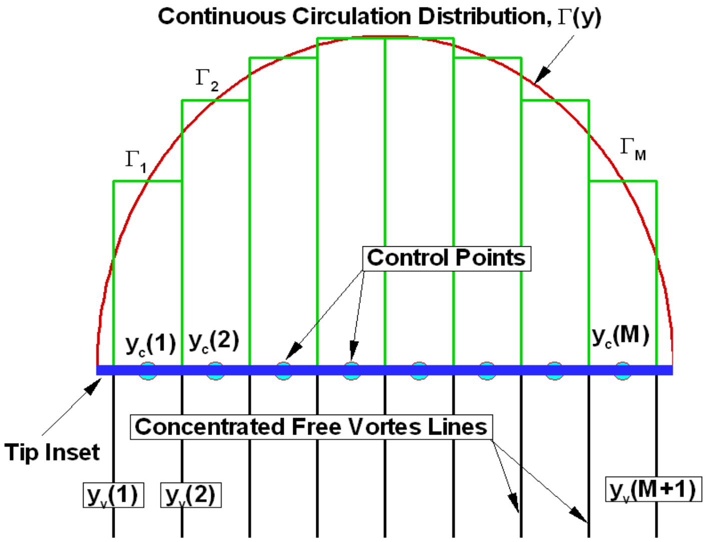

Figure 59: *Notation for a vortex lattice lifting line. In this case, there are 8 uniformly spaced panels, with a* 1/4 *panel inset at each end.*

where $w_{n,m}$ is the velocity induced at the control point $y_c(n)$ by a unit horseshoe vortex surrounding the point $y_c(m)$. Since the bound vortex segment of the horseshoe does not induce any velocity on the lifting line itself, the influence function $w_{n,m}$ consists of the contribution of two semi-infinite trailing vortices of opposite sign,

$$w_{n,m} = \frac{1}{4\pi(y_v(m) - y_c(n))} - \frac{1}{4\pi(y_v(m+1) - y_c(n))} \tag{140}$$

However, it is clear that the resulting velocity will not be accurate for all values of y. In particular, the velocity will become ±∞ as y_c is moved past any of the vortex coordinates y_v. Nevertheless, our intuition says that the result might be accurate at points that are more or less midway between the vortices.

This is illustrated in figure 60. This shows the distribution of induced velocity $w^*(y)$ for an elliptically loaded lifting line using ten equally spaced panels inset one quarter panel from each tip. The velocity has been computed at a large number of points within each panel, and one can clearly see the velocity tending to ±∞ near each of the panel boundaries. The velocity can obviously not be calculated exactly on the panel boundaries, so what is shown in the graph is a sequence of straight lines connecting the closest points computed on each side.

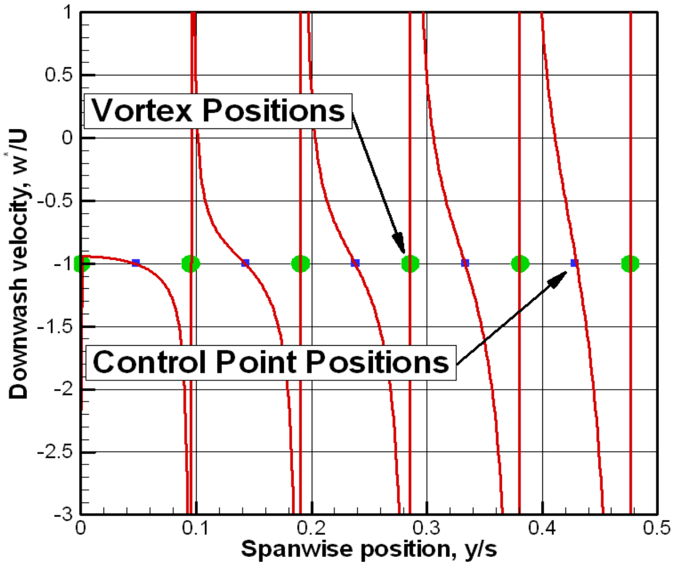

Figure 60: *Spanwise distribution of velocity induced by a vortex lattice. The spacing is uniform, with ten panels and 25% tip inset. Due to symmetry, only half the span is shown.*

Also shown in the figure is the exact solution for the induced velocity, which in this case is simply a constant value $w^*(y)/U = -1$. The numerical solution does not look at all like this, but if you look closely, you can see that the numerical values are correct at the mid points of each of the intervals. We would therefore get the right answer if we chose the midpoints of each interval as the control points.

The lift and induced drag can now be written as sums of the elementary lift and drag forces on each panel,

$$\bar{F}_z = \rho U \sum_{n=1}^{M} \Gamma(n)[y_v(n+1) - y_v(n)] \tag{141}$$

$$\bar{F}_x = -\rho \sum_{n=1}^{M} w^*(n)\Gamma(n)[y_v(n+1) - y_v(n)] \tag{142}$$

Equation 139 can represent the solution to two different types of problems. The first is the *design problem*, where the circulation distribution $\Gamma(y)$, and hence the total lift, is given. We can use equation 139 directly to evaluate w^*, and we can then use equation 142 to obtain the induced drag. We will also see later that the downwash velocity is an important ingredient in establishing the spanwise distribution of angle attack required to achieve the design circulation. The second is the *analysis* problem where we are given the spanwise distribution of downwash, w^*, and we wish to determine the circulation distribution. If we write down equation 139 for M different control points $y_c(1) \ldots y_c(n) \ldots y_c(M)$ we obtain a set of simultaneous equations where $w_{n,m}$ is the coefficient matrix, w^* is the right hand side, and Γ is the unknown. Once Γ is found, we can obtain both the lift and the drag from equations 141 and 142.

The remaining question is how to determine the optimum arrangement of vortex and control points. While much theoretical work in this area has been done, right now we will use a cut and try approach. This is facilitated by a simple *FORTRAN90* program called *HVLL*, which calculates both the exact and the numerical values of the induced velocity, total lift and total induced drag for a circulation distribution defined by any specified number of Glauert coefficients a_j . The *design* problem is first exercised by calculating the numerical approximation to the downwash induced by the specified circulation distribution. The *analysis* option is then exercised by calculating the numerical approximation to the circulation starting from the exact downwash associated with the originally specified circulation distribution. In both cases, the total lift and induced drag can be computed and compared with the exact values. Thus, the accuracy of a given lattice arrangement and the convergence of the method with increasing numbers of panels can be studied.

The simplest arrangement consists of equally spaced panels with no tip inset, and with the control points at the mid point of each panel. This scheme will be demonstrated for the simple case of elliptical loading, where the exact downwash is a constant. The results for $M = 8$ panels is shown in figure 61. Here we see that the predicted circulation distribution has the correct shape, but is uniformly too high. The numerical result for the downwash is quite good in the middle of the span, but gets worse at the tips.

The following table shows the effect of number of panels on the computed forces. For example, if the circulation is specified, the error in predicted lift is 1.3% with 8 panels, and reduces to 0.1% with 64 panels. But, the error in drag is much greater, ranging from 10.1% with 8 panels to 1.3% with 64 panels. On the other hand, if the downwash is specified, the computed lift and drag is in error by about the same amount, ranging from 12.5% with 8 panels to 1.6% with 64 panels.

While this might not seem too bad, it is easy to get much better results without any extra computing effort. The problem with the tip panel is that the strength of the free vortex sheet in the continuous case has a square root singularity at the tips, which is not approximated well in the present arrangement.

Figure 62 shows what happens if the tip panels are inset by one quarter of a panel width. Now the induced velocity in the tip panel is much better (but still not as good as for the rest of the panels), and the error in forces is around one percent for 8 panels, and 0.1 percent or less for 64 panels. One can explore the result of changing the tip inset and find values which will either make the induced velocity at the tip, the total lift, or the induced drag correct. However, no single value will be best for all three. Thus, a tip inset of one quarter panel is considered to be the best. A proof that a quarter panel inset is correct in the analogous situation of the square root singularity at the leading edge of a two dimensional flat plate was published by James[33].

Another possible spacing arrangement is motivated by the change in variables used by Glauert in the solution of the lifting line problem. We saw that this arrangement worked very well for the 2-D problem. In this case the vortices and control points are spaced equally in the angular coordinate $\tilde{y}$. This arrangement is called cosine spacing, and the equations for $y_v(n)$ and $y_c(n)$ can be found in the code. In this case no tip inset is required. Proofs that this arrangement is correct may be found in Lan[34] and Stark[35].

Figure 63 shows what happens when cosine spacing is used with 8 panels, but where the control points are located midway between the vortices, as is the case with constant spacing. Figure 64 is an illustration of how a fast computer can make up for a certain amount of human stupidity. Using 64 panels, the predicted circulation looks quite good—although it is still a little high. The downwash is again accurate over a lot of the mid span, but the results at the tips are a even more of a disaster. Increasing the number of elements localizes the problem, but the computed values at the tip are still way off. In spite of this, the total forces seem to be converging, with an error of around two percent with 64 elements.

Fortunately this is not the *real* cosine spacing, and is included as a cautionary tale for numerical hackers. In *real* cosine spacing, the control points are mapped with the same cosine transformation as the vortices. They are therefore not in the middles of the intervals, but are biased towards the tips. Figure 65 results shows that this arrangement is extremely accurate, even with 8 panels. Note, in particular, that the lift and drag obtained from the circulation found by specifying w^* is exact, and that the ratio of drag to lift squared, F_x/F_z^2 is exact for any number of panels.

All of the examples considered so far are for elliptical loading. The remaining two figures show the results of adding an additional coefficient with a value of $a_3 = -0.2$ to the Glauert series for the circulation. This unloads the tips (which may be desired to delay tip vortex cavitation inception), producing large upward induced velocities in

---

[33] James,R.M.,"On the Remarkable Accuracy of the Vortex Lattice Method",*Comput. Methods Appl. Mech. Eng.* Vol.1,1972

[34] Lan,C.E.,"A Quasi-Vortex Lattice Method in Thin Wing Theory,"*J.Aircraft*,Vol 11, No.9, September,1974

[35] Stark,V.J.E.,"A Generalized Quadrature Formula for Cauchy Integrals,"*AIAA Journal* Vol 9, No. 9,1970

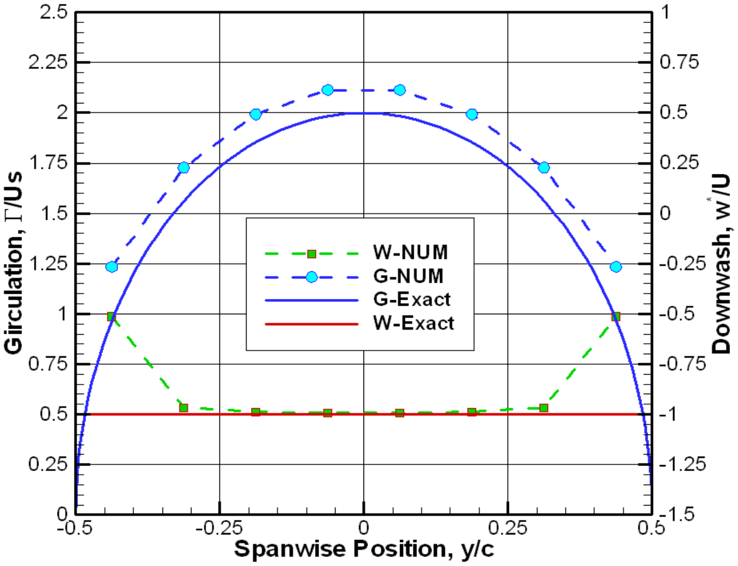

Figure 61: *Comparison of vortex lattice and exact results for an elliptically loaded lifting line with* $a_1 = 1.0$*. The solution was obtained with 8 panels, using uniform spacing with zero tip inset.*

the tip region, and increase the induced drag. Figure 66 shows the results obtained using “good” cosine spacing with 8 panels. The results are extremely close to the exact value, although a small discrepancy is visible in the graph. Figure 67 shows the same case calculated with 32 panels. The results now appear to be right on top of the exact results. In addition, the increased number of panels provides much better resolution of the behavior of the circulation and downwash near the tips.

Constant Spacing - Zero Tip Inset						
Percent Errors in Vortex Lattice Predictions For F_z, F_x and $F_x/(F_z)^2$						
Panels	Given $\Gamma(y)$			Given $w^*(y)$		
8	1.3	-7.6	-10.1	12.5	12.5	-11.1
16	0.5	-4.2	-5.1	6.3	6.3	-5.9
32	0.2	-2.3	-2.6	3.1	3.1	-3.0
64	0.1	-1.2	-1.3	1.6	1.6	-1.5

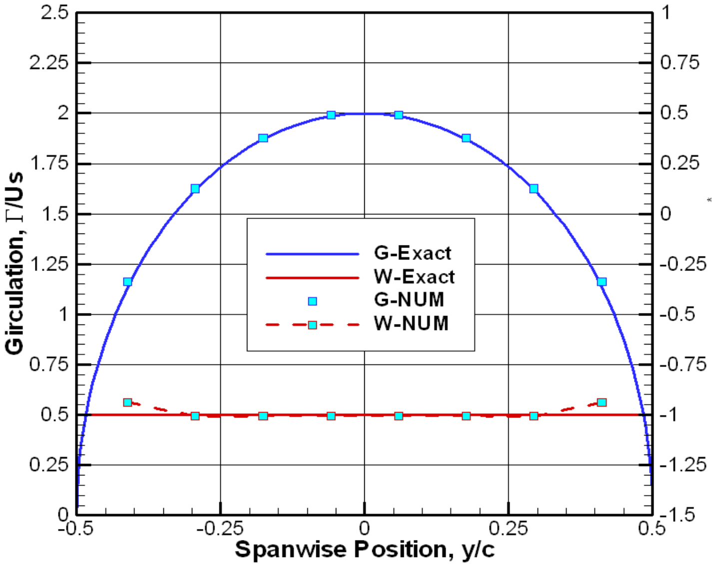

Figure 62: *Comparison of vortex lattice and exact results for an elliptically loaded lifting line with* $a_1 = 1.0$*. The solution was obtained with 8 panels, using uniform spacing with 25 % tip inset.*

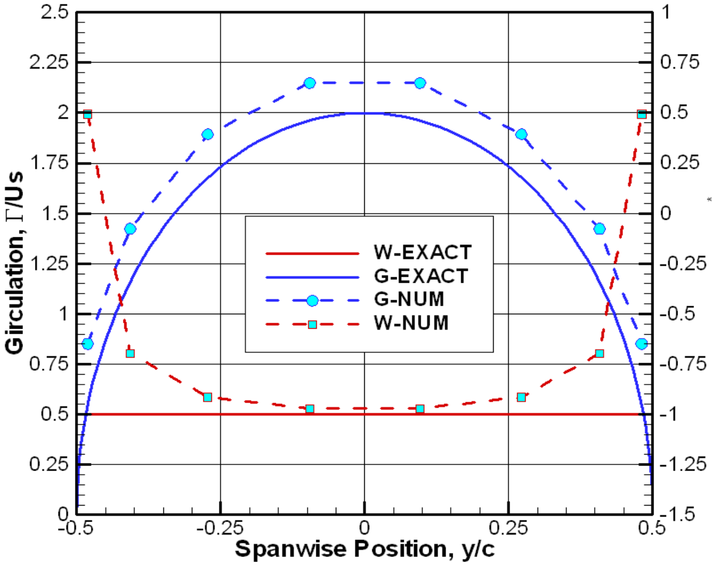

Figure 63: *Comparison of vortex lattice and exact results for an elliptically loaded lifting line with* $a_1 = 1.0$*. The solution was obtained with 8 panels, using cosine spacing with central control points.*

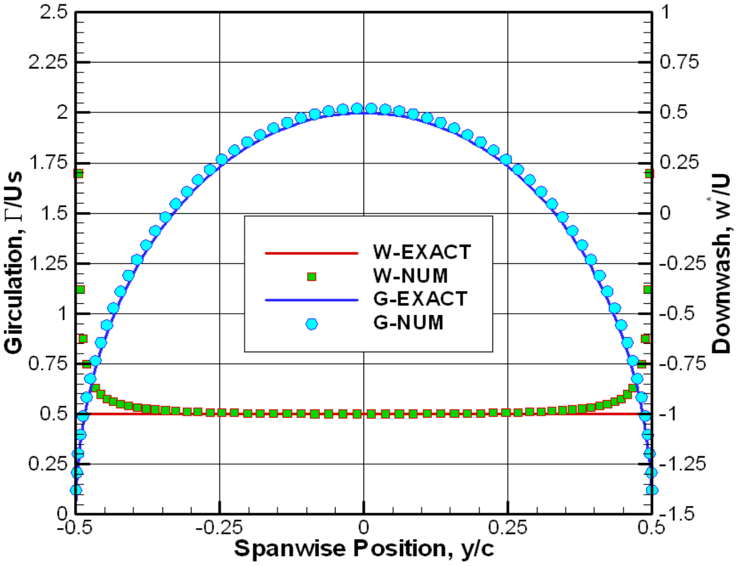

Figure 64: *Comparison of vortex lattice and exact results for an elliptically loaded lifting line with* $a_1 = 1.0$. *The solution was obtained with 64 panels, using cosine spacing with central control points.*

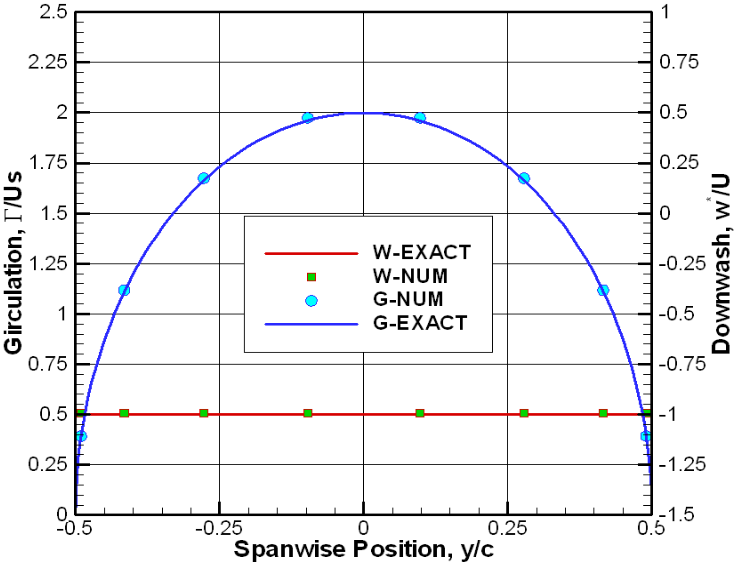

Figure 65: *Comparison of vortex lattice and exact results for an elliptically loaded lifting line with* $a_1 = 1.0$. *The solution was obtained with 8 panels, using cosine spacing with cosine control points.*

Constant Spacing - 25 % Tip Inset						
Percent Errors in Vortex Lattice Predictions For F_z, F_x and $F_x/(F_z)^2$						
Panels	Given $\Gamma(y)$			Given $w^*(y)$		
8	-1.0	-1.6	0.4	-0.3	-0.3	0.3
16	-0.4	-0.6	0.1	-0.1	-0.1	0.1
32	-0.1	-0.2	0.0	0.0	0.0	0.0
64	0.0	-0.1	0.0	0.0	0.0	0.0

Cosine Spacing- Central Control Points						
Percent Errors in Vortex Lattice Predictions For F_z, F_x and $F_x/(F_z)^2$						
Panels	Given $\Gamma(y)$			Given $w^*(y)$		
8	1.1	-12.1	-14.0	15.2	15.2	-13.2
16	0.3	-6.9	-7.4	7.7	7.7	-7.1
32	0.1	-3.6	-3.8	3.9	3.9	-3.7
64	0.0	-1.9	-1.9	1.9	1.9	-1.9

Cosine Spacing - Cosine Control Points						
Percent Errors in Vortex Lattice Predictions For F_z, F_x and $F_x/(F_z)^2$						
Panels	Given $\Gamma(y)$			Given $w^*(y)$		
8	-0.6	-1.3	0.0	0.0	0.0	0.0
16	-0.2	-0.3	0.0	0.0	0.0	0.0
32	0.0	-0.1	0.0	0.0	0.0	0.0
64	0.0	0.0	0.0	0.0	0.0	0.0

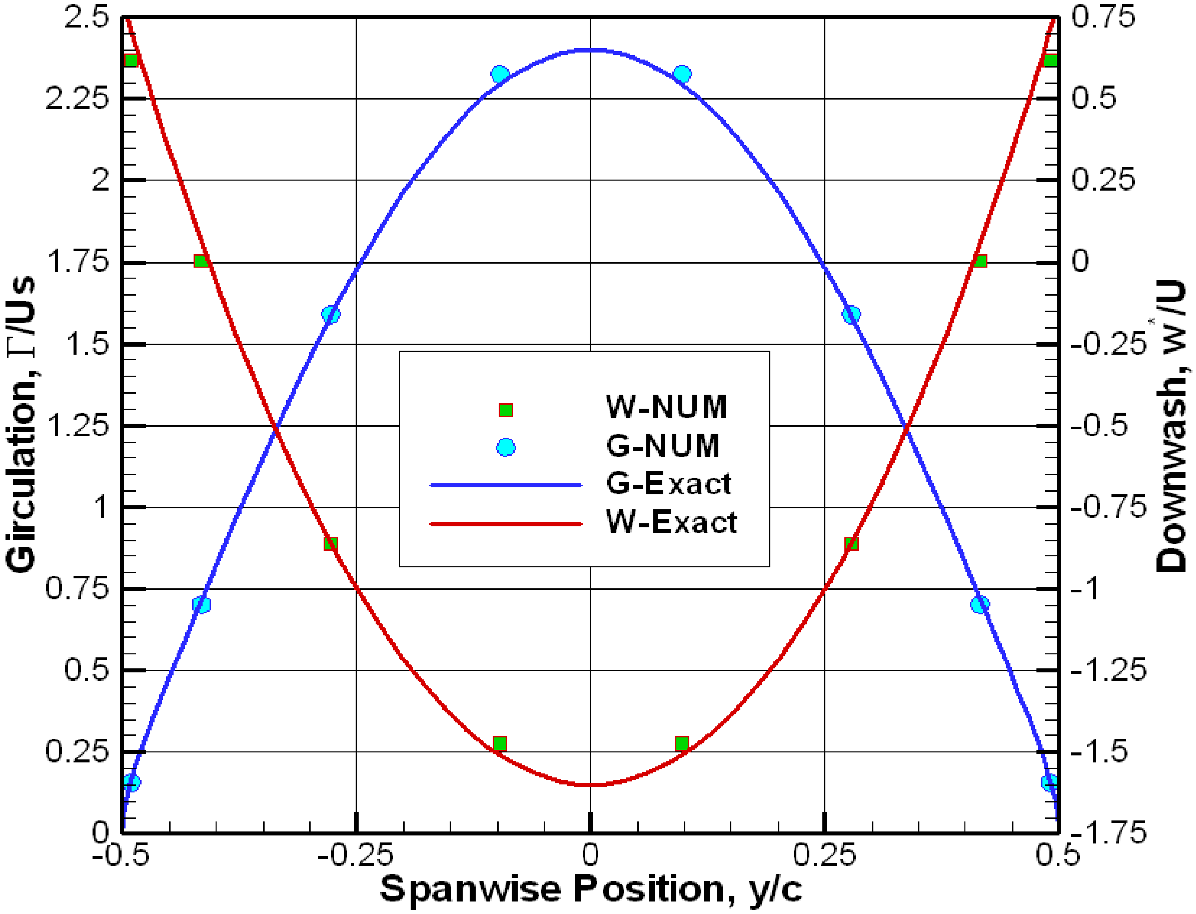

Figure 66: *Comparison of vortex lattice and exact results for a tip-unloaded lifting line with* $a_1 = 1.0$ *and* $a_3 = -0.2$*. The solution was obtained with 8 panels, using cosine spacing with cosine control points.*

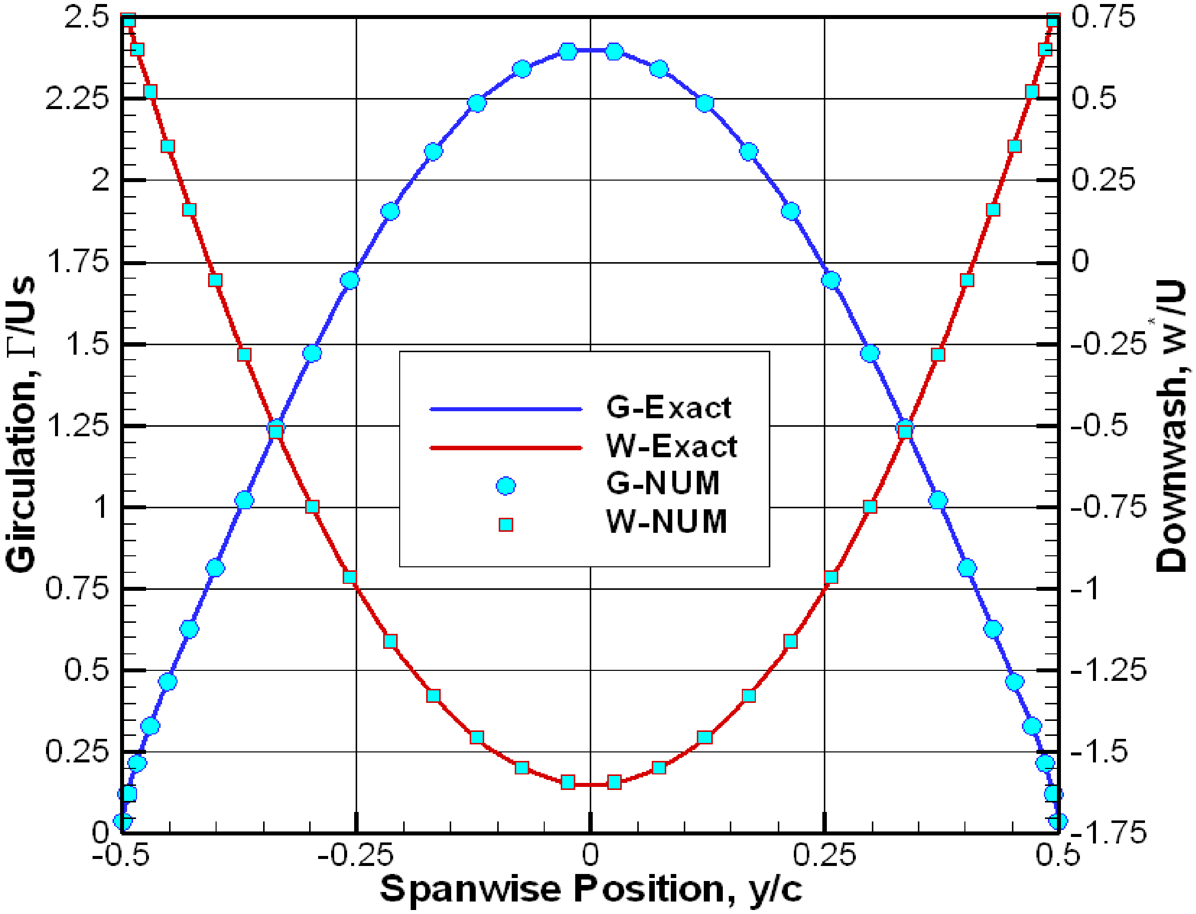

Figure 67: *Comparison of vortex lattice and exact results for a tip-unloaded lifting line with* $a_1 = 1.0$ *and* $a_3 = -0.2$. *The solution was obtained with 32 panels, using cosine spacing with cosine control points.*

2.7.3 The Prandtl Lifting Line Equation

Our discussion of lifting line theory so far has addressed the question of relating the spanwise distribution of circulation to the downwash, lift and induced drag. In addition, we have found the spanwise distribution of circulation which minimizes the induced drag.

Lifting line theory, by itself, does not provide any way of determining the lift generated by a particular foil shape, since the details of the flow over the actual surface are completely lost in the idealization of a lifting line. While the lifting surface equations developed earlier will provide the means to solve this problem, a simpler alternative exists if the aspect ratio of the foil (the ratio of the span to the mean chord) is high.

This idea was originated by Prandtl, who reasoned that if the aspect ratio is sufficiently high, the foil section at a given spanwise position acts as though it were in a two-dimensional flow (remember the near-sighted bug), but with the inflow velocity altered by the downwash velocity obtained from lifting line theory. The solution to the problem of analyzing the flow around a given foil then requires the solution of two coupled problems; a local two-dimensional problem at each spanwise position, and a global three-dimensional lifting line problem. This idea was formalized many years later by the theory of matched asymptotic expansions where the solution to the wing problem could be found in terms of an expansion in inverse powers of the aspect ratio. The matched asymptotic solution may be found in Van Dyke [36], but we will only present Prandtl's original method here.

First recall that the sectional lift coefficient, C_L is,

$$C_L(y) = \frac{F_z(y)}{\frac{1}{2}\rho U^2 c(y)} = \frac{2\Gamma(y)}{Uc(y)} \tag{143}$$

where $c(y)$ is the local chord as illustrated in figure 50. To keep things as simple as possible for the moment, let us assume that the foil sections have no camber. Then if the flow were two-dimensional, the lift coefficient at spanwise position y would be

$$C_L(y) = \frac{2\Gamma(y)}{Uc(y)} = 2\pi\alpha(y) \tag{144}$$

Following Prandtl's theory, equation 144 can be modified to account for three-dimensional effects by reducing the angle of attack by the induced angle,

---

[36] Van Dyke,M.,**Perturbation Methods in Fluid Mechanics**, Parabolic Press,1975

$$C_L(y) = \frac{2\Gamma(y)}{Uc(y)} = 2\pi\left[\alpha(y) - \alpha_i(y)\right] = 2\pi\left[\alpha(y) + w^*(y)/U\right] \tag{145}$$

Both the circulation Γ and the downwash w^* can be expressed in terms of the coefficients in Glauert's expansion, from equations 126 and 130. Equation 145 then becomes

$$C_L(y) = \frac{4s}{c(\tilde{y})}\sum_{n=1}^{\infty} a_n \sin(n\tilde{y}) = 2\pi\left[\alpha(\tilde{y}) - \sum_{n=1}^{\infty}\frac{na_n\sin(n\tilde{y})}{\sin\tilde{y}}\right] \tag{146}$$

Equation 146 must hold for any spanwise position $\tilde{y}$ along the foil. Given a distribution of chord length $c(\tilde{y})$ and angle of attack $\alpha(y)$, we can find the first M coefficients in the Glauert expansion for the circulation by satisfying equation 146 at M spanwise positions. The solution will presumably become more accurate as M is increased.

Another alternative is to go back to equation 145 and use a vortex lattice method to solve for discrete values of the circulation. Since equation 139 gives us the downwash, w^* at the $n'th$ panel as a summation over the M panels, we obtain the following set of simultaneous equations for the M unknown vortex strengths Γ_n,

$$\frac{2\Gamma_n}{Uc_n} = 2\pi\left[\alpha_n + \sum_{m=1}^{M}\Gamma_m w_{n,m}\right] \quad n = 1,\ldots M \tag{147}$$

Both methods work well, but are approximations, since the results depend either on the number of terms retained in the Glauert series, or on the number of panels used in the vortex lattice.

An exact solution to equation 146 can be obtained by inspection in the special case that the chord distribution is elliptical and the angle of attack is constant. If we define c_0 as the chord length at the mid-span, we can write the chord length distribution as

$$c(y) = c_0\sqrt{1 - \left(\frac{2y}{s}\right)^2} \tag{148}$$

which has a projected area $\mathcal{S} = \pi c_0 s/4$ and an aspect ratio $\mathcal{A} = s^2/\mathcal{S} = 4s/(\pi c_0)$. Before introducing this chord length distribution in 146 we must transform it into the $\tilde{y}$ variable using equation 36,

$$c(y) = c_0 \sin\tilde{y} \tag{149}$$

Equation 146 then becomes

$$C_L(y) = \pi \mathcal{A} \sum_{n=1}^{\infty} a_n \frac{\sin(n\tilde{y})}{\sin \tilde{y}} = 2\pi \left[\alpha - \sum_{n=1}^{\infty} \frac{n a_n \sin(n\tilde{y})}{\sin \tilde{y}} \right] \tag{150}$$

but this equality can only hold if the circulation distribution is elliptical, i.e. if $a_n = 0$ for $n > 1$. In this case, the local lift coefficient, $C_L(y)$ and the total lift coefficient $\bar{C}_L = \pi \mathcal{A} a_1$ are equal, and equation 150 reduces to

$$C_L(y) = \bar{C}_L = \frac{2\pi\alpha}{(1 + 2/\mathcal{A})} \tag{151}$$

This remarkably simple formula captures the essential role of aspect ratio controlling the rate of change of lift with angle of attack. As the aspect ratio approaches infinity, the lift slope approaches the two-dimensional value of 2π. As the aspect ratio becomes small, the lift slope approaches zero. This result is plotted in figure 68, together with accurate numerical results obtained from lifting surface theory and with results obtained from the theory of matched asymptotic expansions. This figure comes from Van Dyke, and also appears in chapter 5 of Newman's *Marine Hydrodynamics*.

An amazing attribute of Prandtl's theory as applied to an elliptical wing is how well it works even for low aspect ratios. Of course, if you look closely at the figure, you can see that Prandtl's theory always over-predicts the lift, and that the percent error increases with decreasing aspect ratio. Another important observation is that, even at an aspect ratio of $\mathcal{A} = 8$, the lift slope is substantially below the two-dimensional value of 2π.

The three curves labeled *2nd approx, 3rd approx* and *modified 3rd approx* are a sequence of solutions obtained from the theory of matched asymptotic expansions. The first of these looks almost like Prandtl's result, namely

$$C_L(y) = \bar{C}_L = (2\pi\alpha)(1 - 2/\mathcal{A}) \tag{152}$$

which is a little more accurate for high aspect ratios, but falls apart for low aspect ratios—Note that it predicts that a foil with an aspect ratio of two will have zero lift at all angles of attack!. The higher order matched asymptotic approximations remain accurate for progressively lower values of aspect ratio.

Figure 69 shows the application of Prandtl's equation to determine the effect of planform taper on circulation distribution. As expected, the circulation near the tips decreases

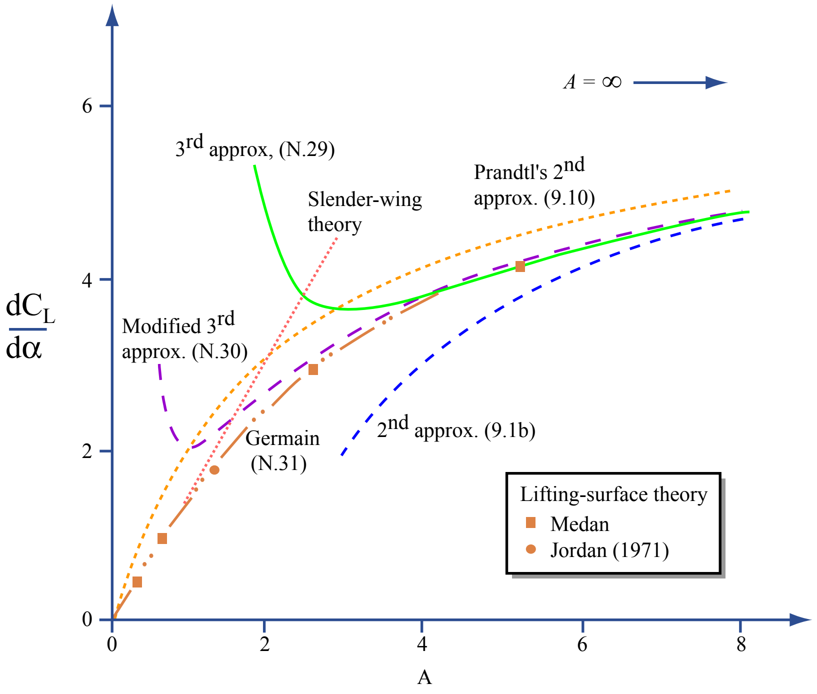

Lift slope, $dC_L/d\alpha$, of an elliptic wing as a function of aspect ratio.

Figure by MIT OCW. Adapted from van Dyke, 1975.

(and the circulation at the root increases) as the ratio of tip chord to root chord, c_t/c_r, is decreased.

Before leaving our discussion of Prandtl's lifting line equation, let us consider what happens if the foil sections have camber. Since the coupling between three-dimensional lifting-line theory and a local two-dimensional flow is based on the total lift at each spanwise section, it doesn't matter whether the lift is generated by angle of attack, camber, or some combination of the two. We can therefore generalize equation 144 by including the two-dimensional angle of zero lift of the local section, $\alpha_{0L}(y)$

$$C_L(y) = \frac{2\Gamma(y)}{Uc(y)} = 2\pi\left[\alpha(y) - \alpha_{0L}(y)\right] \tag{153}$$

For a section with positive camber, the angle of zero lift is generally negative, thus increasing the lift in accordance with 153. All we have to do is replace $\alpha(y)$ with $\alpha(y) - \alpha_{0L}(y)$ in equations 145 and 146 to treat the general case of cambered sections. It is also easy to include real fluid effects, by replacing the two-dimensional lift slope of 2π and the theoretical angle of zero lift with experimentally determined values. In this way, the results of two-dimensional experiments can be applied to three-dimensional flows—

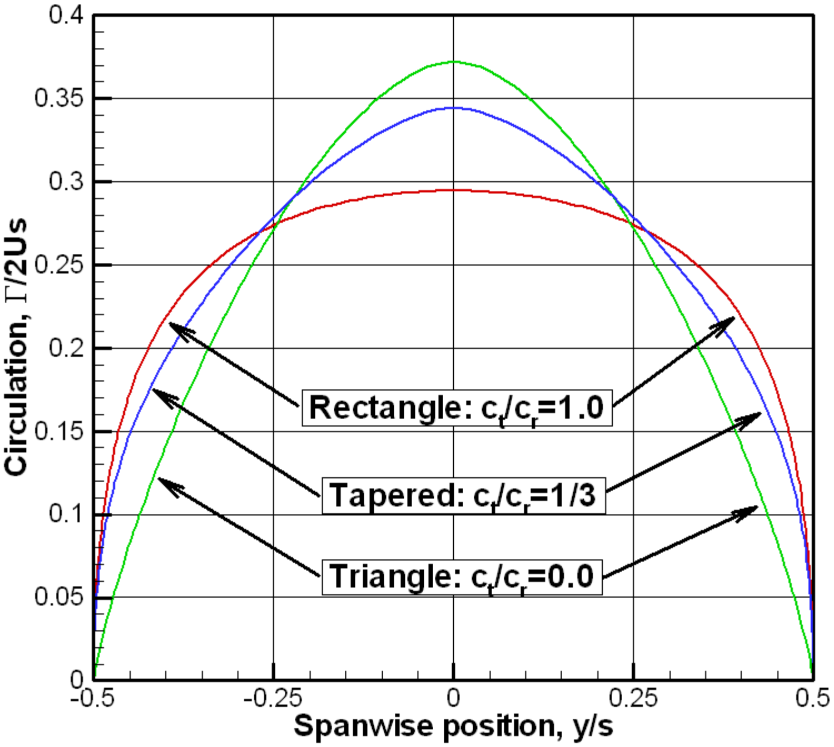

Figure 69: *Effect of planform shape on spanwise distribution of circulation obtained from Prandtl's lifting line equation. The foils all have an aspect ratio of* $= 4$*, and are at unit angle of attack. Equation 146 was used with* $M = 32$*, which is more than enough for a converged solution.*

provided that the aspect ratio is high.

For the special case of an elliptical foil, the spanwise distribution of circulation will be elliptical if $\alpha(y)-\alpha_{0L}(y)$ is constant over the span. This can be achieved, for example, by having both the angle of attack and the zero lift angle constant over the span, or by some combination of the two whose difference is constant. In the former case, the spanwise distribution of lift will remain elliptical if the angle of attack of the entire foil is changed by a constant amount (say due to some different operating condition). However, in the latter case, a constant increment in angle of attack will introduce a spanwise variation in the quantity $\alpha(y) - \alpha_{0L}(y)$. In that case, elliptical loading will only be generated at one particular angle of attack.

2.8 Lifting Surface Results

2.8.1 Exact Results

The solution of the linearized problem of a planar foil involves the solution of a singular integral equation whose main ingredients are given in equations 109,110 and 112. We would expect that an analytical solution could be found in the simple case of a rectangular planform and with zero camber, yet this is unfortunately not the case. E.O Tuck [37] developed highly accurate numerical solutions for this case by a combined analytical/numerical approach which involved an extrapolation of the error obtained by different levels of discretization. In particular, Tuck found that the lift slope of a square (aspect ratio $\mathcal{A} = 1.0$) foil is

$$\frac{C_L}{\alpha} = 1.460227 \tag{154}$$

with a confidence of "about" 7 figures. Obviously this degree of accuracy is of no practical value, but it is important to have exact solutions for specific cases to test the accuracy of numerical methods. For example, if you are examining the convergence of a numerical method as a function of panel density, you might be misled if the "exact" value that you are aiming for is even slightly off.

A large number of investigators have published values for the lift slope of a flat, circular wing (a flying manhole cover) over the time period from around 1938-1974. Their values range from 1.7596 to 1.8144, with several agreeing on a value of 1.790. None of these are closed form analytic solutions, and some of the differences can be attributed to insufficient numbers of terms used in series expansions. But in 1986, Hauptman and Miloh [38] obtained an exact solution based on a series expansion of ellipsoidal harmonics. In particular, they were able to derive the following simple equation for the lift slope of a circular wing,

$$\frac{C_L}{\alpha} = \frac{32}{8 + \pi^2} = 1.790750 \tag{155}$$

and also obtained a somewhat more complicated equation for the lift slope of any elliptical planform.

---

[37] E.O. Tuck," Some Accurate Solutions of the Lifting Surface Integral Equation", J. Australian Mathematical Society (Ser. B), 1991

[38] A. Hauptman and T. Hiloh," On The Exact Solution of the Linearized Lifting Surface Problem of an Elliptic Wing",Journal of Mechanics and Applied Mathematics, Vol. 39, Pt.1, 1996

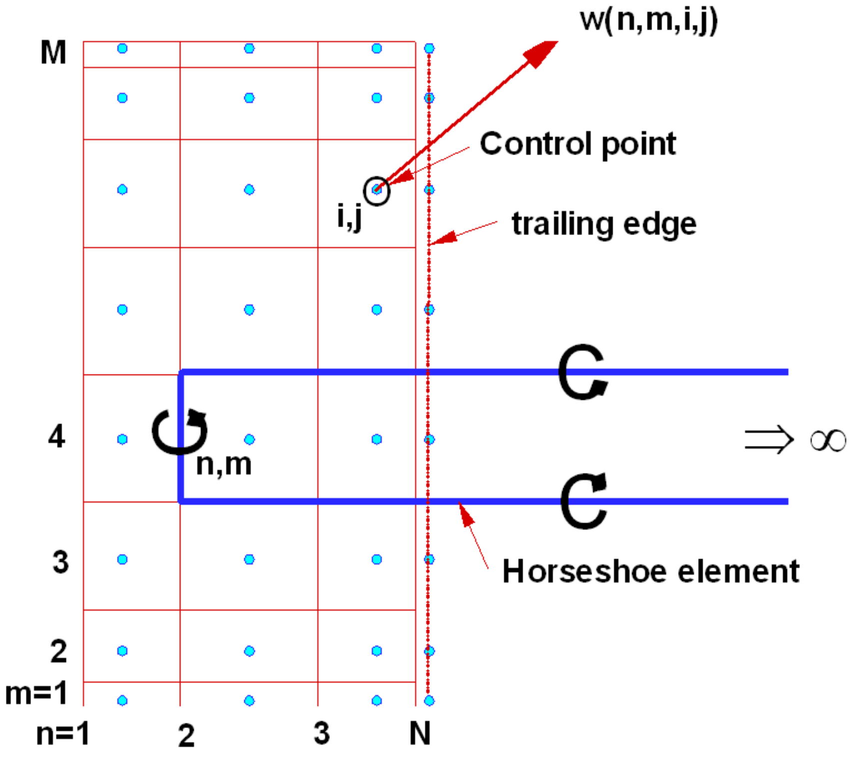

Figure 70: *Notation for a vortex lattice solution for a rectangular foil.*

To my knowledge, no other exact solutions exist. However, these two results are extremely valuable in validating the vortex lattice method, that we will explore in the next section.

2.8.2 Vortex Lattice Solution of the Linearized Planar Foil

We would obviously not have gone to all the trouble of developing the vortex lattice solution for the two-dimensional foil and for the planar lifting line if we hadn't anticipated putting these two together to solve the lifting surface problem. This can be done very simply in the case of a rectangular foil, as shown in figure 70.

As in two-dimensional flow, the chord of the foil is divided into N cosine spaced panels, with concentrated vortex lines and control points spaced in accordance with equation 70. Similarly, the span of the foil is divided into M cosine spaced panels as was done in the development of vortex lattice lifting line theory. Each concentrated bound vortex element of strength Γ_{nm} is combined with a pair of free vortices of strength $\pm\Gamma$ extending downstream to infinity, thus forming a *horseshoe vortex* element. If we let i, j denote the chordwise and spanwise indices of a control point, then the vertical velocity at a particular control point will be,

$$w_{ij} = \sum_{n=1}^{N} \sum_{m=1}^{M} \Gamma_{nm} \bar{w}_{nm,ij} \tag{156}$$

where $\bar{w}_{nm,ij}$ is the *horseshoe influence function*, which is defined as he vertical velocity at the $(i, j)^{th}$ control point induced by a horseshoe vortex element of unit strength centered at the $(n, m)^{th}$ grid point. Each horseshoe consists of three straight vortex segments, whose velocity at any control point position can be obtained from equation 106 developed earlier.

From the linearized boundary condition,

$$\frac{w}{U} = \frac{\partial z_s}{\partial x}$$

we can form a set of $N \times M$ simultaneous equations for the $N \times M$ unknown vortex strengths Γ_{nm}. Once the circulation strengths are known, we can obtain the spanwise distribution and total value of lift using the same equations as in vortex lattice lifting line theory.

Figure 71 shows the vortex lattice arrangement for a foil with aspect ratio $\mathcal{A} = 2.0$ using a relatively fine grid, with 32 spanwise and 16 chordwise panels. Note that the panels near the leading and trailing edges at the tip are extremely small.

The following table shows the computed lift slope for a foil with aspect ratio $\mathcal{A} = 1.0$ using a systematically refined grid ranging from $N = 1, 128$ panels in the chordwise direction and $M = 4, 128$ panels in the spanwise direction. The finest grid in the study required the solution of a set of 8,192 simultaneous equations! [39] Note that this result agrees *to seven significant figures* with Tuck's result. But note also, that a very coarse 4×8 grid produces a result which is in error by only 0.07 percent.

---

[39] Advantage was taken of port-starboard symmetry. Otherwise there would have been 16,384 equations.

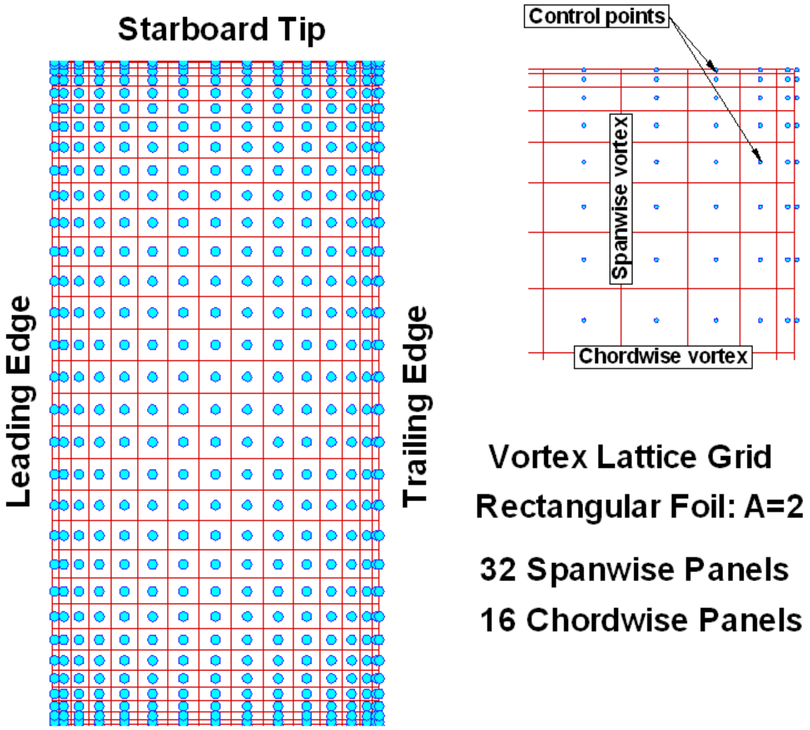

Figure 71: *Vortex lattice grid for a rectangular foil with aspect ratio* $\mathcal{A} = 2$. *In this example, there are 32 spanwise and 16 chordwise panels. The plot on the upper right is an enlargement of the starboard tip near the trailing edge.*

M/N	1	4	8	16	32	64	128
4	1.428988	1.458702	1.459285	1.459351	1.459357	1.459357	1.459357
8	1.428994	1.459262	1.460010	1.460097	1.460105	1.460106	1.460106
16	1.428994	1.459306	1.460085	1.460196	1.460209	1.460210	1.460210
32	1.428994	1.459309	1.460091	1.460206	1.460222	1.460224	1.460224
64	1.428994	1.459309	1.460091	1.460207	1.460224	1.460226	1.460226
128	1.428994	1.459309	1.460091	1.460207	1.460224	1.460226	1.460227

Figure 72: *Convergence of vortex lattice calculation for rectangular foil with aspect ratio 1.0. Tabulated values of* $dC_L/d\alpha$. *Each row shows convergence with number of chordwise vortices. Each column shows convergence with number of spanwise panels.*

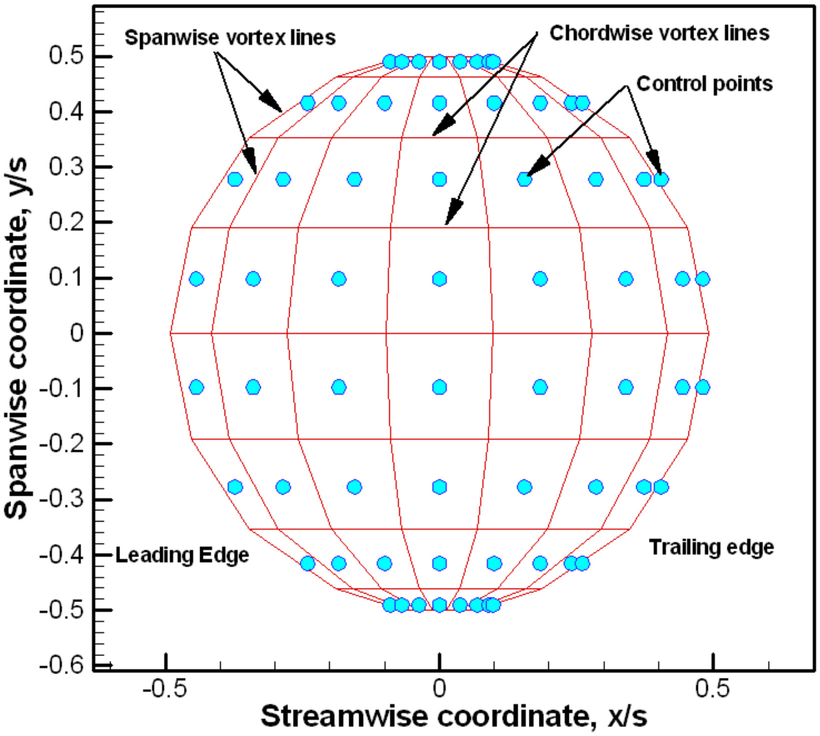

Figure 73: *Vortex lattice grid for a circular foil with an* 8×8 *grid.*

The next step in complexity is to develop a vortex lattice scheme for foils with arbitrary planform, including ones with curved leading and trailing edges. The natural model problem for this case is the circular foil, since we know the exact solution.

Early vortex lattice schemes maintained a Cartesian grid, with bound vortex elements oriented in the y direction, and trailing vortex elements oriented in the x direction. This meant that as the chord length changed with spanwise position, the vortex lattice grid had to have abrupt steps between each chordwise panel. A better arrangement is to adapt the grid to the planform, as shown in figure 73. The vortex lines that follow the general shape of the leading and trailing edges are no longer necessarily in the y direction, and are therefore not necessarily *bound vortices*.

We will therefore call them *spanwise vortex lines*, and will have to be careful when computing forces. From Stokes theorem, the total circulation around the foil at a particular spanwise location y_c is the sum of the circulations of the spanwise elements, no matter how they are inclined. Suppose we let δ be the inclination of a particular spanwise vortex with respect to the y direction, the force per unit length on the vortex is

$\rho U \Gamma \cos(\delta)$. But, the length of the spanwise vortex is $\delta y / cos(\delta)$, where δy is the width of the panel in the spanwise direction. So, the force per unit span is still equal to $\rho U \Gamma$, *regardless of the inclination of the vortex*, δ. In addition, Kelvin's theorem is satisfied if the vortex system is built from horseshoe elements, originating from a spanwise vortex element.

The only trick in dealing with a circular planform is to provide for a finite chord at the tip in order to prevent having all the spanwise vortices coming together at a single point. This can be done rationally by solving for the tip chord such that the area of the approximate quadrilateral tip panel is equal to the area of the actual circular arc segment. This is shown in figure 73. Figure 74 shows a much finer grid, with 64 panels over the span and 32 panels over the chord. Figure 75 shows an enlargement of the tip region, where the finite, equal area tip chord is barely visible.

The computed lift coefficients for these two cases are $C_L = 1.782$ for the 8×8 grid and $C_L = 1.790$ for the 64×32 grid. Recall that the exact solution for a flat circular foil is $C_L = 1.791$, so it is clear that the vortex lattice method works well for non-rectangular planforms.

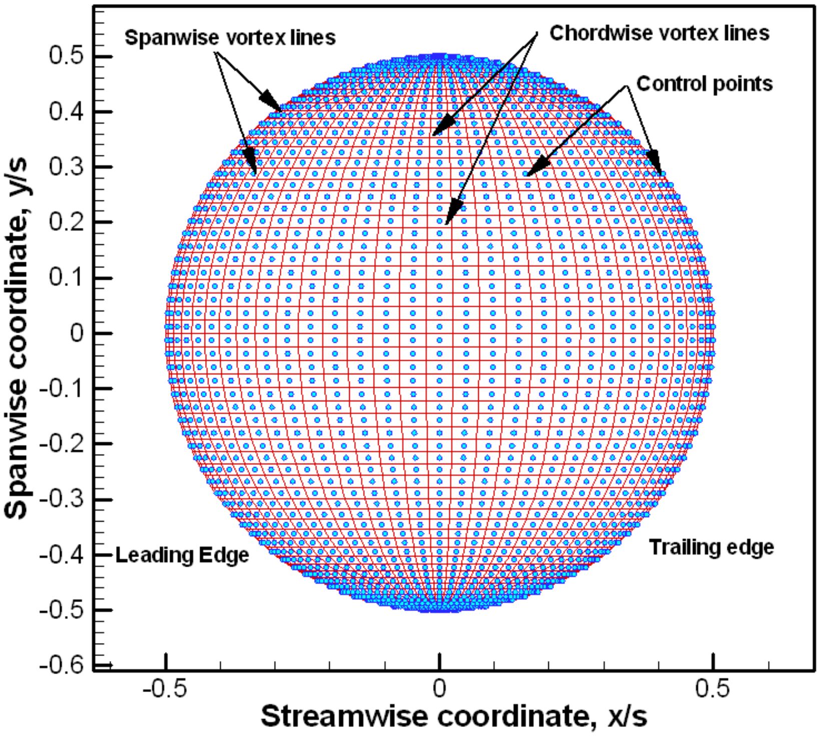

Figure 74: *Vortex lattice grid for a circular foil with 64 spanwise and 32 chordwise panels.*

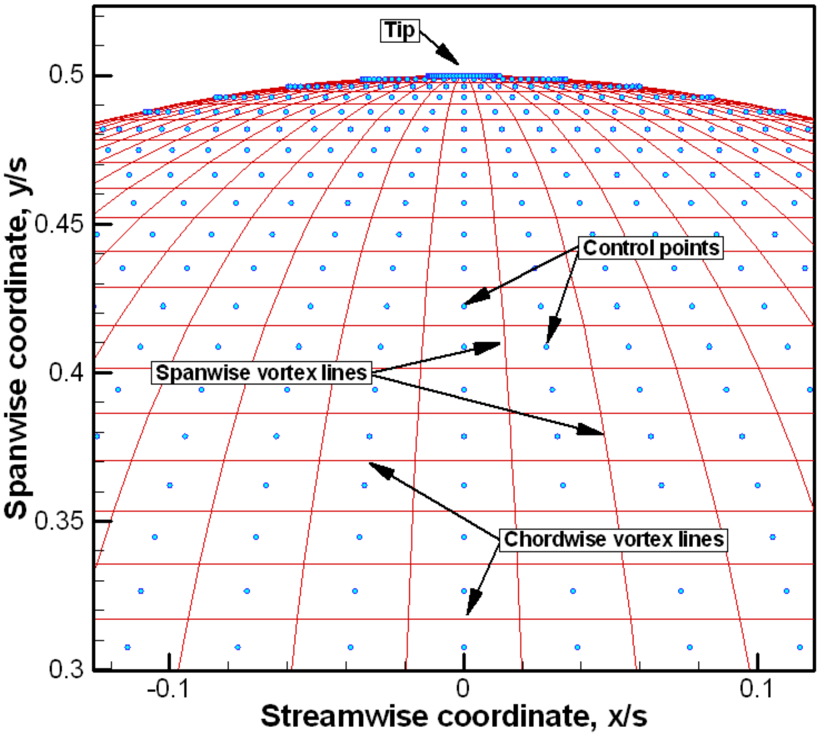

Figure 75: *Enlargement of the tip region of the vortex lattice grid for a circular foil with 64 spanwise and 32 chordwise panels.*

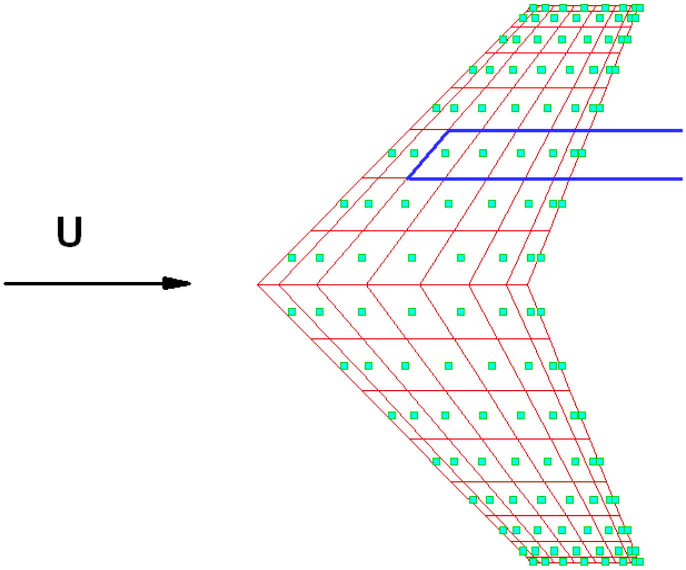

Figure 76: *Vortex lattice grid for a swept, tapered foil. The root chord is* $c_r/s = 0.5$ *and the tip chord is* $c_t = 0.2$*. The leading edge is swept back* 45 *degrees. The grid consists of* 16 *spanwise and* 8 *chordwise panels. One particular horseshoe element is highlighted.*

Estension of the vortex lattice method to swept and tapered planforms is relatively simple. Figure 76 shows the vortex lattice grid for a tapered foil whose leading edge is swept back 45 degrees. One particular horseshoe vortex element is highlighted in the figure. The influence function for this element again consists of the contribution of three straight vortex segments.

Figure 79 shows the effect of sweep on the spanwise distribution of circulation, $\Gamma(y)$ for a series of three foils with zero camber and constant angle of attack. The foils have a constant chord length of $c = 0.2s$, and therefore have an aspect ratio of $\mathcal{A} = 5.0$. The foil with zero sweep has an (almost) elliptical circulation distribution. The swept back foil, as shown in figure 77, has substantially increased circulation at the tip, and decreased circulation at the root. On the other hand, the foil with forward sweep, as shown in figure 78, has reduced circulation at the tips and increased circulation at the root. This means that if one wanted to have a swept back foil with an ellitical distribution of circulation over the span, the angle of attack of the tip sections would have to be

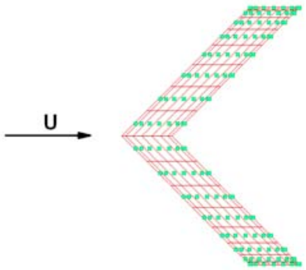

Figure 77: *Vortex lattice grid for a swept, un-tapered foil. The root chord is* $c_r/s = 0.2$ *and the tip chord is* $c_t = 0.2$*. The leading edge is swept back* 45 *degrees. The grid consists of* 16 *spanwise and* 8 *chordwisae panels.*

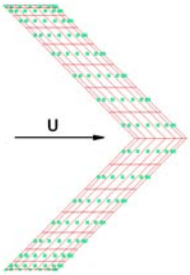

Figure 78: *Vortex lattice grid for a swept, un-tapered foil. The root chord is* $c_r/s = 0.2$ *and the tip chord is* $c_t = 0.2$*. The leading edge is swept forward* 45 *degrees. The grid consists of* 16 *spanwise and* 8 *chordwisae panels.*

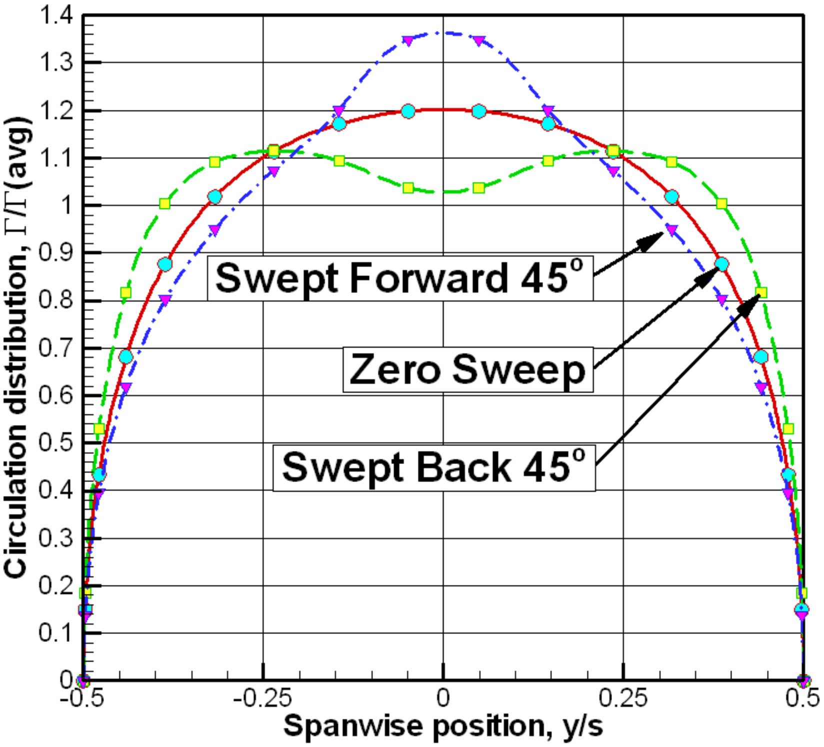

Figure 79: *The effect of sweep on the spanwise circulation distribution.*

reduced, compared with those at the root. The converse would be true for a foil with forward sweep.

3 PROPELLERS

3.1 Inflow

Propellers generally operate in the very complex flow field that exists at the stern of a ship. This flow may be highly turbulent and spatially non-uniform. To add to the difficulty, this flow may be altered significantly by the presence of the propeller. While the velocity distribution in the plane of the propeller is partially due to the potential flow around the ship, its origin is largely viscous. Unlike a purely potential flow, the vorticity in this flow field interacts with itself as it is accelerated by the action of the propeller. This means that the total velocity at a point near the propeller is not simply the linear superposition of the inflow (in the absence of the propeller) and the velocity induced by the propeller, but includes an additional interactive component. A full numerical simulation of the combined flow problem requires massive computational resources, and the validity of the outcome is limited by present empirical modeling of turbulence. It is therefore a practical necessity to employ a simpler flow model for most propeller design and analysis applications.

Rather than including this complex interaction in the solution of the propeller flow problem, it is traditionally assumed that the specified inflow is an *effective inflow* which is defined in a coordinate system fixed on the ship as *the total time-averaged velocity in the presence of the propeller minus the time-average potential flow velocity field induced by the propeller itself* . The *nominal inflow* is defined as the flow that would be presence in the absence of the propeller. If there is no vorticity in the inflow field, this definition reduces to the usual result that the total velocity is the linear superposition of the inflow in the absence of the propeller, and the velocity induced by the propeller. Thus, in this case, the nominal and effective inflows are the same. We will come back later to the question of how one actually determines this elusive *effective inflow.* For now, we will focus on the propeller itself, and assume that the inflow is given.

In order to represent a given inflow field, we first define a ship-fixed cylindrical coordinate system, with the x axis coincident with the axis of rotation of the propeller. The origin of the coordinate is in the *plane of the propeller*, which serves as the reference point for all axial dimensions of the propeller blade surfaces. The radial coordinate is denoted by r, and the angular coordinate by θ_o, which is measured in a clockwise (right-handed) sense when looking downstream with $\theta_o = 0$ being at 12 o'clock. Since the inflow is periodic in θ_o, the three components of the time-averaged velocity in the ship-fixed cylindrical coordinate system , V_a, V_r, V_t can be expressed as a Fourier series. The harmonic coefficients for each component, A_n, B_n are functions of position in the meridional plane, (x, r),

$$V_a(x,r,\theta_o) \quad = \quad A_0^a(x,r) + \sum_{n=1}^{\infty} A_n^a(x,r)\cos(n\theta_o) + \sum_{n=1}^{\infty} B_n^a(x,r)\sin(n\theta_o)$$

$$
\begin{aligned}
V_r(x,r,\theta_o) &= A_0^r(x,r) + \sum_{n=1}^{\infty} A_n^r(x,r)\cos(n\theta_o) + \sum_{n=1}^{\infty} B_n^r(x,r)\sin(n\theta_o) \\
V_t(x,r,\theta_o) &= A_0^t(x,r) + \sum_{n=1}^{\infty} A_n^a(x,r)\cos(n\theta_o) + \sum_{n=1}^{\infty} B_n^t(x,r)\sin(n\theta_o) \qquad (157)
\end{aligned}
$$

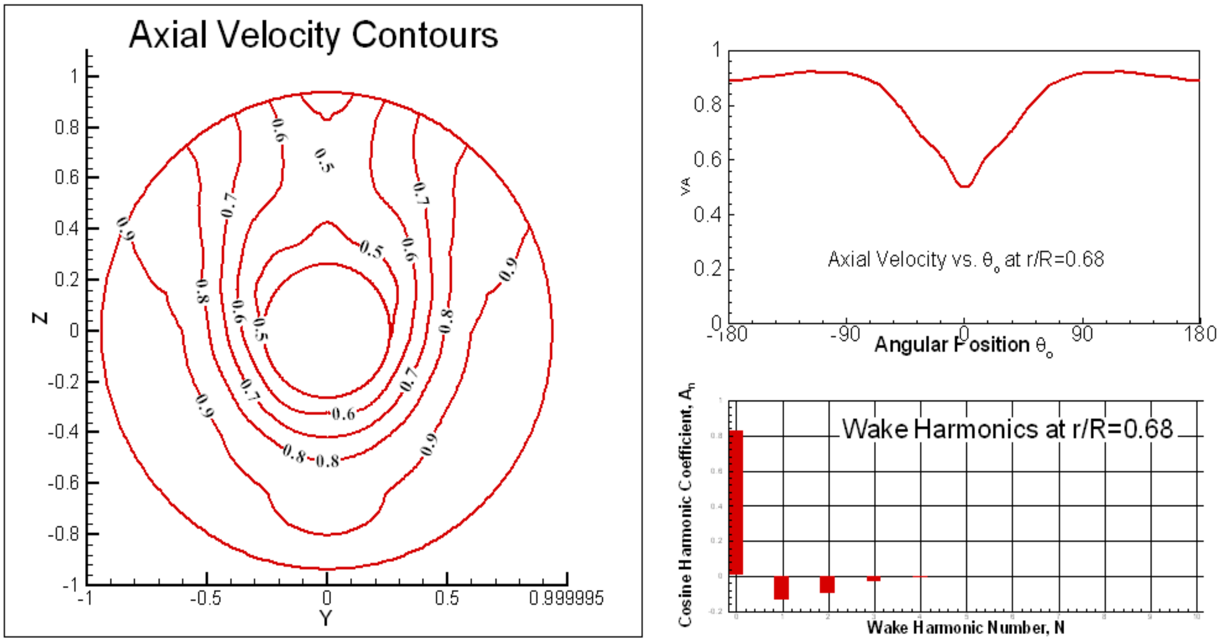

Figure 80: *Typical nominal axial wake field for a single-screw container ship*

Figure 80 shows a typical nominal inflow field as measured in a towing tank. Iso-velocity contours are shown on the left, while a circumferential cut through the flow field at one radius is shown on the right, together with a bar graph showing the A_n^a coefficients. Since the flow field is symmetrical about the ship's center plane in this case, the B_n coefficients are zero. Note that the inflow harmonic coefficients decrease rapidly with increasing harmonic number. While it would seem from figure 80 that only the first few harmonics are of importance, we will see later that the apparently invisible higher harmonics are actually responsible for producing unsteady propeller shaft and bearing forces.

A similar diagram could be made for a series of axial positions over the extent of the propeller. However, in most cases we would find that the variation in inflow velocity would be slight. It is therefore customary to assume that the inflow field is independent of x, and that the inflow stream tubes are therefore cylindrical. To be consistent with this assumption, conservation of mass then requires that the circumferential mean radial inflow velocity be considered to be zero. However, tangential inflow velocities may be present.

We next introduce another cylindrical coordinate system which rotates with the propeller. The x and r coordinates are the same as before, but, θ represents the angular coordinate of an arbitrary point relative to the angular coordinate of a reference point on the *key blade* of the rotating propeller. If a propeller is rotating with angular velocity ω in a counter-clockwise direction when looking downstream [40], the relationship between the fixed and rotating coordinate system is,

$$\theta_o = \theta - \omega t \tag{158}$$

If the inflow is non-uniform with respect to θ_o in the ship-fixed coordinate system, an observer rotating with the propeller will see a time-varying velocity. Under normal operating conditions, the response of a propeller blade to each harmonic of the inflow is essentially linear. Thus, each inflow harmonic gives rise to an unsteady blade force at a frequency related to its harmonic number. The steady, or time-average force, is therefore determined almost entirely by the zero'th harmonic. One should be cautioned that this assumption may not be valid if massive amounts of blade flow separation or cavitation is present.

To determine steady propeller forces, we have therefore simplified the problem considerably. We now simply have a given radial distribution of axial and tangential effective inflow velocity,

$$V_A(r) = A_0^a(0,r) \qquad V_T(r) = A_0^t(0,r) \tag{159}$$

These velocities are generally non-dimensionalized with respect to the ship speed, V_S.

3.2 Notation

Figure 81 shows a right-handed propeller placed in the rotating coordinate system described in the preceding section, together with the inflow $V_A(r), V_T(r)$.

The propeller has a maximum radius R (or diameter D) and is located in the vicinity of the origin of the coordinate system[41].

---

[40] This is commonly referred to as a right-handed propeller, which rotates clockwise when looking upstream. This is generally the assumed direction of rotation when developing equations for propeller flow.

[41] Variations in placement of the propeller in the x direction will simply add a constant to the rake, while variations in the angular placement of the y axis will add a constant to the skew, as shown in Section ?.

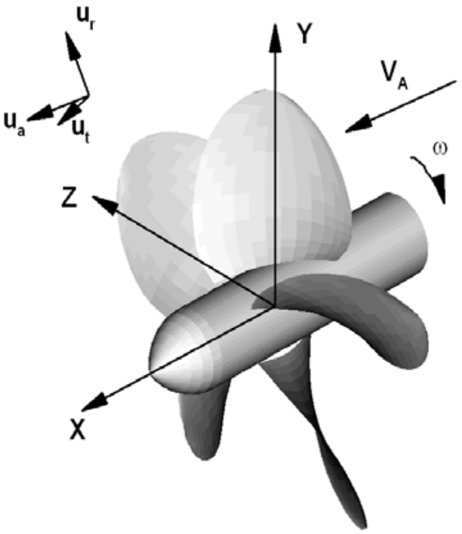

Figure 81: *Propeller coordinate system and velocity notation.*

The propeller has $\mathcal{Z}$ identical blades which are symmetrically placed on a hub, which in turn, is attached to a shaft. The hub and shaft can be thought of as an arbitrary axisymmetric body aligned with the x axis, but it is frequently idealized as a cylinder of radius r_H, as shown in figure 81 or ignored entirely in preliminary hydrodynamic analyzes.

The propeller induces a velocity field with Cartesian components (u, v, w) or cylindrical components (u_a, u_r, u_t) in the axial, radial and circumferential directions, respectively. The total velocity field is then the superposition of the propeller advance speed, rotational speed and induced velocity field and has components

$$V_A(r) + u_a, \quad u_r, \quad \omega r + V_T(r) + u_t \tag{160}$$

in the axial, radial and circumferential directions.

The propeller produces a thrust force T in the negative x direction, and absorbs a torque Q about the x axis, with a positive value following a right-handed convention. These can be non-dimensionalized either on the basis of ship speed, V_S,

$$C_{Ts} = \frac{T}{\frac{1}{2}\rho V_S^2(\pi R^2)}$$

$$C_{Qs} \quad = \quad \frac{Q}{\frac{1}{2}\rho V_S^2(\pi R^3)} \tag{161}$$

or on a volumetric mean inflow,

$$\begin{aligned} C_{Ta} &= \frac{T}{\frac{1}{2}\rho \bar{V}_A^2(\pi R^2)} \\ C_{Qa} &= \frac{Q}{\frac{1}{2}\rho \bar{V}_A^2(\pi R^3)} \end{aligned} \tag{162}$$

where the volumetric mean inflow is,

$$\bar{V}_A = \frac{2}{(R^2 - r_h^2)} \int_{r_h}^{R} r V_A(r) dr \tag{163}$$

Alternatively, the forces may be non-dimensionalized with respect to a nominal rotational velocity, $\mathbf{n}D$, where $\mathbf{n} = \frac{\omega}{\mathbf{2}\pi}$ is the number of propeller revolutions per second,

$$\begin{aligned} K_T &= \frac{T}{\rho \mathbf{n^2} D^4} \\ K_Q &= \frac{Q}{\rho \mathbf{n^2} D^5} \end{aligned} \tag{164}$$

The kinematics of the flow depends only on the ratio of the inflow and rotational velocities, and this is customarily expressed as an *Advance Coefficient* J_S,

$$J_S = \frac{V_S}{\mathbf{n}D} \tag{165}$$

or

$$J_A = \frac{\bar{V}_A}{\mathbf{n}D} \tag{166}$$

By introducing Eq. 165 into Eq. 161, we see that the two systems of force coefficients are related as follows;

$$\begin{aligned} C_{Ts} &= \frac{8}{\pi}\frac{K_T}{J_S^2} \\ C_{Qs} &= \frac{16}{\pi}\frac{K_Q}{J_S^2} \end{aligned} \tag{167}$$

with a similar relationship for C_{Ta} and C_{Qa}.

In most cases, the K_T, K_Q system is preferred, since the propeller rotational speed, $\mathbf{n}$, can be precisely measured both in the laboratory and on shipboard, and the coefficients remain finite in the case of static thrust, when $V_A = 0$. However, as we will see from the next section, the C_T, C_Q system has a more direct relationship to propeller efficiency. Thus, both systems are useful and have therefore been retained over the years.

3.3 Actuator Disk

We will first consider the simplest possible idealization of a propeller— the so-called *Actuator Disk*, which was first introduced by Rankine and Froude. The physical propeller is replaced by a permeable disk of radius R, with vanishing thickness in the x direction. The disk introduces a uniform jump in total pressure,Δp_t, to the fluid passing through the disk, which tends to accelerate the fluid in the positive axial direction and thus results in a thrust force in the negative x direction. No tangential velocities, or *swirl*, are introduced by the disk, and as a consequence of the principle of conservation of angular momentum, there is no torque supplied.

It is difficult, at this point, to relate this amazing device to a real propeller. however, we will ultimately see that the actuator disk is really the limit, in an ideal fluid, of a propeller with an infinite number of blades, zero chord length, and infinite rotational speed. But right now, we will develop expressions for the thrust and efficiency of an actuator disk based on conservation of momentum and energy.

The device is assumed to be operating in an unbounded, inviscid fluid, with a uniform inflow velocity, V_A and uniform static pressure, p_0 far upstream. Since the flow is axisymmetric and without swirl, we are left with axial and radial velocities, $u_a(x,r)$, $u_r(x,r)$ as a function of x and r only.

Since the flow is inviscid, the total pressure in accordance with Bernoulli's equation is constant along any streamline, except for those that pass through the disk, where a total pressure rise of Δp_t occurs. Far downstream of the disk, we can expect that flow quantities will be independent of x, with the tip streamline achieving some limiting radius R_w. The axial perturbation velocity will be $u_w(r)$ for $r < R_w$, and will be zero for $r > R_w$. The radial velocity will be zero for all radii, and the static pressure will be independent of radius, with a value equaling the upstream value of p_0. [42]

Since no fluid is created within the disk, axial and radial velocities are continuous. The increase in total pressure Δp_t is therefore felt entirely as an increase in static pressure, Δp. Writing Bernoulli's equation between a point far upstream and a point far downstream along any stream tube which passes through the disk,

$$\begin{aligned} p_0 + \frac{1}{2}\rho V_A^2 + \Delta p &= p_0 + \frac{1}{2}\rho \left(V_A + u_w(r)\right)^2 \\ \Delta p &= \rho u_w(r)\left(V_A + \frac{u_w(r)}{2}\right) \end{aligned} \tag{168}$$

---

[42] In the absence of tangential velocities, a radial pressure gradient would imply a curvature to the streamlines. But, far downstream the streamline curvature must be zero since $\frac{\partial u_a}{\partial x} = 0$ and $u_r = \frac{\partial u_r}{\partial x} = 0$.

Since Δp is independent of radius, Eq. 168 yields the important result that the perturbation velocity in the slipstream far downstream is independent of radius,

$$u_w(r) = u_w = const \tag{169}$$

The total thrust, T, on the actuator disk can be written down immediately as

$$T = \pi R^2 \Delta p = \pi R^2 \rho u_w \left(V_A + \frac{u_w}{2} \right) \tag{170}$$

Introducing the definition of thrust coefficient from Eq. 161, we obtain a compact non-dimensional form of Eq. 170 which only involves the ratio of the slipstream velocity to the advance speed,

$$C_T \equiv \frac{T}{\frac{1}{2}\rho \pi R^2 V_A^2} = 2\frac{u_w}{V_A}\left(1 + \frac{1}{2}\frac{u_w}{V_A}\right) \tag{171}$$

We can also obtain an independent expression for the thrust based on conservation of momentum, and this will enable us to obtain information about the velocity field at the disk. The general vector form of the momentum equation is,

$$\vec{F} + \int\int_S p\vec{n} dS = \rho \int\int_S \vec{V}(\vec{V} \cdot \vec{n}) dS \tag{172}$$

which states that the flux in momentum of the fluid passing through an arbitrary control volume is equal to the sum of the pressure forces acting on the boundary of the volume and the total body force, $\vec{F}$, acting within the volume. In this case, the resultant body force is the total thrust, T, which acts in the negative x direction. Thus, the x component of the momentum equation can be written as,

$$T = -\int\int_S p n_x dS + \rho \int\int_S (V_A + u_a) n_x dS \tag{173}$$

We will dispose of the pressure integral first, since it fortunately will turn out to be zero! Referring to figure 82, we choose a control volume whose outer surface corresponds to the stream surface which passes through the tip of the disk, and whose upstream and downstream boundaries are sufficiently far from the disk for the velocity and pressure to have reached their limiting values. Thus, at the upstream boundary, the control volume radius is R_u, the pressure is p_o, and the velocity is V_A. At the downstream boundary, the radius is R_w, the pressure is again p_o and the velocity is $V_A + u_w$. Conservation of mass requires that

$$R_u^2 V_A = R_w^2 (V_A + u_w) \tag{174}$$

The net pressure force acting on the two ends is therefore $\pi p_o(R_u^2 - R_w^2)$ in the positive x direction. Determining the x component of the pressure force acting on the outer surface presents a problem since we do not know the details of its shape or pressure distribution. To overcome this problem, we will examine another control volume whose inner boundary matches the outer boundary of the present control volume. The outer boundary will be a stream surface whose upstream and downstream radii, R_u^∞, R_d^∞ are large enough for the velocity to have returned to the free stream value V_A. Since the new control volume lies outside the propeller slipstream, the velocity at both the upstream and downstream faces are V_A. Conservation of mass requires that the two faces have equal area, and since the pressures are equal there is no net pressure force. Again, conservation of mass requires that

$$(R_u^\infty)^2 - (R_d^\infty)^2 = R_u^2 - R_d^2 \tag{175}$$

so that the x component of the pressure force acting on the outer boundary is $\pi p_o(R_u^2 - R_w^2)$ in the negative x direction. Since there is no momentum flux out of, and no body force within the outer control volume, the net integral of pressure must be zero. Hence the pressure force on the inner boundary of the outer control volume is $\pi p_o(R_u^2 - R_w^2)$ in the positive x direction, which must be equal and opposite to the force on the outer surface of the inner control volume. Now we see that this force just balances the difference in pressure force on the ends of the control volume, thus proving the assertion that the net pressure force is zero.

We need to be a little careful in developing the expression for the momentum flux, since the velocities in the plane of the disk cannot be assumed to be independent of radius. We first introduce the following notation for the perturbation velocity at the disk

$$\begin{aligned} u_a^*(r) &\equiv u_a(0,r) \\ u_r^*(r) &\equiv u_r(0,r) \end{aligned} \tag{176}$$

which will also be used later in developing propeller lifting-line theory. Now consider a differential stream tube of radius dr at the disk. The mass flow through the stream tube is

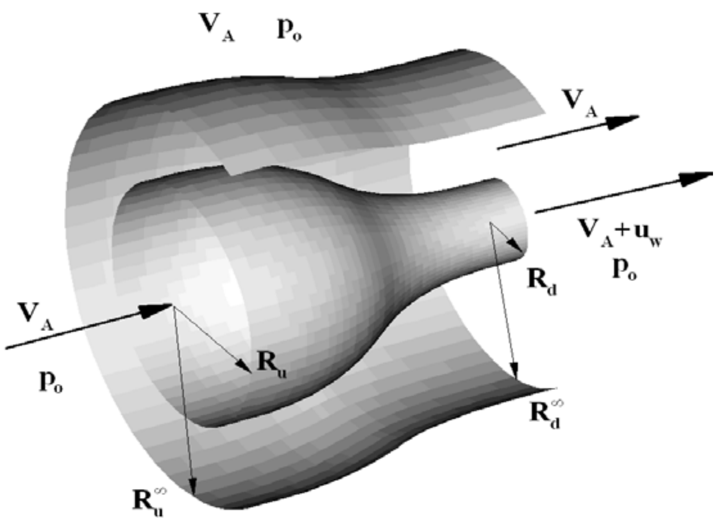

Figure 82: *Control volume for actuator disk momentum calculation. The stream tube contraction has been exaggerated for clarity.*

$$\frac{dm}{dt} = 2\pi r\rho(V_A + u_a^*(r))dr \tag{177}$$

and the total thrust is

$$\begin{aligned} T &= 2\pi\rho u_w \int_0^R \left(V_A + u_a^*(r)\right) r dr \\ &= \rho\pi R^2 u_w V_A + 2\pi\rho u_w \int_0^R u_a^*(r) r dr \\ &= \rho\pi R^2 u_w \left(V_A + \tilde{u}_a^*\right) \end{aligned} \tag{178}$$

where

$$\tilde{u}_a^* = \frac{2}{R^2}\int_0^R u_a^*(r) r dr \tag{179}$$

is the mass–averaged axial perturbation velocity at the disk. Comparing Eq.s 170 and 178, we see that the mass-averaged axial perturbation velocity at the disk is exactly half of the perturbation velocity far downstream,

$$\tilde{u}_a^* = \frac{u_w}{2} \tag{180}$$

If we introduce equation 180 into equation 171, we obtain a very useful expression that relates the axial velocity at the disk to the thrust coefficient,

$$\frac{\tilde{u}_a^*}{V_A} = \frac{-1 + \sqrt{1 + C_T}}{2} \tag{181}$$

For small values of thrust coefficient, $C_T << 1$, equation 181 becomes,

$$\frac{\tilde{u}_a^*}{V_A} \approx \frac{C_T}{4} \tag{182}$$

Most textbook presentations of actuator disk theory, for simplicity, do not distinguish between averaged flow quantities and their actual radial distribution, and therefore leave the impression that the perturbation velocity at the disk is independent of radius. In fact, detailed computations show that the axial perturbation velocity is nearly constant over most of the disk but decreases significantly as the radius approaches the radius of the disk. This can be seen from figure 83 which shows the results of a numerical calculation for the entire flow field for a thrust coefficient of $C_T = 2.0$ A detailed analysis of the flow right at the tip shows that the velocity field has a logarithmic singularity at this point, so that the actual flow in the immediate neighborhood of the tip is actually quite complex. Fortunately, for low and moderate values of thrust coefficient, this region is very local and is invisible in a numerical simulation.

We can now write down an exact expression for the radius of the slipstream far downstream, R_w by applying conservation of mass,

$$\begin{aligned} \pi R^2 (V_A + \frac{1}{2} u_w) &= \pi R_w^2 (V_A + u_w) \\ \frac{R_w}{R} &= \sqrt{\frac{1 + \frac{1}{2}\frac{u_w}{V_A}}{1 + \frac{u_w}{V_A}}} \\ &= \sqrt{\frac{1 + \sqrt{1 + C_T}}{2\sqrt{1 + C_T}}} \end{aligned} \tag{183}$$

Thus, we see that as the thrust loading increases, the ultimate slipstream radius, R_w,

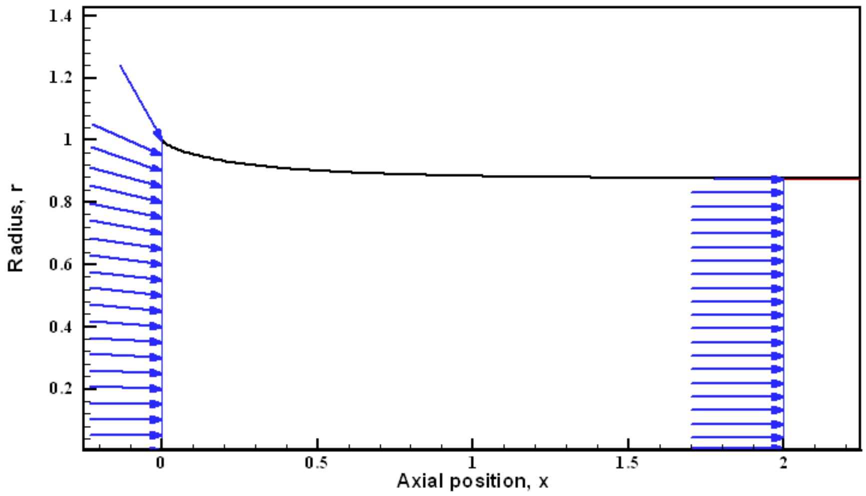

Figure 83: *Results of numerical calculation of slipstream radius and velocity field in the plane of the disk and far downstream. The thrust coefficient is* $C_T = 2.0$.

decreases. In the limit of static thrust [43], when the advance speed is zero, the thrust coefficient becomes infinite, and the slipstream radius reaches an asymptotic limit of $R_w = 1/\sqrt{2}$, as shown in figure 84

In this case, Schmidt and Sparenberg [44] have shown that the tip stream tube has a logarithmic spiral behavior in the immediate vicinity of the tip, passes upstream, and then doubles back to pass through the disk at a radius of approximately $0.97R$, as shown in figure 85. Furthermore, stream tubes just outside cross the disk twice. Fluid particles traversing these stream tubes experience no net total pressure rise, so that their pressure and velocity far downstream return to free stream values. In spite of this complex flow behavior near the tip, Eq. 183 is still theoretically exact. However, one should remember that an exact solution to the actuator disk problem does not imply that it is a physically realizable flow.

The efficiency of the actuator disk can be defined as the ratio of the useful work done by the device to the total energy supplied to it. As shown in figure 86, in a fixed coordinate system, the disk will be moving in the negative x direction with speed V_A. In a time increment δt, the disk moves $\delta x = V_A \delta t$ in the negative X direction, and the output

---

[43] This is sometimes referred to as *bollard pull*, signifying that the ship is being held stationary at a dock while power is applied to the propeller. It is also a condition encountered initially when a ship starts from rest.

[44] G.H. Schmidt and J.A. Sparenberg, " On the Edge Singularity of an Actuator Disk with Large Constant Normal Load", Journal of Ship Research, June 1977, Volume 21, Number 2.

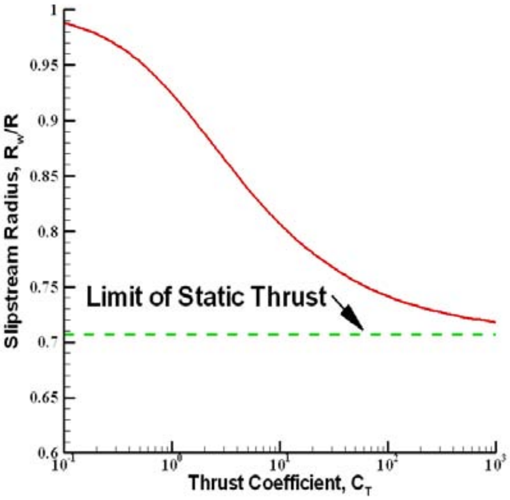

Figure 84: *Ultimate slipstream radius as a function of thrust coefficient, C_T from Eq. 183*

work will be $W = T\delta x$. At the same time, the total amount of kinetic energy imparted to the fluid will be increased by some amount which we will call E. Conservation of energy then requires that the total energy input be $(T\delta x + E)$. The efficiency will then be

$$\eta = \frac{T\delta x}{T\delta x + E} = \frac{T}{T + E/\delta x} \tag{184}$$

We now need to obtain an expression for E. During the time interval δt, a fluid particle in the slipstream far downstream will have moved a distance

$$\delta x_w = (V_A + u_w)\delta t = \frac{(V_A + u_w)}{V_A}\delta x \tag{185}$$

relative to the disk. The increase in kinetic energy imparted to the fluid is therefore the kinetic energy contained in a cylindrical volume of fluid of radius R_w and axial length δx_w,

$$E = \left[\frac{1}{2}\rho u_w^2\right]\left[\pi R_w^2\right]\left[\delta x \frac{V_A + u_w}{V_A}\right] \tag{186}$$

Introducing Eq. 183, we obtain,

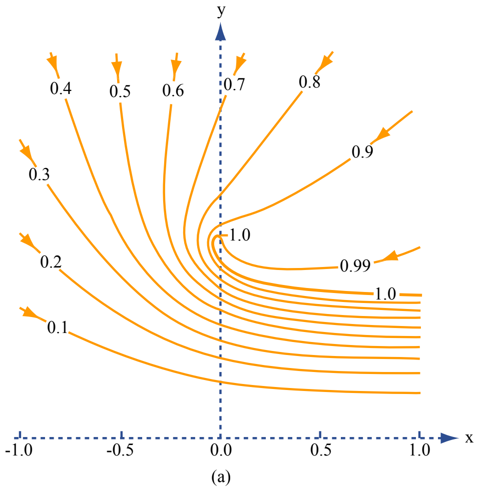

Stream tubes near the tip of an actuator disk in static thrust. Note that the tip streamtube (labeled 1.0) initially goes upstream. Adapted from Schmidt and Sparenburg.

Figure by MIT OCW. Adapted from Schmidt and Sparenburg, 1977.

$$\frac{E}{\delta x} = \frac{1}{2}\rho u_w^2 \pi R^2 \frac{V_A + u_w/2}{V_A} \tag{187}$$

But, we also know from Eq. 178 that

$$T = \rho \pi R^2 u_w (V_A + u_w/2) \tag{188}$$

so that Eq. 187 can be written explicitly in terms of thrust,

$$\frac{E}{\delta x} = \frac{1}{2}\left(\frac{u_w}{V_A}\right) T \tag{189}$$

which we can introduce in Eq. 184 to obtain an expression for the efficiency,

$$\eta = \frac{T\delta x}{T\delta x + E} = \frac{2}{1 + \sqrt{1 + C_T}} \tag{190}$$

Eq. 190 is exact, in spite of the fact that the simple momentum/energy analysis presented here cannot quantify the complex local flow near the disk. This important equation shows how efficiency reduces with increasing thrust coefficient, and serves as an upper bound on efficiency for “real” propulsors. This result is plotted in figure 87, together with the results for the more general case which we will consider later.

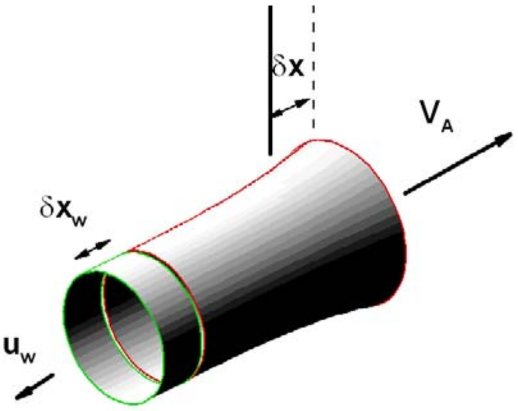

Figure 86: *Control volume for actuator disk energy balance*

The results developed so far are for the simplest possible case of an actuator disk with uniform total pressure rise with no addition of swirl. While one can treat the general case, we will defer this until we have developed the fundamentals of lifting line theory. We will then be able to show that the actuator disk can be recovered as a special limit of lifting line theory.

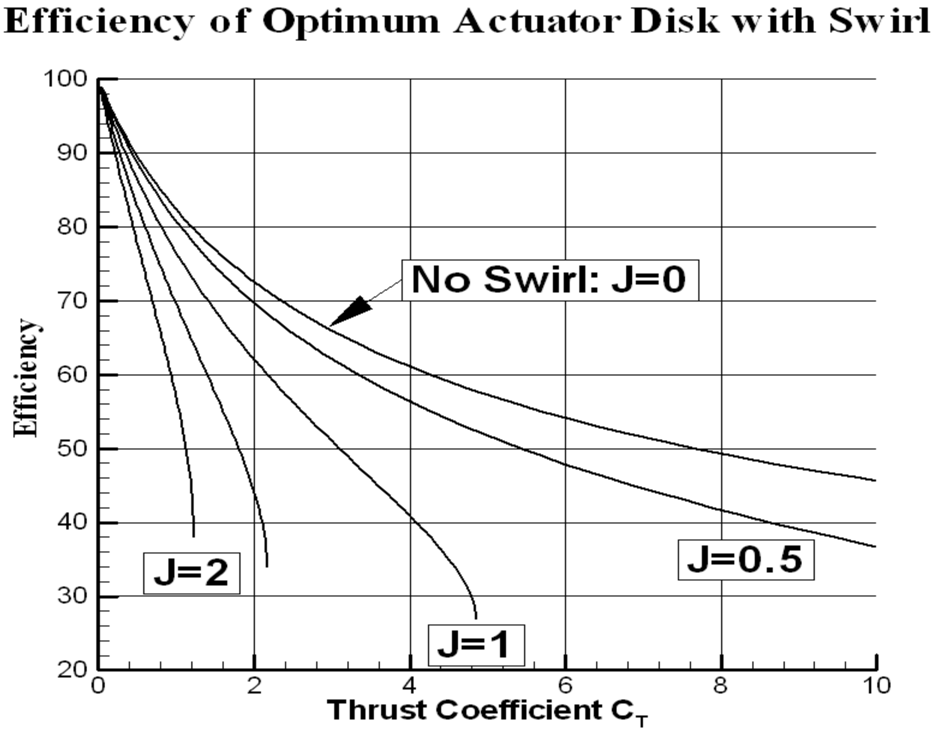

Figure 87: *Efficiency as a function of thrust coefficient for the general case of an actuator disk with swirl. The curve for* $J = 0$ *corresponds to Eq. 190.*

3.4 Propeller Lifting Line Theory

We will now take one step closer to the real world and develop a lifting line representation of a propeller. As shown in figure 88, each propeller blade can be considered as a lifting surface with some distribution of bound and free vortex sheet strength. We then consider the limiting case of vanishing chord length, which is represented in the right hand portion of the figure. As in the case of the planar foil, the bound vortex sheet reduces to a single concentrated vortex of strength $\Gamma(r)$ on each blade. Since all blades will have the same circulation distribution in circumferentially uniform flow, we can select one blade (or lifting line) and designate it as the *key blade*.

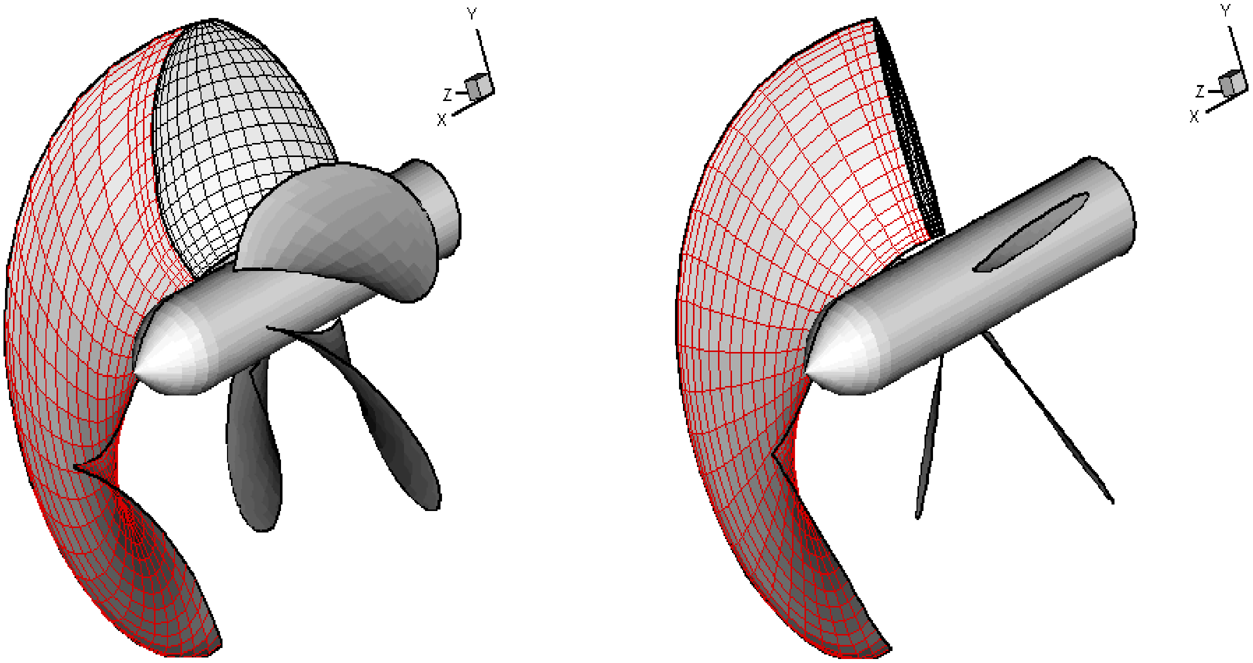

Figure 88: *Illustration of the concept of a lifting-line propeller as a limit of vanishing chord length. The radial distribution of blade circulation,* $\Gamma(r)$ *remains the same, so that the strength of the trailing vortex sheet,* $\gamma_f(r)$ *is unchanged.*

The strength of the free vorticity in the wake may be found from the relationships developed in section 2.2. In this case, the s_2 curvilinear coordinate, as illustrated in figure 88, will be more or less helical in form, but may also contract (as we saw with the actuator disk) as it progresses downstream. However, if we make the assumption that the free vortex lines are convected downstream with a constant radius, the free vortex sheet strength, as in the case of the planar lifting line, can be obtained directly from the derivative of the spanwise (in this case, radial) distribution of circulation,

$$\gamma_f(r) = -\frac{d\Gamma}{dr} \tag{191}$$

We can develop expressions for the forces acting at radius r on the key lifting line from a local application of Kutta-Joukowski's law. Figure 89, shows a combined velocity and force diagram. The axial and tangential induced velocities due to the helical free vortex system, $u_a^*(r)$, $u_t^*(r)$ combine with the effective inflow velocity components $V_A(r)$, $V_T(r)$ and the propeller rotational speed ωr to produce an inflow velocity V^* oriented at an angle β_i with respect to the plane of rotation,

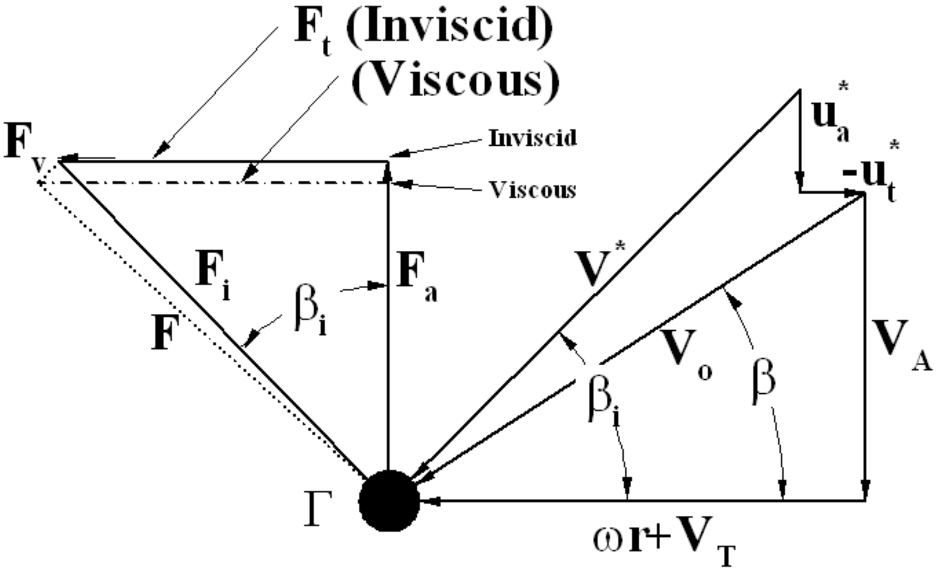

Figure 89: *Velocity and force diagram at a particular radial position on a lifting line.*

$$V^*(r) = \sqrt{(V_A(r) + u_a^*(r))^2 + (\omega r + V_T(r) + u_t^*(r))^2}; \tag{192}$$

$$\beta_i(r) = \tan^{-1}\left[\frac{V_A(r) + u_a^*(r)}{\omega r + V_T(r) + u_t^*(r)}\right]. \tag{193}$$

The quantity $\beta_i - \beta$ is therefore analogous to the induced angle in wing lifting-line theory.

The force per unit radius on the vortex, $F(r)$ is therefore

$$F(r) = \rho V^*(r)\Gamma(r), \tag{194}$$

and is directed at right angles to V^*.

It is relatively simple to include the effect of viscous drag at this stage by adding a force $F_v(r)$ acting in a direction parallel to V^*. This force may be estimated on the basis of an experimentally determined, or theoretically calculated two-dimensional sectional drag coefficient $C_{Dv}(r)$. This means, of course, that the section chord lengths $c(r)$ must be specified. The viscous drag force will then be

$$F_v(r) = \frac{1}{2}\rho(V^*(r))^2 c(r) C_{Dv}(r). \tag{195}$$

These forces can then be resolved into components in the axial and tangential direction, integrated over the radius and summed over the number of blades to produce the total propeller thrust and torque.

$$T = \rho \mathcal{Z} \int_{r_h}^{R} \left[V^* \Gamma \cos\beta_i - \frac{1}{2}(V^*)^2 c C_{Dv} \sin\beta_i \right] dr; \tag{196}$$

$$Q = \rho \mathcal{Z} \int_{r_h}^{R} \left[V^* \Gamma \sin\beta_i + \frac{1}{2}(V^*)^2 c C_{Dv} \cos\beta_i \right] r dr. \tag{197}$$

Note that $V^* \cos\beta_i$ is simply the total tangential velocity acting at the lifting line, $(V_t + \omega r + u_t^*)$, and that $V^* \sin\beta_i$ is the axial velocity, $(V_a + u_a^*)$.

The Velocity Induced by Helical Vortices

The velocity induced at radius r_c on the *key* lifting line by a set of $\mathcal{Z}$ unit strength helical vortices shed at radius r_v can be expressed as an integral using the law of Biot-Savart as developed in equation 104.

$$\bar{u}_a(r_c, r_v) = \frac{1}{4\pi} \sum_{k=1}^{\mathcal{Z}} \int_0^\infty \frac{r_v[r_v - r_c \cos(\phi + \delta_k)]}{[(r_v \phi \tan\beta_w)^2 + r_v^2 + r_c^2 - 2 r_v r_c \cos(\phi + \delta_k)]^{3/2}} d\phi \tag{198}$$

$$\bar{u}_t(r_c, r_v) = \frac{1}{4\pi} \sum_{k=1}^{\mathcal{Z}} \int_0^\infty \frac{r_v \tan\beta_w[(r_c - r_v \cos(\phi + \delta_k)) - (r_v \phi \sin(\phi + \delta_k)]}{[(r_v \phi \tan\beta_w)^2 + r_v^2 + r_c^2 - 2 r_v r_c \cos(\phi + \delta_k)]^{3/2}} d\phi \tag{199}$$

In the above expressions, β_w is the pitch angle of the helix at r_v. According to linear theory, $\beta_w = \beta$, but we will leave β_w unspecified at the moment in order to facilitate subsequent refinements to the theory. The variable of integration, ϕ, is the angular coordinate of a general point on the helix shed from the key blade. The corresponding angular coordinate of a point on the $k'th$ blade is found by adding the blade indexing angle,

$$\delta_k = 2\pi \frac{k-1}{\mathcal{Z}} \quad k = 1, \ldots, \mathcal{Z} \tag{200}$$

The total induced velocity on the lifting line can now be obtained by integrating the contributions of the helical vortices over the radius,

$$\begin{aligned} u_a^*(r_c) &= \oint_{r_h}^{R} -\frac{\partial \Gamma(r_v)}{\partial r} \bar{u}_a(r_c, r_v) dr_v \\ u_t^*(r_c) &= \oint_{r_h}^{R} -\frac{\partial \Gamma(r_v)}{\partial r} \bar{u}_t(r_c, r_v) dr_v \end{aligned} \tag{201}$$

However, Equations 198-199 cannot be evaluated analytically, so that one must resort to some form of numerical solution. On the other hand, if the limits of integration are changed from $0, \infty$ to $-\infty, \infty$, they would then represent the velocities induced along a radial line by a set of helical vortices extending to infinity in both directions. This would be equivalent to the velocity induced infinitely far downstream by the free vorticity shed from the original lifting line. Since the integrands in Eq. 198-199 are even with respect to the variable of integration, ϕ, [45] the velocities infinitely far downstream are double their values at the lifting line.

Now imagine a helicoidal coordinate system, with one coordinate along the helix, one coordinate radial, and the third coordinate normal to the first two. Far downstream, the flow will be independent of the helical coordinate. Thus, the flow is two-dimensional in terms of the two remaining helicoidal coordinates.

The potential problem for this type of flow was solved in dependently by Kawada and Lerbs, and a derivation may be found in Appendix 1 of Lerbs' paper [46].

The resulting potential can be expressed in terms of infinite sums of modified Bessel functions. While direct evaluation of these functions might be as time consuming as numerical integration of the Biot-Savart law result, fortunately highly accurate asymptotic

---

[45] Provided that the order of summation over the blade index, k, is reversed when ϕ is replaced by $-\phi$.

[46] Lerbs,H.W.,"Moderately Loaded Propellers with a Finite Number of Blades and an Arbitrary Distribution of Circulation",Trans. SNAME,Vol. 60,1952

formulas for the sums of Bessel functions exist. This enabled Wrench [47] to develop the following closed form approximations to the induced velocities;

For $r_c < r_v$:

$$\begin{aligned}
\bar{u}_a(r_c) &= \frac{\mathcal{Z}}{4\pi r_c}\left(y - 2\mathcal{Z} r_v F_1\right) \\
\bar{u}_t(r_c) &= \frac{\mathcal{Z}^2}{2\pi r_c} y_0 F_1
\end{aligned} \tag{202}$$

For $r_c > r_v$:

$$\begin{aligned}
\bar{u}_a(r_c) &= -\frac{\mathcal{Z}^2}{2\pi r_c} y y_0 F_2 \\
\bar{u}_t(r_c) &= \frac{\mathcal{Z}}{4\pi r_c}\left(1 + 2\mathcal{Z} y_0 F_2\right)
\end{aligned} \tag{203}$$

where

$$\begin{aligned}
F_1 &\approx -\frac{1}{2\mathcal{Z} y_0}\left(\frac{1+y_0^2}{1+y^2}\right)^{0.25} \{ \frac{1}{U^{-1}-1} + \frac{1}{24\mathcal{Z}}\left[\frac{9y_0^2+2}{(1+y_0^2)^{1.5}} + \frac{3y^2-2}{(1+y^2)^{1.5}}\right] \\
&\quad \ln\left(1 + \frac{1}{U^{-1}-1}\right)\} \\
F_2 &\approx -\frac{1}{2\mathcal{Z} y_0}\left(\frac{1+y_0^2}{1+y^2}\right)^{0.25} \{ \frac{1}{U-1} - \frac{1}{24\mathcal{Z}}\left[\frac{9y_0^2+2}{(1+y_0^2)^{1.5}} + \frac{3y^2-2}{(1+y^2)^{1.5}}\right] \\
&\quad \ln\left(1 + \frac{1}{U-1}\right)\}
\end{aligned} \tag{204}$$

and

$$\begin{aligned}
U &= \left\{\frac{y_0(\sqrt{1+y^2}-1)}{y(\sqrt{1+y_0^2}-1)} \exp\left(\sqrt{1+y^2} - \sqrt{1+y_0^2}\right)\right\}^{\mathcal{Z}} \\
y &= \frac{r_c}{r_v \tan\beta_w} \\
y_0 &= \frac{1}{\tan\beta_w}
\end{aligned} \tag{205}$$

Figure 90 shows the results of Equations 202 and 203 for a particular case. As one would expect, the velocity tends to ±∞ as the control point radius approaches the vortex

---

[47] Wrench,J.W.,"The Calculation of Propeller Induction Factors",,DTMB Report 1116, Feb. 1957.

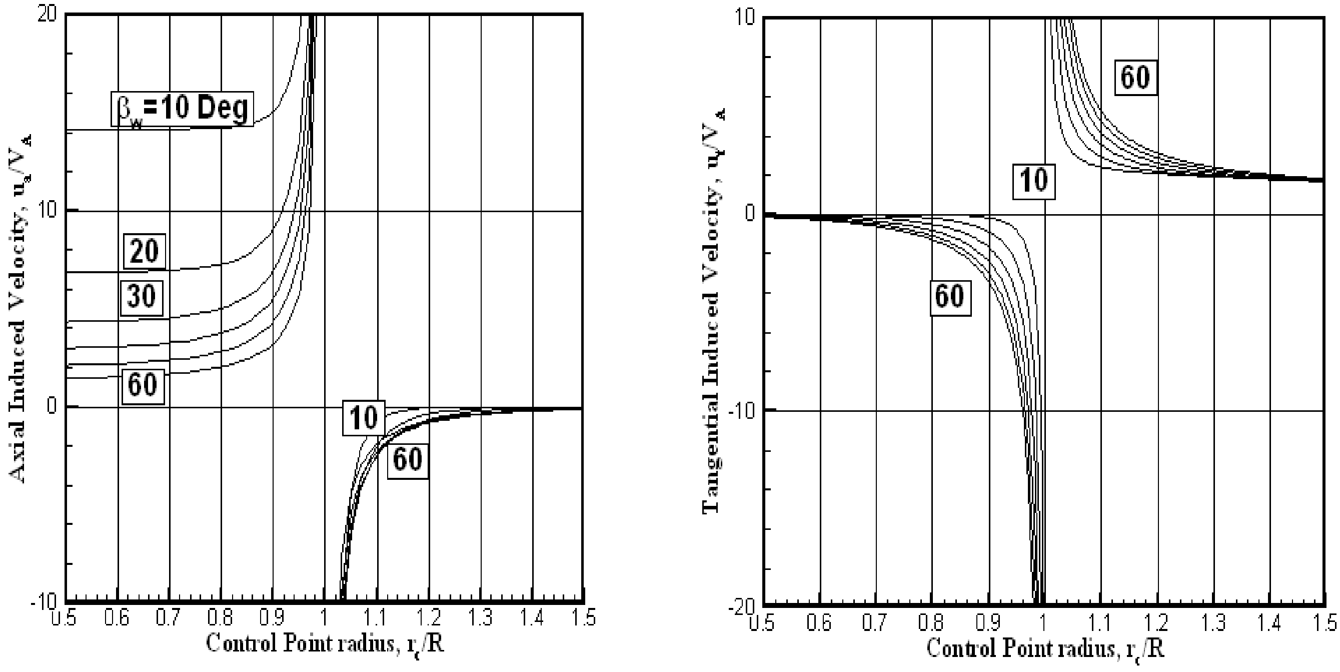

Figure 90: *Velocity induced on a lifting line at radius* r_c *by a set of semi-infinite helical vortices originating at* $r_v = 1.0$. *The number of blades in this case is* $\mathcal{Z} = 5$. *Results are shown for pitch angles* $\beta_w = 10, 20, 30, 40, 50, 60$ *degrees.*

radius. When the control point is well inside the vortex, the axial velocity approaches a constant value, which increases with *decreasing* pitch angle of the helix. When the control point is outside the vortex, the axial velocity approaches zero rapidly with increasing radius, and is relatively insensitive to pitch angle.

The reverse is true with the tangential velocity. Inside the vortex, the tangential velocity approaches zero with decreasing radius. Outside the vortex, the tangential velocity appears to reduce slowly with increasing radius. The tangential velocity is relatively insensitive to pitch angle, except in the immediate vicinity of the vortex. This is in contrast to the axial velocity, which is extremely sensitive to pitch angle when the control point is inside the vortex.

The limit of infinite number of blades is of particular importance, since this will yield an axisymmetric flow that we can relate to the actuator disk. As the blade number is increased, the quantity U in Equation 204 becomes infinite, and as a result, F_1 and F_2 both approach zero. Equations 202 and 203 then reduce to the simple expressions, For $r_c < r_v$:

$$
\begin{aligned}
\bar{u}_a(r_c) &= \frac{\mathcal{Z}}{4\pi r_v \tan\beta_w} \\
\bar{u}_t(r_c) &= 0
\end{aligned}
\tag{206}
$$

For $r_c > r_v$:

$$
\begin{aligned}
\bar{u}_a(r_c) &= 0 \\
\bar{u}_t(r_c) &= \frac{\mathcal{Z}}{4\pi r_c}
\end{aligned}
\tag{207}
$$

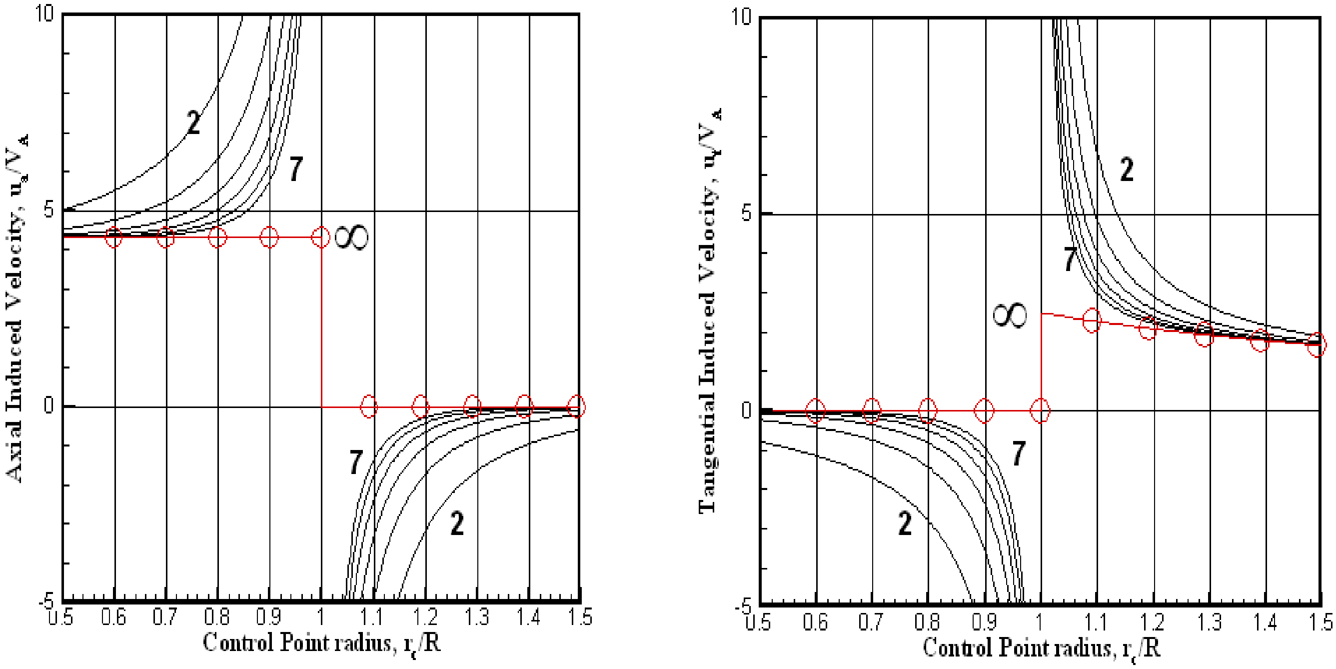

Figure 91: *Effect of blade number on the velocity induced on a lifting line at radius r_c by a set of semi-infinite helical vortices originating at $r_v = 1.0$. The pitch angle is $\beta_w = 30$ degrees. Results are also shown for an infinite number of blades from Equations 206-207. The total circulation, $\mathcal{Z}\Gamma$, is kept constant as the blade number is varied, and matches the value used for the five bladed propeller shown in Figure 90*

The singular behavior of the induced velocities is similar to that of a straight vortex, where we know that the velocity behaves as $1/(r_c - r_v)$. It is therefore useful to factor out the singular part, leaving a regular function that depends on the geometry of the helix. Lerbs defined an *induction factor* as the ratio of the velocity induced by $\mathcal{Z}$ helical vortices to the velocity induced by a semi-infinite straight vortex of the same strength,

$$\begin{aligned} i_a(r_v, r_c) &\equiv -\frac{\bar{u}_a(r_v, r_c)}{\frac{1}{4\pi(r_c - r_v)}} \\ i_t(r_v, r_c) &\equiv \frac{\bar{u}_t(r_v, r_c)}{\frac{1}{4\pi(r_c - r_v)}} \end{aligned} \tag{208}$$

As the radius of the vortex, r_v, approaches the radius of the control point, r_c, the velocity induced by the helical vortices will approach the value induced by a semi-infinite vortex oriented in a direction tangent to the helix at its starting point on the lifting line. Therefore, as $r_c \to r_v$, we find that

$$\begin{aligned} \bar{u}_a(r_v, r_c) &\to \frac{-\cos\beta_i}{4\pi(r_c - r_v)} \\ \bar{u}_t(r_v, r_c) &\to \frac{\sin\beta_i}{4\pi(r_c - r_v)} \end{aligned} \tag{209}$$

Comparing 209 with 208 we see that in the limit as $r_c \to r_v$, the axial and tangential induction factors become, respectively, $\cos\beta_i$ and $\sin\beta_i$. Therefore, the induction factors remain finite as the vortex point and control point coincide, while the actual velocity tends to infinity. The reason for the minus sign in the definition of the axial induction factor is strictly for the convenience of making the induction factors positive.

With the helical vortex influence functions known, we are now ready to tackle the evaluation of the singular integrals for the induced velocities given in Eq. 201. However, before we do this, we will revisit actuator disk theory— this time from the point of view of a lifting line vortex model.

3.4.1 The Actuator Disk as a Particular Lifting Line

It turns out that we can construct an actuator disk, using the concepts of propeller lifting line theory. Consider the limiting case of an infinite bladed lifting line with zero hub radius, and *uniform* circulation $\Gamma(r) = \Gamma$ over the radius. In the limiting process, we will keep the product of the number of blades, and the circulation per blade, $\mathcal{Z}\Gamma$ constant. Furthermore, since we saw that an actuator disk generates zero tangential induced velocity (and hence absorbs zero shaft torque), we will need to adopt one of the following models,

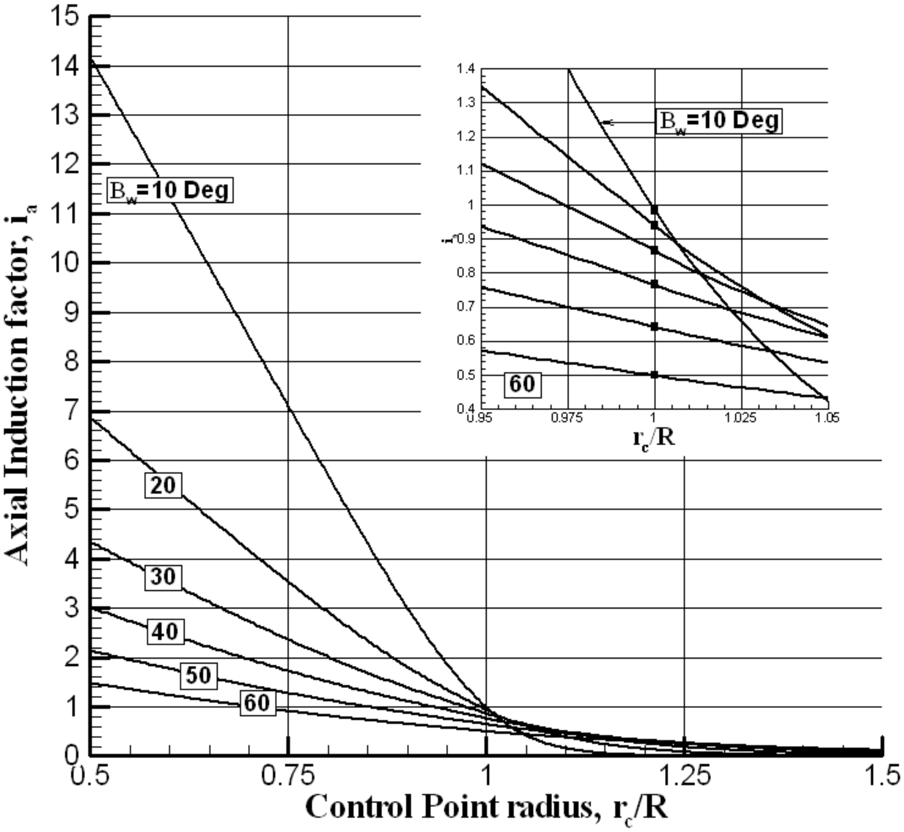

Figure 92: *Axial induction factors for a 5 bladed propeller derived from Figure 90. The enlarged plot shows the local behavior near* $r_c/r_v = 1$*. The analytical limit of* $i_a = \cos\beta_w$ *is plotted as square symbols on the graph.*

1. We can assume that the rotational speed, ω is high, so that $u_t^* << \omega r$. This is equivalent to taking the limit of zero advance coefficient, J_A.

2. We can construct an ideal counter rotating propeller by superimposing two identical, infinite bladed lifting lines rotating in opposite directions. In this case, the axial induced velocities from each lifting line component will add, while the tangential component will cancel. The quantity $\mathcal{Z}\Gamma$ will be divided equally between the two components, but the sign of Γ will be opposite. With the counter rotating model, the specification of advance coefficient is arbitrary.

We will next show that either model will recover the results obtained previously by momentum/energy considerations. Be begin by writing down the relationship between thrust and circulation, using equation 196. Setting the viscous drag to zero, and making the assumption that $u_t^* << \omega r$,

$$T = \int_0^R \rho V^* \cos\beta_i \mathcal{Z}\Gamma dr \approx \int_0^R \rho\omega r \mathcal{Z}\Gamma dr = \frac{\rho}{2}\omega\mathcal{Z}\Gamma R^2 \tag{210}$$

which we can also express as a thrust coefficient,

$$C_T = \frac{\frac{\rho}{2}\omega\mathcal{Z}\Gamma R^2}{\frac{1}{2}\rho V_a^2 \pi R^2} = \frac{\omega\mathcal{Z}\Gamma}{\pi V_a^2} \tag{211}$$

We next obtain an expression for the axial induced velocity, u_a^*. Since the circulation is constant, there will be a concentrated helical tip vortex of strength Γ shed from each blade, and from equation 206, these will induce a *constant* axial velocity,

$$u_a^* = \frac{\mathcal{Z}\Gamma}{4\pi R \tan\beta_w(R)} \tag{212}$$

and zero tangential velocity. But, there will also be a concentrated *hub* vortex of strength $-\Gamma$ shed from each blade at $r = 0$. From equation 207 these will induce zero axial velocity. The tangential velocity induced by the hub vortex will not be zero (unless we use the counter rotating option), but we have assumed, no matter what, that it will be negligible.

If we make the linearizing assumption that the tangent of the pitch angle of the tip vortices, β_w is equal to the that of the undisturbed flow, $\tan\beta$, we can eliminate $\mathcal{Z}\Gamma$ in equation 212 using 211

$$\frac{u_a^*}{V_a} = \left(\frac{\pi V_a^2 C_T}{\omega}\right)\left(\frac{1}{4\pi R}\right)\left(\frac{\omega R}{V_a}\right)\left(\frac{1}{V_a}\right) = \frac{C_T}{4} \tag{213}$$

This agrees with the actuator disk result in the limit of vanishing C_T where $u_a^*/V_a << 1$, as derived previously in equation 182. However, we can obtain a more accurate result if we recognize that the pitch angle of the tip vortices is not the undisturbed angle β, but that, at least initially, is the angle β_i. Since

$$\tan\beta_i = \frac{V_a + u_a^*}{\omega R} \tag{214}$$

we can rewrite equation 212 as

$$u_a^* = \frac{\mathcal{Z}\Gamma}{4\pi R \tan\beta_i(R)} = \frac{\mathcal{Z}\Gamma\omega R}{2\pi R(V_a + u_a^*)} \tag{215}$$

$$2\pi R(V_a + u_a^*)u_a^* = \mathcal{Z}\Gamma\omega R \tag{216}$$

and eliminate $\mathcal{Z}\Gamma$

$$\mathcal{Z}\Gamma = \frac{\pi V_a^2 C_T}{2\omega} \tag{217}$$

to obtain the result

$$(V_a + u_a^*)u_a^* = \frac{V_a^2 C_T}{4} \tag{218}$$

Finally, we can put equation 218 in standard quadratic form and solve it for u_a^*/V_a

$$(u_a^*)^2 + u_a^* V_a - \frac{V_a^2 C_T}{4} = 0 \tag{219}$$

$$\frac{u_a^*}{V_a} = \frac{-1 + \sqrt{1 + C_T}}{2} \tag{220}$$

which is exactly the actuator disk result given in equation 181. This is remarkable, in a way, since the actuator disk result includes the contraction of the slipstream (but is unaware of tip vortices), while the present result models the tip vortices as constant radius helical lies with constant (although suitably adjusted) pitch angle. We will see later how this relates to the so-called *moderately loaded theory* of propellers.

We can now easily derive the expression for efficiency. The input power is

$$Q\omega = \rho\omega \int_0^R r(V_a + u_a^*)\mathcal{Z}\Gamma dr = \frac{\rho}{2}\omega\mathcal{Z}\Gamma(V_a + u_a^*)R^2 \tag{221}$$

while the output power is

$$TV_a = \frac{\rho}{2}\omega V_a \mathcal{Z}\Gamma R^2 \tag{222}$$

So the efficiency, η is the ratio of the two,

$$\eta = \frac{1}{1 + \frac{u_a^*}{V_a}} = \frac{2}{1 + \sqrt{1 + C_T}} \tag{223}$$

This is also the exact actuator disk result given in equation 190.

3.5 Optimum Circulation Distributions

We would like to obtain the radial distribution of circulation, $\Gamma(r)$, which will minimize the torque, Q, for a prescribed thrust, T. The diameter, advance coefficient, blade number, and effective inflow are specified. [48] While other considerations, such as the inception of tip vortex cavitation, may require us to depart from this optimum, this is generally a logical starting point in the design process. This problem can be solved using the method of calculus of variations, and one can find detailed accounts of this approach in Yim[], Coney[] and Breslin[]. While the resulting equations can be solved rapidly on current computers, they are non-linear, intricate in appearance, and provide little direct physical insight.

On the other hand, an earlier approach developed by Betz in 1919 for a propeller in uniform inflow, V_S, and later extended by Lerbs in 1952, is relatively simple to derive and is physically intuitative. Suppose we have a distribution of circulation which is optimum, and which generates the desired thrust. Now suppose that we perturb this circulation by adding an increment of circulation $\delta\Gamma$ over some increment of radius δr at some arbitrary radial location r. This will result in incremental changes in thrust and torque, δT and δQ. The efficiency of this process is the ratio of the output to input power,

$$\eta^* = \frac{\delta T V_S}{\delta Q \omega} \tag{224}$$

If $\Gamma(r)$ is truly optimum, then η^* must be independent of radius. Otherwise, circulation could be decreased at a radius where η^* is low, and increased by a corresponding amount at a different radius where η^* is high. The result would be a reduction in torque for a fixed thrust, thus contradicting the assertion that $\Gamma(r)$ is optimum. So far, this is essentially a physically based statement of the variational principle.

However, if we attempted to express Eq. 224 in terms of circulation and induced

---

[48] Alternatively, we may wish to maximize thrust for a prescribed torque. In either case, the resulting propeller will have the highest possible efficiency.

velocity influence coefficients, the resulting expressions would be far from simple. This is because the increment of circulation introduced at a particular radius, r, not only changes the force locally, but alters the force over the entire radius as a result of its altering of the induced velocity distribution. Betz overcame this obstacle by employing a principle developed by Munk that states that the total force on a lifting surface is unchanged if an element of bound circulation is displaced in a streamwise direction. Munk's theorem follows from the principle that the force on a lifting surface can be obtained solely from a far-field momentum/energy analysis (as we did for the planar lifting surface), and that the far-field flow depends only on the strength of the trailing vorticity. This, in turn, is unaffected by a streamwise displacement of the bound vorticity.

Betz therefore added the increment of bound vorticity far downstream, so that there would be no interaction between the added circulation and the flow at the propeller lifting line. On the other hand, the local force acting on the added element of bound circulation must include the effect of the doubling of the induced velocities far downstream,

$$\begin{aligned} \delta F_x(r) &= \rho\left[\omega r + 2u_t^*(r)\right]\delta\Gamma \\ \delta F_t(r) &= \rho\left[V_S + 2u_a^*(r)\right]\delta\Gamma. \end{aligned} \tag{225}$$

If we assume that $u_t^*(r) \ll \omega r$ and that $u_a^*(r) \ll V_S$ we can perform some algebraic manipulations,

$$\begin{aligned} \frac{\delta T V_S}{\delta Q \omega)}\left(\frac{\omega r}{V_S}\right) &\approx \frac{\omega r + 2u_t^*(r) + ([u_t^*(r)]^2)/(\omega r)}{V_S + 2u_a^*(r) + ([u_a^*(r)]^2)/(V_S)} \\ &= \frac{V_S}{\omega r}\left[\frac{(\omega r)^2 + 2\omega r u_t^* + (u_t^*)^2}{V_S^2 + 2V_S u_a^* + (u_a^*)^2}\right] = \frac{V_S}{\omega r}\left[\frac{\omega r + u_t^*}{V_S + u_a^*}\right]^2. \end{aligned} \tag{226}$$

If we put equation 226 together with equations 193 and 77 the efficiency then becomes

$$\frac{\delta(T V_S)}{\delta(Q\omega)} \approx \left[\frac{\omega r + u_t^*(r)}{V_S + u_a^*(r)}\right]^2 \left[\frac{V_S}{\omega r}\right]^2 = \left[\frac{\tan\beta(r)}{\tan\beta_i(r)}\right]^2. \tag{227}$$

For a propeller with optimum radial load distribution equation 227 must be independent of radius, otherwise a redistribution of circulation could increase the overall efficiency. We therefore have the result

$$\frac{\tan\beta(r)}{\tan\beta_i(r)} = \text{constant}. \tag{228}$$

This result was first published by Betz in 1919 and is now known as the "Betz Condition."

For this condition to hold the induced inflow at the lifting line must form a constant pitch helicoidal surface. In other words, if our friendly bug and one of his cousins both had their feet stuck to this surface, as they spin around and go downstream they would not think they were moving in relation to each other. Betz condition is the correct linear result for the inviscid, open water case. The unknown constant in equation 228 is a function of the desired thrust. To find that thrust the lifting line velocities must be determined. The first solution for the circulation distribution which satisfies the Betz condition was developed by Prandtl, using an approximate method to obtain the induced velocity. This was followed by an exact solution, which was published by Goldstein in 1929.

Similar arguments can lead one to the following result for non-uniform or wake-adapted axial inflow. In this case

$$\frac{\tan\beta(r)}{\tan\beta_i(r)} = \Upsilon\sqrt{1 - w_x(r)}. \tag{229}$$

Here the axial inflow $V_a(r)$ is given by

$$V_a(r) = [1 - w_x(r)]\,V_S, \tag{230}$$

and Υ is an unknown constant. Equation 229 was published in 1952 by Lerbs and is known as "Lerbs Criterion."

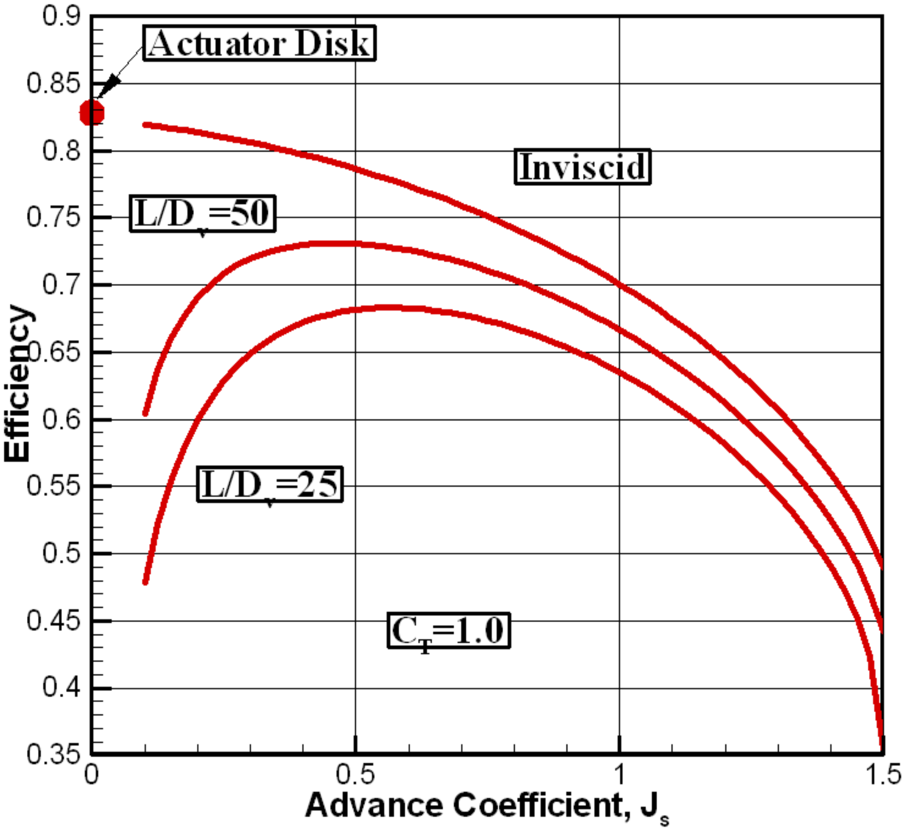

Figure 93: *Efficiency versus advance coefficient for a five bladed propeller with optimum radial distribution of circulation in uniform flow. Results are given for inviscid flow, and for viscous flow with sectional Lift/Drag ratios of* 25 *and* 50*. The actuator disk result is shown as the symbol plotted at* $J_s = 0.0$.

3.5.1 Assigning The Wake Pitch Angle β_w

It is evident from figure 89 that the pitch angle of the local flow at the lifting line, β_i, is greater than the pitch angle of the undisturbed flow, β. This difference becomes greater as the propeller loading, and hence induced velocities, increases. This means that the linearizing assumption that the free vortices are shed on helical surfaces of pitch angle β becomes less valid for increased propeller loadings.

A much better assumption, which carries the name *moderately loaded propeller theory*, is to require that the free vortices follow helical paths with pitch angle β_i rather than β. This is still not exact, since both the pitch and radius of each vortex filament should continuously deform in order to be aligned with the local flow. However, the assumption of a constant radius and pitch helical vortex with pitch angle β_i has the merit of being more or less correct in the immediate vicinity of the lifting line without unduly complicating the problem. In addition, we saw that this assumption recovered the actuator disk result *exactly* in the limit of infinite number of blades.

One should also note that the computation of the helical vortex influence functions is unchanged. We already can calculate them for arbitrary values of the pitch angle β_w. We can therefore just as easily substitute β_i for β in equations 198-200 or in equation 205 when calculating the influence functions. However, the problem is now more complicated since the equations for the induced velocities now involve β_i, which, in turn, depends on the induced velocities. An iterative solution is therefore required, and robust and efficient methods of accomplishing this will be discussed subsequently.

The actual geometry of the trailing vortex sheets is extremely complex. As we saw with the actuator disk, mass conservation requires that the stream tubes contract. But in addition, the edges of the vortex sheet roll-up in a manner similar to that observed for a wing, so that their ultimate radius is actually less than the circumferential mean value derived from mass conservation. In an ideal fluid, the rolling-up process develops into a tightly wound spiral, but in a real fluid viscous stresses causes the individual turns of the spiral to blend into a concentrated vortex core, or "tip vortex". While this process can be modeled, the computational burden is extremely large and is clearly inappropriate at the lifting-line design stage. In fact, the precise details of the deformed trailing vortex wake are not critical in determining the flow at the propeller blades, so that even lifting-surface and panel method calculations can generally be made either with the "moderately loaded" wake model or with a semi-empirical model which introduces the gross characteristics of the contraction and roll up process [49]

---

[49] Greeley,D.S. and Kerwin, J.E.,**Numerical Methods for Propeller Design and Analysis in Steady Flow**, Trans SNAME(90),1982.

3.5.2 Properties of Constant Pitch Helical Vortex Sheets

We saw in Section 3.5 that for an optimum propeller in uniform flow, $r \tan\beta_i(r) = constant$. Therefore, whether we use linear theory or moderately loaded theory, the free vortex wake will lie on a constant pitch helicoidal surface. In this case, it can be proved that the resultant induced velocity is normal to the helix. We will prove this by showing that the component along the helix is zero.

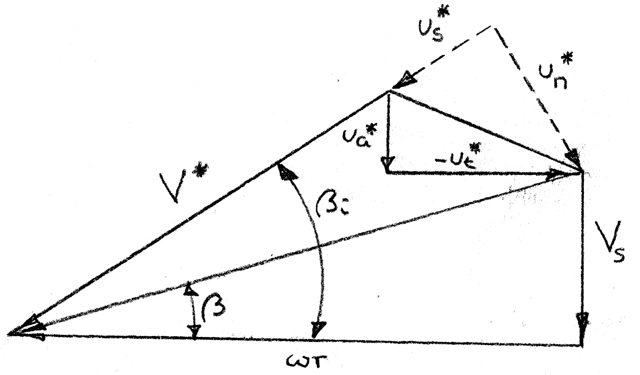

Figure 94: *Induced velocities resolved into components normal to and along the helical surface.*

As shown in figure 94, the axial and tangential component of the induced velocity at r_c can be resolved into components normal to and along the helix. Since we have to distinguish between the pitch angle at the control point, r_c, and the vortex, r_v, we will have to be careful to label them $\tan\beta(r_c) \equiv \tan\beta_c$ and $\tan\beta(r_v) \equiv \tan\beta_v$, respectively. Since the helical surface has constant pitch,

$$r_c \tan\beta_c = r_v \tan\beta_v \tag{231}$$

The induced velocity along the helix will be identified as $\bar{u}_s(r_c, r_v)$ and may be found from the axial and tangential components using the relationship

$$\bar{u}_s(r_c, r_v) = \bar{u}_a(r_c, r_v)\sin\beta_c + \bar{u}_t(r_c, r_v)\cos\beta_c \tag{232}$$

Multiplying equation 198 by $\sin\beta(r_c)$ and equation 199 by $\cos\beta(r_c)$ we obtain

$$\bar{u}_s(r_v, r_c) = \frac{1}{4\pi}\sum_{k=1}^{\mathcal{Z}}\int_0^\infty \frac{F}{D^3} d\phi \tag{233}$$

where to save writing we have temporarily designated the numerator and denominator of the integrand as

$$D = \sqrt{(r_v \phi \tan \beta_v)^2 + r_v^2 + r_c^2 - 2 r_v r_c \cos(\phi + \delta_k)} \tag{234}$$

and

$$\begin{aligned} F &= r_v^2 \sin \beta_c - r_v r_c \cos(\phi + \delta_k) \sin \beta_c + r_v r_c \tan \beta_v \cos \beta_c \\ &\quad - r_v^2 \cos(\phi + \delta_k) \tan \beta_v \cos \beta_c - r_v^2 \phi \sin(\phi + \delta_k) \tan \beta_v \cos \beta_c \end{aligned} \tag{235}$$

Equation 235 can be simplified by replacing $r_v \tan \beta_v$ with $r_c \tan \beta_c$ and by making use of the definition of D,

$$F = \sin \beta_c \left[D^2 - (r_v \phi \tan \beta_v)^2 - r_v r_c \sin(\phi + \delta_k) \right] \tag{236}$$

Substituting 236 for F in 233 gives the result,

$$\bar{u}_s(r_v, r_c) = \frac{\sin \beta_c}{4\pi} \sum_{k=1}^{\mathcal{Z}} \left[\int_0^\infty \frac{d\phi}{D} \phi - \int_0^\infty \frac{\phi (r_v^2 \tan \beta_v^2 \phi + r_v r_c \sin(\phi + \delta_k))}{D^3} d\phi \right] \tag{237}$$

So far it doesn't look like we are gaining much ground. However, the second integral in equation 237 can be simplified by noting that

$$\frac{\partial}{\partial \phi} \left(\frac{1}{D} \right) = - \frac{r_v^2 \tan \beta_v^2 \phi + r_v r_c \sin(\phi + \delta_k)}{D^3} \tag{238}$$

so that equation 237 may now be written

$$\bar{u}_s(r_v, r_c) = \frac{\sin \beta_c}{4\pi} \sum_{k=1}^{\mathcal{Z}} \left[\int_0^\infty \frac{d\phi}{D} + \int_0^\infty \phi \frac{\partial}{\partial \phi} \left(\frac{1}{D} \right) d\phi \right] \tag{239}$$

The second integral in 239 can be integrated by parts, giving the result

$$\bar{u}_s(r_v, r_c) = \frac{\sin\beta_c}{4\pi} \sum_{k=1}^{\mathcal{Z}} \left[\int_0^\infty \frac{d\phi}{D} + \left| \frac{\phi}{D} \right|_0^\infty - \int_0^\infty \frac{d\phi}{D} \right] \tag{240}$$

The first and third terms in 240 cancel, and the middle term is zero at the lower limit and $1/r_v \tan\beta_v$ at the upper limit. Since the integral is independent of the blade index, the sum over the number of blades simply multiplies the result by $\mathcal{Z}$. The final expression for the velocity along the helix is then

$$\bar{u}_s(r_v, r_c) = \frac{\mathcal{Z}\cos\beta_c}{4\pi r_c} \tag{241}$$

After all this analysis, a little assurance that equation 241 is the right answer wouldn't hurt. The following table lists the axial and tangential induced velocity influence functions for a five bladed propeller at $r_c = 0.65$. The vortices are shed on a constant pitch helix with $r_v \tan\beta(r_v) = 0.25$. The component of induced velocity along the helix is then computed from equation 232 and listed in the last column. The velocity is indeed constant, and the value agrees with equation 241.

r_v	$\tan\beta(r_v)$	$\bar{u}_a^*$	$\bar{u}_t^*$	$\bar{u}_s^*$
0.200	1.25000	-.00002	0.61214	0.57133
0.300	0.83333	-.00037	0.61228	0.57133
0.400	0.62500	-.00484	0.61399	0.57133
0.500	0.50000	-.05407	0.63293	0.57133
0.600	0.41667	-.77324	0.90953	0.57133
0.700	0.35714	2.47548	-.33997	0.57133
0.800	0.31250	1.66977	-.03009	0.57133
0.900	0.27778	1.60142	-.00380	0.57133
1.000	0.25000	1.59285	-.00050	0.57133

We started out by saying that we would prove that the resultant induced velocity was normal to the helix. The remaining step is to recognize that the total velocity at radius r_c is obtained by integrating the product of the influence functions and the free vortex strength over the radius,

$$\begin{aligned} u_s^*(r_c) &= -\int_{r_h}^{R} \bar{u}_s(r_v, r_c) \frac{d\Gamma}{dr} dr \\ &= -\bar{u}_s(r_c) \int_{r_h}^{R} \frac{d\Gamma}{dr} dr \end{aligned}$$

$$\begin{aligned} &= -\bar{u}_s(r_c)\left|\Gamma(r)\right|_{r_h}^{R} \\ &= 0 \end{aligned} \tag{242}$$

Another way to look at this is to consider that the vortex sheet is made up of discrete horseshoe vortex elements, each consisting of a pair of helical vortices of equal magnitude and opposite sign. The sum of this pair of vortices will therefore induce zero velocity along the helix. A horseshoe vortex therefore induces a velocity which is normal to a helical surface whose pitch matches its own. The summed effect of all the horseshoes, or the integrated effect of the whole vortex sheet, therefore induces a velocity normal to the helical surface.

3.5.3 The Circulation Reduction Factor

Since an optimum propeller in uniform flow has a constant pitch free vortex sheet, the resultant induced velocity, as shown in Appendix 2, is normal to a helix of pitch angle β_i. Therefore if we know the circulation and either the axial or tangential induced velocity, we will have all the information we need to complete the velocity/force diagram shown in figure 89. Since circulation and tangential velocity are closely related, it makes sense to chose the latter.

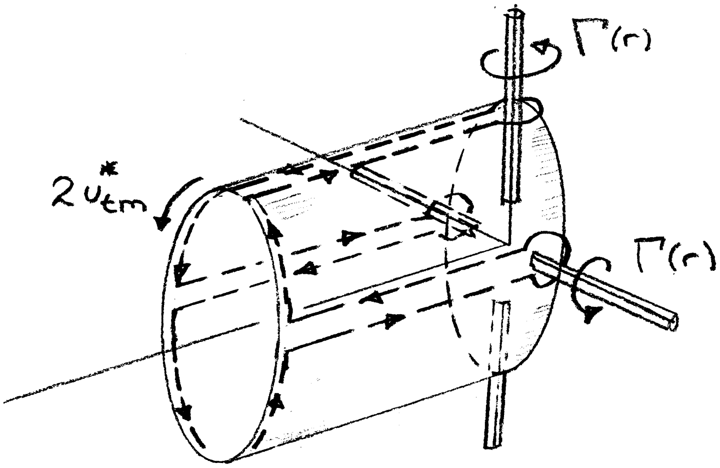

Figure 95: *Circulation path relating circulation around blades to circumferential mean tangential velocity.*

The *circumferential mean* tangential velocity, $u^*_{tm}(r)$ can be related to the circulation applying Kelvin's theorem to the path illustrated in figure 95,

$$\mathcal{Z}\Gamma(r) + 4\pi r u^*_{tm}(r) \;=\; 0$$

$$\Gamma(r) \;=\; -\frac{4\pi r u^*_{tm}}{\mathcal{Z}} \tag{243}$$

For a propeller with a large number of blades, the circumferential mean tangential velocity and the local velocity at the lifting line would be about the same, and this would provide at least a rough estimate of the desired solution. However, for a finite number of blades, the circumferential mean velocity is different from the local value at the blade, and in particular, is substantially less near the blade tip. The ratio

$$\kappa(r) \equiv \frac{u^*_{tm}(r)}{u^*_t(r)} \tag{244}$$

is called the *Circulation Reduction Factor* which depends on the number of blades, the pitch of the helical vortex wake and the non-dimensional radius, r/R. Clearly, once κ is known, the problem of the optimum propeller in uniform flow can be reduced to a sequence of simple trigonometric evaluations at each radius. In particular, since the resultant induced velocity is normal to β_i, the tangential velocity at the lifting line is

$$\frac{u^*_t}{V_s} = -\frac{\sin\beta_i \sin(\beta_i - \beta)}{\sin\beta} \tag{245}$$

and an expression for the circulation can be found by combining Equations 243 and 245,

$$G(r) \equiv \frac{\Gamma(r)}{2\pi R V_s} = \frac{2\frac{r}{R}\kappa(r)\sin\beta_i \sin(\beta_i - \beta)}{\mathcal{Z}\sin\beta} \tag{246}$$

However, determining κ is far from simple. The first attempt was made by Prandtl in 192? [50] using the ingenious analogy between the real flow induced by helical vortices and the flow of a uniform vertical free-stream past an infinite array of semi-infinite flat plates, as illustrated in Figure 96. Far outboard of the tips of the array of plates, the vertical velocity is uniform, and equal to the free stream value. Far inboard of the tips of the plates, the flow must be zero. Near the tips, some of the free stream "leaks" in between the plates, and this is analogous to the reduction in mean tangential velocity between an array of helical vortex sheets. This problem can be solved by classical conformal mapping techniques, and the resulting approximate expression for the circulation reduction factor (which became known as the *Prandtl tip factor*) is,

---

[50] Prandtl,lŁ,"Application of Modern Hydrodynamics to Aeronautics", NACA Report 116

$$\kappa(r) = \frac{2}{\pi}\cos^{-1} exp\left[\frac{\pi}{2}\frac{R-r}{R}\frac{\sqrt{1+\tan^2\beta_w(R)}}{\tan\beta_w(R)}\right] \tag{247}$$

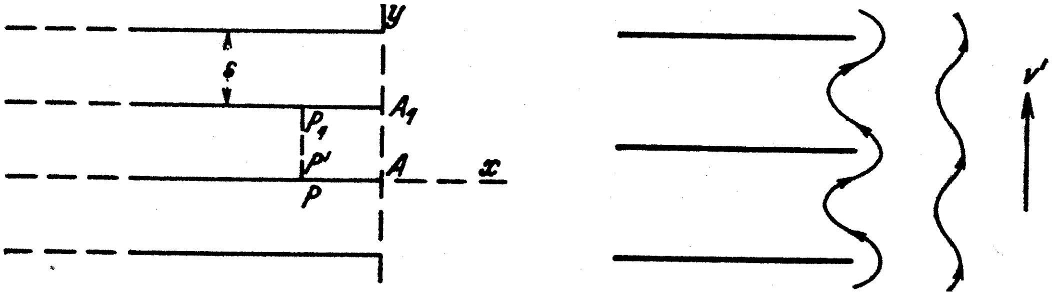

Figure 96: *Prandtl's simplified representation of the flow induced by helical vortex sheets.*

Prandtl's work was followed in 1929 by Goldstein [51] who solved the exact problem of the potential field of an infinite helical surface translating with uniform axial velocity. As with Lerb's solution for individual vortex filaments, a separation of variables solution can be found in helicoidal coordinates. The solution is periodic in coordinate normal to the vortex sheets and can thus be expanded in a trigonometric series. The solution in the radial direction was found to be expressible as a series of Lommel functions, which are related to Bessel functions. Goldstein's elegant solution to this problem is not for the mathematically timid, but both theoreticians and practical designers should appreciate the tremendous contribution to ship' and aircraft propeller design that this represents.

While some numerical results were included in Goldstein's original paper, more complete and accurate computations were subsequently carried out when computers became available. Tachmindji and Milam [52] published graphs and tables of the Goldstein factor in 1956, and Wrench [53] computed high-precision values in 19??.

The preceding results were all for the idealized case of a propeller with zero hub radius. Tachmindji [54] extended Goldstein's theory to incorporate an infinite cylindrical hub of arbitrary radius. Finally, circulation reduction factors can always be determined after the fact from a general-purpose numerical lifting-line computation using Equation 246 where both the circulation and induced velocities are computed. If one runs such a code (which will be described later in this Chapter) for the special case of an optimum propeller in uniform flow, Goldstein's result *should* be recovered. An example of the circulation reduction factor is given in Figure 97, where the Goldstein factor (actually obtained from

---

[51] Goldstein,S.,"On the vortex theory of screw propellers",Proc. Royal Soc. 123 A, 1929

[52] Tachmindji and Milam, "The calculation of Goldstein factors for three, four, five and six bladed propellers", DTMB Report 1051, 1956.

[53] Wrench, ???

[54] Tachmindji, " Something like Goldstein Factors for Finite Hubs"

a numerical lifting-line code) is compared with the Prandtl tip factor, Equation 247. The simple Prandtl approximation is surprisingly accurate at the outer radii for relatively low pitch angles. At the inner radii, the Prandtl result approaches a value of unity, while the Goldstein reduction factor can be substantially greater, particularly at large pitch angles.

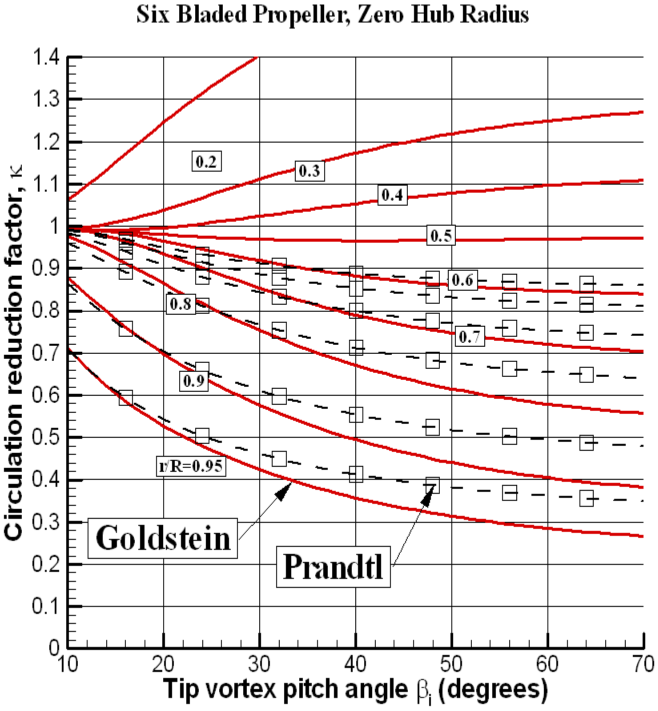
Six Bladed Propeller, Zero Hub Radius

Figure 97: Example of Circulation Reduction Factors

3.5.4 Application of the Goldstein Factor

If we start with a given speed, V_S, diameter, D and revolutions per second, n, we can calculate the advance coefficient $J_S = V_S/(nD)$ and the pitch angle of the undisturbed flow, $\beta(r)$ at selected radii between the hub and the tip. For an optimum propeller in uniform flow, the Betz condition requires that $\beta_i(r)$ be a constant multiple of $\beta(r)$. The inverse of this multiplier is the ideal efficiency (the efficiency in an ideal fluid with no viscous drag) of the propeller. Suppose, for the moment, that we arbitrarily pick a value for this multiplier. We can then construct a velocity diagram similar to the one shown in figure 89 for each of the selected radii. We can also read the values of the Goldstein factor, κ, from the diagram corresponding to the number of propeller blades, i.e. figure 97 for a six bladed propeller.

We can then calculate $\Gamma(r)$ from equation 246, and we can also calculate the thrust and torque from equations 196 and 197. If the resulting thrust is not what we want, the process will have to be repeated a number of times with different trial values of the multiplier.

This kind of an iterative process would have been impractical in pre-computer days. To avoid this, Kramer, in 1939, made systematic calculations for different numbers of blades, advance coefficients and ideal efficiencies. For each combination, Kramer found the circulation distribution and the resulting ideal [55] thrust coefficient, C_{Ti}.

The result is the Kramer diagram, which is reproduce in Figure 98 [56]. One could enter this diagram with the desired thrust coefficient and advance coefficient, and find the ideal efficiency. The designer could then proceed as described before to look up the Goldstein factors, and compute the circulation.

This general procedure formed the basis for "*high tech*" ship and airplane propeller design in the pre-computer era. However, it was soon recognized that ship propellers generally operate in radially non uniform inflow, and that cavitation and vibration considerations may force the designer to depart from the Betz/Lerbs optimum radial distribution of circulation. While the application of the Goldstein factor (and the associated assumption that the total induced velocity is normal to β_i) is invalid in this case, a pragmatic solution was to apply them anyway and hope for the best. The development of theoretical design methods based on this assumption is largely due to Van Manen [57] and to Eckhart and Morgan [58]. These methods proved to be quite effective and represented a vast improvement over the existing alternative of selecting propellers solely from experimentally based propeller charts.

Of course, manual design procedures based on the Goldstein factors have been largely replaced by computerized methods which can treat the general case of arbitrary inflow velocity and non-optimum circulation distributions. The Goldstein factor and the Kramer chart, however, remains as very concise and instructive picture of the key elements of propeller flow.

As an example of the use of the Kramer diagram, suppose that we wanted a quick estimate of the ideal (inviscid) efficiency of a five bladed propeller operating in uniform flow at an advance coefficient of $J_s = 1.0$ with a thrust coefficient of $C_T = 1.0$. We

---

[55] The thrust coefficient in the absence of viscous drag forces

[56] Kramer, K.N.,"Induzierte Wirkungsgrade von Best-Luftschrauben endlicher Blattzahl",Luftfahrtforshung, July 1938, Vol 15. An English Translation appears in NACA TM 884, January 1939

[57] Van Manen,J.D.,**Fundamentals of Ship Resistance and Propulsion**, International Shipbuilding Progress,(4), 1957

[58] Eckhart,M.K. and Morgan,W.B, "A Propeller Design Method", Trans. SNAME, Vol 63, 1955.

saw from figure 93 that the efficiency should be very nearly 70%. We can enter the Kramer diagram at advance coefficient of $\Lambda = J/\pi = 1.0/\pi = 0.318$. We next slide up the diagonal line until we reach the horizontal line corresponding to $\mathcal{Z} = 5$ blades, and then move vertically upward until we reach the horizontal line at a thrust coefficient of $C_T = 1.0$. If we did it right, we will be right on the 70% efficiency line. We can also confirm the actuator disk efficiency by entering the Kramer diagram at the left end of the scale, corresponding to an advance coefficient 0f $\lambda = 0.001 \approx 0$. Moving up to $C_T = 1.0$, we see that the efficiency is $\eta = 0.83$, which again agrees with figure 93.

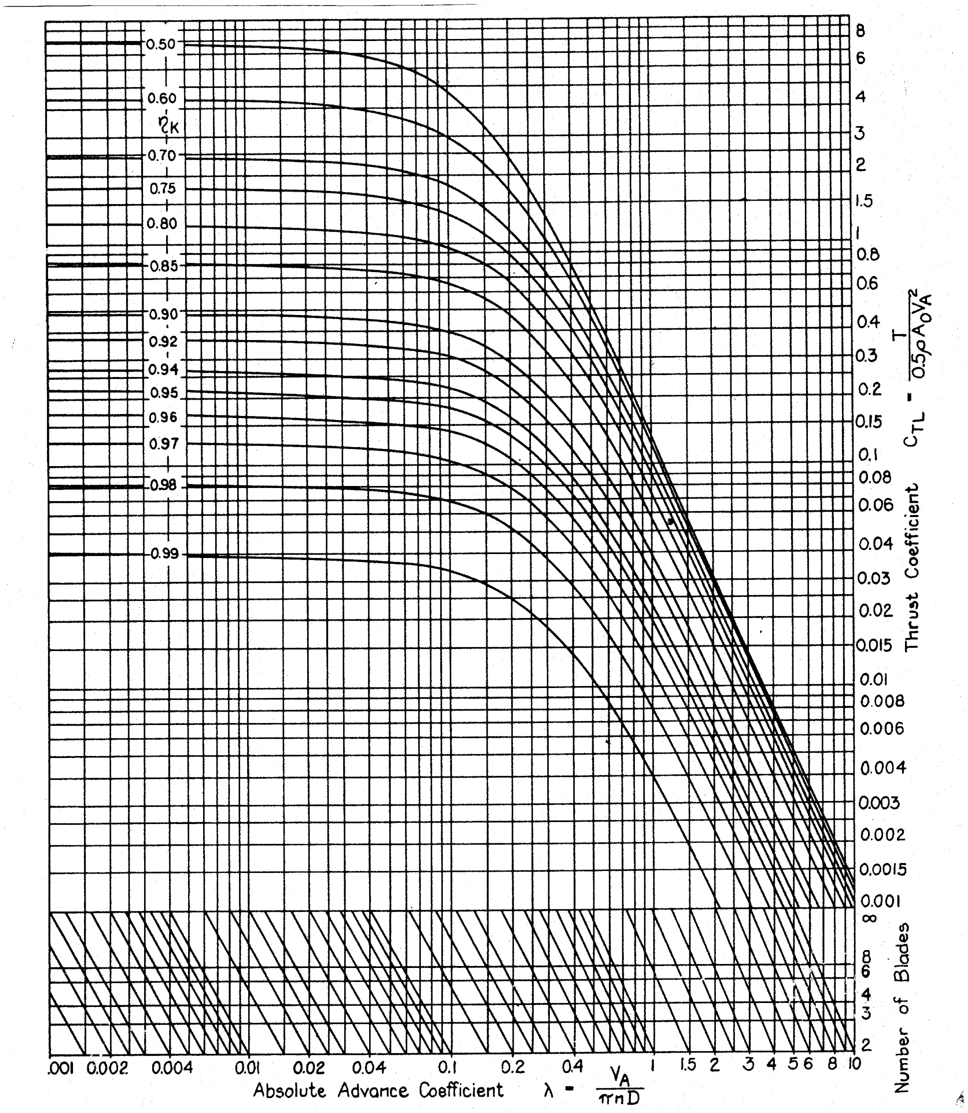

Figure 98: *Kramer Diagram for Ideal Propeller Efficiency*

3.6 Lifting Line Theory for Arbitrary Circulation Distributions

3.6.1 Lerbs Induction Factor Method

A major advance came in 1952, with the introduction by Lerbs [59] of a rigorous lifting line theory which could handle the general case of a propeller in radially non-uniform inflow with an arbitrary distribution of circulation. We will not develop Lerbs theory in complete detail here, but will describe the essential ideas.

Since Betz criterion, equation 228, and Lerbs criterion 229 for the optimum circulation distribution are expressed in terms of the distribution of hydrodynamic pitch angle, $\beta_i(r)$, the problem which will be solved is to determine the distribution of circulation, $\Gamma(r)$, for a prescribed $\beta_i(r)$. The latter may either be the optimum distribution derived from 228 or 229, or may be a suitably modified distribution of the hydrodynamic pitch angle designed to unload the tip or hub for cavitation reasons. For the moment, we will not worry about how we came to specify $\beta_i(r)$.

We also know the ship speed, V_S, the propeller rotational speed ω, and the distribution of effective axial inflow velocity $V_a(r)$. . From the velocity diagram in figure 89 we know that

$$\omega r \tan \beta_i = \omega r \tan \beta + u_a^* - u_t^* \tan \beta_i \tag{248}$$

which can be written as,

$$\frac{u_a^*}{V_S} - \frac{u_t^*}{V_S} \tan \beta_i = \frac{\omega r}{V_S}(\tan \beta_i - \tan \beta) \tag{249}$$

but since $V_a/\omega r = \tan \beta$ we can eliminate ωr and obtain the final result

$$\frac{u_a^*}{V_S} - \frac{u_t^*}{V_S} \tan \beta_i = \frac{V_a}{V_S} \left(\frac{\tan \beta_i}{\tan \beta} - 1 \right) \tag{250}$$

The right hand side of equation 250 is known. The induced velocities on the left hand side are related to the circulation $\Gamma(r)$ by the Cauchy principal value integrals over the radius given in 201. We therefore have a singular integral equation for the circulation. Lerbs developed a procedure for solving this equation by extending the method developed

---

[59] Lerbs, H.W., “Moderately Loaded Propellers with a Finite Number of Blades and an Arbitrary Distribution of Circulation”,Trans. SNAME, vol.60, 1952.

by Glauert [60] for a lifting-line wing. The key steps of Glauert's theory is contained in the Appendix.

The first step was to transform the physical radial coordinate, r to an angular coordinate, $\tilde{r}$, which takes on a value of zero at the hub and π at the tip,

$$\tilde{r} = \cos^{-1}\left(\frac{R + r_h - 2r}{R - r_h}\right) \tag{251}$$

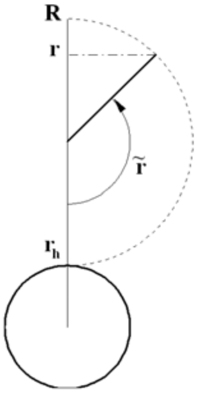

Figure 99: Geometric representation of the Glauert cosine transformation .

This "*cosine*" transformation is shown graphically in Figure 99. Next, the radial distribution of circulation is approximated by a finite sine series in the transformed variable $\tilde{r}$,

$$G(\tilde{r}) \equiv \frac{\Gamma(\tilde{r})}{2\pi R V_S} = \sum_{j=1}^{J} a_j \sin(j\tilde{r}) \tag{252}$$

with the unknown coefficients, a_j, to be determined. The maximum number of terms

---

[60] Glauert,H.,**The Elements of Aerofoil and Airscrew Theory**, Cambridge University Press, 1959

retained in the sine series, J, can be selected to provide the desired level of accuracy. A sine series was chosen to ensure that the circulation would vanish at the hub and tip for any choice of the coefficients a_j. It is clear on physical grounds that the circulation must go to zero at the tip (except in the case of a ducted propeller with vanishing tip gap) but this is not necessarily true at the hub. Lerbs argued that the close proximity of the blades at the hub juncture would tend to equalize the pressures on both sides of the blades and thus reduce the circulation to zero. In fact, subsequent calculations with lifting-surface and panel methods have demonstrated that the circulation may be non-zero at the hub. However, since the local behavior at the hub has little effect on overall propeller performance, Lerbs' idealization of the "hubless" propeller is not a serious shortcoming of the theory. We will consider the effect of the hub on propeller performance in more detail in a subsequent section.

Introducing the definition of the induction factors from Equation 208, and converting to the non-dimensional circulation, G, we can write equation 201 as

$$\begin{aligned} \frac{u_a^*}{V_S} &= \frac{1}{1-r_h/R}\int_0^\pi \frac{i_a(r_v,r_c)\sum_{j=1}^J j a_j \cos(j\tilde{r}_v)}{\cos\tilde{r}_v - \cos\tilde{r}_c} d\tilde{r}_v \\ \frac{u_t^*}{V_S} &= \frac{-1}{1-r_h/R}\int_0^\pi \frac{i_t(r_v,r_c)\sum_{j=1}^J j a_j \cos(j\tilde{r}_v)}{\cos\tilde{r}_v - \cos\tilde{r}_c} d\tilde{r}_v \end{aligned} \tag{253}$$

This is beginning to look more like Equation 130 in Glauert's lifting line theory, except for the presence of the induction factors. In order to make use of Glauert's integral, Equation 131, Lerbs next approximated the induction factors at a given value of r_c by a Fourier cosine series in $\tilde{r}_v$. This is permissible, since the singularity has been removed from the induction factors, so that what remains is a well behaved function, as shown in Figure 92. The coefficients in the Fourier expansion were obtained by evaluating Equations 203-206 at J positions over the radius, and using standard harmonic analysis techniques to obtain the Fourier coefficients. The numerator in Equation 253 then consists of sums of cosines whose coefficients are combinations of the unknown circulation series and the known coefficients of the Fourier expansion of the induction factors. This can then be integrated analytically term by term using Equation 130. The resulting set of algebraic equations may then be solved for the unknown circulation coefficients, a_j. While this sounds (and is) intricate, the resulting algorithm is extremely robust and computationally efficient. The resulting procedure is a good example of a semi-analytic method, in which the singular integrals over the radius are carried out analytically, while the circulation and the induction factors are approximated by series with a finite number of terms.

Once the coefficients a_j of the circulation are found, the circulation, thrust and torque can be computed. If the thrust (or torque) is not equal to the desired value, the input

$\tan \beta_i(r)$ can be adjusted until the desired value is obtained. The matching of the specified thrust is accomplished by first computing two initial guesses, and then applying Newton's method to find the multiplier to be applied to the first approximation to $\tan \beta_i$ which produces in the correct thrust (to within a specified tolerance). Generally three or four Newton iterations are sufficient to achieve a thrust coefficient to within a practical tolerance. An example of this procedure will be shown together with corresponding results obtained by a vortex lattice method.

3.7 Propeller Vortex Lattice Lifting Line Theory

A vortex lattice solution to the propeller lifting line problem is conceptually very similar to the solution of the planar lifting line problem. The span of the key blade is divided into M panels extending from $r = r_h$ to $r = R$, as shown in figure 88. The radial distribution of (bound) circulation, $\Gamma(r)$, is approximated by a set of M vortex elements of constant strength Γ_m extending from $r_v(m)$ to $r_v(m+1)$. A discrete trailing (free) vortex line is shed at each of the panel boundaries, with a strength equal to the difference in strengths of the adjacent bound vortices. However, as with planar lifting line theory, it is more convenient to consider that the vortex system is built from a set of M horseshoe elements, each consisting of a bound vortex segment of strength Γ_m and two free vortex lines of strength $\pm\Gamma_m$. But in addition, each horseshoe element actually represents a set of $\mathcal{Z}$ identical elements of equal strength, one originating from each blade.

Each set of horseshoe vortex elements, *of unit strength*, induces an axial and tangential velocity at a specified control point, $r_c(n)$ on the key blade. The contribution of the two free vortices can be found from equations 202 and 203, or if one wishes to solve the problem of an infinite bladed propeller, from equations 206 and 207. The contribution of the bound vortex element of the set of horseshoe vortices is zero, provided that the lifting line is radial and that the blades have uniform angular spacing. Clearly the bound vortex on the key lifting line induces zero velocity anywhere along that line. Bound vortex elements on another blade may induce a velocity on the key blade, but their summed effect will cancel due to symmetry. The total induced velocity at control point $r_c(n)$ is therefore,

$$\begin{aligned} u_a^*(r_c(n)) &= \sum_{m=1}^{M} \Gamma_m \bar{u}_a(n,m) \\ u_t^*(r_c(n)) &= \sum_{m=1}^{M} \Gamma_m \bar{u}_t(n,m) \end{aligned} \tag{254}$$

where $\bar{u}_a(n,m)$ and $\bar{u}_t(n,m)$ are the horseshoe influence functions.

As with planar foil lifting line theory, it is best to use cosine spacing for the vortex and control points. Defining $h = 0.5(R - r_h)$ and $\delta = \pi/(2M)$, their coordinates are,

$$\begin{aligned} r_v(m) &= r_h + h\,[1 - \cos(2(m-1)\delta)] \\ r_c(n) &= r_h + h\,[1 - \cos(2n-1)\delta)] \end{aligned} \tag{255}$$

There are a number of possible approaches to solving for the circulation. The method used in **PVL** is similar to Lerbs method— except, of course, that a vortex lattice is used instead of Lerbs extension of Glauert's sine series method. The objective will be to find the circulation distribution (and hence, forces) for a propeller with a specified thrust coefficient, C_T.

Figure 101 shows a sample input data file for **PVL**. The first entry is the number of panels, which in this case is $M = 32$. The last part of the data file consists of a tabulation of the chord/diameter ratio, c/D, the viscous drag coefficient, C_d, the axial inflow velocity, V_a, and the tangential inflow velocity, V_t, at a user-specified set of non-dimensional radii, r/R starting with the hub and ending with the tip. The number of input radii is arbitrary, and is given in the 5'th entry in the table— in this case 11. With this information, equation 255 is used to compute the vortex lattice grid, and the items tabulated at the input radii are interpolated to the vortex lattice grid by a cubic spline procedure.

In particular, the inflow angle β at any radius can be computed from,

$$\tan\beta(r) = \frac{V_a(r)}{\frac{\pi r}{J_s} + V_t(r)} \tag{256}$$

where the advance coefficient, J_s is given in the 7'th entry in the input file— in this case $J_s = 0.8$. A plot of β for this particular case may be found in the lower right of figure 102.

The next step is to specify a trial value of $\beta_i(r)$. This can either be the optimum distribution, as given by equation 228 or 229, or may be altered to unload the hub or tip, which we will discuss later. In either case, $\tan\beta_i$ is obtained from $\tan\beta$ in terms of an unknown multiplicative constant. We know that for an optimum propeller in uniform, inviscid flow, the multiplier is simply the inverse of the ideal efficiency. Since the thrust coefficient is specified, we can easily compute the efficiency of an actuator disk. We will therefore use 90% of the efficiency of the actuator disk as a first guess in establishing $\beta_i(r)$. We will then solve for the circulation and for C_T using this value, and then iteratively adjust the multiplier until the desired C_T is achieved. This, of course, is done internally in the program using Newton's method, which converges very rapidly. The maximum number of iterations is given as the second entry in the file— in this case 10. Usually, convergence to six significant figures is achieved in three or four iterations. The converged value for β_i for this example is also shown in the bottom right of figure 102.

With $\beta_i(r)$ known, the induced velocities must satisfy the same kinematic relationship as is equation 250 in Lerbs method,

$$\frac{u_a^*}{V_S} - \frac{u_t^*}{V_S}\tan\beta_i = \frac{V_a}{V_S}\left(\frac{\tan\beta_i}{\tan\beta} - 1\right) \tag{257}$$

and by combining equation 254 with equation 257, we obtain the following set of simultaneous equations for the unknown circulation values, Γ_n,

$$\sum_{m=1}^{M} \left[\bar{u}_a(n,m) - \bar{u}_t(n,m) \tan\beta_i(n) \right] \Gamma_m = \frac{V_a(n)}{V_S} \left(\frac{\tan\beta_i(n)}{\tan\beta(n)} - 1 \right) \quad n = 1, \ldots M \tag{258}$$

Once the simultaneous equations for Γ are solved, equations 195 and 196 can be used to evaluate the forces, including the effects of viscous drag (based on the drag coefficient values tabulated in the input). The integrals over the radius for the forces are simply replaced by sums over the vortex lattice. The solved value of the circulation and the induced velocities for this example is shown on the left side of figure 102.

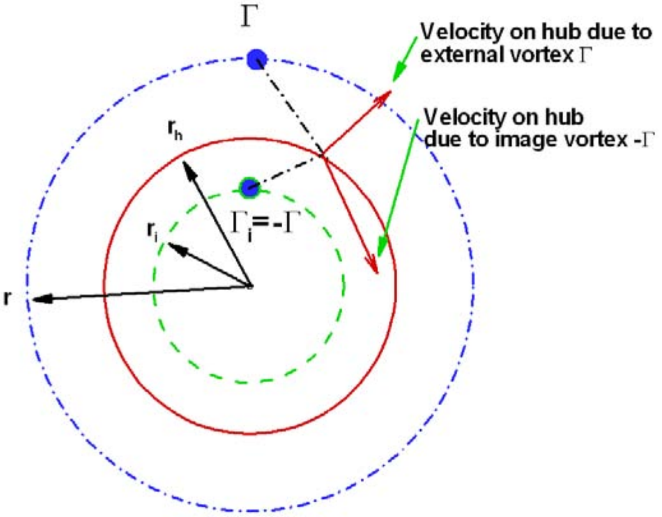

Figure 100: *Illustration of the image of a 2-D point vortex in a circle of radius* r_h. *The vortex is at radius* r, *while the image is at radius* $r_i = r_h^2/r$. *If the two vortices have equal and opposite strengths, the normal (radial) component of the velocity induced by the pair of vortices cancels at all points on the circle of radius* r_h. .

3.7.1 Hub effects

So far, we have ignored the presence of the hub, except for the fact that the lifting lines representing the blades start at the "hub radius", r_h. This is equivalent to assuming that the blades have a free tip at both ends, and that some magical magnetic force is present to keep them rotating about the shaft axis. In this case, the circulation goes to zero at both the hub and the tip, as shown in figure 102. In reality, a propeller hub is present,

```
 Sample PVL input file: Propeller in idealized 1/7 power law wake field
  32             : NUMBER OF VORTEX PANELS OVER THE RADIUS
  10             : MAXIMUM ITERATIONS IN WAKE ALIGNMENT
   0             : HUB IMAGE FLAG: 1=YES, 0=NO
  0.25           : HUB VORTEX RADIUS/HUB RADIUS
  11             : NUMBER OF INPUT RADII
   5             : NUMBER OF BLADES
  0.8            : ADVANCE COEFFICIENT, J, BASED ON SHIP SPEED
  1.000          : DESIRED THRUST COEFFICIENT, CT
  0.000          : HUB UNLOADING FACTOR: 0.0=OPTIMUM (NO UNLOADING)
  0.000          : TIP UNLOADING FACTOR  1.0=REDUCED LOADING
  1.000          : CRP SWIRL CANCELLATION FACTOR: 1.0=NO CANCELATION
    r/R      c/D       Cd        Va/Vs     Vt/Vs
  0.20000   0.17400   0.00800   0.71969   0.00000
  0.25000   0.19700   0.00800   0.74300   0.00000
  0.30000   0.22900   0.00800   0.76260   0.00000
  0.40000   0.27500   0.00800   0.79460   0.00000
  0.50000   0.31200   0.00800   0.82034   0.00000
  0.60000   0.33700   0.00800   0.84198   0.00000
  0.70000   0.34700   0.00800   0.86073   0.00000
  0.80000   0.33400   0.00800   0.87731   0.00000
  0.90000   0.28000   0.00800   0.89218   0.00000
  0.95000   0.24000   0.00800   0.89911   0.00000
  1.00000   0.00200   0.00800   0.90572   0.00000
```

Figure 101: *Sample input data file for* **PVL**. *This file was used to generate the results plotted in figure 102*

which is either an integral part of the solid propeller casting or is a separate unit that contains the controllable pitch mechanism. In the latter case, each blade flange is bolted to a spindle in the hub.

While the hub geometry can be included in a detailed panel method calculation of the flow around the propeller, a simpler approximation is appropriate at the lifting-line design stage. It is known that in two-dimensional flow, the velocity field of a point vortex situated at radius r outside a circle of radius r_h can be found by superimposing the flow field of a vortex in an unbounded fluid with the velocity field of an *image vortex* situated within the circle. As shown in figure 100, if the image vortex is located at a radius

$$r_i = \frac{r_h^2}{r} \tag{259}$$

the total velocity normal to the circle can easily be shown to be zero. As the radius of the hub is increased, we obtain the limiting case of a vortex outside of an infinite wall, and in this case the image vortex is obviously *at the same distance* inside the wall. On the other hand, as the vortex radius is increased (or the hub radius is decreased), equation 259 shows that the image vortex moves to the axis.

No simple image exists for a helical vortex, but numerical calculations show that equation 259 works amazingly well. Results obtained with the simple image model agree almost exactly with complete potential flow solution published by Tachmindji [61]. It is therefore a simple matter to supplement each helical horseshoe vortex with it's image inside the hub. If the $m'th$ horseshoe vortex extends from $r_v(m)$ to $r_v(m+1)$, it's image will extend from $r_h^2/r_v(m)$ to $r_h^2/r_v(m+1)$. The velocity induced by the image horseshoe vortex can be combined with the influence function for the "real" external horseshoe element in equation 258 so that no additional unknowns are introduced into the problem.

Figure 103 shows the effect of including the hub image. The circulation now has a finite value at the hub, and the derivative of $\Gamma(r)$ with respect to r is zero at the hub. The circulation over the outer part of the blade is essentially the same as for the zero hub case.

The presence of finite circulation at the hub introduces a new problem. This circulation is essentially transferred into the inside of the hub via the hub image, but it must eventually be shed into the flow at the downstream termination of the hub [62] This forms a concentrated *hub vortex*, which is very visible when it's core pressure is sufficiently low

---

[61] A.J. Tachmindji,"Potential Problem of the Optimum Propeller with a Finite Number of Blades", Journal of Ship Research, December, 1958

[62] The only exception is in an experimental facility where the propeller is driven by a downstream shaft. Most early propeller tunnels drove the propeller from downstream, so that the presence of hub vortex cavitation was not observed.

for it to cavitate. This can be shown from the sequence of three photographs reproduced in figures 104,105 and 106. All three photographs were taken at the same tunnel flow speed and pressure. The first photograph shows a propeller operating by itself, while the second photograph shows a pre-swirl stator (designed to operate with the propeller) operating by itself. Finally, the third photograph shows the propeller and stator operating together.

The presence of a concentrated hub vortex also effects the net propeller thrust. The low pressure region in (and near) the core of the vortex acts on the aft side of the hub, thus creating a drag. It would seem simple to integrate the pressure field around a concentrated vortex over the projected downstream face of the hub in order to obtain the drag. However, the unfortunate result is that the drag is infinite! To obtain a physically realistic result, the hub vortex must be modeled as one with a finite viscous core radius. Using the classical Rankine vortex model, in which the velocity field within the core is simply one of solid body rotation, and outside of the core is a potential vortex, M-H Wang [63] computed the hub vortex drag as a function of the ratio of vortex core radius to hub radius. Wang found that the resulting pressure force acting on the downstream end of the hub could be approximated as follows,

$$F_h = \frac{\rho}{16\pi}\left(\ln\frac{r_h}{r_o} + 3\right)(\mathcal{Z}\Gamma_o)^2 \tag{260}$$

where r_o is the core radius of the hub vortex and Γ_o is the circulation at the blade root. The hub vortex core radius must be estimated, but fortunately, due to the logarithmic nature of equation 260, it's precise value is not critical.

The optimum distribution of circulation, if based on an infinitely long hub (and hence zero hub drag), will therefore not produce the most efficient propeller. This is particularly true for propellers with large hub/diameter ratios. It is therefore better to reduce the circulation at the hub, as shown in figure 107.

However, the problem of hub drag can be overcome with a multiple blade row propulsor—either a counter rotating propeller or a combination of a rotor and a set of fixed stator blades. In either case, the net circulation at the hub can be designed to be zero, so that there will be no hub vortex and no hub vortex drag.

Figure 109 shows an optimum counter rotating propeller, in which the tangential induced velocities from each blade row exactly cancel. The optimum circulation distribution shows a large value at the hub. There is no hub drag in this case, since there is no net circulation at the hub.

---

[63] M-H Wang, "Hub effects in Propeller Design and Analysis"",PhD Thesis, Department of Ocean Engineering, MIT, May 1985

3.7.2 The Vortex Lattice Actuator Disk

We can create an actuator disk in **PVL** by setting the hub radius to a very small (but non-zero value) and specifying an infinite number of blades, with zero viscous drag. This is accomplished by specifying a finite number of blades exceeding 20. Figure 110 shows a sample result for a thrust coefficient of $C_T = 1.0$. The number of blades is entered as 25, so that the output circulation per blade is still finite. However, the induced velocity influence coefficients are for an infinite bladed propeller, not a 25 bladed propeller. Tangential velocity cancelation has been specified. The computed axial induced velocity and circulation is constant over the radius, and agrees exactly with the actuator disk value. In this case, the result is independent of the input advance coefficient.

We can also run the code without tangential velocity cancelation, but with an infinite number of blades and zero drag. The results then depend on advance coefficient, as shown in figure 93. Finally, an infinite bladed propeller can be run with a specified viscous lift/drag ratio, and these results are shown on the same figure. Note that there is now an optimum advance coefficient, which depends on the lift/drag ratio.

3.7.3 Hub and Tip Unloading

The user can easily adjust the degree of hub and tip unloading in the **PVL** code by entering values in the $9'th$ and $10'th$ positions in the input file. The unloading factors, H_r and H_t are defined as the fractional amount that the difference between the optimum values of $\tan\beta_i$ and $\tan\beta$ are reduced. For example, if $H_r = 0$, $\tan\beta_i - \tan\beta$ at the hub is retained at it's optimum value from Betz/Lerbs criterion. If $H_r = 1.0$, $\tan\beta_i - \tan\beta$ at the hub is set to zero, and the values up to the mid span of the blade are blended parabolically to the optimum value. The same procedure applies to the tip. Since this adjustment is made before $\tan\beta_i$ is scaled to produce the desired thrust, the final outcome at the hub and tip may not be exactly as specified. However, one can easily adjust H_r and H_t to produce the desired result. Note from the lower right hand plots in figures 107 and 108 how the difference between β_i and β is smoothly reduced, compared to the optimum case shown in figure 103.

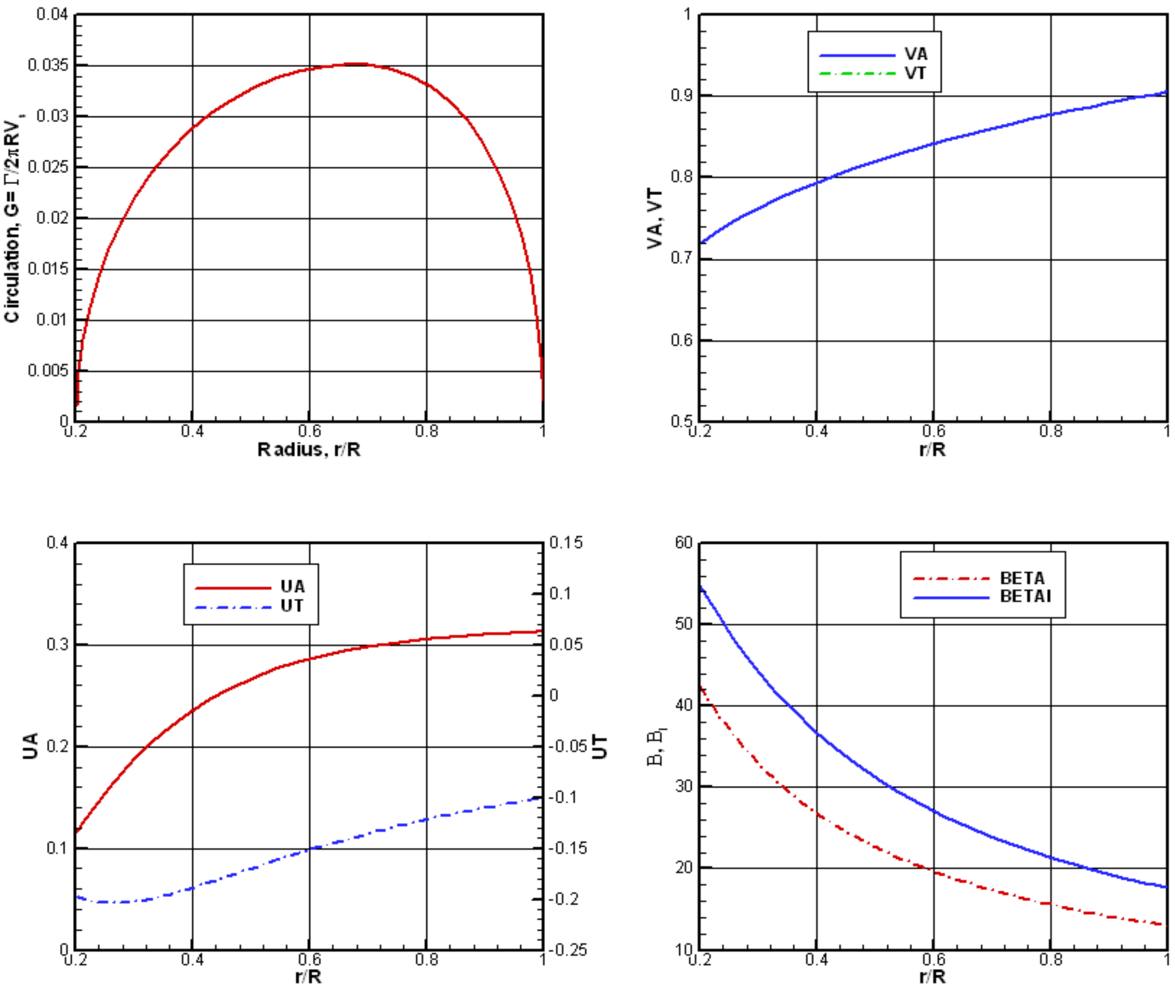

Figure 102: *Lifting line results for a 5 bladed propeller obtained with the* **PVL** *code. In this example, there is no hub, and a Lerbs optimum circulation distribution has been selected.* $C_T = 1.0$ $C_P = 1.3432$ $K_T = 0.2513$ $K_Q = 0.0430$ $V_a/V_s = 0.8526$ $\eta = 63.47\%$.

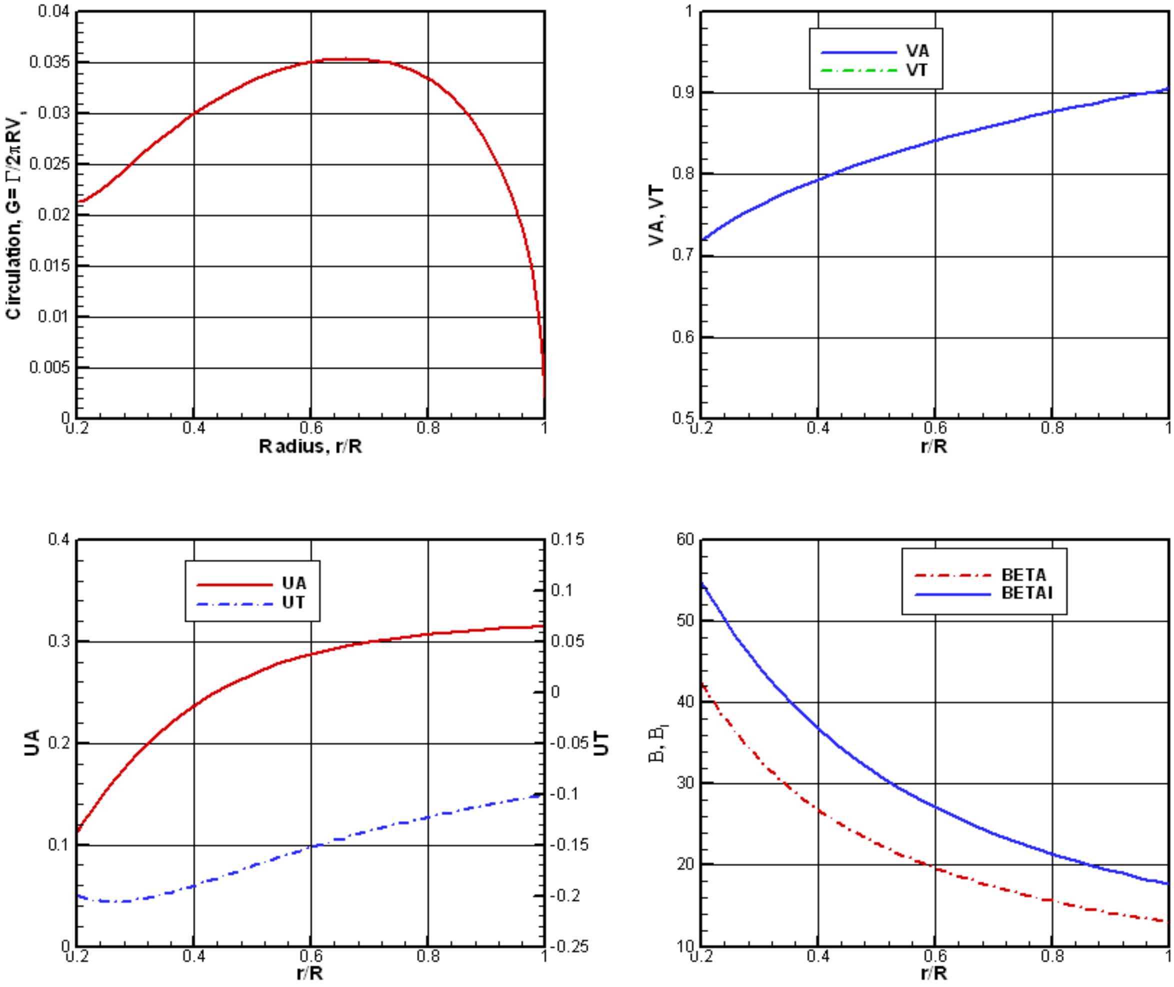

Figure 103: *Lifting line results for a 5 bladed propeller obtained with the* **PVL** *code. In this example, there is an image hub, and a Lerbs optimum circulation distribution has been selected.* $C_T = 1.0$ $C_P = 1.3744$ $K_T = 0.2513$ $K_Q = 0.0440$ $V_a/V_s = 0.8526$ $\eta =$ 62.03%. *The efficiency has been reduced slightly due to hub vortex drag.*

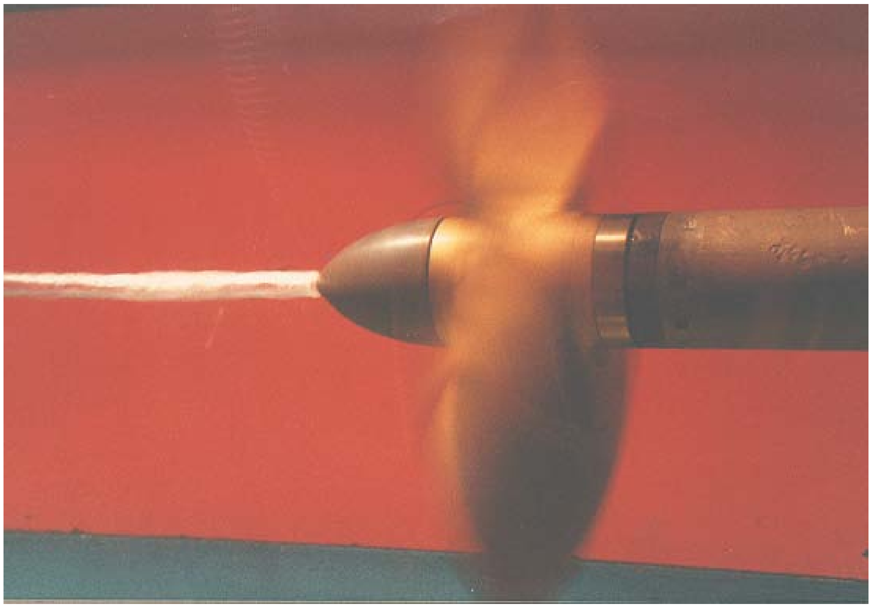

Figure 104: *Propeller operating alone. A substantial cavitating hub vortex is evident.*

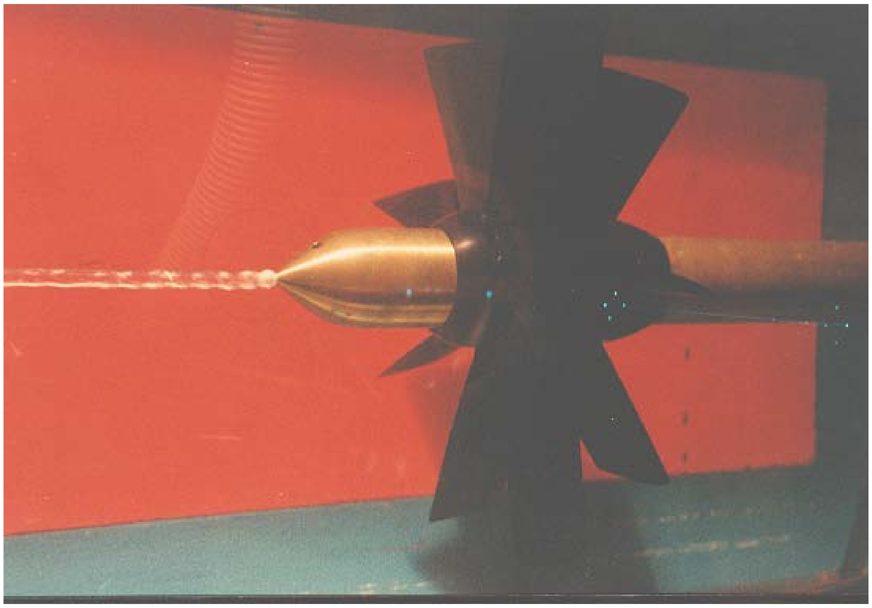

Figure 105: *Pre-swirl stator operating alone. A substantial hub vortex is again evident. The sign of this vortex is opposite from the one shown in figure 104.*

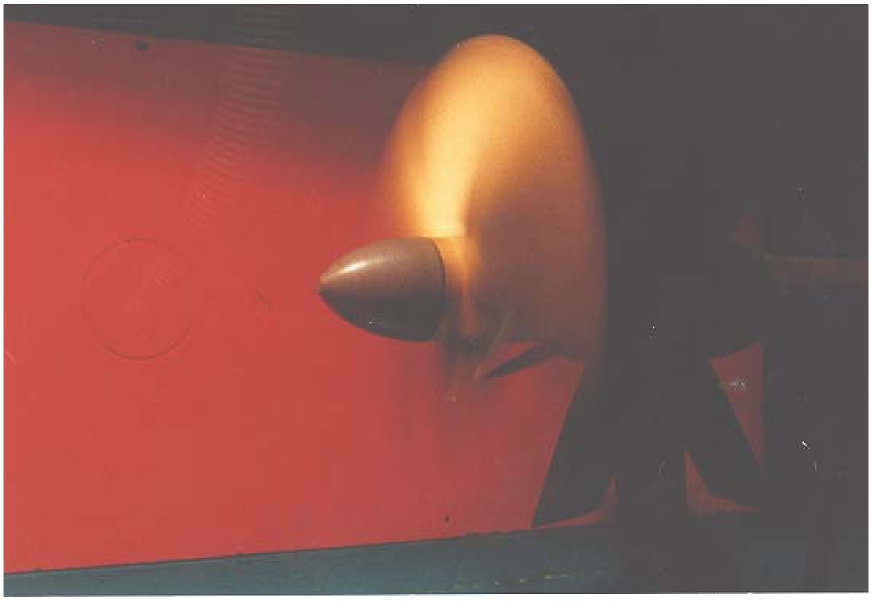

Figure 106: *Propeller and stator operating together. The hub vortex has been canceled.*

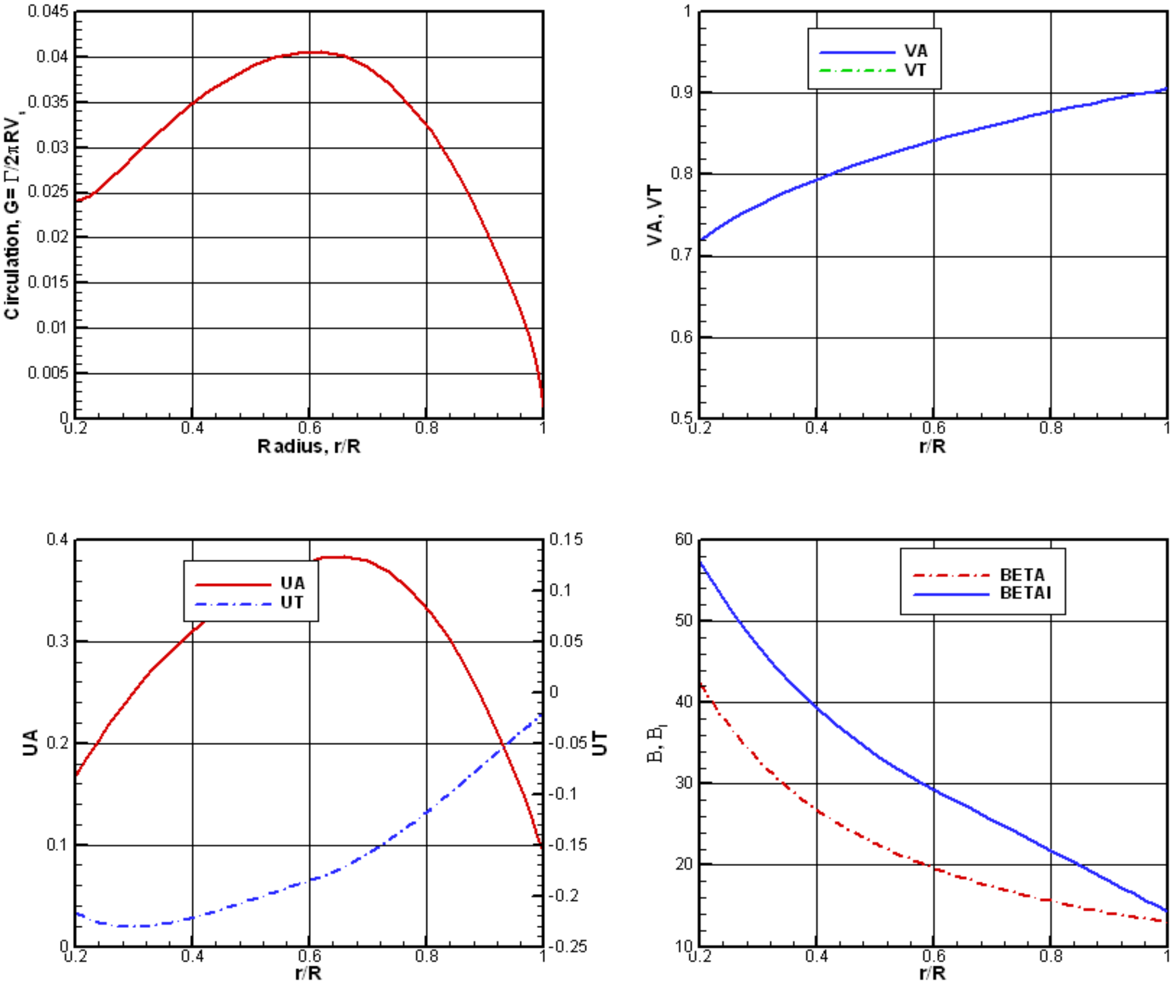

Figure 107: *Lifting line results for a 5 bladed propeller obtained with the* **PVL** *code. In this example, there is an image hub, and a Lerbs optimum circulation distribution has been modified to unload the tip, using* $HT = 1.0$. $C_T = 1.0$ $C_P = 1.4391$ $K_T = 0.2513$ $K_Q = 0.0461$ $V_a/V_s = 0.8526$ $\eta = 59.24\%$. *The efficiency has been further reduced due to tip unloading. Note the very different shape of the axial induced velocity distribution.*

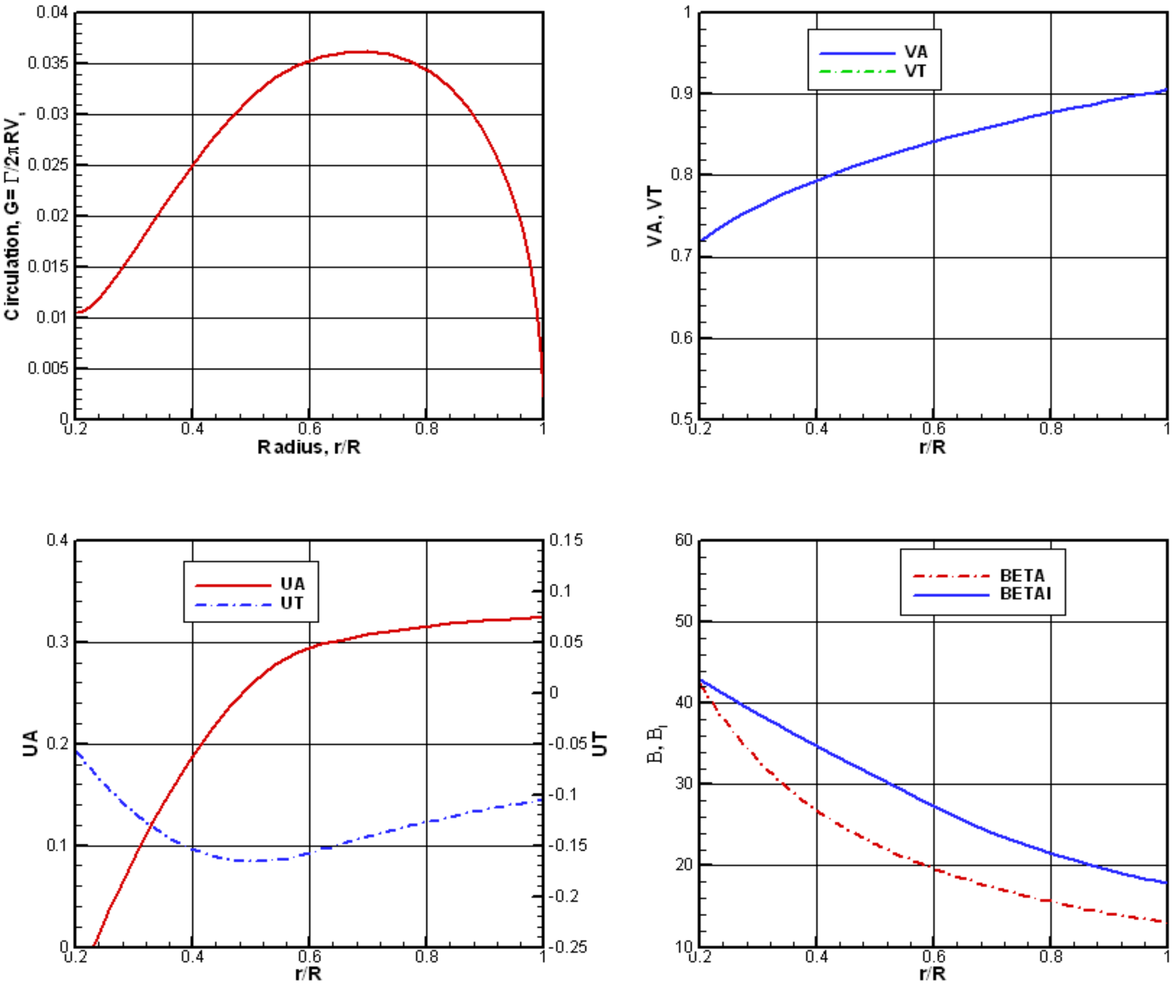

Figure 108: *Lifting line results for a 5 bladed propeller obtained with the* **PVL** *code. In this example, there is an image hub, and a Lerbs optimum circulation distribution has been modified to unload the hub, using* $HR = 1.0$. $C_T = 1.0$ $C_P = 1.3442$ $K_T = 0.2513$ $K_Q = 0.0431$ $V_a/V_s = 0.8526$ $\eta = 63.43\%$. *The efficiency has actually improved, since the reduced hub loading reduces the hub vortex drag.*

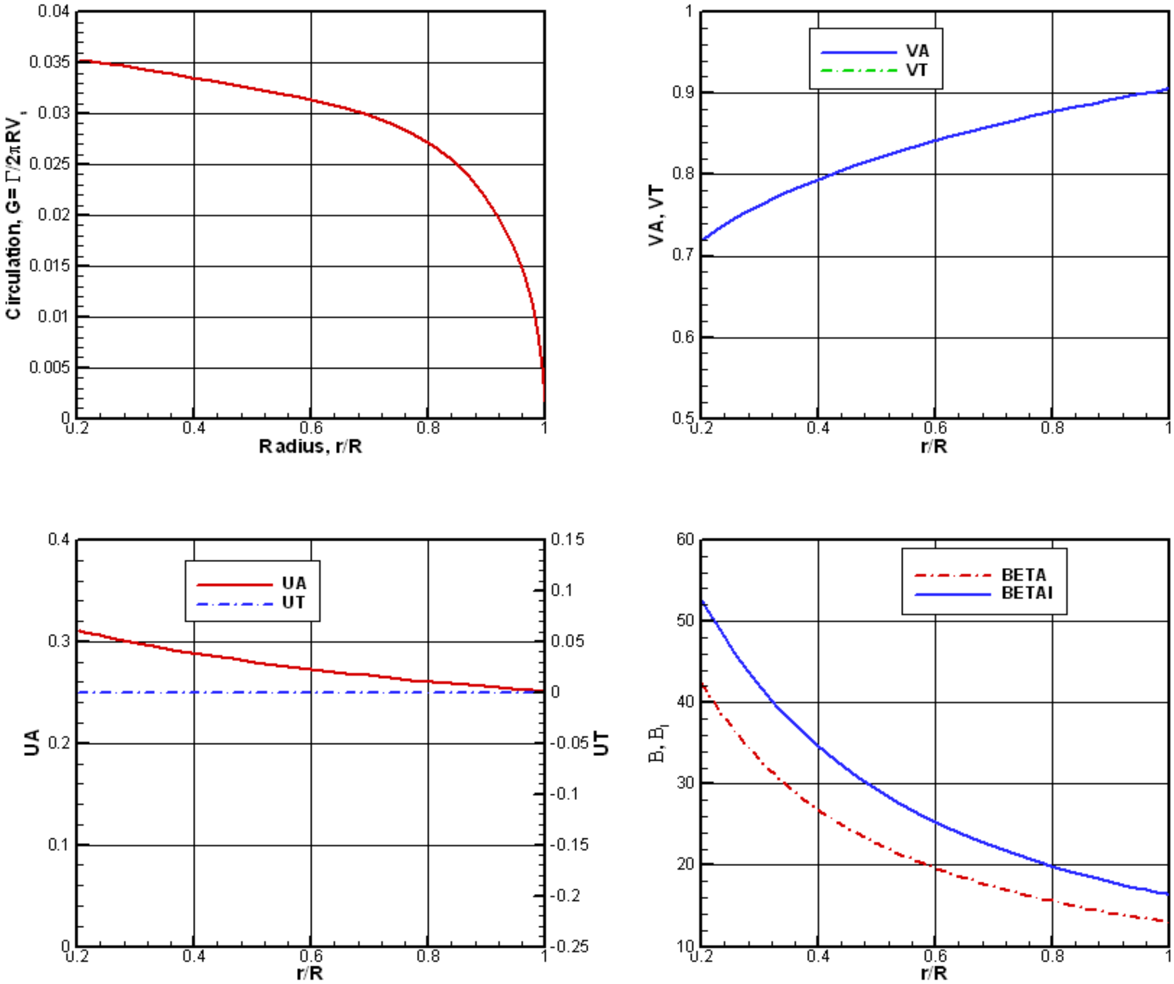

Figure 109: *Lifting line results for a 5 bladed propeller obtained with the* **PVL** *code. In this example, there is an image hub, and a Lerbs optimum circulation distribution has been specified. In addition, the idealized counter rotating propeller option has been selected, so that there are no tangential induced velocities. Note that the circulation near the hub has been greatly increased.* $C_T = 1.0$ $C_P = 1.2532$ $K_T = 0.2513$ $K_Q = 0.0401$ $V_a/V_s = 0.8526$ $\eta = 68.03\%$.

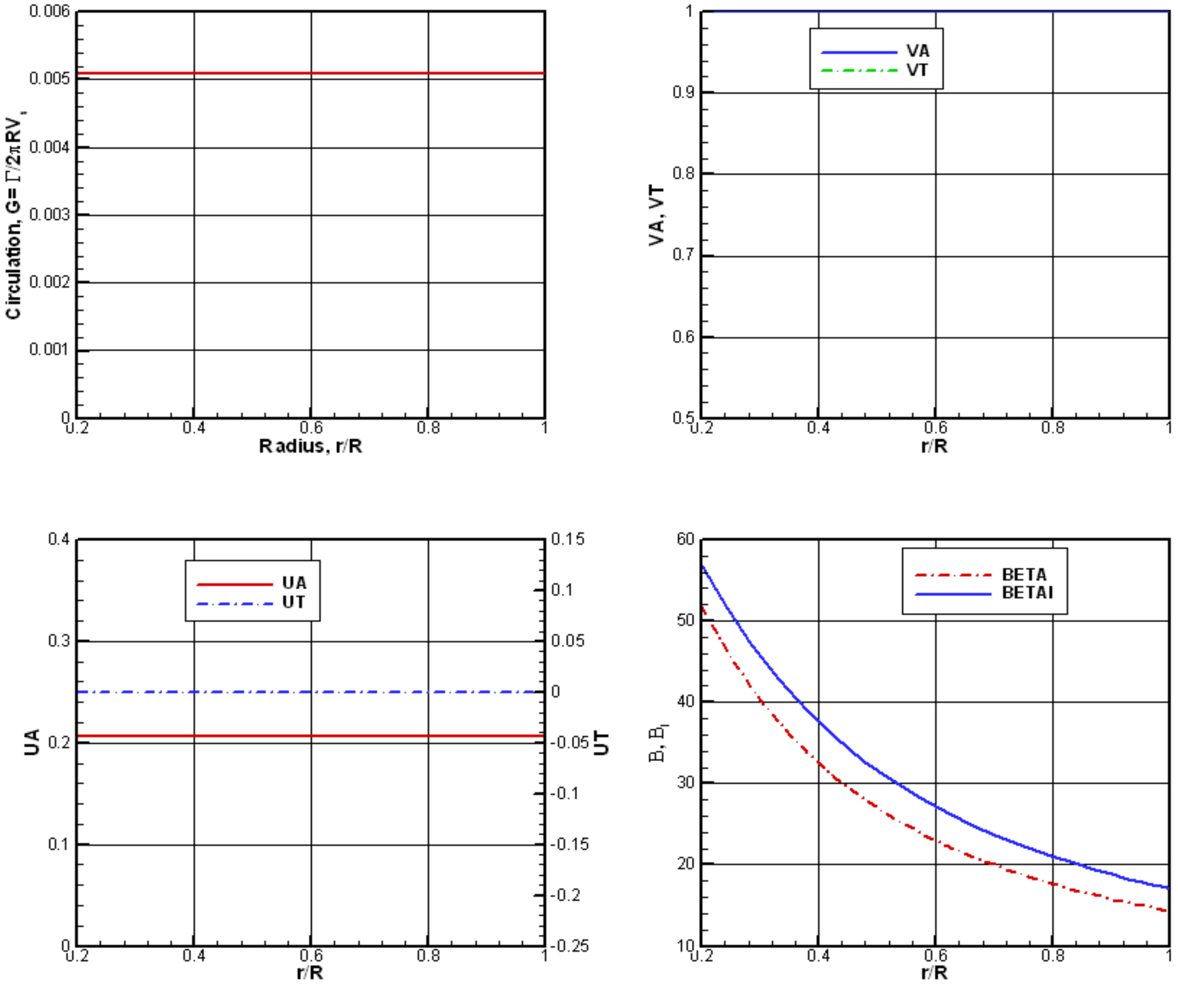

Figure 110: *Lifting line results for a 25 bladed propeller obtained with the* **PVL** *code. The induced velocities correspond to those of an infinite bladed propeller, and the tangential induced velocities have been canceled. Viscous drag has been set to zero. This, therefore, corresponds to an actuator disk.* $C_T = 1.0$ $C_P = 1.2071$ $K_T = 0.2513$ $K_Q = 0.0386$ $V_a/V_s = 1.000$ $\eta = 82.84\%$. *The circulation is a constant, with a value of* $G = 0.005093$ *and the axial induced velocity is* $u_a^*/V_a = 0.20711$, *which agrees exactly with actuator disk theory.*

4 COMPUTER CODE LISTINGS

```
      PROGRAM MAPSL
!-------------------------------------------------------------------------------
!     This program uses the Karman-Trefftz mapping function to compute the flow
!     field and pressure distribution around a foil section. The geometry of the
!     foil is determined by specifying the position of the center of the circle,
!     (XC,YC) and the trailing edge angle (TAU). The circulation is obtained by
!     satisfying the Kutta condition, but the user may override this value to
!     explore the effect on the local trailing edge flow. The output consists
!     of two TECPLOT formatted files. MAPSL.PLT is used to generate a field plot
!     showing the streamlines and pressure field. PLOTCP.PLT is used to generate
!     an x-y plot of the presure distribution on the foil surface.
!     WRITTEN BY: Justin E. Kerwin    December, 2000
!-------------------------------------------------------------------------------

!     Declare the variables-----------------------------------------------------
      IMPLICIT NONE
      CHARACTER*1 YESNO
      REAL, PARAMETER :: PI=3.1415927E00, RAD=1.7453293E-02
      REAL :: X,Y,THETA,RSQ,U,V,R,XC,YC,ALPHA_DEG,ALPHA,RC,BETA,RCSQ,G,GAMMA,   &
              LAMBDA,TAU_DEG,XI,ETA,X_CIRCLE,Y_CIRCLE,FL2,U_FOIL,V_FOIL,        &
              THETA1,THETA2,DTHETA,RMAX,DR,CP,XLE,XTE,CHORD,CL
      REAL, ALLOCATABLE, DIMENSION(:) :: XI_FOIL,CP_FOIL
      COMPLEX :: Z,ZP1,ZM1,ZETA,W_CIRCLE,DZETA_DZ,W_FOIL
      INTEGER :: N,M,NTHETA,NRADIAL

 !    Input the variables defining foil geometry and angle of attack -----------
      WRITE(*,'(A)') ' ENTER XC,YC   '   ! Position of center of circle---------
      READ(*,*) XC,YC                    ! Note: XC must be <= 0   -------------
      WRITE(*,'(A)') ' ENTER TRAILING EDGE ANGLE (DEG)   '
      READ(*,*) TAU_DEG
      LAMBDA=2.0-TAU_DEG/180.0     ! The exponent in the K-T mapping function --
      FL2=4.0*LAMBDA**2            ! Pre-comute a mapping function constant-----
      WRITE(*,'(A)') ' ENTER ALPHA (DEG)  ' ! Note: Enter 180 to get a circle---
      READ(*,*) ALPHA_DEG          ! User selected angle of attack.-------------
      ALPHA=ALPHA_DEG*RAD
      RCSQ=(1.0-XC)**2+YC**2       ! Radius of circle passing through (1,0) ----
      RC=SQRT(RCSQ)
      BETA=ATAN(YC/(1.0-XC))

!     Set circulation from Kutta condition, or override as desired -------------
      GAMMA=-4.0*PI*RC*SIN(BETA+ALPHA) ! Circulation required to satisfy Kutta--
      WRITE(*,'('' GAMMA FOR KUTTA CONDITION='',F12.7)') GAMMA
      WRITE(*,'(A)') ' ENTER "Y" TO ACCEPT, "N" TO OVERRIDE  '
      READ(*,'(A)') YESNO
      IF(YESNO/='Y'.AND.YESNO/='y') THEN
         WRITE(*,'(A)') ' ENTER DESIRED VALUE  '
         READ(*,*) GAMMA
      END IF
      G=GAMMA/(2.0*PI)

!----- Define grid parameters --------------------------------------------------
```

```
      WRITE(*,'(A)') ' ENTER THETA1,THETA2(DEG)  '   ! Angular extent of grid---
      READ(*,*) THETA1,THETA2
      WRITE(*,'(A)') ' ENTER DTHETA(DEG)   '         ! Angular resolution-------
      READ(*,*) DTHETA
      NTHETA=NINT((THETA2+THETA1)/DTHETA)+1        ! Number of radial grid lines
      WRITE(*,'(A)') ' ENTER MAXIMUM GRID RADIUS, RMAX   ' ! Radial extent of
      READ(*,*) RMAX                                       ! the grid-----------
      WRITE(*,'(A)') ' ENTER RADIAL SPACING, DR   '
      READ(*,*) DR                                   ! Radial resolution -------
      NRADIAL=NINT((RMAX-RC)/DR)+1

!     Alocate the arrays and open output files ---------------------------------
      ALLOCATE(XI_FOIL(NTHETA),CP_FOIL(NTHETA))      ! Arrays for foil Cp ------
      OPEN(1,FILE='MAPSL.PLT',STATUS='UNKNOWN',FORM='FORMATTED')  ! Output files
      WRITE(1,'(A)') ' VARIABLES = X,Y,U,V,CP '
      OPEN(2,FILE='PLOTCP.PLT',STATUS='UNKNOWN',FORM='FORMATTED')
      WRITE(2,'(A)') ' VARIABLES = X,CP '

!-----Generate velocity and presure field --------------------------------------
      WRITE(1,'('' ZONE   I='',I4,'' J='',I4)') NTHETA,NRADIAL
      DO M=1,NRADIAL

         R=RC+REAL(M-1)*DR   ! Grid radial coordinate in the Z (circle) plane---
         RSQ=R**2

         DO N=1,NTHETA

            THETA=RAD*(THETA1-REAL(N-1)*DTHETA)     ! Grid angular coordinate---
            X=XC+R*COS(THETA)                       ! Convert to cartesian------
            Y=YC+R*SIN(THETA)

!-----------Compute the velocity field around the circle------------------------
            U=COS(ALPHA)-RCSQ*COS(2.0*THETA-ALPHA)/RSQ-G*SIN(THETA)/R
            V=SIN(ALPHA)-RCSQ*SIN(2.0*THETA-ALPHA)/RSQ+G*COS(THETA)/R

!-----------Express the field point position and velocity in complex form-------
            Z=CMPLX(X,Y)                    ! Form complex number (X+iY)--------
            W_CIRCLE=CMPLX(U,-V)            ! Complex velocity in Z plane-------

!-----------Use the Karman-Trefftz transformation to map points to ZETA plane---
            ZP1=(Z+1.0)**LAMBDA
            ZM1=(Z-1.0)**LAMBDA
            ZETA=LAMBDA*(ZP1+ZM1)/(ZP1-ZM1)
            XI=REAL(ZETA)                   ! Transformed X coordinate----------
            ETA=AIMAG(ZETA)                 ! Transformed Y coordinate ---------

!-----------Compute the derivative of the mapping function; Transform velocities
            DZETA_DZ=FL2*((Z-1.0)**(LAMBDA-1.0)*(Z+1.0)**(LAMBDA-1.0))/         &
                    (ZP1-ZM1)**2
            IF(ABS(DZETA_DZ)>0.0001) THEN
               W_FOIL=W_CIRCLE/DZETA_DZ  ! Complex velocity in foil plane-------
```

```
            ELSE
               W_FOIL=0.0               ! Avoids divide by zero at trailing edge
            END IF
            U_FOIL=REAL(W_FOIL)
            V_FOIL=-AIMAG(W_FOIL)

!-----------Compute the presure coefficient, CP, and output to plotting file----
            CP=ABS(W_FOIL)**2-1.0
            WRITE(1,'(5F12.5)') XI,ETA,U_FOIL,V_FOIL,CP
            IF(M==1) THEN        ! Save presure on foil surface for later use---
               XI_FOIL(N)=XI
               CP_FOIL(N)=CP
            END IF
         END DO
      END DO

!-----Scale the chordwise coordinate to (0,1) and output foil pressure dist.----
      XLE=10.0
      XTE=-10.0
      DO N=1,NTHETA
         XLE=MIN(XLE,XI_FOIL(N))
         XTE=MAX(XTE,XI_FOIL(N))
      END DO
      CHORD=XTE-XLE
      DO N=1,NTHETA
         XI_FOIL(N)=(XI_FOIL(N)-XLE)/CHORD
      END DO

      WRITE(2,'(2F10.5)') (XI_FOIL(N),CP_FOIL(N),N=1,NTHETA)
      CLOSE(2)
      CL=-2.0*GAMMA/CHORD
      WRITE(*,'('' LIFT COEFFICIENT='',F8.4)') CL

!-----Generate coordinates of circle -------------------------------------------
      WRITE(1,'(A)') ' ZONE   I= 361, J=1 '
      DO M=1,361
         THETA=-BETA+REAL(M-1)*RAD
         X_CIRCLE=XC+RC*COS(THETA)
         Y_CIRCLE=YC+RC*SIN(THETA)
         Z=CMPLX(X_CIRCLE,Y_CIRCLE)
         ZP1=(Z+1.0)**LAMBDA
         ZM1=(Z-1.0)**LAMBDA
         ZETA=LAMBDA*(ZP1+ZM1)/(ZP1-ZM1)
         XI=REAL(ZETA)
         ETA=AIMAG(ZETA)
         WRITE(1,'(5F10.5)') XI,ETA,0.0,0.0,0.0
      END DO


      CLOSE(1)
      STOP
```

```
END PROGRAM MAPSL
```

```
!     Last change:  JEK   3 Mar 2001    3:50 pm
!-----------------------------------------------------------------------------
!                  Vortex/Source Lattice Program for 2-D Foils!
!-----------------------------------------------------------------------------
      PROGRAM VLM2D
      USE DUCKMOD    ! Module for spline interpolation and sim.eqn. solver -----
      USE GEOM       ! Module for mean line and thickness form geometry library-

!-----------------------------------------------------------------------------
!                          Declare the variables
      IMPLICIT NONE
      REAL, DIMENSION(:), ALLOCATABLE :: XV,XC,XT,YT,DYDX,DX,B,GAMMA,G,GEXACT,  &
                                         F,UT,UTVP,CPU,CPL
      REAL, DIMENSION(:,:), ALLOCATABLE :: A,CUBIC
      REAL :: DELC,TOP,CL,ALPHA,SUMG,CLNUM,TOC,RLE,QU,QL,FLH
      REAL, PARAMETER :: PI=3.141592653589793E00, HALF=0.5E00, RAD=PI/180.0,    &
                         ZERO=0.0E00, ONE=1.0E00, TWO=2.0E00, ESL=0.0, ESR=0.0
      INTEGER :: MC,N,M,IERR,MLTYPE,NTHICK
      INTEGER, DIMENSION(:), ALLOCATABLE :: IPIVOT

!-----Compute vortex and control point positions and weight functions-----------
      WRITE(*,'(A)') ' Enter number of panels '
      READ(*,*) MC ! MC can be as large as your computer memory permits --------
      ALLOCATE (XV(MC),XC(MC),A(MC,MC),DX(MC),B(MC),GAMMA(MC),IPIVOT(MC),G(MC), &
                GEXACT(MC),F(MC),XT(MC+1),YT(MC+1),DYDX(MC),UT(MC),UTVP(MC),    &
                CUBIC(MC-1,5),CPU(MC+1),CPL(MC+1))
      DELC=PI/REAL(MC)
      DO N=1,MC
         XV(N)=HALF*(ONE-COS((N-HALF)*DELC))  ! Vortex/source positions --------
         XC(N)=HALF*(ONE-COS(N*DELC))         ! Control point positions --------
         DX(N)=PI*SQRT(XV(N)*(ONE-XV(N)))/FLOAT(MC) ! Vortex weight factors ----
      END DO

!-----Compute influence coefficient matrix A(N,M) and invert -------------------
      TOP=ONE/(TWO*PI)
      DO N=1,MC
         DO M=1,MC
            A(N,M)=TOP/(XV(M)-XC(N))
         END DO
      END DO
      CALL FACTOR(A,IPIVOT,IERR)  ! FACTOR does LU decomposition of matrix A ---
      WRITE(*,'('' RETURN CODE FROM SUBROUTINE FACTOR (1 MEANS OK)='',I3)') IERR

!-----Solve for GAMMA(X) FOR NACA A=.8 or PARABOLIC meal line-------------------
      WRITE(*,'(A)') ' Enter ideal lift coefficient.... '
      READ(*,*) CL
      WRITE(*,'(A)') ' Enter Alpha-Alpha(ideal) (deg)..... '
      READ(*,*) ALPHA
      WRITE(*,'(A)') ' ENTER 1 FOR NACA A=.8, 2 FOR PARABOLA  '
      READ(*,*) MLTYPE
```

```
      IF (MLTYPE==1) CALL AEIGHT(XV,XC,B,F,GEXACT)
      IF (MLTYPE==2) CALL PARABL(XV,XC,B,F,GEXACT)
      DO N=1,MC
         B(N)=CL*B(N)-ALPHA*RAD ! RHS of equation. Slope of mean line -alpha ---
         F(N)=CL*F(N)           ! Mean line camber at desired ideal CL ---------
      END DO
      CALL SUBST(A,B,GAMMA,IPIVOT) ! Obtain solution of A matrix with RHS B ----

!-----Sum circulation over chord and convert to vortex sheet strength-----------
!     Note: These vortex strengths are the NEGATIVE of a strict RH rule notation
      SUMG=ZERO
      DO N=1,MC
         SUMG=SUMG+GAMMA(N)
         G(N)=GAMMA(N)/DX(N)
      END DO
      CLNUM=TWO*SUMG
      WRITE(*,'('' Computed total lift coefficient='',F8.4)') CLNUM

      OPEN(1,FILE='VLM2D.PLT',STATUS='UNKNOWN',FORM='FORMATTED')
      WRITE(1,'(A)') ' ZONE T=" Camber"'
      WRITE(1,'(2F10.5)') (XC(N),F(N),N=1,MC)
      WRITE(1,'(A)') ' ZONE T=" -Point Vortex Strengths"'
      WRITE(1,'(2F10.5)') (XV(N),GAMMA(N),N=1,MC)
      WRITE(1,'(A)') ' ZONE T=" -Vortex Sheet Strengths"'
      WRITE(1,'(2F10.5)') (XV(N),G(N),N=1,MC)

!-----Velocity due to thickness-----------------------------------------------
      XT(1)=0.0
      DO N=1,MC
         XT(N+1)=XC(N)
      END DO
      WRITE(*,'(A)') ' Enter 1 for NACA66, 2 for Karman-Trefftz...   '
      READ(*,*) NTHICK

      IF(NTHICK==1)Then
         WRITE(*,'(A)') ' Enter thickness/chord ratio... '
         READ(*,*) TOC
         CALL NACA66(TOC,RLE,XT,YT,XV,DYDX)
      ELSE
         CALL KARGEO(TOC,RLE,XT,YT,XV,DYDX)
      END IF
      WRITE(*,'('' T/C='',F10.5,'' R_L/C='',F10.5)') TOC,RLE
      WRITE(1,'(A)') ' ZONE T=" Thickness"'
      WRITE(1,'(2F10.5)') (XT(N),YT(N),N=1,MC+1)

!-----Compute the velocity induced by the thickness sources --------------------
      DO N=1,MC
         UT(N)=ZERO
         DO M=1,MC
            UT(N)=UT(N)+TOP*(YT(M+1)-YT(M))/(XC(N)-XV(M))
         END DO
```

```
      END DO
      WRITE(1,'(A)') ' ZONE T=" UT at control points" '
      WRITE(1,'(2F10.5)') (XC(N),UT(N),N=1,MC)

!-----Interpolate thickness velocity to vortex points --------------------------
      CALL UGLYDK(1,1,XC,UT,0.0,0.0,CUBIC)
      CALL EVALDK(XV,UTVP,CUBIC)
      WRITE(1,'(A)') ' ZONE T=" UT at vortex points"'
      WRITE(1,'(2F10.5)') (XV(N),UTVP(N),N=1,MC)

!-----Compute surface velocities:First get value at leading edge----------------
      QU=ALPHA*RAD*SQRT(TWO/RLE)
      CPU(1)=QU**2-ONE
      CPL(1)=CPU(1)
!-----Next get remaining values over the chord----------------------------------
      DO N=1,MC
         IF(DYDX(N)>0.0) THEN
            FLH=1.0/SQRT(1.0+DYDX(N)**2)  ! Scherer/Riegels modified Lighthill--
         ELSE
            FLH=1.0   ! No leading edge correction beyond point of max thickness
         END IF
         QU=(ONE+UT(N)+HALF*G(N))*FLH
         CPU(N+1)=QU**2-ONE
         QL=(ONE+UT(N)-HALF*G(N))*FLH
         CPL(N+1)=QL**2-ONE
      END DO

      WRITE(1,'(A)') ' ZONE T= -Cp upper surface"'
      WRITE(1,'(2F10.5)') ZERO,CPU(1)
      WRITE(1,'(2F10.5)') (XV(N),CPU(N+1),N=1,MC)
      WRITE(1,'(A)') ' ZONE T=" -Cp lower surface"  '
      WRITE(1,'(2F10.5)') ZERO,CPL(1)
      WRITE(1,'(2F10.5)') (XV(N),CPL(N+1),N=1,MC)
      CLOSE(1)

      STOP
      END PROGRAM VLM2D
```

```
!     Last change:  JEK   3 Mar 2001    1:42 pm
      MODULE GEOM
         INTERFACE AEIGHT
            SUBROUTINE AEIGHT(XV,XC,B,F,GEXACT)
               REAL, DIMENSION(:), INTENT(IN) :: XV,XC
               REAL, DIMENSION(:), INTENT(OUT) :: B,F,GEXACT
            END SUBROUTINE AEIGHT
         END INTERFACE

         INTERFACE PARABL
            SUBROUTINE PARABL(XV,XC,B,F,GEXACT)
               REAL, DIMENSION(:), INTENT(IN) :: XV,XC
               REAL, DIMENSION(:), INTENT(OUT) :: B,F,GEXACT
            END SUBROUTINE PARABL
         END INTERFACE

         INTERFACE NACA66
            SUBROUTINE NACA66(THK,RLE,XT,YT,XV,DYDX)
               REAL, INTENT(IN) :: THK           ! Section thickness/chord ratio
               REAL, INTENT(OUT) :: RLE              ! Leading edge radius/chord
               REAL, DIMENSION(:), INTENT(IN) :: XT,XV     ! Chordwise positions
               REAL, DIMENSION(:), INTENT(OUT) :: YT,DYDX  ! thickness and slope
            END SUBROUTINE NACA66
         END INTERFACE

         INTERFACE KARGEO
            SUBROUTINE KARGEO(THK,RLE,XT,YT,XV,DYDX)
               REAL, INTENT(OUT) :: THK          ! Section thickness/chord ratio
               REAL, INTENT(OUT) :: RLE              ! Leading edge radius/chord
               REAL, DIMENSION(:), INTENT(IN) :: XT,XV     ! Chordwise positions
               REAL, DIMENSION(:), INTENT(OUT) :: YT,DYDX  ! Thickness and slope
            END SUBROUTINE KARGEO
        END INTERFACE

      END MODULE GEOM

!-------------------------------------------------------------------------------

      SUBROUTINE AEIGHT(XV,XC,B,F,GEXACT)
      IMPLICIT NONE
      REAL, DIMENSION(:), INTENT(IN) :: XV,XC
      REAL, DIMENSION(:), INTENT(OUT) :: B,F,GEXACT

      REAL, PARAMETER ::  PI=3.141592653589793E00, ONE=1.0E00, TWO=2.0E00,      &
                          A=0.8E00, HALF=0.5E00, QUART=0.25E00
      REAL :: G,H,AIDEAL,CONST,G1,C1,CA,P,R,S,T
      INTEGER :: N,MC

      MC=SIZE(XV)
      G=-(A**2*(HALF*ALOG(A)-QUART)+QUART)/(ONE-A)
```

```
H=(HALF*(ONE-A)**2*ALOG(ONE-A)-QUART*(ONE-A)**2)/(ONE-A)+G
AIDEAL=-H/(TWO*PI*(A+ONE))
CONST=TWO*PI*(A+ONE)
G1=ONE/(ONE+A)
DO N=1,MC
   C1=MAX(ONE-XV(N),1.0E-06)
   CA=A-XV(N)
   IF(ABS(CA)<1.0E-06) CA=CA+1.0E-05
   P=HALF*CA**2*LOG(ABS(CA))-HALF*C1**2*LOG(C1)+QUART*(C1**2-CA**2)
   F(N)=(P/(ONE-A)-XV(N)*LOG(XV(N))+G-H*XV(N))/CONST+C1*AIDEAL
   IF(XV(N)<=A) THEN
      GEXACT(N)=G1
   ELSE
      GEXACT(N)=G1*(ONE-XV(N))/(ONE-A)
   END IF
END DO

DO N=1,MC
   C1=MAX(ONE-XC(N),1.0E-06)
   CA=A-XC(N)
   IF(ABS(CA)<1.0E-06) CA=CA+1.0E-05
   R=-(A-XC(N))*LOG(ABS(CA))-HALF*CA+C1*LOG(C1)+HALF*C1
   S=-HALF*C1+HALF*CA
   T=-LOG(XC(N))-ONE-H
   B(N)=((R+S)/(ONE-A)+T)/CONST-AIDEAL
END DO

RETURN
END

SUBROUTINE PARABL(XV,XC,B,F,GEXACT)
IMPLICIT NONE
REAL, DIMENSION(:), INTENT(IN) :: XV,XC
REAL, DIMENSION(:), INTENT(OUT) :: B,F,GEXACT

REAL, PARAMETER ::  PI=3.141592653589793E00
INTEGER :: N,MC

MC=SIZE(XV)
DO N=1,MC
   B(N)=(1.0 -2.0*XC(N))/PI
   F(N)=XV(N)*(1.0-XV(N))/PI
   GEXACT(N)=4.0*SQRT(XV(N)*(1.0-XV(N)))/PI
END DO

RETURN
END


SUBROUTINE NACA66(THK,RLE,XT,YT,XV,DYDX)
USE DUCKMOD
```

```
      IMPLICIT NONE
      REAL, INTENT(IN) :: THK                        ! Section thickness/chord ratio
      REAL, INTENT(OUT) :: RLE                       ! Leading edge radius/chord
      REAL, DIMENSION(:), INTENT(IN) :: XT,XV    ! Arrays of chordwise positions
      REAL, DIMENSION(:), INTENT(OUT) :: YT,DYDX ! Section thickness and slope

!----- Database of thickness (T66) versus position (PC) for the DTMB MOD NACA66-
      REAL, DIMENSION(18), PARAMETER ::  PC=(/0.0000,0.0100,0.0250,0.0500,      &
                                             0.1000,0.2000,0.3000,0.4000,      &
                                             0.4500,0.5000,0.6000,0.7000,      &
                                             0.8000,0.9000,0.9500,0.9750,      &
                                             0.9900,1.0000/)

      REAL, DIMENSION(18), PARAMETER :: T66=(/0.0000,0.1870,0.2932,0.4132,      &
                                             0.5814,0.8000,0.9274,0.9904,      &
                                             1.0000,0.9917,0.9256,0.7934,      &
                                             0.5950,0.3306,0.1736,0.0888,      &
                                             0.0360,0.0000/)

      REAL, PARAMETER :: RLE_CONST=0.448
      REAL :: TRLE,XSQ,YSPLN,DY,D2YDX
      REAL, DIMENSION(18) :: PSQ
      REAL, DIMENSION(17,5) :: CUBIC
      INTEGER :: NT,N

      NT=SIZE(XT)
      RLE=RLE_CONST*THK**2
!-----Square root stretched coordinate for spline interpolation ----------------
      PSQ=SQRT(PC)
!-----Get spline coefficients of thickness with LE radius prescribed -----------
      TRLE=2.0*SQRT(2.0*RLE_CONST)
      CALL UGLYDK(2,1,PSQ,T66,TRLE,0.0,CUBIC)

!-----Evaluate spline for thickness at XT positions-----------------------------
      DO N=1,NT
         XSQ=SQRT(XT(N))
         CALL EVALDK(XSQ,YSPLN,CUBIC)
         YT(N)=THK*YSPLN
      END DO

!-----Evaluate derivative of spline to get DY/DX = 0.5*DT/DX at XV(N)-----------
      DO N=1,NT-1
         XSQ=SQRT(XV(N))
         CALL DRIVDK(XSQ,DY,D2YDX,CUBIC) ! Derivative Dy/D(xsq) ----------------
         DYDX(N)=DY*THK/(4.0*XSQ)        ! Transform to Dy/Dx   ----------------
      END DO

      RETURN
      END SUBROUTINE NACA66

      SUBROUTINE KARGEO(THK,RLE,XT,YT,XV,DYDX)
```

```
!-------------------------------------------------------------------------------
!     Evaluates thickness and it's derivative for a Karman Trefftz thickness
!     form from a MAPSL.PLT file.
!-------------------------------------------------------------------------------
      USE DUCKMOD           ! Access module for spline interpolation subroutines
      IMPLICIT NONE
!     Declaring the arguments---------------------------------------------------
      REAL, INTENT(OUT) :: THK                  ! Section thickness/chord ratio
      REAL, INTENT(OUT) :: RLE                  ! Leading edge radius/chord
      REAL, DIMENSION(:), INTENT(IN) :: XT,XV    ! Arrays of chordwise positions
      REAL, DIMENSION(:), INTENT(OUT) :: YT,DYDX ! Section thickness and slope

!     Declaring and alocating the local variables-------------------------------
      CHARACTER*64 :: FNAME,LINES
      REAL :: XSQ,YSPLN,XLE,CHORD,DY,D2YDX
      REAL, DIMENSION(:), ALLOCATABLE :: PSQ,XIN,YIN,YTK
      REAL, DIMENSION(:,:), ALLOCATABLE  :: CUBIC
      INTEGER :: NT,N
      INTEGER, PARAMETER:: NPI=181 ! No.of points from TE to LE from MAPSL -----
      NT=SIZE(XT)
      ALLOCATE(PSQ(NPI),XIN(NPI),YIN(NPI),YTK(NPI),CUBIC(NPI-1,5))

!     Read in MAPSL.PLT file to obtain coordinates of the K-T section-----------
      WRITE(*,'(A)') ' ENTER NAME OF MAPSL OUTPUT FILE....  '
      READ(*,'(A)') FNAME
      OPEN(2,FILE=FNAME,STATUS='OLD',FORM='FORMATTED')
      READ(2,'(A)') LINES   ! Flush through first to lines to get past first----
      READ(2,'(A)') LINES   ! occurence of the character string "ZONE" ---------
      DO
         READ(2,'(A)') LINES
         IF(LINES(2:2)=='Z') EXIT  ! Look for second occurence of "ZONE" -------
      END DO

      DO N=1,NPI   ! Here is the data that we want -----------------------------
         READ(2,*) XIN(N),YIN(N)
      END DO
      CLOSE(2)

      XLE=XIN(NPI)  ! Find the x coordinates of the LE and TE to scale the data-
      CHORD=XIN(1)-XIN(NPI)
      THK=0.0
      DO N=1,NPI
         PSQ(N)=SQRT((XIN(NPI-N+1)-XLE)/CHORD)  ! Trans. coordinate for spline -
         YTK(N)=2.0*YIN(NPI-N+1)/CHORD  ! Scaled to give t/c=2y/c --------------
         THK=MAX(THK,YTK(N)) ! Searching for the maximum thickness/chord ratio--
      END DO

      CALL UGLYDK(1,1,PSQ,YTK,0.0,0.0,CUBIC)    ! Get spline coefficients ------

!-----Evaluate spline for total thickness, YT(N), at XT(N) ---------------------
      DO N=1,NT
```

```
         XSQ=SQRT(XT(N))
         CALL EVALDK(XSQ,YSPLN,CUBIC)
         YT(N)=YSPLN
      END DO

!-----Evaluate derivative of spline to get DY/DX = 0.5*DT/DX at XV(N)-----------
      DO N=1,NT-1
         XSQ=SQRT(XV(N))
         CALL DRIVDK(XSQ,DY,D2YDX,CUBIC) ! Derivative Dy/D(xsq) ----------------
         DYDX(N)=DY/(4.0*XSQ)            ! Transform to Dy/Dx   ----------------
      END DO

      CALL DRIVDK(0.0,DY,D2YDX,CUBIC) ! Derivative Dy/D(xsq) at leading edge----
      RLE=0.125*DY**2    ! Leading edge radius obtained from square of deriv. --

      RETURN
      END SUBROUTINE KARGEO
```

```
!     Last change:  JEK  20 Mar 2001    1:39 pm
      PROGRAM HVLL
!-----------------------------------------------------------------------------
!                HYDROFOIL VORTEX LATTICE LIFTING LINE PROGRAM
!                  Written by: Justin E. Kerwin, March 2001
!-----------------------------------------------------------------------------
      USE DUCKMOD ! Contains interface to simultaneous equations routines ------
      IMPLICIT NONE
      REAL, PARAMETER :: PI=3.1415927E00
      REAL, DIMENSION(:), ALLOCATABLE :: A,YV,YC,GAMMA,WE,WN,GN
      REAL, DIMENSION(:,:), ALLOCATABLE :: WNM
      INTEGER, DIMENSION(:), ALLOCATABLE :: IPIVOT
      REAL :: DELTIP,DEL,ANG,S1,AJSN,FZE,FXE,FRE,FZN,FXN,FRN,FZGN,FXGN,FRGN,    &
              PERLG,PERLW,PERDG,PERDW,PEREG,PEREW
      INTEGER :: MT,KCOS,KMP,NG,N,J,IERR,M

!------------------------- Inputs ---------------------------------------------
      WRITE(*,'(A)') ' Enter number of panels ....  '
      READ(*,*) MT
      WRITE(*,'(A)') ' Enter 1 for const. spacing, 2 for cosine... '
      READ(*,*) KCOS
      IF(KCOS==1) THEN
         WRITE(*,'(A)') ' Enter tip vortex inset/panel width... '
         READ(*,*) DELTIP
         KMP=2
      END IF
      IF(KCOS==2) THEN
         WRITE(*,'(A)') ' Enter 1 for cos control pts, 2 for midpt... '
         READ(*,*) KMP
      END IF
      WRITE(*,'(A)') ' Enter number of Gamma coefficients... '
      READ(*,*) NG
      ALLOCATE(A(NG))
      WRITE(*,'(A)') ' Enter Gamma coefficients....  '
      READ(*,*) A

!---------------- Generate the vortex lattice --------------------------------
      ALLOCATE(YV(MT+1),YC(MT),GAMMA(MT),WE(MT),WNM(MT,MT),WN(MT),GN(MT),       &
               IPIVOT(MT))
      IF(KCOS==1) DEL=1.0/(REAL(MT)+2.0*DELTIP)  ! Panel spacing----------------
      IF(KCOS==2) DEL=PI/REAL(2*MT)
      DO N=1,MT+1   ! Get free vortex positions, YV(N) -------------------------
         IF(KCOS==1) YV(N)=-0.5+(DELTIP+REAL(N-1))*DEL
         IF(KCOS==2) YV(N)=-0.5*COS(2.0*REAL(N-1)*DEL)
      END DO

      DO N=1,MT   ! Get control point positions, YC(N) -------------------------
         IF(KCOS==1.OR.KMP==2) THEN
            YC(N)=0.5*(YV(N)+YV(N+1))
            ANG=ACOS(-2.0*YC(N))
         ELSE
```

```
            ANG=REAL(2*N-1)*DEL
            YC(N)=-0.5*COS(ANG)
         END IF

! Compute exact circulation, GAMMA and exact downwash, WE, from Glauert coeffs--
         S1=SIN(ANG)
         GAMMA(N)=2.0*A(1)*S1
         WE(N)=-A(1)
         IF(NG>=2) THEN
            DO J=2,NG
               AJSN=A(J)*SIN(REAL(J)*ANG)
               GAMMA(N)=GAMMA(N)+2.0*AJSN
               WE(N)=WE(N)-REAL(J)*AJSN/S1
            END DO
         END IF
      END DO

! Compute the exact lift, drag and drag/lift**2 from Glauert -------------------
      FZE=0.5*PI*A(1)
      FXE=0.5*PI*A(1)**2
      IF(NG>=2) THEN
         DO J=2,NG
            FXE=FXE+0.5*PI*REAL(J)*A(J)**2
         END DO
      END IF
      FRE=FXE/FZE**2
      WRITE(*,'('' FZE,FXE,FRE... '',3F10.5)') FZE,FXE,FRE

!-----Compute vortex lattice horseshoe influence functions WNM(N,M) and the ----
!-----resulting downwash, WN(N) based on the exact circulation, GAMMA ----------
      FZN=0.0
      FXN=0.0
      DO N=1,MT
         WN(N)=0.0
         DO M=1,MT
            WNM(N,M)=1.0/(4.0*PI*(YV(M)-YC(N)))-1.0/(4.0*PI*(YV(M+1)-YC(N)))
            WN(N)=WN(N)+GAMMA(M)*WNM(N,M)
         END DO
         FZN=FZN+GAMMA(N)*(YV(N+1)-YV(N))       ! Numerical lift force ---------
         FXN=FXN-WN(N)*GAMMA(N)*(YV(N+1)-YV(N)) ! Numerical drag force ---------
      END DO
      FRN=FXN/FZN**2

!-----Solve for the vortex lattice circulation, GN, based on the exact downwash,
!----- WE, using the simultaneous equation solver FACTOR and SUBST -------------
      CALL FACTOR(WNM,IPIVOT,IERR)
      WRITE(*,'('' RETURN CODE FROM FACTOR (1=OK)='',I4)') IERR
      CALL SUBST(WNM,WE,GN,IPIVOT)
      WRITE(*,'(6F10.5)') (YV(N),YC(N),GAMMA(N),WE(N),WN(N),GN(N),N=1,MT)
      WRITE(*,'(F10.5)') YV(MT+1)
```

```
!-----Get the forces based on the vortex lattice circulation and exact downwash-
      FZGN=0.0
      FXGN=0.0
      DO N=1,MT
         FZGN=FZGN+GN(N)*(YV(N+1)-YV(N))
         FXGN=FXGN-WE(N)*GN(N)*(YV(N+1)-YV(N))
      END DO
      FRGN=FXGN/FZGN**2


!-----Compute the percent errors in forces obtained by both methods ------------
      PERLG=100.0*(FZGN-FZE)/FZE
      PERLW=100.0*(FZN-FZE)/FZE
      PERDG=100.0*(FXGN-FXE)/FXE
      PERDW=100.0*(FXN-FXE)/FXE
      PEREG=100.0*(FRGN-FRE)/FRE
      PEREW=100.0*(FRN-FRE)/FRE

!-----Output TECPLOT file HVLL.PLT containing spanwise distributions for plotting
      OPEN(1,FILE='HVLL.PLT',STATUS='UNKNOWN',FORM='FORMATTED')
      WRITE(1,'(A)') ' VARIABLES=YC,W-EXACT,W-NUM,G-EXACT,G-NUM '
      WRITE(1,'(5F10.5)') (YC(N),WE(N),WN(N),GAMMA(N),GN(N),N=1,MT)
      CLOSE(1)

!-----Output a LATEX file containing the percent errors in forces. Note that this
!----- file appends current results to all previous data stored in HVLL.TEX ----
      OPEN(2,FILE='HVLL.TEX',STATUS='UNKNOWN',FORM='FORMATTED',POSITION='APPEND')
      WRITE(2,'(I8,6F8.1)') MT,PERLW,PERDW,PEREW,PERLG,PERDG,PEREG
      CLOSE(2)
      STOP
      END PROGRAM
```

```
!     Last change:  JEK  30 Apr 2001    5:48 pm
      PROGRAM PVL
!-------------------------------------------------------------------------------
!                  Propeller Vortex Lattice Lifting Line Code
!                    COPYRIGHT (C) 2001  JUSTIN E. KERWIN -------------------------------------------
      USE PVLMOD
      USE DUCKMOD
!------------------------- Declare the Variables -------------------------------
      IMPLICIT NONE
      CHARACTER*36 :: FNAME,LABEL
      CHARACTER*72 :: TITLE
      INTEGER :: MT,NX,ITER,NBLADE,N,M,KTRY,IERR,IHUB
      REAL :: KT,KQ,DEL,HRR,RCWG,RM,DTANB,EDISK,ADVCO,CTDES,HR,HT,CRP,WAKE,    &
              CQ,CP,EFFY,HRF,CTH,RHV
      REAL, PARAMETER :: PI=3.1415927E00, TOL=0.000005, R2D=57.29578E00
      DOUBLE PRECISION :: TANBIW,RCW,RVW,UAIF,UTIF
      REAL, DIMENSION(:), ALLOCATABLE :: XR,XCHD,XCD,XVA,XVT,XRC,RV,TANBV,RC,  &
                                         TANBC,VAV,VTV,VAC,VTC,TANBIV,TANBIC,  &
                                         UAW,UTW,B,G,UASTAR,UTSTAR,T,CT,       &
                                         TANBXV,TANBXC,VBAV,VBAC,CD,CDC
      REAL, DIMENSION(:,:), ALLOCATABLE :: CHCUB,CDCUB,VACUB,VTCUB,UAHIF,      &
                                           UTHIF,A

!------------------ Start reading the input data -------------------------------
      WRITE(*,'(A)') ' ENTER INPUT FILE NAME.....    '
      READ(*,'(A)') FNAME
      OPEN(2,FILE=FNAME,STATUS='OLD',FORM='FORMATTED')
      READ(2,'(A)') TITLE  ! Title describing data file
      READ(2,*) MT   ! Number of vortex lattice panels
      READ(2,*) ITER ! Number of iterations to align wake
      READ(2,*) IHUB ! Hub image flag. IHUB=0 : No hub image, IHUB=1 : Image hub
      READ(2,*) RHV  ! Hub vortex radius/Hub radius. Only used if IHUB=1
      READ(2,*) NX   ! Number of radii used to specify the input data

!------------- Allocate all the arrays before reading rest of input-------------
      ALLOCATE ( XR(NX),XCHD(NX),XCD(NX),XVA(NX),XVT(NX),XRC(NX) )
      ALLOCATE ( CHCUB(NX-1,5),CDCUB(NX-1,5),VACUB(NX-1,5),VTCUB(NX-1,5) )
      ALLOCATE ( RV(MT+1),TANBV(MT+1),RC(MT),TANBC(MT),VAV(MT+1),VTV(MT+1),    &
                 VAC(MT),VTC(MT),TANBIV(MT+1),TANBIC(MT),UAW(MT+1),UTW(MT+1),  &
                 UAHIF(MT,MT),UTHIF(MT,MT),A(MT,MT),B(MT),G(MT),UASTAR(MT),    &
                 UTSTAR(MT),T(ITER),CT(ITER),TANBXV(MT+1),TANBXC(MT),          &
                 VBAV(MT+1),VBAC(MT),CD(MT),CDC(MT) )

!----------------All arrays allocated. read in rest of input data --------------
      READ(2,*) NBLADE     ! Number of blades
      READ(2,*) ADVCO      ! Advance coefficient based on ship speed
      READ(2,*) CTDES      ! Desires thrust coefficient CT (based on ship speed)
      READ(2,*) HR         ! Unloading ratio at hub
      READ(2,*) HT         ! Unloading ratio at tip
      READ(2,*) CRP        ! Tangential velocity cancellation factor
      READ(2,'(A)') LABEL  ! Alphanumeric label for output
```

```
!-------------------------------------------------------------------------------
!     XR=Input radii r/R, XCHD=Input chord length c/D, XCD=Input viscous drag
!     coefficient, Cd or Lift/Drag ratio, XVA,XVT=Input axial and tangential
!     velocities, Va/Vs, V_t/Vs
!-------------------------------------------------------------------------------
      READ(2,*) (XR(N),XCHD(N),XCD(N),XVA(N),XVT(N),N=1,NX)
      CLOSE(2)

!-----Compute volumetric mean inflow velocity ratio VA/VS ----------------------
      WAKE=VOLWK(XR,XVA)

!-----Spline chord over radius using square root stretched coordinates----------
      XRC(:)=1.0-SQRT(1.0-XR(:))
      CALL UGLYDK(0,0,XRC,XCHD,0.0,0.0,CHCUB)

!-----Spline Drag Coefficient Cd, Inflow Vx, Vt using radial coordinate directly
      CALL UGLYDK(0,0,XR,XCD,0.0,0.0,CDCUB)
      CALL UGLYDK(0,0,XR,XVA,0.0,0.0,VACUB)
      CALL UGLYDK(0,0,XR,XVT,0.0,0.0,VTCUB)

!-----Compute cosine spaced vortex radii and get Va,Vt,tanB,Vt*tanB/Va----------
      DEL=PI/(2.0*REAL(MT))
      HRR=0.5*(XR(NX)-XR(1))
      DO M=1,MT+1
         RV(M)=XR(1)+HRR*(1.0-COS(REAL(2*(M-1))*DEL))
         CALL EVALDK(RV(M),VAV(M),VACUB)
         CALL EVALDK(RV(M),VTV(M),VTCUB)
         TANBV(M)=VAV(M)/((PI*RV(M)/ADVCO)+VTV(M))
         VBAV(M)=VTV(M)*TANBV(M)/VAV(M)
      END DO

!-----Cosine spaced control point radii: Evaluate c/D,Va,Vt,tanB,Cd,Vt*tanB/Va -
      DO M=1,MT
         RC(M)=XR(1)+HRR*(1.0-COS(REAL(2*M-1)*DEL))
         RCWG=1.0-SQRT(1.0-RC(M))
         CALL EVALDK(RCWG,CDC(M),CHCUB)
         CALL EVALDK(RC(M),VAC(M),VACUB)
         CALL EVALDK(RC(M),VTC(M),VTCUB)
         TANBC(M)=VAC(M)/((PI*RC(M)/ADVCO)+VTC(M))
         CALL EVALDK(RC(M),CD(M),CDCUB)
         VBAC(M)=VTC(M)*TANBC(M)/VAC(M)
      END DO

!-----First estimate of tanBi based on 90 percent of actuator disk efficiency --
      EDISK=1.8/(1.0+SQRT(1.0+CTDES/WAKE**2))
      TANBXV(:)=TANBV(:)*SQRT(WAKE/(VAV(:)-VBAV(:)))/EDISK  ! Lerbs optimum-----
      TANBXC(:)=TANBC(:)*SQRT(WAKE/(VAC(:)-VBAC(:)))/EDISK

!-----Unload hub and tip as specified by input HR and HT -----------------------
      RM=0.5*(XR(1)+XR(NX))  ! Mid-radius. Unloading is quadratic, starting here
      DO M=1,MT+1
```

```
         IF(RV(M).LT.RM) THEN
            HRF=HR
         ELSE
            HRF=HT
         END IF
         DTANB=HRF*(TANBXV(M)-TANBV(M))*((RV(M)-RM)/(XR(1)-RM))**2
         TANBXV(M)=TANBXV(M)-DTANB
      END DO

      DO M=1,MT
         IF(RC(M).LT.RM) THEN
            HRF=HR
         ELSE
            HRF=HT
         END IF
         DTANB=HRF*(TANBXC(M)-TANBC(M))*((RC(M)-RM)/(XR(1)-RM))**2
         TANBXC(M)=TANBXC(M)-DTANB
      END DO

!-------------------------------------------------------------------------------
!     Iterations to scale tanBi to get desired value of thrust coefficient
!-------------------------------------------------------------------------------

      DO KTRY=1,ITER
         IF(KTRY.EQ.1) THEN
            T(KTRY)=1.0    ! T(KTRY) is the scale factor to apply to tanBi
         ELSE IF(KTRY.EQ.2) THEN
            T(KTRY)=1.0+(CTDES-CT(1))/(5.0*CTDES) ! Guess for second iteration
         ELSE IF(KTRY.GT.2) THEN
            T(KTRY)=T(KTRY-1)+(T(KTRY-1)-T(KTRY-2))*(CTDES-CT(KTRY-1))/        &
                    (CT(KTRY-1)-CT(KTRY-2))  ! Secant method for remaining iters
         END IF

            TANBIV(:)=T(KTRY)*TANBXV(:)    ! Scale tanBi at the vortex radii
            TANBIC(:)=T(KTRY)*TANBXC(:)    ! Scale tanbi at the control points

!-------------------------------------------------------------------------------
!        Compute axial and tangential horseshoe influence coefficients        !
!-------------------------------------------------------------------------------

         DO M=1,MT
            RCW=RC(M)
            DO N=1,MT+1
!--------------Induction of trailing vortices shed at RV(N)---------------------
               TANBIW=TANBIV(N)
               RVW=RV(N)
               CALL WRENCH(NBLADE,TANBIW,RCW,RVW,UAIF,UTIF)
               UAW(N)=-UAIF/(2.0*(RC(M)-RV(N)))
               UTIF=UTIF*CRP  ! Note if CRP=0, the tangential velocity is zero--
               UTW(N)=UTIF/(2.0*(RC(M)-RV(N)))
!--------------Induction of corresponding hub-image trailing vortices (if any)--
```

```
               IF(IHUB/=0) THEN
                  RVW=XR(1)**2/RV(N)
                  TANBIW=TANBIV(1)*RV(1)/RVW
                  CALL WRENCH(NBLADE,TANBIW,RCW,RVW,UAIF,UTIF)
                  UAW(N)=UAW(N)+UAIF/(2.0*(RC(M)-RVW))
                  UTIF=UTIF*CRP
                  UTW(N)=UTW(N)-UTIF/(2.0*(RC(M)-RVW))
               END IF
            END DO
!-----------Final step in building influence functions--------------------------
            DO N=1,MT
               UAHIF(M,N)=UAW(N+1)-UAW(N)
               UTHIF(M,N)=UTW(N+1)-UTW(N)
            END DO
         END DO

!-------------------------------------------------------------------------------
!        Solve simultaneous equations for circulation strengths G(M)           !
!-------------------------------------------------------------------------------
         DO M=1,MT
            B(M)=VAC(M)*((TANBIC(M)/TANBC(M))-1.0)     ! Right-hand side
            DO N=1,MT
               A(M,N)=UAHIF(M,N)-UTHIF(M,N)*TANBIC(M)   ! Coefficient matrix
            END DO
         END DO

         CALL SIMEQN(A,B,G,IERR)           ! Simultaneous equation solver
         IF(IERR/=0) EXIT                  ! Error return for singular matrix


!-------------------------------------------------------------------------------
!        Evaluate the induced velocities from the circulation GM)              !
!-------------------------------------------------------------------------------
         DO M=1,MT
            UASTAR(M)=0.0
            UTSTAR(M)=0.0
            DO N=1,MT
               UASTAR(M)=UASTAR(M)+G(N)*UAHIF(M,N)
               UTSTAR(M)=UTSTAR(M)+G(N)*UTHIF(M,N)
            END DO
         END DO

!-------------------------------------------------------------------------------
!        Compute the forces and test if Ct has converged to desired value      !
!-------------------------------------------------------------------------------
         CALL FORCES(NBLADE,MT,ADVCO,WAKE,RV,RC,TANBC,UASTAR,UTSTAR,VAC,       &
                  CDC,CD,G,CT(KTRY),CQ,CP,KT,KQ,EFFY,RHV,CTH,IHUB)
         WRITE(*,'(I5,'' CT='',F10.5,'' DESIRED VALUE='',F10.5)') KTRY,        &
               CT(KTRY),CTDES
         IF(ABS(CT(KTRY)-CTDES)<TOL) EXIT
```

```
      END DO

!-----Stop run if matrix is sigular---------------------------------------------
      IF(IERR/=0) THEN
         WRITE(*,'(A)') ' MATRIX SINGULAR. RUN TERMINATED..... '
         STOP
      ELSE

!-------------------------------------------------------------------------------
!                     Output results to Tecplot file                           !
!-------------------------------------------------------------------------------

         WRITE(*,'(//'' EFFICIENCY ='',F8.4)') EFFY
         WRITE(*,'('' Kt, Kq'',F8.4,F8.5)') KT,KQ
         WRITE(*,'('' HUB DRAG COEFFICIENT Cth='',F8.4)') CTH

         OPEN(1,FILE='APLOT.PLT',STATUS='UNKNOWN',FORM='FORMATTED')
         WRITE(1,'(A)') ' VARIABLES="R","G","VA","VT","UA","UT","BETA","BETAI",&
                          &"CDC","CD" '
         WRITE(1,'('' TEXT X=0.5, Y=0.50, T="    Ct='',F8.4,'' "'')')          &
               CT(KTRY)
         WRITE(1,'('' TEXT X=0.5, Y=0.46, T="    Cp='',F8.4,'' "'')')          &
               CP
         WRITE(1,'('' TEXT X=0.5, Y=0.42, T="    Kt='',F8.4,'' "'')')          &
               KT
         WRITE(1,'('' TEXT X=0.5, Y=0.38, T="    Kq='',F8.4,'' "'')')          &
               KQ
         WRITE(1,'('' TEXT X=0.5, Y=0.34, T=" Va/Vs='',F8.4,'' "'')')          &
              WAKE
         WRITE(1,'('' TEXT X=0.5, Y=0.30, T="     E='',F8.4,'' "'')')          &
              EFFY
         WRITE(1,'('' TEXT X=0.5, Y=0.26, T="'',A,'' " '')')                   &
              TITLE

         WRITE(1,'(F10.5,F10.6,4F10.5,2F10.3,2F10.5)') (RC(M),G(M),VAC(M),     &
               VTC(M),UASTAR(M),UTSTAR(M),R2D*ATAN(TANBC(M)),                  &
               R2D*ATAN(TANBIC(M)),CDC(M),CD(M),M=1,MT)
         CLOSE(1)
      END IF

      STOP
      END PROGRAM PVL
```

```
!     Last change:  JE   24 Apr 2001   11:41 am
!***************     COPYRIGHT (C) 2001  JUSTIN E. KERWIN    *****************
      SUBROUTINE FORCES(NBLADE,MCP,ADVCO,WAKE,RV,RC,TANBC,UASTAR,UTSTAR,       &
                 VA,CHORD,CD,G,CT,CQ,CP,KT,KQ,EFFY,RHV,CTH,IHUB)
      IMPLICIT NONE
!--------------------- Declare the arguments ----------------------------------
      INTEGER, INTENT(IN) :: NBLADE,MCP,IHUB
      REAL, INTENT(IN) :: ADVCO,WAKE,RHV
      REAL, DIMENSION(:), INTENT(IN) :: RV,RC,TANBC,UASTAR,UTSTAR,VA,CHORD,CD,G
      REAL, INTENT(OUT) :: CT,CQ,CP,KT,KQ,EFFY,CTH

!--------------------- Declare the local variables ----------------------------
      REAL, PARAMETER :: PI=3.1415927E00, TWO=2.0E00, FOUR=4.0E00, EIGHT=8.0E00
      REAL :: DR,VSTAR,VTSTAR,VASTAR,VSTRSQ,DVISC,FKJ
      INTEGER :: M
      LOGICAL :: CD_LD

      CD_LD=.TRUE.  ! Default: Input CD interpreted as viscous drag coefficient
      IF(CD(1)>1.0) CD_LD=.FALSE. ! CD(1)>1 signals that input is L/D ----------
      CT=0.0
      CQ=0.0
      DO M=1,MCP
         DR=RV(M+1)-RV(M)
         VTSTAR=VA(M)/TANBC(M)+UTSTAR(M)
         VASTAR=VA(M)+UASTAR(M)
         VSTRSQ=VTSTAR**2+VASTAR**2
         VSTAR=SQRT(VSTRSQ)
         IF(CD_LD) THEN  ! Interpret CD as viscous drag coefficient, Cd---------
            DVISC=(VSTRSQ*CHORD(M)*CD(M))/(TWO*PI)
         ELSE            ! Interpret CD as the lift/drag ratio L/D -------------
            FKJ=VSTAR*G(M)
            DVISC=FKJ/CD(M)
         END IF
         CT=CT+(VTSTAR*G(M)-DVISC*VASTAR/VSTAR)*DR
         CQ=CQ+(VASTAR*G(M)+DVISC*VTSTAR/VSTAR)*RC(M)*DR
      END DO

      IF(IHUB/=0) THEN  ! Add hub vortex drag if hub image is present ----------
         CTH=0.5*(LOG(1.0/RHV)+3.0)*(REAL(NBLADE)*G(1))**2
      ELSE
         CTH=0.0
      END IF

      CT=CT*FOUR*REAL(NBLADE)-CTH
      CQ=CQ*TWO*REAL(NBLADE)
      CP=CQ*TWO*PI/ADVCO
      KT=CT*ADVCO**2*PI/EIGHT
      KQ=CQ*ADVCO**2*PI/EIGHT
      EFFY=CT*WAKE/CP

      RETURN
```

```
END



REAL FUNCTION VOLWK(XR,XVA)
USE DUCKMOD
IMPLICIT NONE
REAL :: YDX
INTEGER :: NX,N
REAL, DIMENSION(:), INTENT(IN) :: XR,XVA
REAL, DIMENSION(:), ALLOCATABLE :: Y
REAL, DIMENSION(:,:), ALLOCATABLE :: VWCUB
NX=SIZE(XR)
ALLOCATE ( Y(NX),VWCUB(NX-1,5) )
Y(:)=XR(:)*XVA(:)
CALL UGLYDK(0,0,XR,Y,0.0,0.0,VWCUB)
CALL INTDK1(XR(1),XR(NX),YDX,VWCUB)
VOLWK=2.0*YDX/(1.0-XR(1)**2)
DEALLOCATE (Y,VWCUB)
RETURN
END FUNCTION VOLWK
```

```
!     Last change:  JEK  28 Mar 99    5:04 pm
      MODULE PVLMOD
         INTERFACE

         SUBROUTINE SIMEQN(A,B,X,IERR)
            REAL, DIMENSION(:,:), INTENT(IN) :: A    ! Coefficient matrix
            REAL, DIMENSION(:), INTENT(IN)   :: B    ! Right hand side vector
            REAL, DIMENSION(:), INTENT(OUT)  :: X    ! Solution vector
            INTEGER, INTENT(OUT)             :: IERR ! Error flag
         END SUBROUTINE SIMEQN

         SUBROUTINE WRENCH(NB,TANB,RC,RV,UA,UT)
            INTEGER, INTENT(IN) :: NB
            DOUBLE PRECISION, INTENT(IN) :: TANB,RC,RV
            DOUBLE PRECISION, INTENT(OUT) :: UA,UT
         END SUBROUTINE WRENCH

         SUBROUTINE FORCES(NBLADE,MCP,ADVCO,WAKE,RV,RC,TANBC,UASTAR,UTSTAR,    &
                           VA,CHORD,CD,G,CT,CQ,CP,KT,KQ,EFFY,RHV,CTH,IHUB)
            INTEGER, INTENT(IN) :: NBLADE,MCP,IHUB
            REAL, INTENT(IN) :: ADVCO,WAKE,RHV
            REAL, DIMENSION(:), INTENT(IN) :: RV,RC,TANBC,UASTAR,UTSTAR,VA,    &
                                              CHORD,CD,G
            REAL, INTENT(OUT) :: CT,CQ,CP,KT,KQ,EFFY,CTH
         END SUBROUTINE FORCES

         REAL FUNCTION VOLWK(XR,XVA)
            REAL, DIMENSION(:), INTENT(IN) :: XR,XVA
         END FUNCTION VOLWK

         END INTERFACE
      END MODULE PVLMOD
```

5 APPENDIX

5.1 Derivation of Glauert's Integral

The following derivation has been extracted from Glauert's book [64], with the notation changed to conform to the present lecture notes. We start with equation 51, which defines the limiting process of the Cauchy principal value integral,

$$\fint_{0}^{\pi} f(\tilde{\xi})d\tilde{\xi} = \lim_{\epsilon \rightarrow 0} \left[\int_{0}^{\tilde{x}-\epsilon} f(\tilde{\xi})d\tilde{\xi} + \int_{\tilde{\xi}+\epsilon}^{\pi} f(\tilde{\xi})d\tilde{\xi} \right] \tag{261}$$

Considering first the value of I_0,

$$\begin{aligned}
\int_0^{\tilde{\xi}-\epsilon} \frac{d\tilde{\xi}}{\cos\tilde{x}-\cos\tilde{\xi}} &= \left[\frac{1}{\sin\tilde{x}}\log\frac{\sin\frac{1}{2}(\tilde{x}+\tilde{\xi})}{\sin\frac{1}{2}(\tilde{x}-\tilde{\xi})}\right]_0^{\tilde{\xi}-\epsilon} \\
&= \frac{1}{\sin\tilde{x}}\{\log\sin(\tilde{x}-\frac{1}{2}\epsilon)-\log\sin\frac{1}{2}\epsilon\} \\
\int_{\tilde{\xi}+\epsilon}^{\pi} \frac{d\tilde{\xi}}{\cos\tilde{x}-\cos\tilde{\xi}} &= \left[\frac{1}{\sin\tilde{x}}\log\frac{\sin\frac{1}{2}(\tilde{x}+\tilde{\xi})}{\sin\frac{1}{2}(\tilde{x}-\tilde{\xi})}\right]_{\tilde{\xi}+\epsilon}^{\pi} \\
&= \frac{1}{\sin\tilde{x}}\{\log\sin\frac{1}{2}\epsilon-\log\sin(\tilde{x}+\frac{1}{2}\epsilon)\}
\end{aligned} \tag{262}$$

and hence

$$I_0 = \lim\epsilon \rightarrow 0 \left\{\frac{1}{\sin\tilde{x}}\log\frac{\sin(\tilde{x}-\frac{1}{2}\epsilon)}{\sin(\tilde{x}+\frac{1}{2}\epsilon)}\right\} = 0 \tag{263}$$

Then

$$\begin{aligned}
I_1 &= \int_0^{\pi} \frac{\cos\tilde{\xi}}{\cos\tilde{\xi}-\cos\tilde{x}}d\tilde{\xi} \\
&= \int_0^{\pi} \left(1+\frac{\cos\tilde{x}}{\cos\tilde{\xi}-\cos\tilde{x}}\right)d\tilde{\xi} \\
&= \pi + I_0\cos\tilde{x} \\
&= \pi
\end{aligned} \tag{264}$$

---

[64] H. Glauert, *The Elements of Aerofoil and Airscrew Theory*, Cambridge University Press

and more generally if $n > 1$,

$$\begin{aligned} I_{n+1} + I_{n-1} &= \int_0^\pi \frac{\cos(n+1)\tilde{\xi} + \cos(n-1)\tilde{\xi}}{\cos\tilde{x}i - \cos\tilde{x}} d\tilde{\xi} \\ &= \int_0^\pi \frac{2\cos\tilde{\xi}\cos n\tilde{\xi}}{\cos\tilde{x}i - \cos\tilde{x}} d\tilde{\xi} \\ &= \int_0^\pi \left(2\cos n\tilde{\xi} + \frac{2\cos\tilde{\xi}\cos n\tilde{\xi}}{\cos\tilde{x}i - \cos\tilde{x}} \right) d\tilde{\xi} \\ &= 2\cos\tilde{x} I_n \end{aligned} \tag{265}$$

The solution of this recurrence formula

$$I_{n+1} - 2\cos\tilde{x} I_n + I_{n-1} = 0 \tag{266}$$

with the initial conditions $I_0 = 0$ and $I_1 = \pi$, leads to the final result,

$$I_n(\tilde{x}) = \oint_0^\pi \frac{\cos(n\tilde{\xi})}{\cos\tilde{\xi} - \cos\tilde{x}} d\tilde{\xi} = \pi \frac{\sin n\tilde{x}}{\sin\tilde{x}} \tag{267}$$

Finally, since the denominator in equation 50 contains $\tilde{\xi}$ and $\tilde{x}$ in the reverse order, the sign of the final result in equation 52 is also reversed.